UNIVERSIDAD COMPLUTENSE DE MADRID

FACULTAD DE CIENCIAS FÍSICAS

Departamento de Física Atómica, Molecular y Nuclear

TESIS DOCTORAL

Prestaciones del detector AMS-02 para el estudio del canal de positrones de los rayos cósmicos

AMS-02 detector capabilities for cosmic ray positron measurements

MEMORIA PARA OPTAR AL GRADO DE DOCTOR

PRESENTADA POR

David Crespo Roces

Director

Jorge Casaus Armentano

Madrid, 2013

David Crespo Roces

Prestaciones del detector AMS-02 para el estudio del canal de positrones de los rayos cósmicos

AMS-02 detector capabilities for cosmic ray positron measurements

Tesis Doctoral dirigida por

Dr. Jorge Casaus Armentano

Ciemat Centro de Investigaciones Energéticas, Medioambientales y Tecnológicas

Universidad Complutense de Madrid

Departamento de Física Atómica, Molecular y Nuclear

Programa de Doctorado de Física Nuclear

Memoria de tesis doctoral presentada para optar al título de Doctor en Ciencias Físicas

Prestaciones del detector AMS-02 para el estudio del canal de positrones de los rayos cósmicos

AMS-02 detector capabilities for cosmic ray positron measurements

David Crespo Roces

Tesis Doctoral dirigida por

Dr. Jorge Casaus Armentano

Curso académico 2011/2012

Preface

Este trabajo de investigación se ha llevado a cabo en el Departamento de Investigación Básica del Centro de Investigaciones Científicas, Tecnológicas y Medioambientales (CIEMAT) gracias a una beca de formación de personal investigador (FPI) concedida por el propio centro en el año 2006. El doctorando David Crespo Roces, matriculado en el programa de doctorado de Física Nuclear de la Facultad de Ciencias Físicas de la Universidad Complutense de Madrid, presenta esta tesis doctoral en el Departamento de Física Atómica, Molecular y Nuclear para optar al título de Doctor en Ciencias Físicas. Tras una petición y posterior autorización de la Comisión de Doctorado, la memoria de tesis doctoral se presenta escrita en lengua inglesa junto a un resumen amplio en español.

Contents

List of Figures

List of Tables

Introduction

AMS is an international collaboration involving universities and institues from America, Europe and Asia founded to construct a magnetic spectrometer to put into orbit. The flight of AMS-02 onboard the space shuttle Endeavour and its installation in the ISS in May 2011, was the culmination of the work started in the 1990s. From now on, there are more than ten years ahead until the end of life of the ISS to collect and analyse the composition and spectrum of cosmic rays.

The aim of this work is to obtain the cosmic ray positron signal with a Monte Carlo (MC) simulation of the AMS-02 detector with the flight configuration. To validate this result, there are available data from a test-beam of the detector with a previous configuration, data from a test-beam of the detector with the flight configuration, and MC simulation. This work relies on the first test-beam to extract the detector performances since constitutes the most suitable data sample to calibrate the electromagnetic calorimeter, a key subsystem to suppress the vast background of cosmic ray protons. The results from this test-beam are compared with the MC simulation and the flight configuration test-beam to emphasize the agreement in the performance of the subsystems involved in the proton suppression despite the last upgrade of the detector.

The thesis is divided in four parts. The first part constitutes the theoretical introduction that gives an insight into the motivation to study cosmic ray positrons and how AMS-02 makes it possible. The second part is devoted to the experiment itself, from the start to the AMS-02 launch, including a hardware and software description. The third part comprises the analysis of the electromagnetic calorimeter and the transition radiation detector using the data from the first test-beam of the detector. The last part gives the capabilities of the detector to study the cosmic ray positron signal with a MC simulation of the flight configuration, which is utterly validated with the comparison of the results from previous chapters with the detector flight configuration test-beam data. A brief description of each chapter comes next:

Chapter 1: This chapter starts with a brief galactic structure description to highlight the key features necessary to introduce the cosmic rays origin and propagation. Besides, the geomagnetic and solar effects on the low energy spectrum are summarize, to finish with the cosmic ray positron component and the latest measurements from other experiments.

Chapter 2: This chapter introduces how AMS-02 carries out the particle identification combining information from several detectors based on physical phenomena associated with the interaction of charged particles and photons with matter. There are specific sections dedicated to the ring imaging Cherenkov detectors, the transition radiation detectors and the electromagnetic calorimeters.

Chapter 3: This chapter summarizes the whole experiment, from its beginning to the launch of AMS-02, including a description of the first detector AMS-01 and its results, and a description of AMS-02 including the last detector upgrade.

Chapter 4: This chapter gives an insight into the workings of the AMS reconstruction software, and dedicates a special attention to the calorimeter and transition radiation detector own reconstructions, since they will be used throughout the following chapters.

Chapter 5: The electromagnetic calorimeter provides an electron/proton separation that is needed to reduce the cosmic proton background. The data collected in the first test-beam of the detector is used in this chapter to develop a calibration method for the calorimeter and to evaluate its electron/proton separation performance, which is compared to MC data to validate the cosmic ray positron analysis.

Chapter 6: The transition radiation detector provides an additional electron/proton separation that contributes to reduce the proton background. The data collected in the first test-beam of the detector is used in this chapter to analize the transition radiation detector performance at the same time that it is compared to MC data. A good agreement between test-beam data and MC data is required to validate the cosmic ray positron analysis.

Chapter 7: The previous results are compared in this chapter to the detector flight configuration test-beam data. A good agreement between both configurations, together with the MC simulation comparison carried out in previous chapters, validates the cosmic ray positron analysis.

Chapter 8: Since the proton suppression result obtained with test-beam data is limited to a fixed energy point, a Monte Carlo simulation of the detector flight configuration is used to extend the rejection factor to other energies in order to determine and upper limit in the positron measurement without being compromise by any contamination.

Part I

Cosmic Ray Astrophysics and Particle Detectors

1

Cosmic Ray Astrophysics

AMS-02 is a particle detector deployed in the International Space Station to measure the cosmic rays composition and spectrum. This chapter starts with a brief galactic structure description, to highlight the key features, necessary to introduce the cosmic rays origin and propagation. Besides, the geomagnetic and solar effects on the low energy spectrum are summarize, to finish with the cosmic ray positron component and the latest measurements from other experiments.

THE cosmic rays consist principally of fully ionized atomic nuclei that bombard the Earth from outer space. They were discovered from measurements carried out by Hess in 1912 with balloons (Fig. 1.1 [1]), that pointed out a rise in the intensity of the radiation with the altitude, which was explained by the existence of an external radiation entering the atmosphere [1]. The development of the cloud chamber by Wilson during those years, made possible the detection of the ionizing particle tracks. The cosmic ray study has played an important role in the development of the particle physics and their interactions, with the discovery of positrons, pions, muons, and strange particles in the 1930s and 1940s

Fig. 1.1: *Victor Hess in a balloon expedition.*

1.1 Galactic Structure

The Milky Way consists of a flat disk with a radius of $\simeq 15\,\text{kpc}$ ($1\,\text{kpc} = 3.086 \times 10^{21}\text{cm}$) and a thickness of approximately 0.5 kpc, rotating around its center [2] (Fig. 1.2(a)). Our galaxy contains $\sim 10^{11}$ stars, and new stars are formed in the interstellar medium (ISM). The old stars of earlier generations end their lives sometimes with an explosion (*supernova*, *planetary nebula*), expelling new chemical composition to the ISM as a result of the nuclear burning in the stars. With each new star generation the Galaxy becomes a little richer in heavy elements [2].

The solar system falls at a distance of 8.5 kpc from the galactic center, and the distance from the Sun center to the Earth is 1 astronomical unit ($1\,\text{UA} = 1.5 \times 10^{23}\text{cm} = 5 \times 10^{-9}\text{kpc}$). Charged particles, mainly protons, are expelled from the *solar corona* due to the solar activity (*flares*

[1] Photo from `http://www.aps.org/publications/apsnews/201004/physicshistory.cfm`.

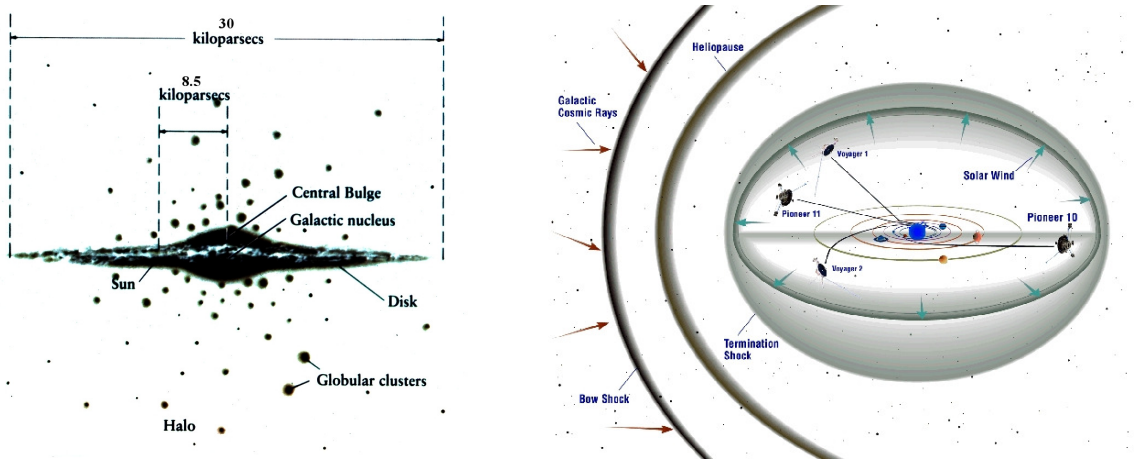

(a) (b)

Fig. 1.2: *Milky Way structure (1.2(a)). Heliosphere structure (1.2(b)).*

and *sunspots*) (Fig. 1.4 [2]). This solar wind, that carries the Sun magnetic field, blows a cavity in the interstellar medium called heliosphere, that has a radius of $\simeq 100\,\mathrm{UA}$ [2] (Fig. 1.2(b) [3]).

1.1.1 Interstellar Medium

Gas and dust are the two constituents of the interstellar medium with an average mass ratio of 100:1 [2]. The interstellar dust absorbs ultraviolet and optical photons and re-emits the radiation at infrared wavelengths [2], while the interstellar gas is composed of hydrogen (70 % of the mass gas), helium (28 %) and 2 % of heavier elements. The hydrogen appears in different states: atomic hydrogen (H_I), molecular hydrogen (H_2), and ionized hydrogen (H_{II}) [2–4] (Fig. 1.3(a) and 1.3(b)).

1.1.2 Cosmic Magnetic Fields

Different observational methods, based on *synchrotron* emission, *Faraday rotation* , *Zeeman splitting*, polarization of starlight and polarization of dust infrared emission, are used to probe the interstellar magnetic fields that are along the spiral arms [6]. The observed field strengths are of the order of $10^{-6}\,\mathrm{G}$ [2] and there exits several theoretial models that have been proposed to describe the spatial structure of the large-scale magnetic fields in the Galaxy: the *ring model*, the *axisymmetric spiral model* (ASS), and the *bisymmetric spiral model* (BSS) [6].

1.2 Cosmic Ray Clasification

The cosmic ray particles have a wide energy spectrum and depending in their origin can be clasified as: solar, anomalous, and galactic.

[2] Photo from `http://sohowww.nascom.nasa.gov/gallery/images.html`.
[3] Image from `http://science.nasa.gov/headlines/y2001/ast03may_1.htm`.

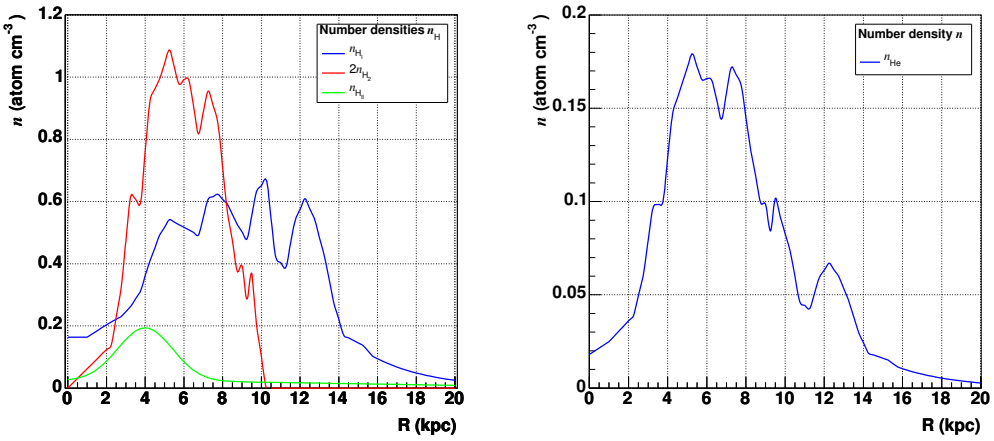

(a) H_I, $2H_2$ and H_{II} (b) He

Fig. 1.3: *Number densities of atomic hydrogen (H_I), molecular hydrogen (H_2), ionized hydrogen (H_{II}), and helium (He) as function of the galaxy radius R and galactic height $z = 0$ kpc. The figures have been plotted using data extracted from GALPROP [5].*

1.2.1 Solar Cosmic Rays

The solar cosmic rays are the product of solar flare eruptions and *coronal mass ejections* (Fig. 1.4[4]), both originated on regions of the Sun's surface with *sunspots*. The expelled charged particles (protons, electrons and heavy nuclei), known as well as solar energetic particles (SEP), have energies from few tens of keV/nucleon to several GeV/nucleon [2, 7].

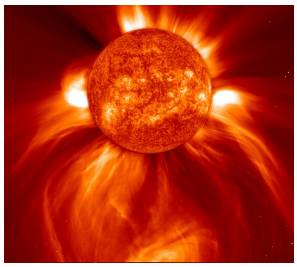

Fig. 1.4: *Coronal mass ejection (CME) seen by the Solar and Heliospheric Observatory (SOHO).*

1.2.2 Anomalous Cosmic Rays

Reported as an anomalous enhancement in the low-energy espectra of elements like O, N, He and Ne in the 1970s [2,8] and confirmed in the 1980s from Voyager observations [9], their origin is in the interstellar neutral particles that become ionized in the heliosphere by the solar wind and then accelerated to energies within 1-100 MeV/nucleon, probably at the solar wind *termination shock* [10, 11].

1.2.3 Galactic Cosmic Rays

Their origin is associated with the most energetic processes in the universe such as *supernova* explosions, and they are accelerated by shock waves associated with the expansion of the supernova remnants (SRNs) into the interstellar medium [12]. They can arrive directly from the source (primary cosmic rays) or as a product of the interaction and spallation (fragmentation) of the former in the interstellar medium (secondary cosmic rays).

The cosmic radiation that arrives at the heliosphere is made up of nucleons (98 %) and electrons and positrons (2 %). Within the energy range 10^8–10^{10} eV/nucleon, the nuclear

[4] Photo from `http://sohowww.nascom.nasa.gov/gallery/images.html`

component consists of hydrogen ($\sim$ 87 %), helium ($\sim$ 12 %), and heavier nuclei ($\sim$ 1 %) [2]. The relative elemental abundances exhibit similarities, but also significant differences, with the solar system abundances (Fig. 1.5(a)):

- Both of them show the odd-even effect, a result of the pairing interaction [13] that make the even-even nuclei (even N and even Z) more stable than odd-even nuclei and odd-odd nuclei. Therefore, the production of even-even nuclei is more frequent in the thermonuclear reactions in stars. The likeness in the peaks of C, N, O, and Fe suggests that many of the cosmic ray nuclei must be of stellar origin.

- The differences between the cosmic and solar abundances in the peaks of Li, Be, and B are due to the spallation of C and O nuclei in the interstellar medium. In a similar way, the abundance of Sc, Ti, V, and Mn in the cosmic rays is due to the spallation of the Fe and Ni nuclei [14].

The galactic cosmic rays energy spectrum follows a power law (Fig. 1.5(b)):

$$\frac{dN}{dE}(E) = kE^{-\gamma} \tag{1.1}$$

The spectral index γ has a value of 2.7 up to 10^{15} eV/nucleon. Above this energy, the spectrum steepens to an index 3. This feature (knee) is attributed to the leakage of cosmic rays from the galaxy [1, 15] together with the fact that 10^{15} eV/nucleon is the maximum energy that *supernova* explosions can supplyd [15]. Above 5×10^{18} eV the spectrum flattens again (ankle), probably a sign of a harder component of extragalactic origin emerging over the galactic component [1, 15]. Above 4×10^{19} eV, protons would rapidly loss energy by their interaction with the cosmic microwave radiation (CMB) [15]:

$$p + \gamma \longrightarrow p + \pi^0 \qquad , \qquad p + \gamma \longrightarrow n + \pi^+ \tag{1.2}$$

The GZK cutoff, confirmed for the highest energies by HiRes [16] and Auger [17] observations, is also an evidence of the dominance of the proton component [18]. Another signature of extragalactic protons in the spectrum is the dip [19]

$$p + \gamma \longrightarrow p + e^+ + e^- \tag{1.3}$$

clearly seen in the spectra observed by Yakutsk [20], AGASA [21], HiRes [16], and Auger [22] arrays. This good agreement must be considered as a proof of a large fraction of protons in the spectrum [19]. The most obvious candidates for events with energies above 10^{20} eV are *active galactic nuclei* (AGN) and *gamma ray burst* (GRB) [17, 23].

1.2.3.a Galactic Cosmic Rays Propagation

The measurements of the secondary to primary cosmic ray ratios indicate that particles traverse on average a column density of 5–10 g/cm^2, but the amount of matter along the line of sight through the galactic disk is about 10^{-3} g/cm^2. This implies travel distances thousands of times greater than the thickness of the galactic disk, suggesting that diffusion processes take place in the galactic cosmic rays propagation [25]. The transport equation for a particular cosmic ray particle species can be written in a general form as [26]:

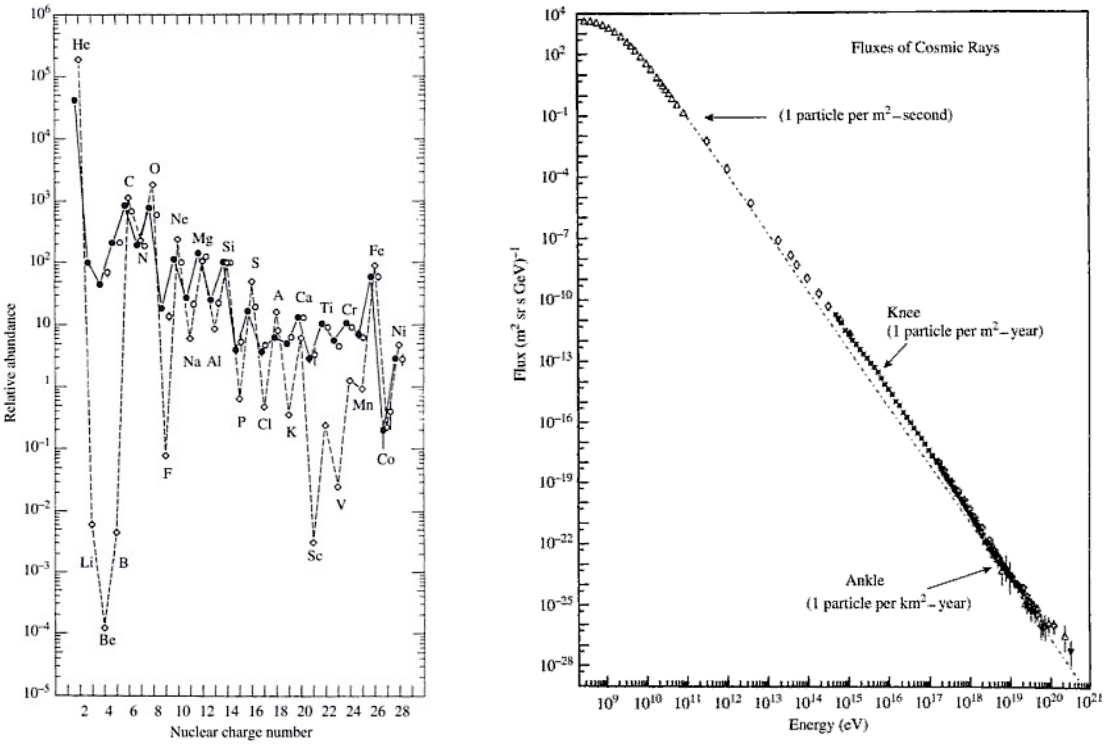

(a) (b)

Fig. 1.5: *Cosmic ray nuclei abundances (solid line) compared with the solar abundances (dash line) (Fig. 1.5(a) from [24]). Spectrum of cosmic rays (Fig. 1.5(b) from [1]).*

$$\frac{\partial\psi(\vec{r},p,t)}{\partial t} = \overbrace{q(\vec{r},p,t)}^{1} + \overbrace{\nabla\cdot D\nabla\psi}^{2} - \overbrace{\nabla\cdot\vec{V}\psi}^{3} + \overbrace{\frac{\partial}{\partial p}p^2 D_{pp}\frac{\partial}{\partial p}\frac{1}{p^2}\psi}^{4} - \overbrace{\frac{\partial}{\partial p}\left[\dot{p}\psi - \frac{p}{3}(\nabla\cdot\vec{V})\psi\right]}^{5} - \overbrace{\frac{1}{\tau_f}\psi}^{6} - \overbrace{\frac{1}{\tau_r}\psi}^{7} \tag{1.4}$$

where $\psi(\vec{r},p,t)$ is the cosmic ray density per unit of particle momentum p at position $\vec{r}$, D is the spatial diffusion coefficient, $\vec{V}$ is the convection velocity, D_{pp} is the diffusion coefficient in momentum space, τ_f is the timescale for loss by fragmentation and τ_r is the timescale for radioactive decay. The differents terms of the equation are:

1. Source term that includes primary, spallation, and decay contributions.

2. Diffusion term due to the scattering of cosmic ray particles on random magnetohydrodynamic (MHD) waves and discontinuities.
   The diffusion coefficient is $D \sim 3\text{–}5\times10^{28}\,\mathrm{cm^2 s^{-1}}$ at energy $\sim 1\,\mathrm{GeV/nucleon}$.

3. Convection term due to galactic winds.

4. Energy loss term (see section 1.5 for different energy loss processes).
5. Reacceleration term due to the scattering of cosmic ray particles on random MHD waves that leads to stochastic acceleration.
6. Interaction term (spallation).
7. Radioactive decay term.

1.3 Geomagnetic and Solar Effects

Charged particles below 10 GeV/nucleon show directional and time dependence, since they are affected by the Earth's magnetic field and also by the solar wind.

1.3.1 Rigidity Cut-off

The Earth's magnetic field is a barrier for cosmic ray particles with low rigidities, since they follow spiral trajectories along the field lines losing their energy. The minimal rigidity ($R = pc/|Z|e$) that a particle must have in order to go through the magnetic field is called the rigidity cut-off. The Earth's magnetic field can be approximated by a dipole field, and the rigidity cut-off can be calculated using the Størmer equation [14, 27]

$$R = M \frac{\cos^4 \lambda}{r^2 \left(1 + \sqrt{1 - \sin\theta \cos^3 \lambda}\right)^2} \tag{1.5}$$

where r is the distance from the dipole center expressed in earth radii, λ is the geomagnetic latidude, θ is the incident particle azimuthal angle, and the dipole moment M has a value of $\sim$ 58 GV for the IGRF [5] 2000 magnetic field model [27]. The angle θ is called positive for particles moving from east to west, while it is negative for particles moving in the opposite direction. For vertically approaching particles ($\theta = 0$) the rigidity cut-off is reduced to

$$R = 14.5\,\mathrm{GV} \frac{\cos^4 \lambda}{r^2} \tag{1.6}$$

From Eq. 1.6, the rigidity cut-off at the magnetic equator ($\lambda = 0$) and at a distance from the center of the dipole equal to the Earth radius ($r = 1$) is 14.5 GV. For particles from the eastern horizon ($\sin\theta = +1$) at the magnetic equator and $r = 1$, using the Eq. 1.5, the rigidity cut-off is 58 GV, while for particles from the western horizon ($\sin\theta = -1$) is 9.95 GV. This east-west asymmetry is observed at all altitudes, and it is the so-called east-west effect.

The Earth's magnetic field is not a perfect dipole, and an accurate determination of the geomagnetic cut-off requires a detailed model of the geomagnetic field together with a computational method to calculate the allowed particle trajectories.

1.3.2 South Atlantic Anomaly

The Earth's magnetic field is anomalously weak in the region above the South Atlantic [28], which allows charged cosmic rays to reach lower into the atmosphere, increasing the local flux. The location of the South Atlantic Anomaly (SAA) is also found to drift westwards [29]. The existence of the SAA interferes the communication with satellites and other spacecrafts.

[5] International Geomagnetic Reference Field

1.3.3 Solar Modulation

The plasma of protons and electrons ejected from the *solar corona* to the interplanetary medium is known as solar wind. The Sun magnetic field is frozen into this plasma, and is dragged radialy outward from the Sun, so the resulting large-scale field pattern is an Archimedes spiral. Superimposed on this large-scale field are numerous small-scale field irregularities generated by the turbulance and inestabilities in the *solar corona* and interplanetary medium. The charged extrasolar cosmic rays with rigidity $\lesssim 10\,\mathrm{GV}$ move along the large-scale interplanetary magnetic field and they are scattered by the small-scale magnetic field irregularities with the result of a lower density of extrasolar cosmic rays observed at Earth [2].

The modulation models are based in the cosmic ray transport equation formulated by Parker [30], which describes the propagation of the cosmic rays through the heliosphere taking into account different processes such as convection, gradient and curvature drifts, diffusion, adiabatic energy changes and sources [31].

Gleeson and Axford [32] found an approximation of that equation, the so-called force-field approximation. The modulated flux $F(r, R, t)$ at a radial distance r from the Sun, at a time t and for a cosmic ray particle of energy E, is related to the time independent interstellar flux $F(\infty, E)$ by the function [33]

$$F(r, E, t) = \frac{E^2 - E_0^2}{(\Phi(t) + E^2) - E_0^2} F(\infty, \Phi(t) + E) \tag{1.7}$$

where $\Phi(t)$ is a parameter that can be interpreted as the energy loss suffered by the cosmic ray particle along its path to the Earth from out of the heliosphere. The paremeter Φ is related to the solar modulation parameter ϕ by the expression $\Phi = |Z|e\phi$.

It is known that the modulation depends upon the sign of the particle's charge [34]. The orientation of the solar magnetic field leads to an alternating magnetic polarity in successive solar cycles (11 yr for each polarity) and more precise models take into account this effect [35]. The precise measurements of the electron and positron spectra could be used to obtain information on the charge sign dependence of the solar modulation.

1.4 Cosmic Rays Interaction with Earth Atmosphere

When the cosmic rays reach the top of the Earth's atmosphere (approximately at 40 km of altitude, $1000\,\mathrm{g/cm^2}$ of column density and $5\,\mathrm{g/cm^2}$ of residual column density [15]) interact with atomic nuclei of the air and iniate electromagnetic and hadronic cascades or 'showers'. The *radiation length* for photons and electrons in air is $X_0 = 36.66\,\mathrm{g/cm^2}$, and the *interaction length* for hadrons in air is $\lambda = 90.0\,\mathrm{g/cm^2}$. Therefore, the atmosphere corresponds to a depth of 27 radiation lengths, for photons and electrons, and to 11 interaction lengths for hadrons, leaving slim probability to the arrival of original cosmic rays at sea level. Approximately 80 % of the charged component at sea level are muons, the rest are nucleons (protons and neutrons), electrons, and positrons. Apart from charged particles, there are detected photons and electron and muon neutrinos at sea level [15, 25]. The proton/muon ratio at sea level varies with the momentum of the particles. At low momenta ($\approx 500\,\mathrm{MeV}/c$) a p/μ ratio $N(p)/N(\mu)$ of about 10 % is observed, decreasing to larger momenta ($N(p)/N(\mu) \approx 2\,\%$ at $1\,\mathrm{GeV}/c$ and $N(p)/N(\mu) \approx 0.5\,\%$ at $10\,\mathrm{GeV}/c$) [15].

1.5 Cosmic Ray Positrons

Cosmic ray electrons and positrons interact with the interstellar medium exclusively through electromagnetic processes. The following interaction processes may occur (Fig. 1.6) [2]:

- *Synchrotron* radiation emitted when the electrons move within the cosmic magnetic fields.
- Bremsstrahlung radiation emitted when the electrons are deflected in the electrostatic potencial of an atom, ion or molecule. There exists bremsstrahlung in the neutral gas (1) and in the hydrogen plasma (2) of the interstellar medium.
- Ionization and excitation of atoms and molecules when the electrons traverse the interstellar medium.
- Coulomb interactions of electrons with ionized plasmas.
- Inverse Compton scattering of ambient photon gases (CMB and infrared and optical starlight photons).
- Triple pair production in ambient photon gases with photon-electron collisions ($e_0 + \gamma \rightarrow e + e^+ + e^-$).

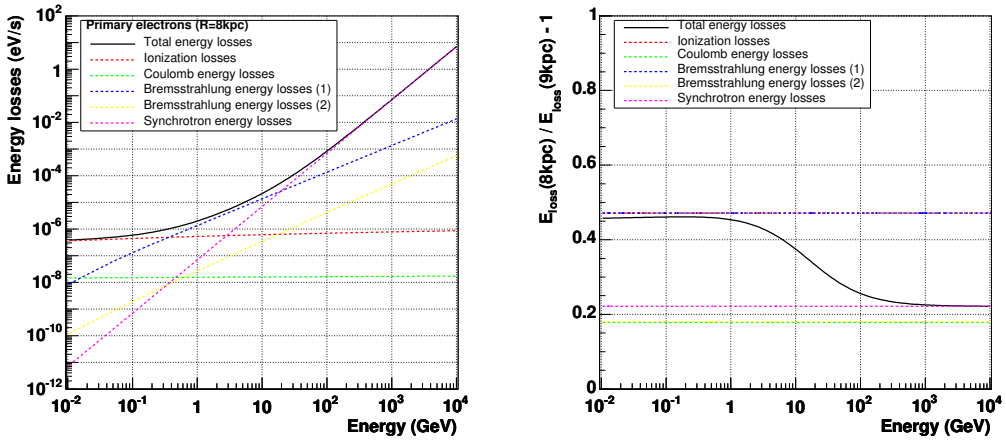

(a) (b)

Fig. 1.6: *Electron energy losses at galaxy radius $R = 8\,kpc$ and galactic height $z = 0\,kpc$ (Fig. 1.6(a)). Electron energy losses variations between galaxy radius $R = 8\,kpc$ and $R = 9\,kpc$ (galactic height $z = 0\,kpc$) (Fig. 1.6(b)). The figures have been plotted using data extracted from GALPROP [5].*

The dominant processes are bremsstrahlung and ionization up to energies of few GeV, and synchrotron radiation and inverse Compton scattering at higher energies. Because of the small electron mass ($m_e = 0.511\,\mathrm{MeV}/c^2$), the electrons and positrons undergo severe energy loss caused by synchrotron, bremsstrahlung and inverse Compton, which do not significantly affect the nucleonic cosmic ray components, since these interactions involve the Thomson cross-section σ_T (proportional to the square of the electron radius $r_0 = e^2/(m_e c^2)$, $\sigma_T = (8\pi/3)r_0^2 = 6.65\times10^{-25}\,\mathrm{cm}^2$). For a cosmic ray nucleus of charge Ze and mass $M = Am_p$ (proton mass $m_p = 938.27\,\mathrm{MeV}/c^2$), the corresponding cross-section σ_N would be

$$\sigma_N = \left(\frac{Z^4}{A^2}\right)\left(\frac{m_e}{m_p}\right)^2 \sigma_T = 1.97 \times 10^{-31}\frac{Z^4}{A^2}\mathrm{cm}^2 \tag{1.8}$$

where σ_N takes into account the nucleon radius $R_0 = (Ze)^2/(Am_pc^2) = (Z^2/A)(m_e/m_p)r_0$. Therefore, the electrons and positrons lose energy more rapidly than nuclei and the energy distributions of the former are expected to be much steeper than the energy distributions of the cosmic ray nuclei. Another consequence is the proximity of the electron sources to the solar system, e.g., TeV electrons accelerated in SNRs at distances larger than $\sim 1\,$kpc do not reach the solar system [36].

Measurements of the combined spectrum $(e^- + e^+)$ [37] have shown that the combined intensity is $\sim 1\,\%$ of the proton intensity at 10 GeV, and that the power-law index (Eq. 1.1) of the electron spectrum above 10 GeV is ~ 3.0, in contrast to the proton index of ~ 2.7.

The hadronic interactions between nuclear cosmic rays and nuclei in the interstellar medium is a secondary source of electrons and positrons in roughly equal numbers, although the observed positron fraction $e^+/(e^-+e^+)$ at the top of the atmosphere is $\sim 10\,\%$ at a few GeV [38] with a rise above 10 GeV (Fig. 1.7(a)), increase reported by the PAMELA experiment [39] and more recently by FERMI [40], confirming earlier indications from HEAT [41] and AMS-01 [42]. Hence, the majority of the electrons have to be of primary origin, and the increase in the cosmic ray positron fraction above 10 GeV would require the appearance of a new source of primary positrons, whose nature has been widely discussed, and goes from nearby *pulsars* [43] to dark matter annihilation in the galactic halo [44].

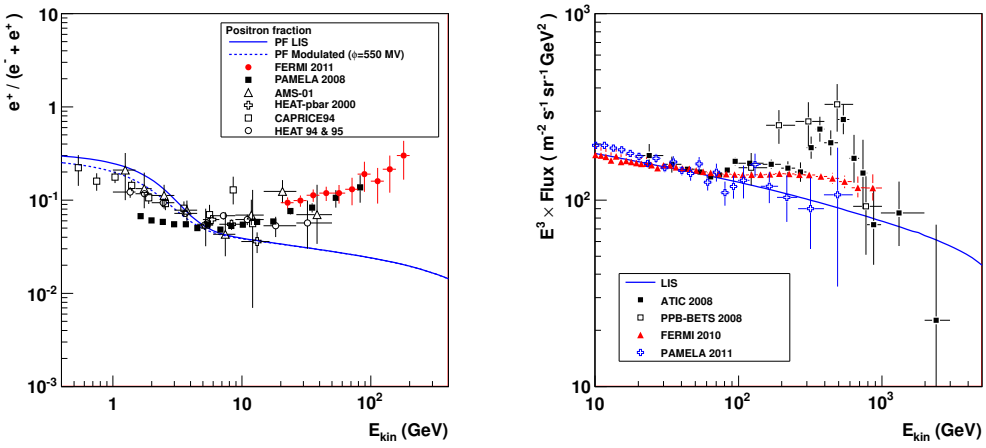

(a) $e^+/(e^- + e^+)$ (b) $e^- + e^+$

Fig. 1.7: *Cosmic ray positron fraction from results of HEAT [41, 45], CAPRICE [46], AMS-01 [42], PAMELA [39], and FERMI [40] together with a propagation model for purely secondary positron production and primary an secondary electron production (solid blue line) from [5, 47] (Fig. 1.7(a)). Electron plus positron spectrum from ATIC [48], PPB-BETS [49], FERMI [50] and electron spectrum from PAMELA [51] together with a propagation model for purely secondary positron production and primary an secondary electron production (solid blue line) from [5, 47] (Fig. 1.7(b)).*

Few years ago, the ATIC [48] and PPB-BETS [49] experiments reported a prominent feature in the cosmic ray electron plus positron spectrum around 600 GeV (Fig. 1.7(b)), that could indicate the presence of a nearby primary source of electrons and positrons. Nevertheless, the

more recent results from FERMI [40, 50] and PAMELA [6] [51] experiments, do not show any significant spectral feature and the data can be interpreted in terms of conventional diffusive propagation models, although it is also consistent with models including new cosmic ray sources that could explain the rise in the positron fraction.

Because of the low intesity of the $e^{\pm}$ signals in contrast to the large proton background (Fig. 1.8(a)), with a flux 10^3–10^5 greater than the positron flux (Fig. 1.8(b)), a rejection factor against protons of 10^4–10^6 is needed to properly identify e^+, plus an accurate measurement of the charge sign to reject e^-.

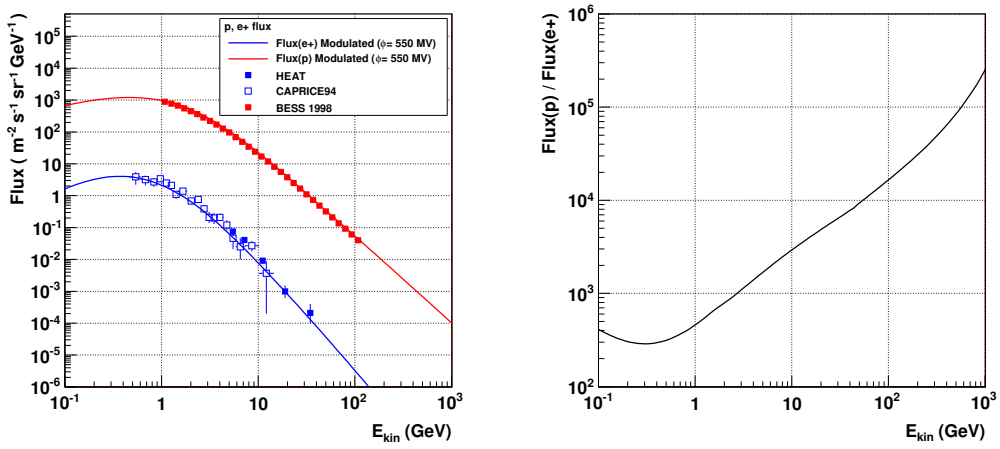

(a) (b)

Fig. 1.8: *Cosmic ray positron flux from results of HEAT [52] and CAPRICE [46], and proton flux from BESS [53] together with a propagation model for positrons (solid blue line) from [47] and a propagation model for protons (solid red line) from [26] (Fig. 1.8(a)). Ratio of the proton and positron fluxes (Fig. 1.8(b)).*

[6] The reference includes only the electron flux

2

Particle Detector Physics

AMS-02 is a magnetic spectrometer that makes possible the distinction between particles and antiparticles to searh primordial antimatter and measure antimatter components of the cosmic rays. This chapter introduces how AMS-02 carries out a particle identification combining information from several detectors based on physical phenomena associated with the interaction of charged particles and photons with matter.

In order to identify a particle it is necessary to determine its mass and electrical charge. The deflection of a particle trajectory with a radius of curvature r in a magnetic field B, can be tracked to provide a measure of the rigidity R ($R = rBc$). Once the rigidity is known, the momentum can be obtained from

$$p = ZeR \tag{2.1}$$

if the charge Ze is measured. The absolute charge value can be determined from the particle energy loss by inozation in active parts of the detector (Bethe-Block formula) or using a Cherenkov detector. The charge sign can be obtained from the bending sign in the magnetic field together with the particle direction. Eventually, if the velocity β is already measured, the particle mass is provided by the equation

$$p = mc\gamma\beta \tag{2.2}$$

where the velocity can be obtained from time of flight measurements or the detection of Cherenkov radiation.

AMS-02 measures the charge sign and absolute value, the velocity and the rigidity of the particles. Besides, in order to reduce the misidentification probability, the detector has been designed to provide multiple redundant measurements of the velocity and the absolute charge. The velocity is measured by a Time of Flight counter (TOF), a Ring Imaging Cherenkov Detector (RICH) and a Transition Radiation Detector (TRD), since the TRD response depends on the particle Lorentz factor γ ($\gamma = 1/\sqrt{1-\beta^2}$). On the other hand, the absolute charge is measured by the TOF, the RICH and the Tracker system. Besides, the TOF is used to distinguish downward from upward going particles, and the inclusion of a Electromagnetic Calorimeter (ECAL) enhancements the electron-proton (e/p) separation provided by the TRD.

2.1 Time Of Flight Counters

The particle velocity $v = \beta c$ can be determined by the measure of its time of flight t between two points separated by a distance L

$$t = \frac{L}{\beta c} \tag{2.3}$$

Besides, a TOF counter can provide a particle identification at low momentum [54]. Two particles of mass m_1 and m_2 have for the same momentum and flight distance L the time of flight difference

$$\Delta t = L\left(\frac{1}{v_1} - \frac{1}{v_2}\right) = \frac{L}{c}\left(\frac{1}{\beta_1} - \frac{1}{\beta_2}\right) \tag{2.4}$$

Using $pc = \beta E$

$$\Delta t = \frac{L}{pc^2}\left(E_1 - E_2\right) = \frac{L}{pc^2}\left(\sqrt{p^2c^2 + m_1^2c^4} - \sqrt{p^2c^2 + m_2^2c^4}\right) \tag{2.5}$$

If $p^2c^2 >> m_{1,2}^2c^4$, the expansion of the square roots leads to

$$\Delta t = \frac{Lc}{2p^2}(m_1^2 - m_2^2) \tag{2.6}$$

For a time of flight difference three times the time resolution ($\Delta t = 3\sigma_t$) and a flight distance of 1.2 m, the e/p separation can be achived up to $p \simeq 1.9\,\mathrm{GeV}/c$ for a time resolution of $\sigma_t = 160\,\mathrm{ps}$. Particle misidentification will occur if Δt is comparable to the detector resolution σ_t, i.e., at hight momentum p.

2.2 Ring Imaging Cherenkov Detectors

The Cherenkov radiation is emitted when the velocity v of a charged particle is greater than the velocity of the light c/n in a medium with refractive index n. The angle between the emitted Cherenkov photons and the trajectory of the charged particle is [54]

$$\cos\theta = \frac{1}{n\beta} \tag{2.7}$$

The radiation is emitted forwards, and is distributed over the surface of a cone with vertical angle 2θ. There exists a threshold in the particle velocity, since $|\cos\theta| \leq 1$ (Fig. 2.1(a))

$$\beta_{th} = \frac{1}{n} \tag{2.8}$$

and when $\beta \to 1$ the Cherenkov angle reaches a maximum

$$\cos\theta_{max} = \frac{1}{n} \tag{2.9}$$

On the other hand, the number of photons emitted per unit path length and per unit energy interval of the photons is proportional to the square ot the particle charge and it is independent on the particle mass [55]

$$\frac{d^2N}{dEdx} = \frac{\alpha z^2}{\hbar c}\left(1 - \frac{1}{\beta^2 n^2(E)}\right) = \frac{\alpha z^2}{\hbar c}\sin^2\theta \tag{2.10}$$

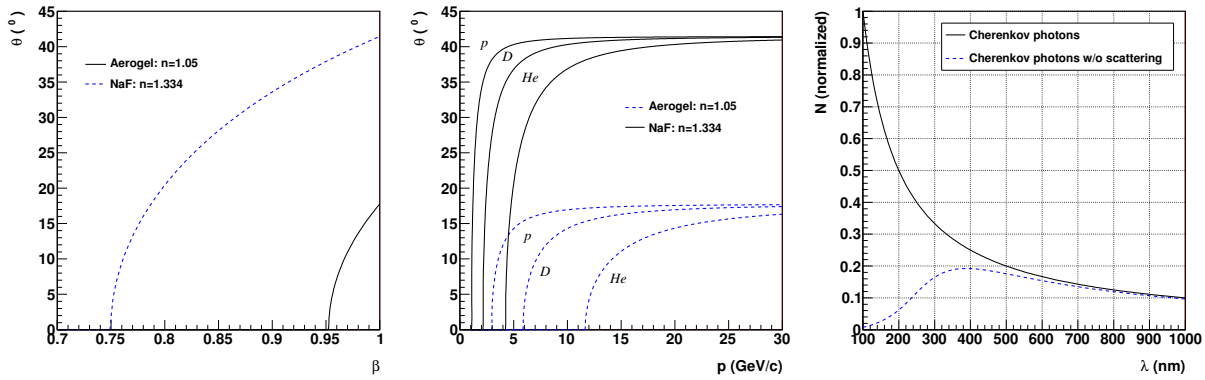

(a) (b) (c)

Fig. 2.1: *Cherenkov angle θ variation with particle velocity β for two different refractive indices: $n = 1.06$ (aerogel) and $n = 1.334$ (*NaF*) (Fig. 2.1(a)). Momentum range covered by a RICH device with two radiators, $n = 1.06$ (aerogel) and $n = 1.334$ (*NaF*), for protons (p), deuterium (D), and helium (*He*) (Fig. 2.1(b)). Cherenkov photons spectrum, Eq.* (2.11)*, and Cherenkov photons spectrum without been scattered (Fig. 2.1(c)).*

where θ is the Cherenkov angle, z is the electric charge of the particle, α is the fine structure constant, and $\hbar$ is the reduced Plank constant ($\hbar = h/2\pi$). Taking into account that $E = \hbar\omega$, $\omega = 2\pi\nu$, and $\nu = c/\lambda$, the Eq. (2.10) can be written as

$$\frac{d^2N}{dxd\lambda} = \frac{2\pi\alpha z^2}{\lambda^2}\left(1 - \frac{1}{\beta^2 n^2(\lambda)}\right) \tag{2.11}$$

A Ring Imaging Cherenkov detector (RICH) consists of two basic elements: a radiator and a photon detector [56]. The radiation emitted in a transparent dielectric medium is detected by the conversion of the Cherenkov photons in a plane of photon detectors. This provides a measurement of the Cherenkov photons position that allows to infer the emission angle θ. From Eq. (2.2), therefore, the particle mass can be determined

$$m = p\sqrt{n^2\cos^2\theta - 1} \tag{2.12}$$

All transparent materials are candidates for Cherenkov radiators, and its election will determine the particle identification momentum range covered by the detector (Fig. 2.1(b)). With a refractive index between liquids and heavy gases, the *silica aerogel* ($1.007 < n < 1.13$) is a commonly used material that has a simple relationship between the index of refraction and the aerogel density (in g/cm^3) [54]

$$n = 1 + 0.21\rho \tag{2.13}$$

The behaviour of visible light in aerogel is dominated by *Rayleigh scattering*, which causes a completely lost of directionality of the Cherenkov radiation. The short wavelengths are the most affected by this scattering mechanism. The measured transmittance T of an aerogel sample of thickness L, as function of the light wavelength λ in the range from 300 nm to 700 nm is [57]

$$t = Ae^{-CL/\lambda^4} \tag{2.14}$$

where C characterizes the aerogel *clarity* ($\mu m^4 cm^{-1}$), and A (no dimensions) is the measured transmission in the long-wavelength region. Values of A and C close to 1 and 0 respectively assures a good optical quality. The fraction N of photons of wavelength λ that are not scattered when they traverse an aerogel sample of thickness L is

$$N = A\lambda^4 \left(\frac{1 - e^{-CL/\lambda^4}}{CL} \right) \tag{2.15}$$

The figure 2.1(c) shows the Cherenkov photons spectrum yielded for protons with $\beta \simeq 1$ that traverse an aerogel sample ($n = 1.05$, $L = 25\,mm$, $A = 0.97$, and $C = 0.005\,\mu m^4 cm^{-1}$). The number of Cherenkov photons that traverse the aerogel without any scattering must be enough to allow the measurement of the Cherenkov angle with the required accuracy.

2.3 Transition Radiation Detectors

The transition radiation is emitted when charged particles move across the interface of two media with different dielectric constants [58]. The energy radiated increases with the Lorentz factor γ of the particle, which is useful for particle identification at high energies. The transition radiation intensity can be expressed as [58]

$$\frac{dW}{d\omega d\theta} = \frac{2\alpha z^2 \hbar}{\pi} f_0(\theta) \tag{2.16}$$

with

$$f_0(\theta) = \theta^3 \left(\frac{1}{\gamma^{-2} + \theta^2 + (\omega_1/\omega_2)^2} - \frac{1}{\gamma^{-2} + \theta^2 + (\omega_2/\omega_2)^2} \right)^2 \tag{2.17}$$

where θ is the angle of emission with respect to the trajectory of the particle, α is the fine structure, ω is the frequency (energy) of the radiated photon, and ω_1 and ω_2 are the *plasma frequencies* of the initial and final medium respectively (for commonly used plastic radiator $\hbar\omega_p \approx 20\,eV$ [54]). The distribution $f_0(\theta)$ has a peak at the narrow angle $\theta \simeq \gamma^{-1}$ and extends to the angle of order $(\gamma^{-2} + (\omega_2/\omega)^2)^{1/2}$ (Fig. 2.2(a) and 2.2(b)). This implies that the transition radiation photons are mostly emitted at very small angles with respect to the charged particle direction, and the ionization loss (dE/dx) of the particle will be deposited in the detector together with the transition radiation component [55].

The integration of Eq. (2.16) over the angles yields the energy spectrum [59]

$$\frac{dW}{d\omega} = \frac{\alpha z^2 \hbar}{\pi} \left(\frac{\omega_2^2 + \omega_1^2 + 2\omega^2\gamma^{-2}}{\omega_2^2 - \omega_1^2} \ln \frac{\gamma^{-2} + (\omega_2/\omega)^2}{\gamma^{-2} + (\omega_1/\omega)^2} - 2 \right) \tag{2.18}$$

For large ω_2^2/ω_1^2 (of the order of 10^3) the radiation yield drops sharply for frequencies $\omega > \gamma\omega_p$. The spectrum of radiation is mostly in the X-ray region, decreasing with the radiation energy (Fig. 2.2(c)). The average energy of the X-ray photons increases with γ.

Integrating the Eq. (2.18) (vacuum as initial medium, $\omega_1 = 0$), the energy radiated from a single boundary is [55]

$$W = \frac{1}{3}\alpha z^2 \hbar \omega_p \gamma \tag{2.19}$$

About half the energy is emitted in the range $0.1\omega_p < \omega < \omega_p$.

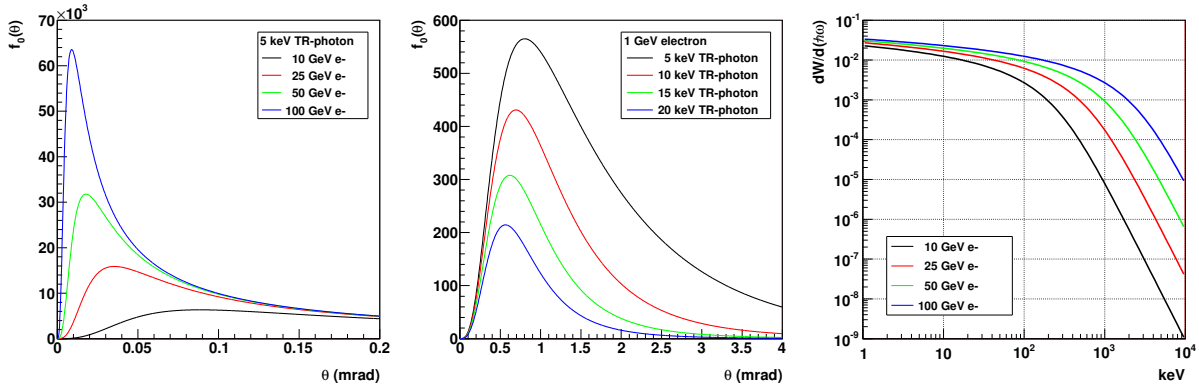

(a) (b) (c)

Fig. 2.2: *Angular distribution, Eq.* (2.17)*, of transition radiation with different charged particle energies (Fig. 2.2(a)) and photon energies (Fig. 2.2(b)). Radiated TR spectrum (Eq.* (2.18) *(keV/keV)) for different charged particle energies (Fig. 2.2(c)). The three figures are for transitions from vacuum* ($\omega_1 = 0$) *to polyethylene* ($\omega_2 = 20.9\,eV$).

The number of emitted transition radiation photons with energy $\hbar\omega$ higher than a certain threshold $\hbar\omega_0$ is [54]

$$N_\gamma(\omega > \omega_0) \approx \frac{\alpha z^2}{\pi}\left[\left(\ln\frac{\gamma\omega_p}{\omega_0} - 1\right)^2 + \frac{\pi^2}{12}\right] \tag{2.20}$$

Because of the small probability of emission for an X-ray photon at each interface ($N \simeq \alpha$, $\alpha \approx 1/137$), the production of transition-radiation photons can be enhanced if the charged particle traverses a large number of boundaries, although must be a balance since increasing the material also increases the absorption.

2.4 Calorimeters

The calorimetric particle identification technique imply the total absorption of the particle energy in a bulk of material, so no further measurements can be made on the particle, in contrast to TOF, Cherenkov and transition-radiation techniques.

In the case of electromagnetic calorimeters, the total particle kinetic energy is deposited in the detector, since the high-energy photons or electrons interact with the material, producing secondary particles which leads to a shower development, e.g. (Fig.2.3(d)), an incoming electron will first emit a bremsstrahlung photon. If the energy of the bremsstrahlung photon is high enough it will produce an electron-positron pair, and each of them will emit bremsstrahlung photons. This cascade process will continue until the secondary particles energy falls below the *critical energy* E_c, position where the maximum of the shower and the maximum number of shower particles N_{max} is reached. Beyond this point, the number of particles decrease due to ionization in the case of electrons and to Compton scattering and photoelectric absorption in the case of photons [54, 60].

The longitudinal distribution of the energy deposition in electromagnetic showers can be described by the equation [54]

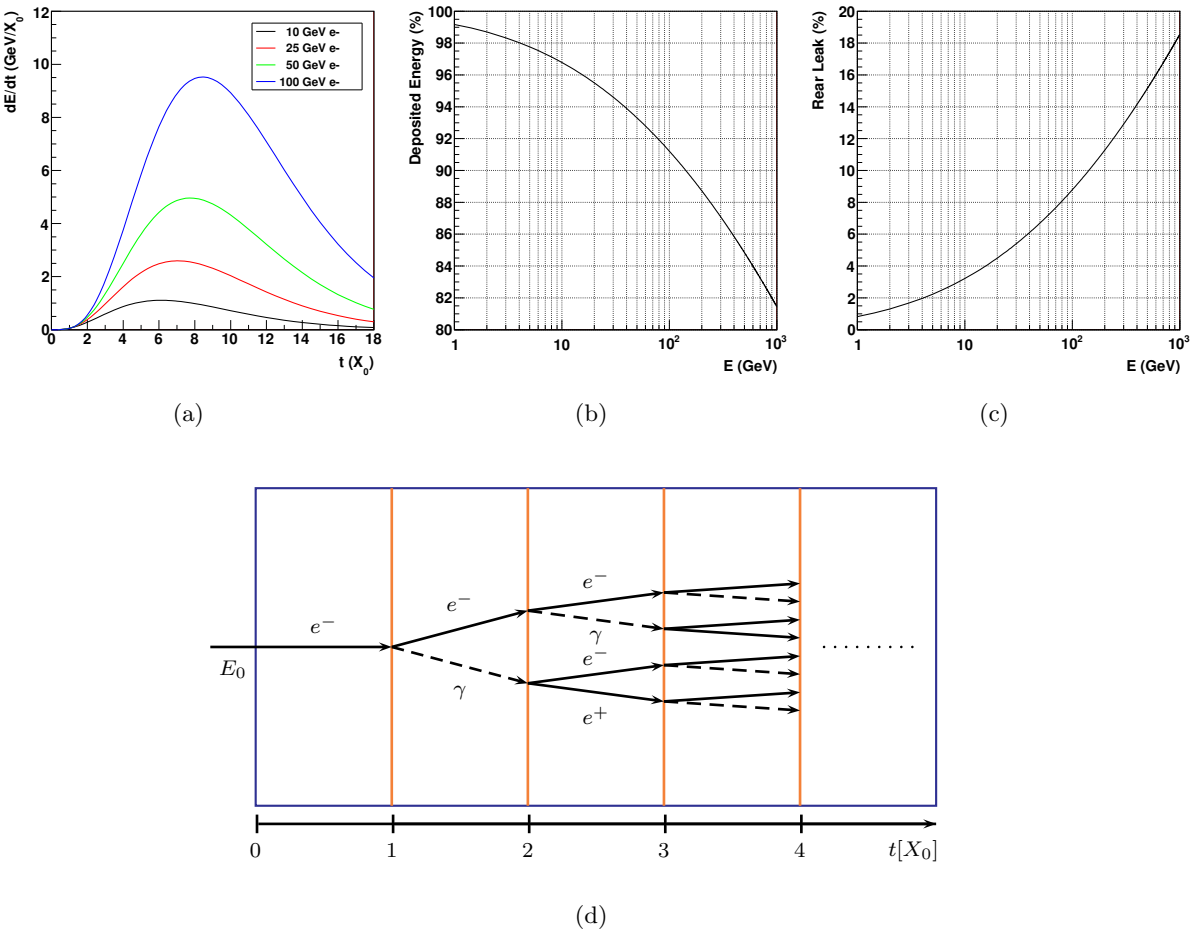

Fig. 2.3: *Longitudinal shower development from Eq.* (2.21) *(Fig. 2.3(a)). Deposited energy for 250 GeV electrons in 17 radiation lengths using Eq.* (2.21) *((Fig. 2.3(b))). Missing energy in 17 radiation lengths for 250 GeV electrons using Eq.* (2.21) *((Fig. 2.3(c))). Sketch of a simple model of electromagnetic shower development (Fig. 2.3(d)).*

$$\frac{dE}{dt} = E_0 b \frac{(bt)^{a-1} e^{-bt}}{\Gamma(a)} \tag{2.21}$$

where $\Gamma(a)$ is Euler's Γ function, t is the distance x normalized in *radiation lengths* ($t = x/X_0$), E_0 is the energy of the incident particle, and a and b are model parameters (Fig.2.3(a)). In this description the maximum of the shower development is reached at

$$t_{max} = \frac{a-1}{b} = \ln\left(\frac{E_0}{E_c}\right) + C_{\gamma e} \tag{2.22}$$

where $C_{\gamma e} = 0.5$ for a gamma-induced shower and $C_{\gamma e} = -0.5$ for an incident electron. The parameter b is ≈ 0.5 for heavy absorbers from iron to lead. Using the parametrization (2.21), an incident electron of 250 GeV deposits 88 % (Fig. 2.3(b)) of the energy in 17 radiation lengths with 12 % of missing energy or rear leak (Fig. 2.3(c)).

On the other hand, the lateral width of an electromagnetic shower can be characterized by the *Moliere radius*

$$R_M = \frac{21\,\mathrm{MeV}}{E_c} X_0\{\mathrm{g/cm^2}\} \tag{2.23}$$

which defines the energy contained in a cylinder around the shower axis, e.g., approximately 90 % of the shower energy is contained in a R_M.

If the energy deposited is sampled at differents depths (sampling calorimetes), the energy resolution is dominated by sampling fluctuations ($\alpha/\sqrt{E}$). At high energies, the nonuniformities, noise, calibration errors, and incomplete shower containment must be taken into account adding a constant term in quadrature [55]

$$\frac{\sigma_E}{E} = \sqrt{\frac{\alpha^2}{E} + \beta^2} \tag{2.24}$$

Therefore, the energy resolution will improve with energy until the constant term dominates the resolution.

Part II

The AMS Experiment

3

The AMS Experiment

The flight of AMS-02 onboard the space shuttle Endeavour and its installation in the ISS in May 2011, was the culmination of the work started in the 1990s. From now on, there are more than ten years ahead to collect and analyse data. This chapter summarizes the whole experiment, from the start to the launch of AMS-02, including a description of the first detector AMS-01 and its results, and a description of AMS-02 including the last detector upgrade.

The AMS experiment is an international collaboration involving universities and institutes from America, Europe and Asia (Table 3.1). The main physic goals of the experiment are the primordial antimatter, the dark matter, and the cosmic ray propagation models.

The first studies to put a magnetic spectrometer into the space appeared in print in 1994 [61], and by April 1995 AMS had been approved by the U.S. Department of Energy (DOE). The first step was the construction of a first detector to prove the feasibility of the project. In June 1998, the AMS-01 detector flew onboard the space shuttle Discovery during 10 days within NASA mission STS-91 (Fig.3.2(a)). The success of the mission gave birth to AMS-02, a new detector to be installed at the International Space Station (ISS), since the absence of atmosphere makes the ISS an ideal laboratory where to deploy a particle detector for a long duration experiment. AMS-02 flew onboard the space shuttle Endeavour in May 2011 (NASA mission STS-134) and was mounted on the upper payload attach point on S3 truss of the ISS (Fig. 3.1).

3.1 The AMS-01 Detector

To assure the feasibility of the project, AMS-01 had to perform correctly with high radiation and extreme temperature shifts as the shuttle completed their orbits around the Earth every 90 minutes. Besides, the detector had also to withstand an acceleration force of 3 g's at launch, up to 10 g's at landing, and a random noise vibration in the cargo bay up to a 150 decibels.

AMS-01 carried an array of precision particle detectors to measure momentum, velocity, charge and trace of particles that penetrated the spectrometer [62] (Fig.3.2(b)):

- A cylindrical shape permanent magnet with 6 silicon microstrip tracker planes inside the magnet.
- The Time of Flight (TOF) scintillator panels at the spectrometer's bottom and top to provide the time of flight and a measurement of the particle energy loss.

TABLE 3.1: *AMS international collaboration.*

AMS COLLABORATION

AMERICA

UNITED STATES
MIT (Cambridge)
Universty of Maryland (IPST Center)
Yale University (New Haven)
NASA Goddard Space Flight Center
NASA Johnson Space Center
NASA Kennedy Space Center
NASA Marshall Flight Center
Florida State University (Tallahassee)
Johns Hopkins University (Baltimore)
Jacobs Engineering Group Inc
Texas A & M University (Houston)
MEXICO
UNAM

EUROPE

GERMANY
RWTH-I
DLR
Max-Planck-Institut (Garching)
KIT (Karlsruhe)
DENMARK
Århus University
SPAIN
CIEMAT (Madrid)
IAC (Canarias)
FINLAND
Helsinki University of Technology
University of Turku
FRANCE
IN2P3 (Montpellier)
LAPP (Annecy)
LPSC (Grenoble)
LPTA (Montpellier)
THE NETHERLANDS
NLR (Emmloord)
NIKHEF (Amsterdam)
ITALY
Italian Space Agency (ASI)
SERMS (Terni)
IROE (Firenze)
INFN and University of Bologna
INFN and University of Milano
INFN and University of Perugia
INFN and University of Pisa
INFN and University of Roma
INFN and University of Siena
PORTUGAL
LIP (Lisboa)
University of Coimbra
ROMANIA
University of Bucharest
RUSSIA
Kurchatov Institute (Moscow)
ITEP (Moscow)
Russian Academy of Sciences
Moscow State University
SWITZERLAND
ETH (Zurich)
University of Geneva
EUROPEAN AGENCIES
European Space Agency (ESA)
CERN

ASIA

CHINA
IEE (Bejijng)
IHEP (Bejijng)
Jiao Tong University (Shanghai)
Southeast University (Nanjing)
Sun Yat-Sen University (Guangzhou)
Shandong University (Tsinan)
TAIWAN
Academia Sinica (Taipei)
National Central University (Taipei)
National Taiwan University (Taipei)
Chung Shan Institute (Lungtan)
National Space Organization
KOREA
Kyungpook National University
Ewha Women's University (Seoul)

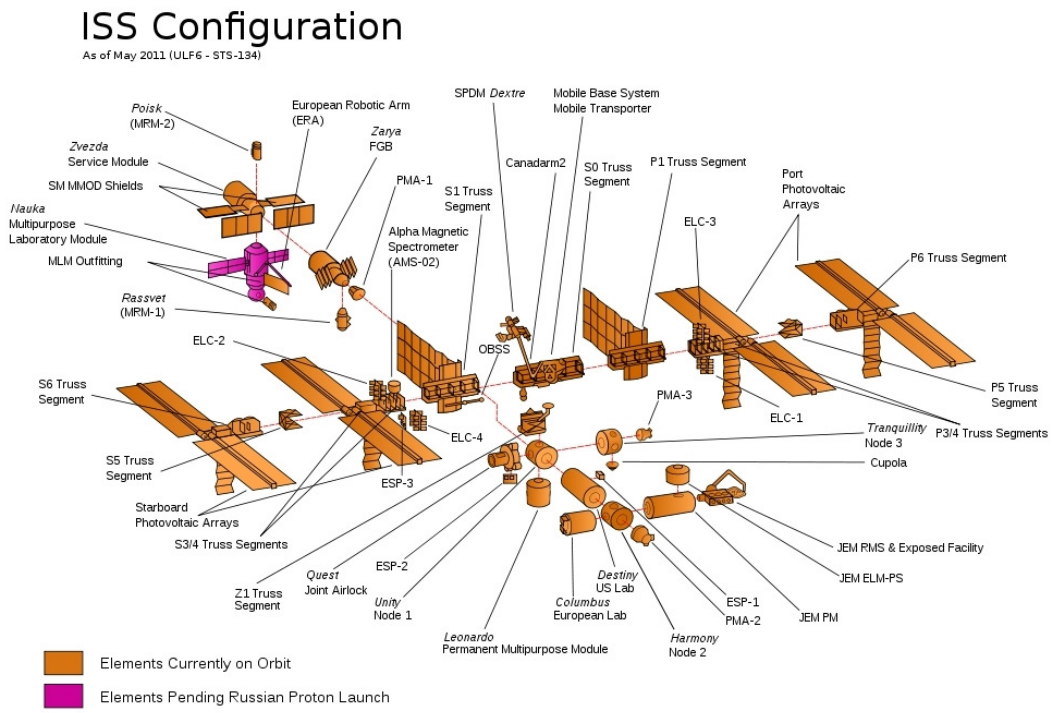

Fig. 3.1: *Exploded view of the International Space Station elements.*

- The threshold Cherenkov counter at the bottom of the spectrometer to distinguish electrons and antiprotons.
- The anti-coincidence counter to reject particles that left or entered through the inner shell of the magnet.
- Trigger and data acquistion electronics.

During the flight, in addition to checking out all systems in actual flight conditions, AMS-01 collected 100 million events and yield significant scientific results as the first magnetic spectrometer ever to be launched into space:

Search for antihelium in cosmic rays: A total of 2.86×10^6 helium nuclei with rigidities up to 140 GV were observed. No antihelium nuclei were detected at any rigidity. An upper limit on the ratio of the flux of antihelium to the flux of helium of less than 1.1×10^{-6} was obtained [63].

Protons in near earth orbit: The proton spectrum in the kinetic energy range 0.1 to 200 GeV was measured. Above the geomagnetic cutoff, the observed spectrum is parameterized by a power law. Below the geomagnetic cutoff, a substantial second spectrum was observed. Most of these second spectrum protons follow complicated trajectories and originate from a restricted geographic region [64, 65].

Leptons in near earth orbit: The lepton spectra in the kinetic energy ranges 0.2 to 40 GeV for e^- and 0.2 to 3 GeV for e^+ were measured. From the origin of the leptons two distinct

spectra were observed: a higher energy spectrum and a substantial second spectrum with positrons much more abundant than electrons. Most of the leptons from the second spectra travel for an extended period of time in the geomagnetic field and the e^+ and e^- originate from two complementary geographic regions [66]. In addition, a measurement of high energy positrons was made [67].

Helium in near earth orbit: The helium spectrum from 0.1 to 100 GeV/nucleon was measured. Above the geomagnetic cutoff, the spectrum is parameterized by a power law. Below the geomagnetic cutoff, a second helium spectrum was observed. In the second helium spectra over the energy range 0.1 to 1.2 GeV/nucleon, in the geomagnetic latitude from -0.4 to $+0.4$ rad, the flux was measured to be $(6.3 \pm 0.9)\times10^{-3}$ /$(\mathrm{m}^{-2}\mathrm{s}^{-1}\mathrm{sr}^{-1})$ and, contrary to expectations, more than ninety percent of the helium was determined to be ^{3}He (at the 90% C.L.) [68].

Deuterons in near earth orbit: A total of 1×10^4 deuterium nuclei in the energy range 0.1 to 1.0 GeV/nucleon were observed allowing the first accurate test of galactic confinement models [69].

Search for antideuterium in cosmic rays: In a total of 1×10^4 deuterium nuclei in the momentum range 1 to 3 GeV/c no antideuterium nuclei were detected at any momentum. The most precise limit on the flux of antideuterium of less than 1×10^{-4} was obtained.

Chemical and isotopic composition of cosmic rays: The relative abundances of light-nuclei lithium, beryllium, boron, and carbon were measured. In addition, the secondary-to-primary ratios Li/C, Be/C, and B/C were measured in the kinetic energy range 0.35 to 45 GeV/nucleon, and the isotopic ratio ^{7}Li/^{6}Li was also determined in the magnetic rigidity interval 2.5 to 6.3 GV. The secondary-to-secondary ratios Li/Be, Li/B, and Be/B were also determined [70]. Besides, isotopic ratios of ^{2}H/^{4}He, ^{3}He/^{4}He, ^{6}Li/^{7}Li, ^{7}Be/(^{9}Be +^{10} Be), and ^{10}B/^{11}B in the range 0.2–1.4 GeV/nucleon was measured [71].

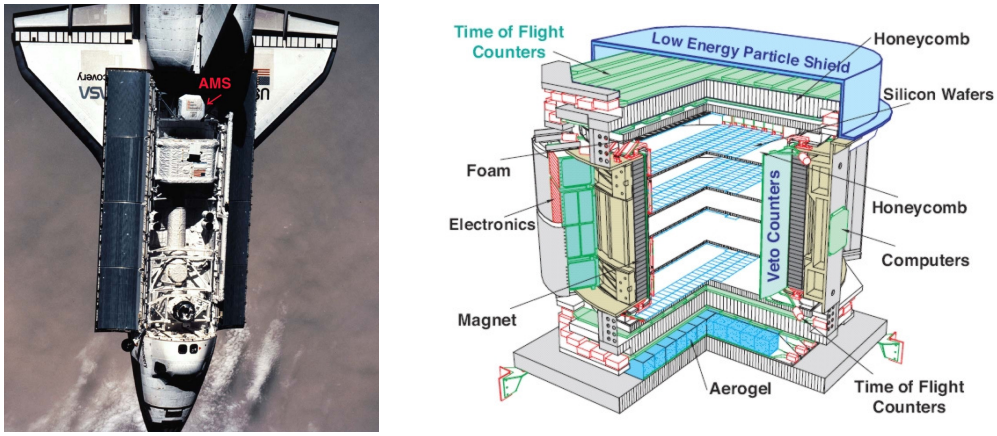

(a) NASA mission STS-91 (b) AMS-01

Fig. 3.2: *AMS-01 onboard the space shuttle Discovery seen from space station MIR (Fig. 3.2(a)). Schematic view of AMS-01 (Fig.3.2(b)).*

3.2 The AMS-02 Detector

Since May 2011 AMS-02 is orbiting the Earth on the ISS at an altitude of about 350 km(Fig. 3.3) The detector, with a weight of 8500 kg, a volumen of 64 m^3, and a power cosumption of 2.5 kW, will not return back to Earth, and the mission duration will span the lifetime of the ISS, until the year 2020–2028. The main subsystems of AMS-02 are:

- Magnet.
- Transition Radiation Detector (TRD).
- Time of Flight System (TOF).
- Silicon Tracker.
- Ring Imaging Cherenkov Detector (RICH).
- Electromagnetic Calorimeter (ECAL).
- Anti-Coincidence Counter (ACC).

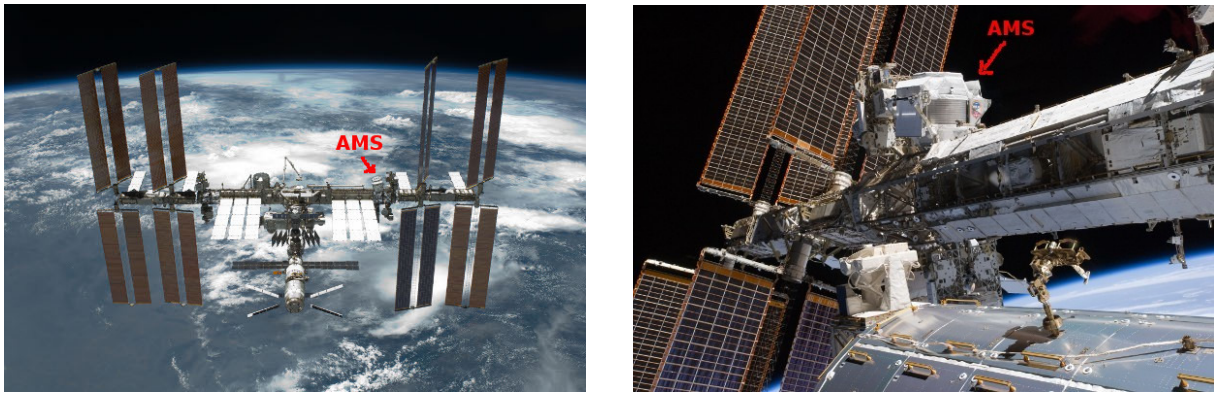

(a) (b)

Fig. 3.3: *AMS-02 photos at the ISS* [1].

Two types of magnets have been developed by the AMS Collaboration to be used in space: a permanent magnet (PM) and a superconducting magnet (SCM). The permanent magnet was already used in AMS-01, and the superconducting magnet has been developed since then with the same inner diameter as the AMS-01 permanent magnet. Besides, all the AMS-02 detector subsystems have been designed with fully compatible interfaces to the permanent magnet.

AMS is a long exposure time experiment with large acceptance, excellent particle identification and accurate rigidity and charge measurements, that will be able to extend the current knowledge of the cosmic rays flux composition and energy spectrum, search for primordial antimatter (anti-nuclei), and measure the faintest signals of the cosmic rays. The measurement of this weak signals, such as positrons, over the vast background of protons will be possible thanks to the e/p separation provide by the ECAL, TRD and Tracker.

[1] NASA mission STS-134 photo gallery: `http://www.nasa.gov/mission_pages/shuttle/shuttlemissions/sts134/multimedia/index.html`

3.2.1 The Superconducting Magnet Configuration

AMS-02 was constructed for a 3 year mission on the ISS, and the superconducting magnet was the ideal option for this scenario. The individual AMS subsystems underwent several flight qualification tests (thermal, vibration, and electromagnetic interference tests), as well as individual test-beams [72–76] before the final integration carried out at CERN facilities in the year 2009. In February 2010, AMS-02 was tested in a test-beam at CERN with 400 GeV protons and 180, 250 and 300 GeV electrons with the SCM configuration (Fig. 3.4).

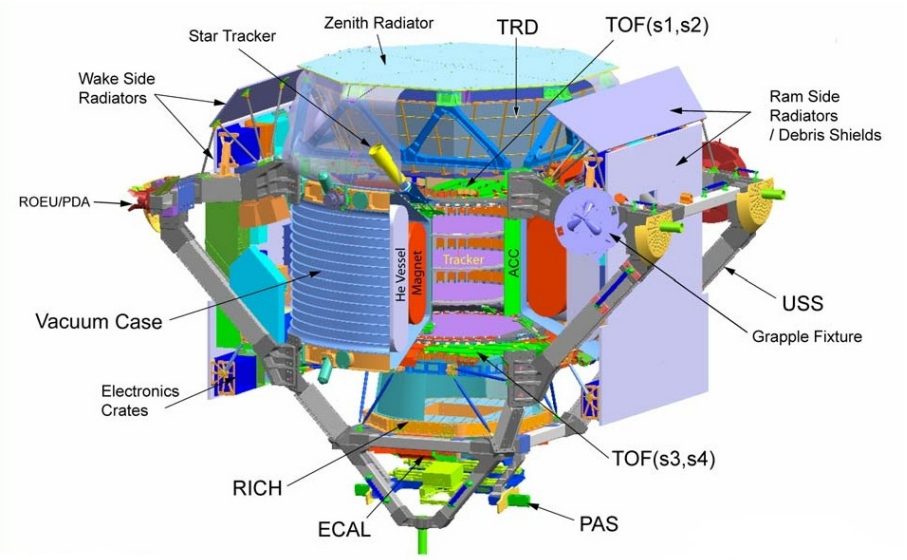

Fig. 3.4: *AMS-02 layout of SCM configuration.*

3.2.1.a The Superconducting Magnet

The superconducting magnet system (Fig. 3.5(a)) consists of superconducting coils, a superfluid helium vessel and a cryogenic system, all enclosed in a vacuum tank [77, 78]. The coil system consists of a set of 14 superconducting racetrack shaped coils (Fig. 3.5(b)). A large pair of coils generates the magnetic dipole field perpendicular to the z experiment axis, and two series of 6 smaller coils minimized the stray field outside the magnet at the same time that contribute to the dipole field. It is mandatory to reduce the stray field outside the magnet to prevent interference with systems on the ISS, and to reduce the magnetic torque resulting from the interaction between the AMS and the Earth's magnetic field. The magnetic flux density at the geometric centre of the system is 0.8 T.

The vacuum tank has a toroidal shape with inner diameter of 1.1 m and outer diameter of 2.7 m. The geometry of the superconducting magnet defines the acceptance of the detector ($0.5\,\mathrm{m^2sr}$). The magnet operates at a temperature of 1.8 K, cooled by superfluid helium stored in the vessel with a capacity of 2500 litres.

This SCM system was tested during the AMS-02 integration at CERN in 2009 [79], and used in the February 2010 test-beam.

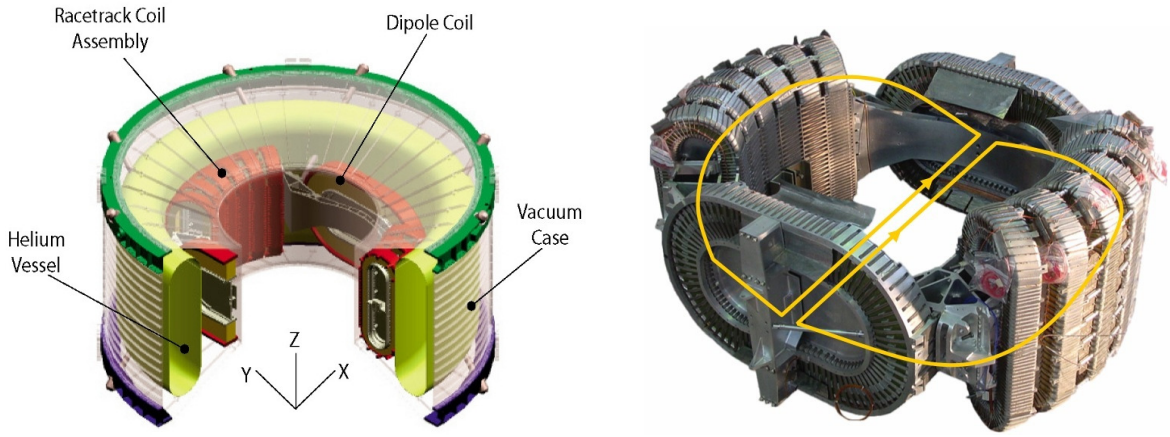

(a) SCM system layout (b) SCM coils assemble

Fig. 3.5: *The superconducting magnet of AMS-02.*

3.2.1.b The Transition Radiation Detector (TRD)

The transition radiation detector [80] provides an electron/hadron separation to the experiment. It is located on top of the detector and is made up of 20 layers of modules of 16 straw tubes (Fig. 3.6) and 20 mm fleece supported by a conical octagon structure (width of 1.5 m at bottom and 2.2 m at top, Fig 3.7(a)) built of carbon fiber and aluminum honeycomb sandwich material for the sidewalls, the top and bottom covers. The top and bottom 4 layers run parallel to the magnetic field direction (x axis) and the 12 central layers in the perpendicular direction (y axis) to provide 3D tracking. There are 328 modules (5248 straw tubes) with lengths from 0.8 m to 2.0 m.

The fleece material used (LRP 375 BK) for TR yield has a density of 0.06 g/cm^3 and polypropylene/polyethylene fibers with a thickness of 10 mm. On the other hand, the straw tubes, filled with a Xe : CO_2 (80:20) gas mixture, have a diameter of 6 mm and a double-layer kapton-aluminum foil wall of 72 µm (Fig. 3.7(b)). The anode wires are 30 µm gold plated tungsten.

The TRD is able to perform electron to proton separation over the energy range 1.5–300 GeV with a rejection factor 10^2–10^3 for 90 % signal efficiency [72].

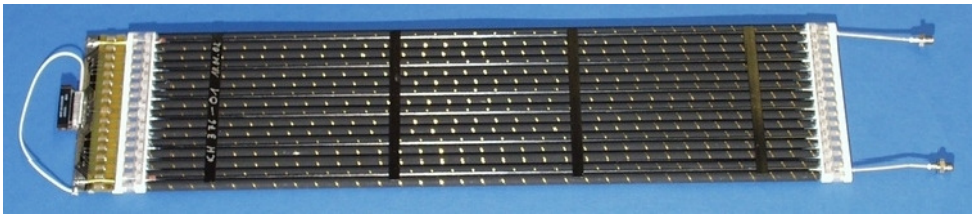

Fig. 3.6: *The TRD modules made up of 16 straw tubes.*

(a) (b)

Fig. 3.7: *The TRD octagon support structure (Fig. 3.7(a)). The tubes wall (Fig. 3.7(b)).*

3.2.1.c The Time of Flight System (TOF)

The time of flight system [81] provides the fast trigger (FT) to the AMS readout electronics (the first level of the data acquisition chain), the measurement of the particle velocity (distinguishing downward going charged particles from upward going at the level of 10^9), and the measurement of the absolute charge by the energy loss measurement. In addition to the FT, the TOF system also flags cosmic rays with charge greater than one, that makes possible the suppresion of the CR proton component at the trigger level without strongly affecting the measurement of the flux of higher charge nuclei.

The TOF system is composed by two planes with two scintillator layers within each plane (Fig. 3.8). The first plane is situated at the entrance of the magnet bore and the second one at the exit. Each layer is made up of 8 or 10 paddles of 1 cm thick and different lengths (117 to 134 cm) that overlapped by 0.5 cm in the same layer to avoid geometrical inefficiencies and have perpendicular directions in each layer. This two-fold arrangement, the overlapping and crossed paddle geometry, results in a granularity of about $12 \times 12\,\mathrm{cm}^2$. Each paddle has two or three PMTs at each end that increase the redundancy of the system, since only one is required.

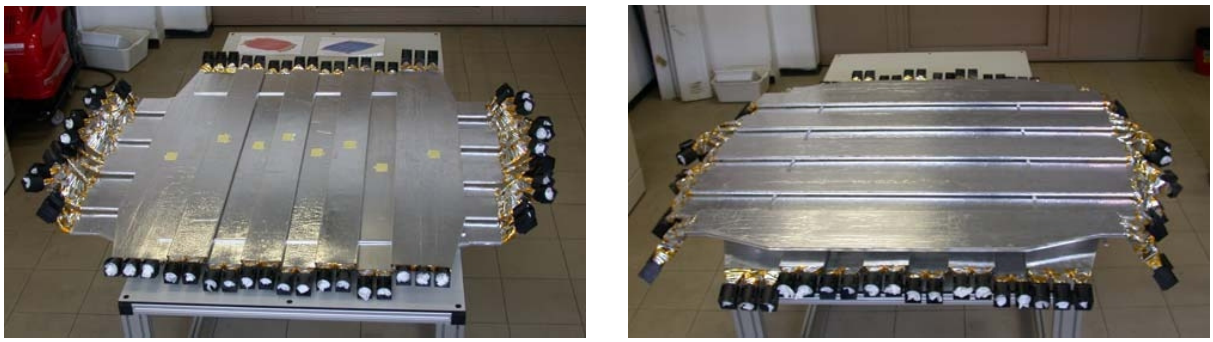

(a) Upper TOF (b) Lower TOF

Fig. 3.8: *The upper plane (Fig. 3.8(a)) and lower plane (Fig. 3.8(b)) of the time of flight system of AMS-02.*

The average time resolution has been measured to be 160 ps (1 ps = 10^{-12} s), with an overall velocity β ($\beta = v/c$) resolution of the system of 4 % for $\beta \sim 1$ particles. Besides, nuclei ($Z > 1$) can be identified up to charge $Z \approx 15$ with a velocity β resolution near 2 % [81].

3.2.1.d The Silicon Tracker

The silicon tracker system [82] is composed of a carbon fiber cylindrical shell enclosed in the magnet bore with 5 planes in it of low density aluminum honeycomb structure. The external planes (diameter of 1.4 m and average density of 0.032 g/cm^3) are equipped with silicon detectors only on one side, while the inner 3 planes (diameter of 1 m and average density of 0.016 g/cm^3) are equipped on both sides (Fig. 3.9(a)). The resulting 8 layers of silicon detectors provide the measurement of the particle trajectory in the magnet bore.

The double-sided silicon micro-strip sensors ($41.360 \times 72.045 \times 0.300\,\mathrm{mm}^3$) are grouped together for readout in ladders of different lengths to match the cylindrical geometry of the AMS magnet until add up to 192 ladders (Fig. 3.9(b)). The effective sensible area is about 6.2 m^2 with 196 k readout channels.

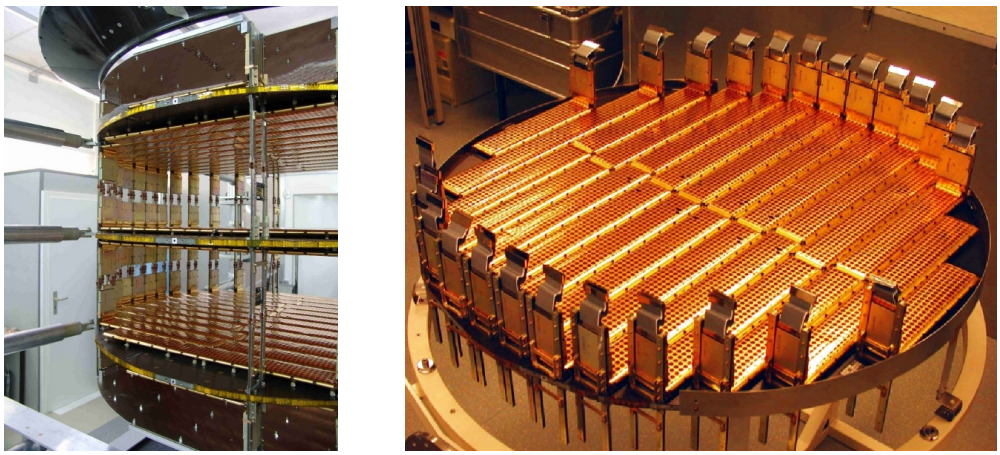

(a) (b)

Fig. 3.9: *The 3 inner planes equipped with silicon detectors on both sides (Fig. 3.9(a)). A single plane equipped with silicon detector ladders (Fig. 3.9(b)).*

The performance of the silicon ladders has been measured in relativistic proton and ion beams. The estimated proton and helium maximum detectable rigidities are 2.2 and 3.7 TV with 1–3 % rigidity resolution in the rigidity range 1–50 (1–100) GV for protons (helium nuclei) [74]. The energy losses recorded in the silicon allow to distinguish the particle charge up to $Z = 26$ [83]. During the pre-integration phase of AMS-02 (years 2007–2008 without magnet) the position resolution measured with cosmic-ray muons was 12.5 mm in the bending plane ($y - z$) and 35 mm in the non-bending plane ($x - z$) [84], which are compatible with the results obtained in the relativistic proton beam.

3.2.1.e The Ring Imaging Cherenkov Detector (RICH)

The ring imaging Cherenkov detector [85] provides a precise measurement of velocity ($\sigma_\beta/\beta \sim 1.0 \times 10^{-3}$) and absolute charge ($Z < 26$ with 10^{-2} charge confusion probability). It makes use of the proximity focusing technique and include a radiator plane at the top (radius of 60 cm, covering 90 % of the geometrical acceptance), a lateral mirror and a detection plane at the bottom (radius of 67 cm) situated at 46.8 cm from the radiator (expansion lenght).

The top plane holds 92 tiles of aerogel ($n = 1.05$) of 2.5 cm thick and a central square of 16 tiles of NaF($n = 1.334$) of 0.5 cm thick. The presence of sodium fluoride at the center of the radiator plane serves to increase the photon detection efficency due to greater Cherenkov emission angle (see section 2.2, pag. 14) and to increase the detector dynamical range since its threshold velocity is $\beta = 0.75$.

The lower plane, which has a $64 \times 64\,\mathrm{cm}^2$ square central hole to reduce the interaction material for particles within the ECAL geometrial acceptance, supports an array of 680 light guides and 4×4 multi-anode PMTs, with a pixel dimension of $4 \times 4\,\mathrm{mm}^2$ that add up to 10880 channels (Fig. 3.10(a)).

The conical mirror that encloses the volume between the radiator an the detector plane (Fig. 3.10(b)) increases the detector acceptance since ~ 33 % of the photons are reflected on it and re-directed to the photon detectors. Its reflective coating is made up of 100 nm of aluminum and 300 nm of SiO_2 an has a reflectivity of 85 % for $\lambda = 420$ nm.

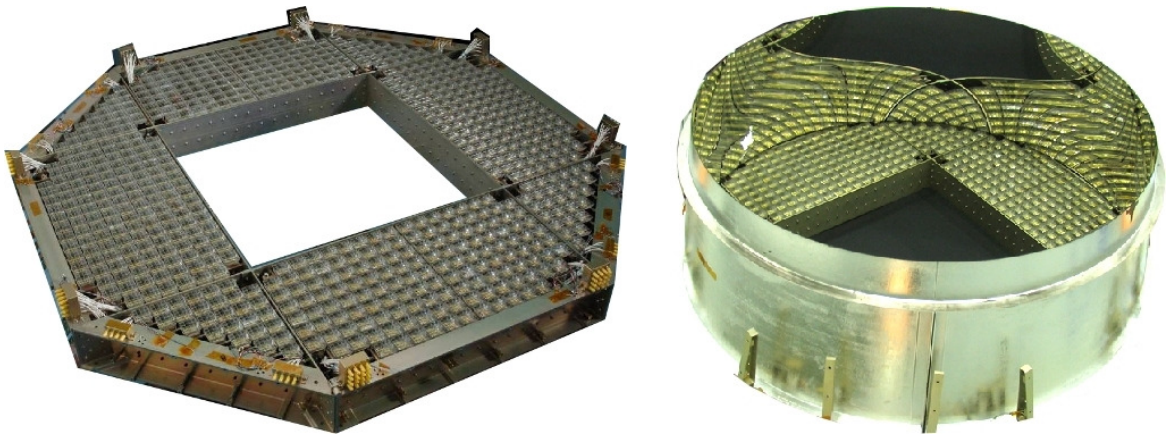

(a) (b)

Fig. 3.10: *The plane detector equipped with 680 light guides and 4×4 multi-anode PMTs (Fig. 3.10(a)). The conical mirror mounted together with the plane detector (Fig. 3.10(b)).*

3.2.1.f The Electromagnetic Calorimeter (ECAL)

The electromagnetic calorimeter [86] provides the measurement of the energy of electromagnetic particles to give a rejection against hadrons, identify gamma-rays, and produce a stand-alone gamma trigger.

The AMS-02 ECAL (Fig.3.11(a)) is made up of lead foils of 1 mm thick and scintillating fibers of 1 mm diameter glued together with epoxy. The resulting average density is $6.83 \pm 0.08\,\mathrm{g/cm}^3$. It has an active area of $648 \times 648\,\mathrm{mm}^2$ and a thickness of 166.5 mm (~ 17 radiation lengths X_0).

It is composed by 9 superlayers (18.5 mm thick), five of them with scintillating fibers running along the x axis (Y-View) and the other four with scintillating fibers running along the y axis (X-View) to enable a 3D image of the electromagnetic showers. The fibers are read at the ECAL edges by 2×2 multi-anode photomultipliers (36 PMTs per superlayer). These PMT channels cover an active area of $9 \times 9\,\mathrm{mm}^2$ and 35 fibers, defininig the region called cell and dividing the calorimeter in 18 layers (Fig.3.11(b)). This allows to sample the longitudinal shower profile by 18 independent measurements.

The calorimeter has a high dynamic range, since the signals that it must detect go from a few photoelectrons of minimum ionizing particles (MIPs) to about $\sim 10^5$ photoelectrons of electromagnetic showers in the TeV range. Therefore, the front-end electronics is designed with two gains and a ratio high to low ~ 33 on average.

The energy resolution for high energy electrons (100–300 GeV) is measured to be 2.5–3 %, the angular resolution is $\sim 1^\circ$ and the hadron rejection factor is $\sim 10^4$ for $E < 1\,\mathrm{TeV}$ [76, 86].

(a) (b)

Fig. 3.11: *The electromagnetic calorimeter brick, the PMTs are stuck into the square holes (Fig. 3.11(a)). Cross section of the ECAL lead-fiber-glue composite structure (Fig. 3.11(b)).*

3.2.1.g The Anti-Coincidence Counter (ACC)

The anti-coincidence counter system [87] surrounds the silicion tracker within the magnet bore to suppress tracks from outside the main tracker acceptance to avoid a distortion in the measurement of the sign of the charge, and to reduce the trigger rate during periods of high flux, e.g., in the South Atlantic Anomaly. Besides, combined with the tracker, can be used to detect backscattering from the electromagnetic calorimeter.

The ACC cylinder, with a diameter of 1.1 m and a height of 0.83 m, is made up of 16 scintillation panels (8 mm thick). The ionization light ($\lambda \approx 400\,\mathrm{nm}$) is absorbed by wavelength shifting fibers (WLS) embedded in grooves milled into the panels, which transform the light to a wavelength of about 480 nm. This fibers are routed on 2 bunches of 37 fibers each at both ends of the counters to transition connectors located on the upper and lower conical flanges of the magnet vacuum case. From these transition connectors the light is routed through clear fibers to the photomultipliers mounted on the outer rim of the vaccum case. The ACC is instrumented with 16 PMTs, 8 at the top and 8 at the bottom . One PMT is used to read 2 panels from the top and other PMT is used to read the same panels from the bottom in order to have redundancy (Fig. 3.12).

With an inefficiency below 10^{-4} (ratio of missed tracks out of the total number of particle tracks crossing the ACC) [87], the ACC guarantees that an antimatter signal will not be simulated due to laterally entering particles.

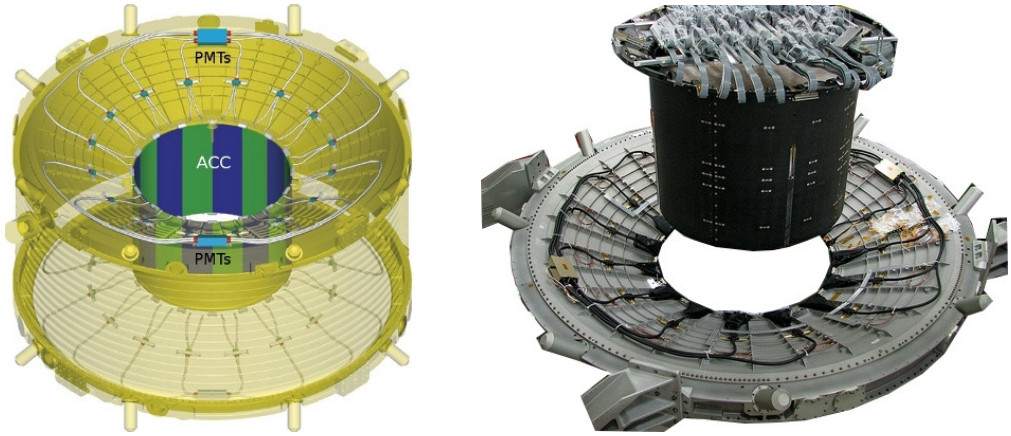

(a) (b)

Fig. 3.12: *The anti-coincidence counter layout (Fig. 3.12(a)). The anti-coincidence counter cabling before the tracker integration (Fig. 3.12(b)).*

3.2.2 The Permanent Magnet Configuration

After February 2010 test-beam, the detector was sent to the European Space Research and Technology Centre (ESTEC), the European Space Agency (ESA) facility at Noordwijk, the Netherlands. During March–April 2010, AMS underwent Thermal Vacuum/Thermal Balance (TV/TB) testing in the Large Space Simulator. Although most components of AMS have already been tested in thermal vaccum chambers, the TV/TB test was required to verify the integrated performance of the detector in a wide range of temperatures close to those on the Space Station, and to verify the AMS thermal model. The measurements were used to estimate the endurance of the AMS cryostat on orbit, and the results showed a superconducting magnet life-time of 28 ± 6 months [88].

On March 11 2010, the heads of the ISS agencies announced [2] their intentions to prolongue the life of the ISS until at least 2020, delaying the de-orbiting of the ISS initially programmed to 2015, and ratified by the NASA Authorization Act of 2010 [89]. This fact togheter with the SCM endurance results and the termination of the Shuttle program, was the turning point for a new scenario where the superconducting magnet was replaced by the AMS-01 permanent magnet (Fig. 3.13). The new AMS configuration was tested at CERN in August 2010 in a test-beam with protons, electrons and positrons at different energies. The test-beam was devoted to the Tracker alignment, although there were configurations dedicated to other subsystems. However, to perform ECAL calibration studies, the number of configurations in the August test-beam was fewer than in the February test-beam.

3.2.2.a The Permanent Magnet

The permanent magnet has a cylindrical shape, with a length of 80 cm, an inner diameter of 111.5 cm and an outer diameter of 129.8 cm. It is made from 64 high-grade Nd–Fe–B sectors. Each sector is composed of 100 blocks (5.08 cm $\times$ 5.08 cm $\times$ 2.54 cm) glued together with epoxy that is also able to protect the magnet from corrosion. The magnetic field is directed orthogonally

[2] Nasa press realese archive: `http://www.nasa.gov/home/hqnews/2010/mar/HQ_10-063_HOA_statement.html`

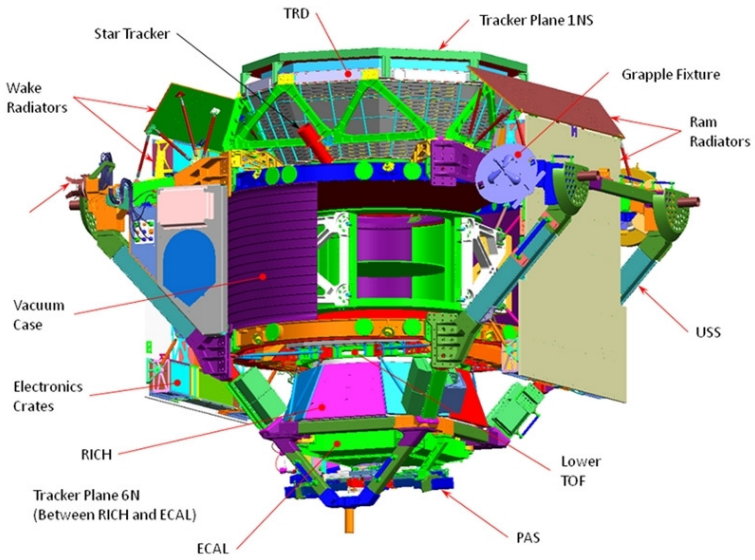

Fig. 3.13: *AMS-02 layout of PM configuration.*

to the cylinder longitudinal axis and the magnetic flux density at the geometric centre of the system is 0.15 T. The field outside the magnet at a distance of 2 m from the magnet center is less than 3 G [3] (NASA requires a leakage field lower than 300 G) [62].

After returning from the AMS-01 flight in June 1998, the permanent magnet was stored in a clean room and installed into AMS-02 after the TV/TB testing at ESTEC. The measurements of the field carried out in 1997 and April 2010 are the same within 1 %, the accuracy of the measuring device, which verify the stability in time of the field.

Although the permanent magnet has ~ 5 times lower magnetic field than the superconducting magnet, it has an unlimited lifetime, and the reduced bending power can be compensated by a different Tracker plane configuration.

3.2.2.b The Silicon Tracker

The new silicon tracker planes configuration (Fig. 3.14(a) [4]) extends the lever arm of the tracking measurement by moving the first plane on top of TRD and rearranging silicon ladders of other planes to make a new single-sided plane which was inserted between the RICH and ECAL with no needs of new electronics. With this rearrangement the maximal detectable rigidity (MDR [5]) of AMS-02 is not affected (2.14 TV for protons and 3.75 TV for He nuclei, Fig.3.14(b)) [88].

3.2.2.c The AMS-02 upgrade

The modifications include in AMS-02 to assure a long term operation on the ISS do not affect the AMS-02 acceptance for most of the physics topics, including dark matter searches, for particle rigidities up to approximately 400 GV. Above that and up to the MDR of 2.2 TV the acceptance

[3] 1 T=10000 G
[4] Image from `http://www.ams02.org/what-is-ams/tecnology/magnets-comparison`
[5] The MDR corresponds to a rigidity measurement error of 100 %

is reduced by a factor between 1.5 and 2 [90]. Taking into account 8 Tracker layers in the PM configuration, the 7 inner layers and the external layer on top of the ECAL, the geometrical acceptance exposure not suffer changes if it is compared with the SCM configuration acceptance. However, the MDR is reduced to 0.8 TeV [91] (protons). To recover the SCM configuration MDR within the PM configuration scenario, the 2 new external Tracker layers must be used with the 7 inner layers at the same time ($\sim 3\,\mathrm{m}$ of track path length), but at a price of a lower acceptance. However, the statistical accuracy is recovered by a much longer exposure time.

In order to ensure the lifetime of AMS-02 along the lifetime of the ISS, evaluations were made on all components, including [90]:

- The lifetime of the TRD straw tube CO_2. The measured long term leak rate of CO_2 amounts to $5\,\mu\mathrm{g/s}$ for the entire TRD. The onboard storage of $5\,\mathrm{kg}$ CO_2 at launch corresponds to a lifetime of 30 years.
- The lifetime of the magnet. From the measurements of the field that determined a B-field degradation whitin a margin of 1 % in 12 years, it is infered that the field will remain the same for the next 20 years.
- The lifetime of materials. To mitigate the long term exposure to atomic oxygen and to solar ultraviolet rays, additional single and double layer beta cloth has been added to cable harnesses.

This upgrade brings additional particulars, like a lower stray magnetic field that the subsystems must withstand, which benefits its performance. Subsystems that remain all the same, except the Tracker, with the upgrade. Besides, the absence of the cryogenic system and the Helium tank makes AMS-02 technically simpler.

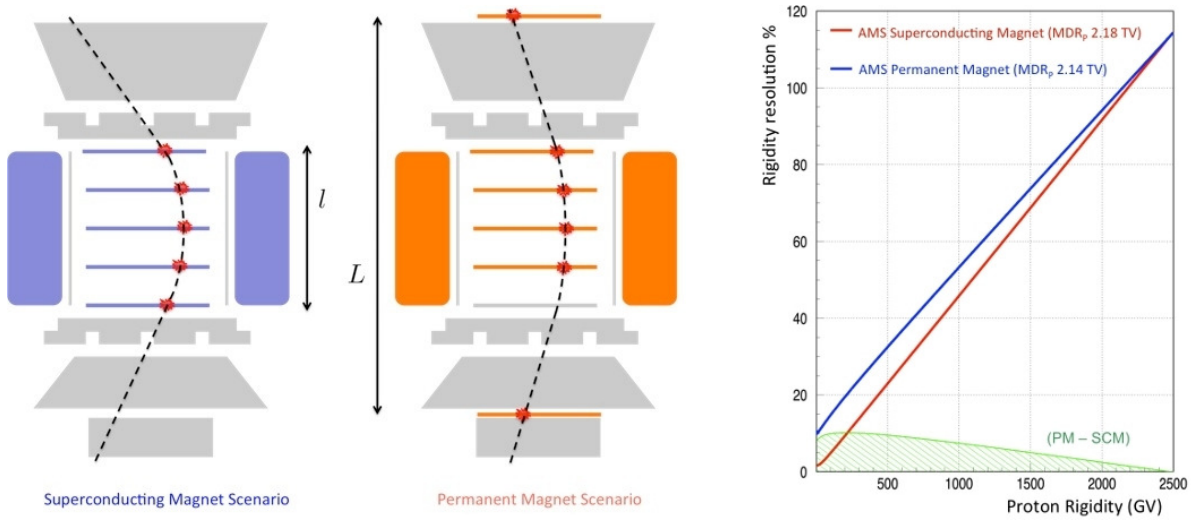

(a) (b)

Fig. 3.14: *Schematic view of the SCM and PM silicon tracker planes configuration (Fig. 3.14(a)). Rigidity resolution of the SCM configuration (red), the PM configuration (blue) and the difference between both (green) (Fig. 3.14(b)).*

4

AMS Software

The physical variables of the particles that go through the detector are reconstructed from the recorded events in raw format. This chapter gives an insight into the workings of the AMS reconstruction software, and dedicates a special attention to the ECAL and TRD own reconstructions, since they will be used throughout the following chapters.

The AMS software provides to the experiment the necessary tools to simulate the AMS-02 response to the passage of particles through the detector and to reconstruct the recorded events:

- The simulation software is based on the *GEANT* package [92], and it makes use of the detector geometry to simulate the deposited energy and particles interactions in the different subdetectors.
- The reconstruction software, that can be fed with real or simulated data, processes the recorded events to generate and ouput compresssed data file in *ROOT* format with collections of C++ objects. Therefore, the most direct way to analyse these data files, is to use the C++ language and the *ROOT* framework [93].

4.1 Event Reconstruction

The first step in the event reconstruction chain is to process the subsystems raw data to look for collected signals, i.e. read-out channels above a threshold, in order to identify simple patterns. These patterns are stored in a C++ object with the pertinent information and used subsequently to identify higher level patterns specific to each subdetector. The result is a processed data organised into hierarchical structures (Fig. 4.1 [94]) that allows a versatil analysis, since the top level information can be used directly or in case of necessity recover the low level information to re-reconstruct the high level patterns [94, 95].

Once the top level structures from each subdetector are built, namely `TrdTrackR` from the TRD, `TrTrackR` from the Tracker, `RichRingR` from the RICH and `EcalShowerR` from the ECAL, another structures are built, `BetaR`, `ChargeR`, `ParticleR`, and `AMSEventR`:

- The `BetaR` object contains the velocity of the particle built using the TOF information and the lenght of the `TrTrackR`.

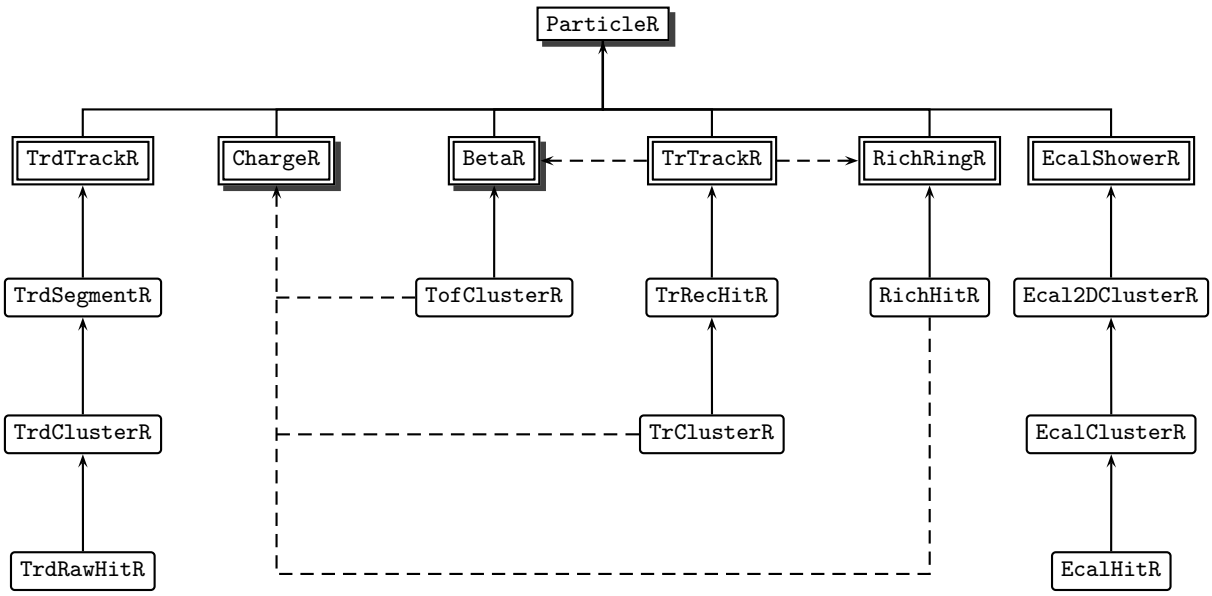

Fig. 4.1: *Simplified tree diagram of the C++ objects hierarchies within the reconstructed event.*

- The `ChargeR` object contains the absolute charge of the particle using the TOF, Tracker, and RICH information.
- The `ParticleR` object is the highest level structure of the reconstruction that contains information about the velocity, the charge, the momentum, and the mass of the particle. Within the AMS reconstruction sofware framework, a normal particle derives from `BetaR`, `ChargeR`, and `TrTrackR` objects. Besides, it can contains a `TRDTrackR`, an `EcalShowerR` , and a `RichRingR`.
- The `AMSEventR` object gives access to all data.

4.1.1 ECAL Event Reconstruction

When a particle impinges at the ECAL entry and develops a shower, the ECAL cells make a sample of the transverse profile of the energy at each layer. The cells with recorded signals represent the lowest level pattern of the interaction of an incident particle with the calorimeter. The coordinates and deposited energy are stored in the `EcalHitR` object in the reconstruction process that continues with a cluster searching process to eventually end with a reconstructed shower [96]:

1. `EcalClusterR`: The `EcalHitR` of the same layer are clustered around the cell with the highest deposited energy (used hits).
2. `Ecal2DClusterR`: The `EcalClusterR` of consecutive layers of the same view are grouped together taken into account a proximity criterion and energy difference criterion.
3. `EcalShowerR`: The X and Y view `Ecal2DClusterR` are grouped together to form a 3-dimensional shower.

The shower parameters calculated during the reconstruction are store in the `EcalShowerR` object, e.g, the center of gravity of the deposited energy, the coordinates of the incident particle impact point at the ECAL entry, the direction of the axis of the shower, and the incident particle energy (deposited energy + rear leakage).

4.1.2 TRD Event Reconstruction

The TR photons emitted at the fleece radiator are collected in the straw tubes together with the ionization background. These tubes with recorded signals are the lowest level pattern of the TRD track reconstruction, the `TrdRawHitR`. From now on, the TRD reconstruction follows a cluster searching and straight line fitting process:

1. `TrdClusterR`: Collection of adjacent `TrdRawHitR` where it is stored the `TrdClusterR` coordinates, the energy deposition in keV, and the multiplicity of hits.

2. `TrdSegmentR`: The next reconstruction level group together `TrdClusterR` in two x and two y segments at the same time that a straight line fit is performed in each segment to the clusters coordinates.

3. `TrdTrackR`: The reconstructed track consists of at least one x and one y `TrdSegmentR` and a final straight line fit is done.

The TRD track for a single particle would be formed at most by four segments, whereas a number of segments greater than four is probably connected to secondaries production [97].

Part III

AMS-02 Superconducting Magnet Configuration Performance

5

Electromagnetic Calorimeter

The electromagnetic calorimeter provides an e/p separation that is needed to reduce the cosmic proton background. The data collected in the February 2010 test-beam with the AMS-02 superconducting configuration is used in this chapter to develop a calibration method for the AMS-02 ECAL and to evaluate its e/p separation performance, which is compared to MC data to validate the cosmic ray positron analysis.

In February 2010, a test-beam of the AMS-02 detector took place at CERN with the superconducting magnet configuration. During five days, 24 hours a day, the detector was tested using proton, electron, and photon beams to perform an overall detector calibration. The detector was installed on a support structure which allowed 2 axes of translation and 2 axes of rotation to expose the detector to particles from different directions and angles.

5.1 Test Beam Data Sets

The table 5.1 summarizes the different beam statistics, where run stands for a set of data taken under the same trigger conditions:

Table 5.1: *Data-taking statistics.*

Particle	Beam Energy (GeV)	# Runs	# Processed Events
Electron	180	5	4.61×10^6
Electron	250	58	1.17×10^7
Electron	300	7	2.70×10^6
Proton	400	211	2.26×10^7
Photon	100	13	6.5×10^6

5.1.1 Proton and electron runs

Different sets of positions were used during the test-beam. The Ecal1 block comprises 10 positions of the beam impinging at the ECAL entry in different parts and with different angles. The Ecal2 block comprises 38 positions diagonally arranged with the aim to illuminate all the

ECAL cells. The EcalTrig Block comprises 2 positions with two different angles. The table 5.2 summarizes the runs used in this analysis.

TABLE 5.2: *Runs used in the data analysis.*

Particle	Beam Energy (GeV)	Block	Angle (°)	# Runs
Electron	180	Ecal1	0	1
Electron	180	Ecal1	5	1
Electron	180	Ecal1	10	1
Electron	180	Ecal1	15	1
Electron	250	Ecal1	0	3
Electron	250	Ecal1	5	1
Electron	250	Ecal1	10	4
Electron	250	Ecal1	15	2
Electron	300	Ecal1	0	1
Electron	300	Ecal1	5	2
Electron	300	Ecal1	10	1
Electron	300	Ecal1	15	1
Electron	250	EcalTrig	0	4
Electron	250	EcalTrig	10	4
Electron	250	Ecal2	0	38
Proton	400	Ecal1	0	1
Proton	400	Ecal1	5	1
Proton	400	Ecal1	10	1
Proton	400	Ecal1	15	1

5.1.2 Data Sample Preselection

The total data sample needs to be normalized to a set of preselection cuts in order to define a sample of events suitable for a specific analysis. The Fig. 5.1 shows the set of preselection cuts applied in this analysis. The number of events processed (runs of protons plus runs of electrons) is $\sim 2 \times 10^7$, which is reduced to $\sim 2.4 \times 10^6$ when the set of preselection cuts is applied. The table 5.3 collects the efficiencies of the cuts following the sequence. The *Acc* cut selects clean events to perform the calibration since there exists backsplash at the ECAL entry, which is higher in electrons than in protons. It will be revisited in the section 5.4.2 (pag. 70) dedicated to the e/p separation when the signal acceptance must be maximize.

TABLE 5.3: *Preselection cuts efficiency.*

Level1 (%)	*Acc* (%)	*Particle* (%)	*Tracker* (%)	*Trd* (%)	*Ecal* (%)
100	57.1	52.9	35.5	30.4	12

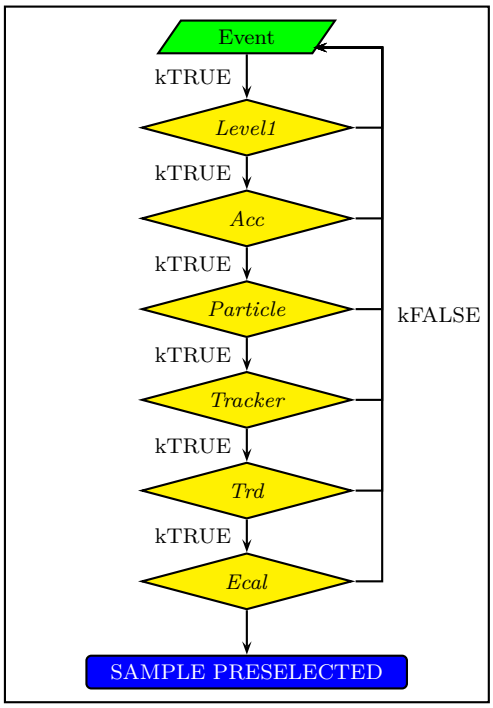

1. ***Level1*:** Level1 trigger present.
2. ***Acc*:** No Anticounters fired.
3. ***Particle*:** 1 Particle reconstructed.
4. ***Tracker*:** $0 <$ Tracker tracks reconstructed ≤ 3.
5. ***Trd*:** 1 TRD track reconstructed.
6. ***Ecal*:**
   (a) 1 Shower reconstructed.
   (b) $|x(track)| < 32\,\text{cm}$ (Particle track at ECAL entry).
   (c) $|y(track)| < 32\,\text{cm}$ (Particle track at ECAL entry).
   (d) $|x(track) - x(ecal)| < 1\,\text{cm}$ (Spatial matching at ECAL entry, Fig. 5.2(a)).
   (e) $|y(track) - y(ecal)| < 1\,\text{cm}$(Spatial matching at ECAL entry, Fig. 5.2(b)).

Fig. 5.1: *Preselection cuts used in the data analysis.*

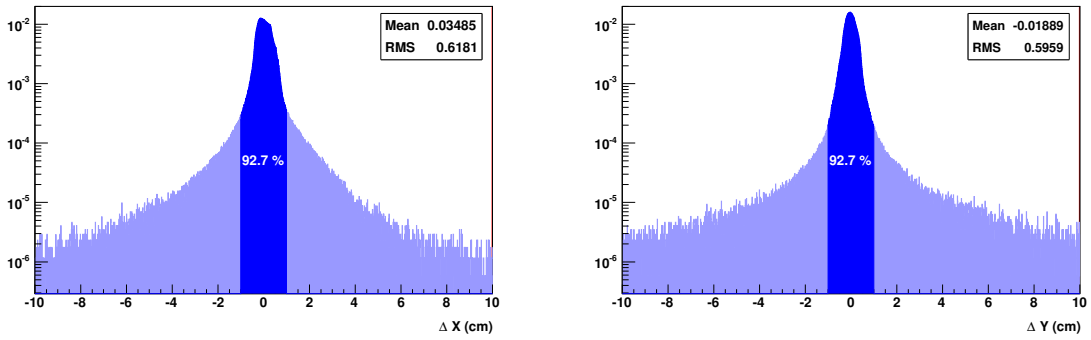

(a) (b)

Fig. 5.2: *Residuals distribution in x ($|x(track) - x(ecal)|$) (Fig. 5.2(a)) and residuals distribution in y ($|y(track) - y(ecal)|$) (Fig. 5.2(b)) normalized to 1 for a MIPs sample. The 93 % of the events fulfill the spatial matching cuts (d) and (e).*

5.1.3 ECAL Performance Verification

All the ECAL cells were active during the test-beam and the fraction of used hits is $\sim 85\,\%$ in the last layers for 250 GeV electrons (Fig. 5.3). On the other hand, the reconstructed energy has a shower entry point dependence (Fig. 5.4), with the consequence of a worse resolution in the measurement of the energy, which suggests that either the ECAL it is not well calibrated or the beam is not monoenergetic, although a mixture of both can not be ruled out. Therefore,

the first step is to verify the ECAL calibration with MIPs, since they are used to equalize the channels in the high gain range.

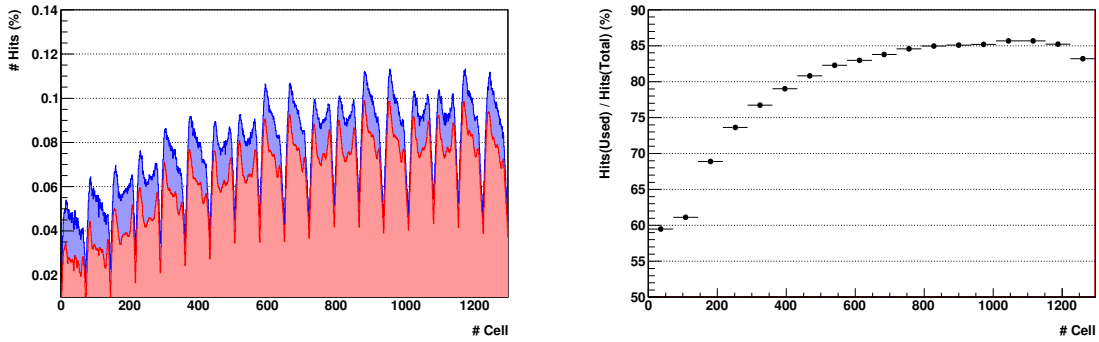

(a) (b)

Fig. 5.3: *Distribution of cells occupancy (Fig. 5.3(a)) in total hits (blue) and used hits (red) after preselection cuts and electron selection cuts (see section 5.3.1), using runs of block Ecal2. Ratio of used hits and total hits for each layer (Fig. 5.3(b)). The cell number increases from the top layer to the bottom.*

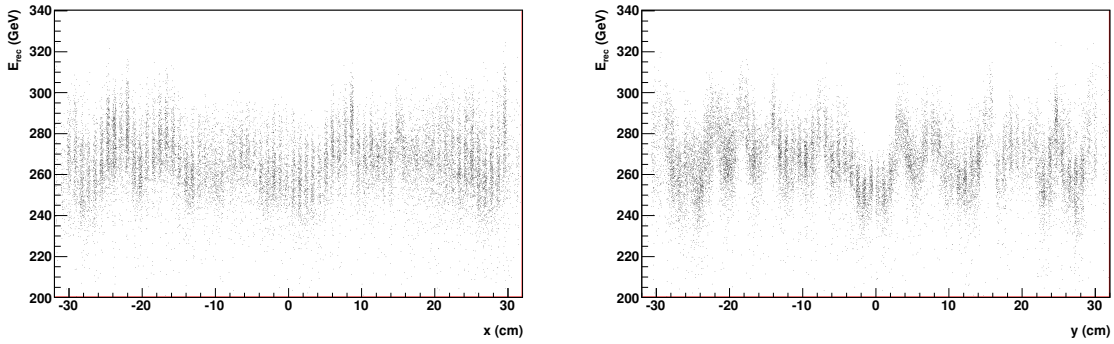

(a) (b)

Fig. 5.4: *Reconstructed energy and shower entry coordinates x (Fig. 5.4(a)), and y (Fig. 5.4(b)) after preselection cuts and electron selection cuts (see section 5.3.1), using runs of block Ecal2.*

5.1.3.a Monte Carlo Comparison

Some runs have been simulated (table 5.4) in order to compare the results obtained with data. The runs replicate the positions of block Ecal1 and Ecal2, and the events are generated following a Gaussian distribution centered at the beam center and with $\sigma_x = 1.5\,\text{cm}$ and $\sigma_y = 2.7\,\text{cm}$, which defines the beam width.

The fraction of used hits in each layer is lower than the fraction of used hits in data (Fig. 5.5(b)), and the number of total and used hits per layer and event is $\approx 10 - 30\,\%$ lower in MC (Fig. 5.6(c)), that is a consequence of a lower multiplicity in the number of hits per cluster (Fig. 5.6(d)). On the other hand, the MC reconstructed energy does not have a shower entry point dependence (Fig. 5.7). The absence in MC of the energy dependence with the

reconstructed position seen in data (Fig. 5.4) confirms the necessity for a verification of the calibration applied to the real data.

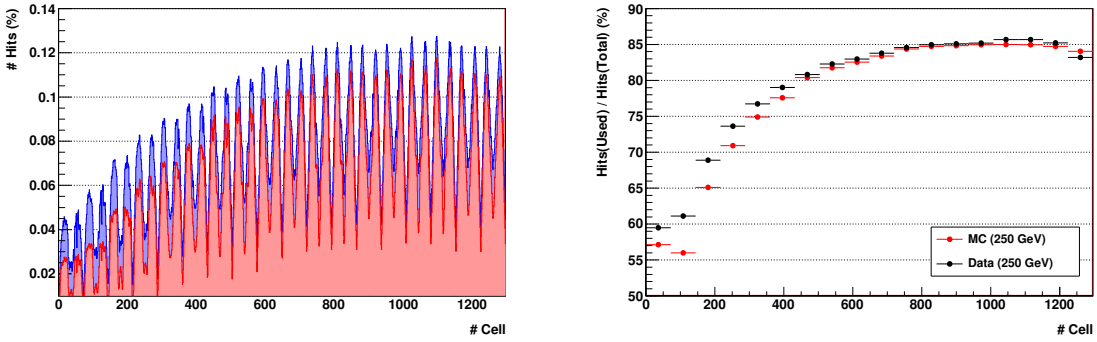

(a) (b)

Fig. 5.5: *Distribution of cells occupancy (Fig. 5.5(a)) in total hits (blue) and used hits (red) after preselection cuts and electron selection cuts, using runs generated of block Ecal2. Ratio of used hits and total hits for each layer (Fig. 5.5(b)). The cell number increases from top layer to the bottom layer.*

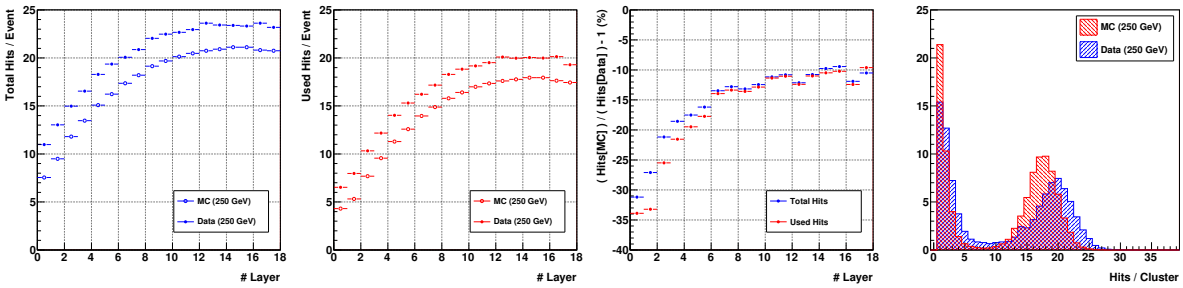

(a) (b) (c) (d)

Fig. 5.6: *Number of total hits (Fig. 5.6(a)) and used hits (Fig. 5.6(b)) per layer and event for MC (empty) and data (solid). Comparison of the number of hits, total (blue) and used (red), between MC and data(Fig. 5.6(c)). Hits per cluster (1D and used) distribution for data (blue) and MC (red) (Fig. 5.6(d))*

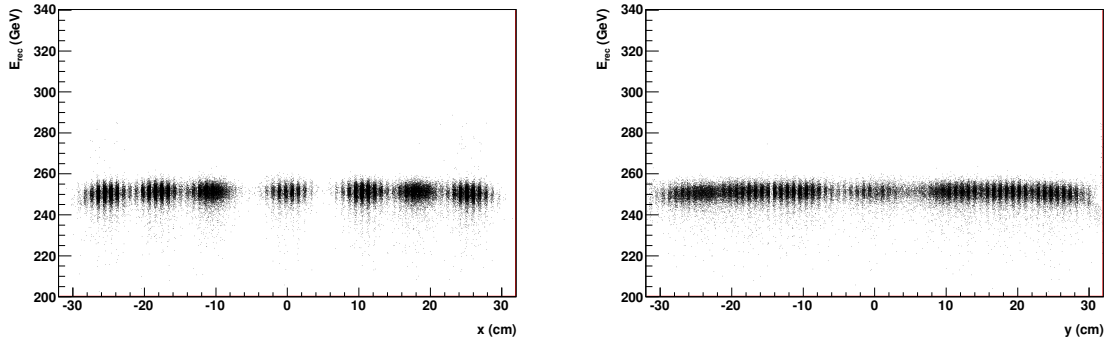

(a) (b)

Fig. 5.7: *Reconstructed energy and shower entry coordinates x (Fig. 5.7(a)) and y (Fig. 5.7(b)) after preselection cuts and electron selection cuts (see section 5.3.1), using the generated runs of block Ecal2.*

TABLE 5.4: *MC simulated runs.*

Particle	Beam Energy (GeV)	Block	Angle (°)	# Runs	# Generated Events
Electron	180	Ecal1	0	1	10000
Electron	180	Ecal1	5	1	10000
Electron	180	Ecal1	10	1	10000
Electron	180	Ecal1	15	1	10000
Electron	250	Ecal1	0	2	20000
Electron	250	Ecal1	5	1	10000
Electron	250	Ecal1	10	4	40000
Electron	250	Ecal1	15	1	10000
Electron	300	Ecal1	0	1	10000
Electron	300	Ecal1	5	1	10000
Electron	300	Ecal1	10	1	10000
Electron	300	Ecal1	15	1	10000
Electron	250	Ecal2	0	13	130000

5.2 ECAL Calibration Cross-Check with MIPs

5.2.1 MIPs Selection

All the runs in the table 5.2 have been used to verify the ECAL calibration, so in order to select the hadrons that go through the calorimeter as minimum ionizing particles, two cuts are applied: one that selects events with practically all the energy deposited along the shower axis [1], and other that selects events with low multiplicity of used hits per layer touched [2]. The sample of events selected as MIPs represents 66.6% of the preselected one. The mean energy of this MIPs sample is 460 MeV with 14 used hits (Fig. 5.8).

5.2.2 Attenuation Correction

The ECAL response is not the same for particles impinging at different positions along the fibers, due to the existence of light attenuation. This fiber feature is parametrized by a double exponential functional form with 17 % of the light with a short attenuation length $\lambda_{att}^{S} \sim 9.8\,\text{cm}$ and the remaining 83 % with a long attenuation length $\lambda_{att}^{L} \sim 235\,\text{cm}$ [76]. The final correction is normalized at the center of the fiber and takes into account the reflected and direct component. Once applied to the PMT channels, the result is an equalized response which is independent of the impact point along the fiber. To check if this correction is working properly in the reconstruction software, the ADC counts (raw and corrected) collected according to the impact point in the fiber by the PMTs channels, are fitted to a straight line (Fig. 5.9) using the ADC distribution mean.

This first approximation of the attenuation links the slope of the fit with the goodness of the correction. When the fit is applied to the raw ADC counts, there are two sets of slopes

[1] Cut applied: `Energy3C[0]` > 0.999, deposited energy in a cylinder of 2 cm of radius (`EcalShowerR` object).
[2] Cut applied: `Hits/Plane` < 2.

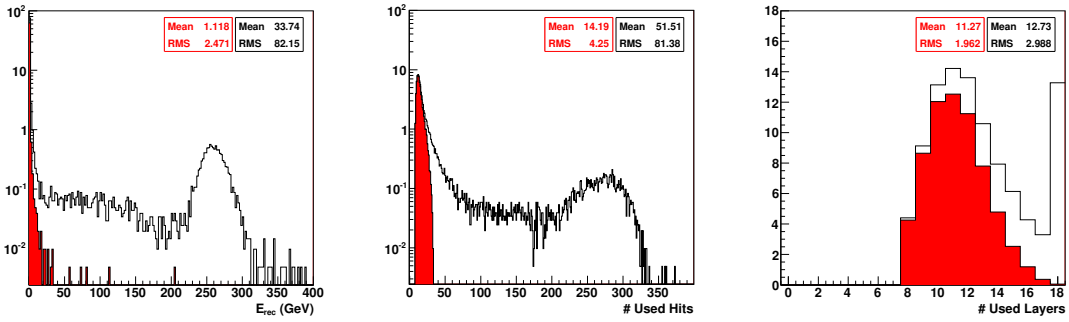

(a) (b) (c)

Fig. 5.8: *Normalized distributions of the shower energy (Fig. 5.8(a)), number of used hits (Fig. 5.8(b)), and number of used layers (Fig. 5.8(c)) using the mips selection (red) for a particular run (RunId 1265493420, Tag 01c6, 250 GeV).*

(negative and positive) (Fig. 5.10(a)) that just reflects the mechanical structure of the ECAL, since the PMTs are arranged alternately at the ECAL edges. On the other hand, when the fit is applied to the corrected ones, the distribution of slopes is centered at 0 with a width of 3.8 %. Due to the proximity of the electronic threshold to the maximum of the distribution, the ADC counts distribution presents an inherent uncertainty. Therefore, a cross-check has been done using the Landau function most probable value (MPV) and the Landau truncated mean of the corrected ADC counts distribution. The slopes distribution width goes from 2.8 % in the former case to 4.9 % in the latter case. Both results are compatible within 1 % with the first result, which validates the attenuation correction on MIPs.

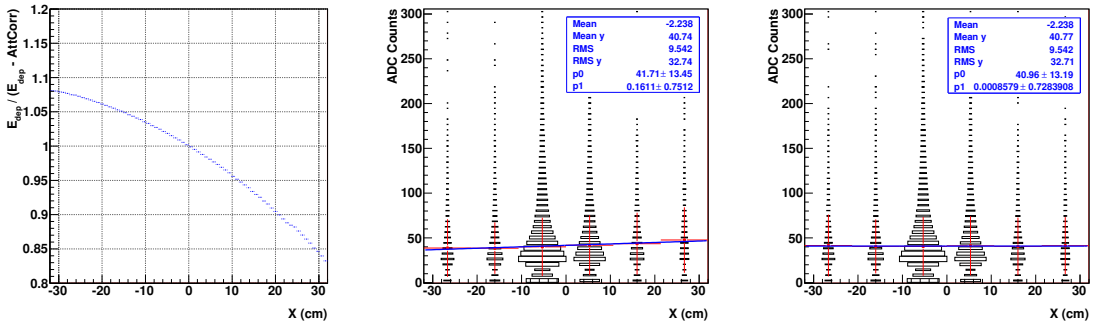

(a) (b) (c)

Fig. 5.9: *The attenuation correction function (Fig. 5.9(a)), the raw ADC counts (Fig. 5.9(b)) and the corrected ADC counts (Fig. 5.9(c)) fitted to a straight line using the distribution mean.*

5.2.3 Gain Equalization

The PMT response to MIPs is used to equalize the channels in high gain. The distribution of signal amplitude in ADC counts is fitted to a Landau function, channel by channel, with the aim to obtain the MPV that is taken as the reference value for the channel equalization.

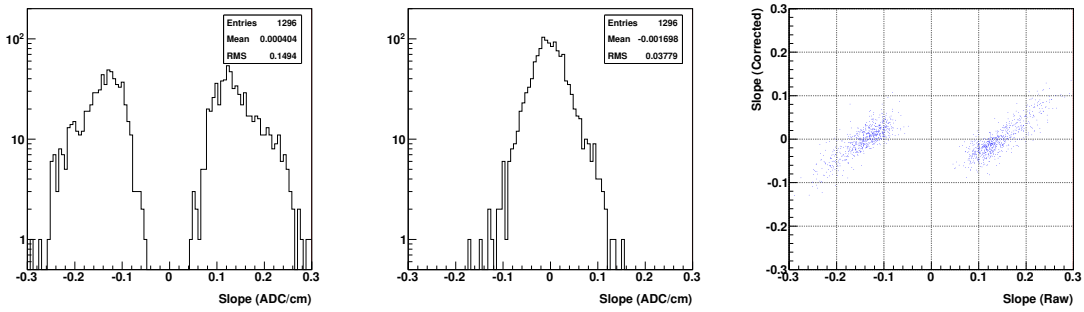

(a) (b) (c)

Fig. 5.10: *Distributions of the slopes obtained from the fit to raw ADC counts (Fig. 5.10(a)), from the fit to the corrected ADC counts (Fig. 5.10(b)), and one distribution versus the other (Fig. 5.10(c)), using the distribution mean.*

5.2.3.a Vertical Runs

The Fig. 5.11(a) shows that the distribution of MPVs for the 1296 channels peaks at 28 ADC counts, and it has a width of 17 % due to an intrinsic spread inside the PMTs. This gain fluctuation can be measured by looking at the anode dispersion within each photomultiplier

$$\text{Dispersion} = \frac{MPV_{ij} - \langle MPV_j \rangle}{\langle MPV_j \rangle} \qquad i = 1, \ldots, 4 \; ; \; j = 1, \ldots, 324 \tag{5.1}$$

The dispersion of 15 % (Fig. 5.11(b)) is in agreement with previuos measurements [98]. On the other hand, a fit to a Landau function channel by channel in the distribution of the hits energy, shows that the MPVs distribution peaks at 13 MeV and has a width of 3 % (Fig. 5.11(c)), showing that most of the channels are well calibrated and only few of them (16 channels with MPV(Channel) $> \langle MPV \rangle + 4\sigma$) require a recalibration.

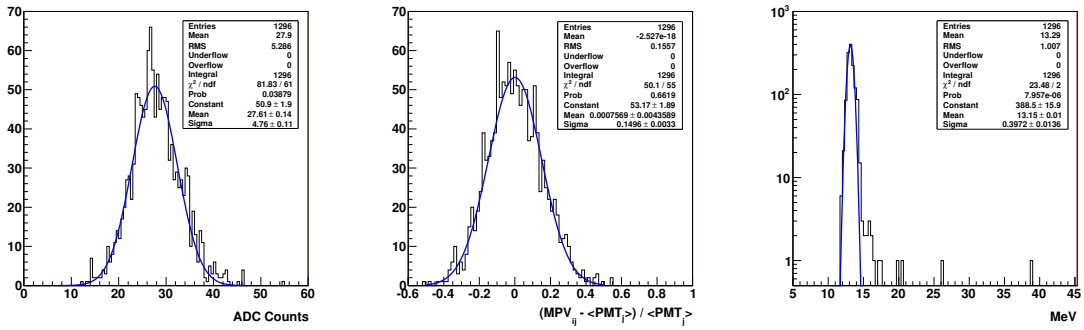

(a) (b) (c)

Fig. 5.11: **[Gain equalization on MIPs]** *Distribution of the MPV values in ADC counts for all the channels (Fig. 5.11(a)). Distribution of the anode dispersion (Fig. 5.11(b)), and distribution of the MPV values in MeV for all the channels (Fig. 5.11(c)).*

Each channel has a particular calibration factor that converts the ADC counts collected into a measurement of the deposited energy, so in order to check the procedure used to calculate the MPV values, the calibration factors extracted from the reconstruction software can be compared with the ones obtained in this analysis when the MPV[MeV] are divided by the MPV[ADC] (Fig. 5.12(a)). This last distribution has a mean value of 0.48 MeV/ADC, 0.9 % lower than the extracted from the reconstruction software, and a width of 1.2 %. To compare these two sets of calibration factors, the energy of the shower has been re-reconstruted from the energy of the hits. The Fig. 5.12(b) shows that the reconstructed energy obtained with the calibration factors from the recontruction software is equal to the shower energy itself, which is a validation of the algorithm used to calculate the energy. The Fig. 5.12(c) shows that the reconstructed energy obtained with the calibration factors from this analysis is on average a 1 % lower than the shower energy itself, although are in close agreement with each other.

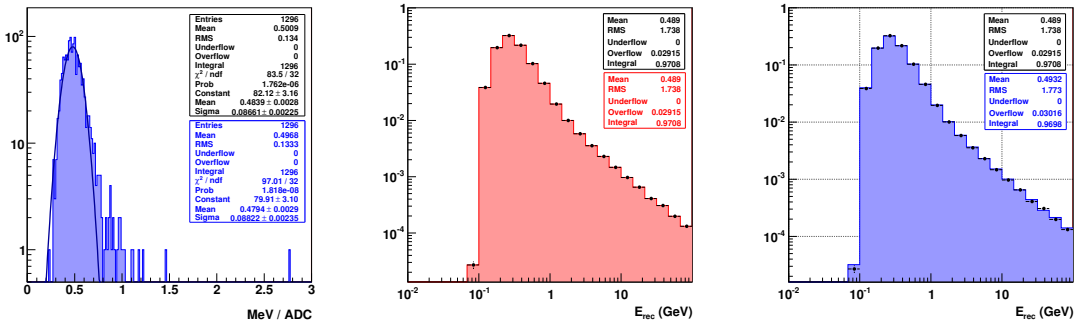

(a) (b) (c)

Fig. 5.12: *Distribution of the calibration factors from the analysis (Fig. 5.12(a)) with the statistic box in blue. The black statistic box is for the calibration factors from the reconstructed software. The distribution of the reconstructed energy using the calibration factors from the reconstruction software (red) and the shower energy itselft (black dots) (Fig. 5.12(b)). The distribution of the reconstructed energy using the calibration factors from the analysis (blue) and the shower energy itselft (black dots) (Fig. 5.12(c)).*

5.2.3.b Inclined Runs

As a final check of the procedure and the calibration factors obtained when the MPV[MeV] are divided by the MPV[ADC], they have been recalculated using runs with different angles. The Fig. 5.13 shows a high correlation in the comparison of the calibration factors obtain in this section with the calibration factors obtain at 0, 5, 10, 15 degrees, remaining stable within 3 % (Fig. 5.14).

5.3 ECAL Calibration with Electromagnetic Showers

Another approach to the calibration is to use electromagnetic showers to equalize the channels' response. There are two constraints to consider: the transverse profile of the energy forces to use only cells along the shower axis and the longitudinal profile of the energy depositions requires a layer by layer equalization. The equalization procedure using electromagnetic showers has been applied in previous ECAL standalone test-beams [99], although the implementation presented in this analysis is slightly different.

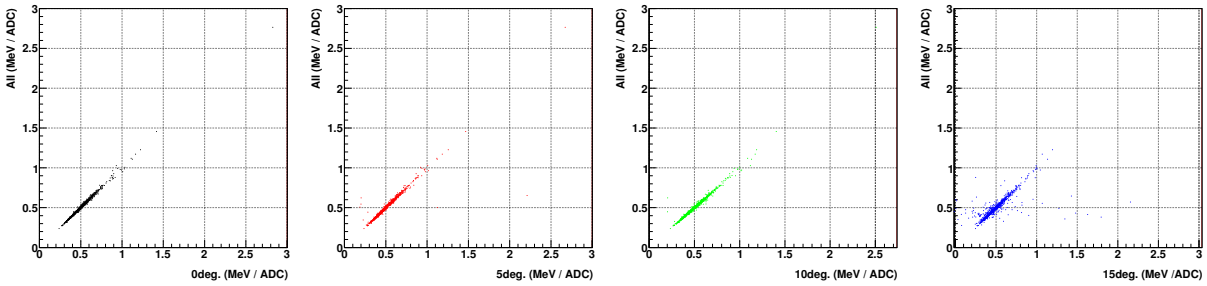

(a) (b) (c) (d)

Fig. 5.13: [**Angular check**] *Comparison of the calibration factors obtained with all the angles and the calibration factors obtained at 0 deg. (Fig. 5.13(a)), 5 deg. (Fig. 5.13(b)), 10 deg. (Fig. 5.13(c)), and 15 deg. (Fig. 5.13(d)).*

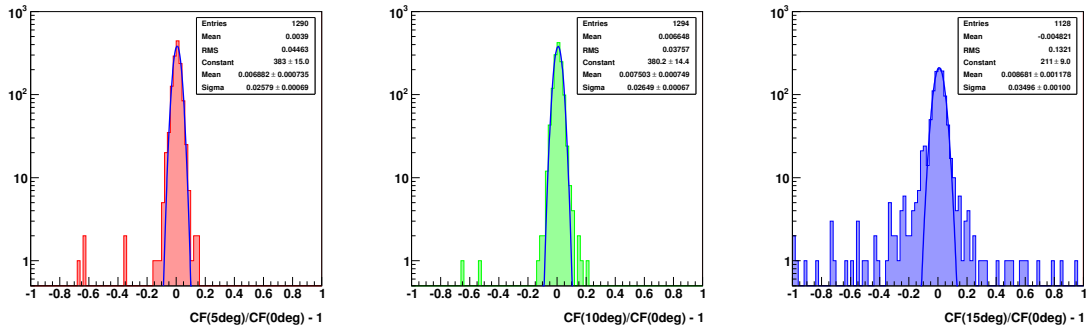

(a) (b) (c)

Fig. 5.14: [**Angular check**] *Comparison of the calibration factors obtained at 0° with the calibration factors obtained at 5° (Fig. 5.14(a)), 10° (Fig. 5.14(b)), and 15° (Fig. 5.14(c)).*

5.3.1 Electromagnetic Showers Selection

The runs taken with the electron beam have contamination of hadrons. Therefore, it is neccesary a set of cuts to select the electron signal. The sequence of cuts on the following quantities, which are explained in the next sections, has been applied in this analysis:

1. Maximum of the shower (*ShowerMax*).
2. Longitudinal leakage (*RearLeak*).
3. Energy per hit (*Energy/Hit*).
4. Shower transverse size (*Moliere*).
5. Matching of the energy with the tracker momentum (*EPMatch*).

None of them is an expendable cut, since the efficiencies of the cuts when their are applied as first cut or last cut in the sequence shows that there is no cut playing a redundant role in the sequence. The efficiencies for runs of 250 GeV and block Ecal2 are summarize in table 5.5.

If the events whithin a certain range of energy, taking into account an exponential background in this region, is considered as the signal (see section 5.4.2, pag. 70) and the remaining ones as the background, the sequence of cuts has a final efficiency of 77 % in the signal and 0.07 % in the background.

TABLE 5.5: *Electron selection cuts efficiencies with binomial errors. The values are normalized to the sample of preselected events.*

Cut	Eff. As First (%)	Eff. As. Last (%)	Eff. As First (Signal) (%)	Eff. Signal (Sequence) (%)	Eff. Background (Sequence) (%)
ShowerMax	72.94 ± 0.09	94.02 ± 0.15	93.57 ± 0.13	93.57 ± 0.13	64.13 ± 0.11
RearLeak	52.95 ± 0.10	91.60 ± 0.17	86.47 ± 0.19	85.98 ± 0.19	35.86 ± 0.11
Energy/Hit	23.33 ± 0.09	99.10 ± 0.06	98.78 ± 0.06	84.92 ± 0.20	1.32 ± 0.03
Moliere	91.26 ± 0.06	94.12 ± 0.15	93.12 ± 0.14	80.30 ± 0.22	0.81 ± 0.02
EPMatch	15.97 ± 0.08	91.36 ± 0.17	93.22 ± 0.14	77.36 ± 0.23	0.07 ± 0.01

5.3.1.a Maximum of the Shower

From section 2.4 (pag. 17), the maximum of the longitudinal profile for an electromagnetic shower is proportional to the logarithm of the shower energy (see Eq. (2.22)). The cut applied [3] in the maximum of the shower has this logarithmic dependence with the reconstructed energy. The results for a beam of 250 GeV electrons can be seen in Fig. 5.15.

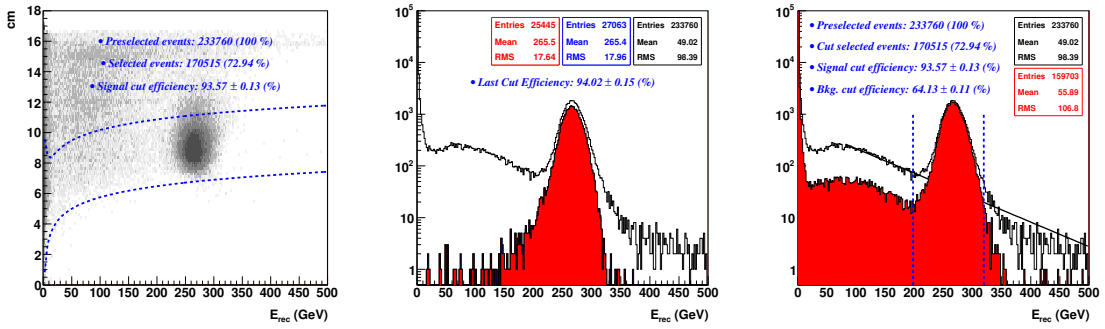

(a) (b) (c)

Fig. 5.15: *Dependence of the maximum of the shower with the energy, where the dash blue lines are the ShowerMax cut (Fig. 5.15(a)). Distribution of the reconstructed energy of the preselected sample (black), for events after the sequence of cuts except the ShowerMax cut (blue), and for events after the sequence of cuts where the ShowerMax cut is the last cut applied (red) (Fig. 5.15(b)). Distribution of the reconstructed energy of the sample preselected (black) and of the events after the first step in the sequence of cuts (red). The dash blue lines defines the signal (Fig. 5.15(c)).*

[3] $\log(E(\text{MeV})/a_0) - a_1 - a_2 \cdot E^{-a_3}(\text{GeV}) < \textit{ShowerMax} < \log(E(\text{MeV})/b_0) + b_1 + \exp(b_2 - b_3 \cdot E(\text{GeV}))$, where the cut parameters are fitted using Monte Carlo samples to $a = \{a_0, a_1, a_2, a_3\} = \{7.803, 3.61, 2.55, 0.71\}$ and to $b = \{b_0, b_1, b_2, b_3\} = \{32.66, 2.143, 1.727, 0.242\}$.

5.3.1.b Longitudinal Leakage

The shower at the test-beam energies is not completely contained in the calorimeter, so the missing energy or rear leak must be estimated [99] in order to give the particle incident energy. The cut applied [4] in the fraction of missing energy has a logarithmic dependence with the reconstructed energy. The results for a beam of 250 GeV electrons can be seen in Fig. 5.16.

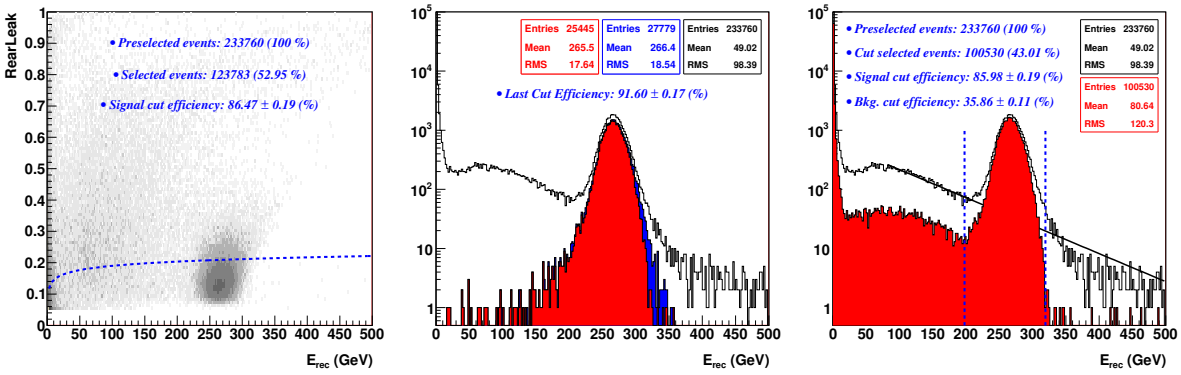

(a) (b) (c)

Fig. 5.16: *Dependence of the fraction of longitudinal leakage with the energy, where the dash blue line is the RearLeak cut (Fig. 5.16(a)). Distribution of the reconstructed energy of the preselected sample (black), for events after the sequence of cuts except the RearLeak cut (blue), and for events after the sequence of cuts where the RearLeak cut is the last cut applied (red) (Fig. 5.16(b)). Distribution of the reconstructed energy of the preselected sample (black) and of the events after the second step in the sequence of cuts (red). The dash blue lines defines the signal (Fig. 5.16(c)).*

5.3.1.c Energy per Hit

The equipartition of the electromagnetic shower energy between the shower hits has a linear dependence with the energy, even when the hits of lower energy are excluded (Fig. 5.17(a)). The Fig. 5.17(c) shows that, for instance, the exclusion of hits with energy lower than 52 MeV means a reduction of 50 % in the hits multiplicity but only 1.5 % reduction in the shower energy (Fig. 5.17(b)).

The cut applied [5] in the energy per hit variable has a linear dependence with the reconstructed energy. The results for a beam of 250 GeV electrons can be seen in Fig. 5.18.

[4] $RearLeak < a_0 + a_1 \cdot \log(E(\mathrm{GeV}))$, where the cut parameters have been tuned for test-beam data to the values $a = \{0.1, 0.0195\}$.

[5] $Energy/Hit > a_0 + a_1 \cdot E(\mathrm{GeV})$, where the cut parameters have been tuned for test-beam data to the values $a = \{9.3147 \times 10^{-2}, 2.538 \times 10^{-3}\}$

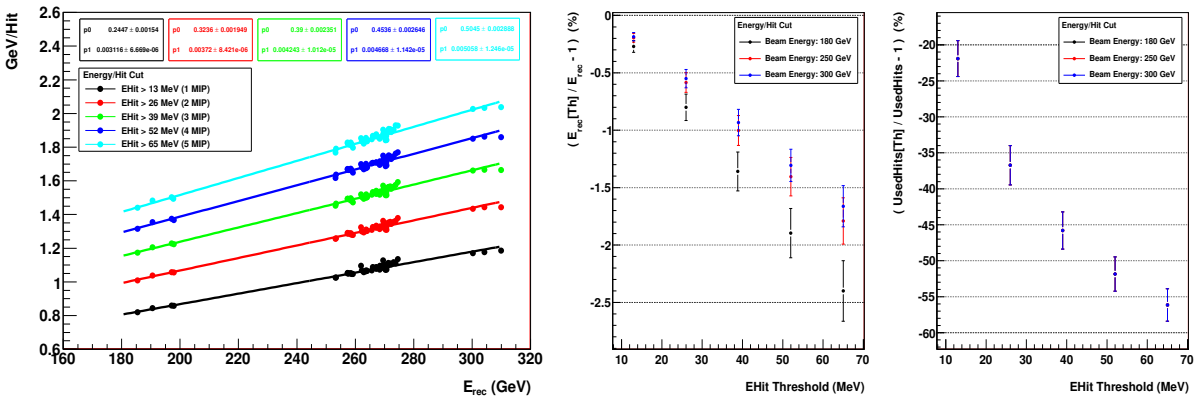

(a) (b) (c)

Fig. 5.17: *Linear dependence of the energy/hit, setting a threshold in the energy of the hit (Fig. 5.17(a)). Variation of the reconstructed energy removing hits with a threshold in the energy of the hits (Fig. 5.17(c)). Variation of the number of used hits with a threshold in the energy of the hits (Fig. 5.17(c)).*

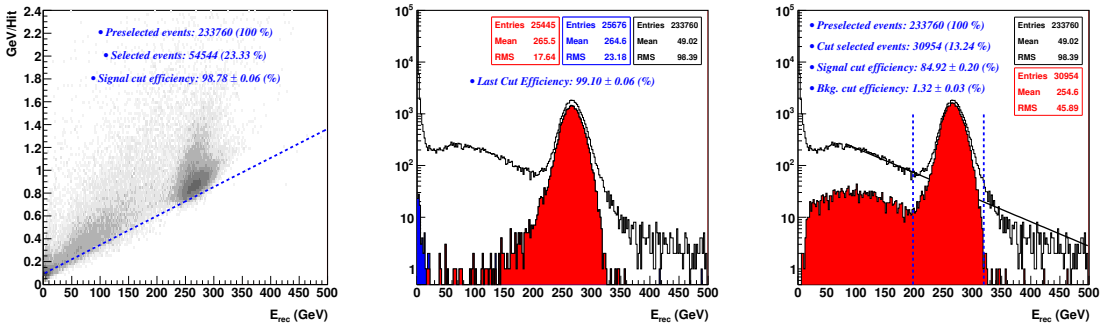

(a) (b) (c)

Fig. 5.18: *Dependence of the energy/hit with the energy, where the dash blue line is the Energy/Hit cut (Fig. 5.18(a)). Distribution of the reconstructed energy of the preselected sample (black), for events after the sequence of cuts except the Energy/Hit cut (blue), and for events after the sequence of cuts where the Energy/Hit cut is the last cut applied (red) (Fig. 5.18(b)). Distribution of the reconstructed energy of the preselected sample (black) and of the events after the third step in the sequence of cuts (red). The dash blue lines defines the signal (Fig. 5.18(c)).*

5.3.1.d Shower Transverse Size

The shower-shape variables related to the transverse profile of the energy depositions are used to identify electromagnetic showers, since e.g, the 95 % of the energy of a electromagnetic shower is contained within 2 Moliere radius (see section 2.4, pag. 17). The cut applied [6] in the energy contained in a cylinder of 2 cm of radius around the shower axis is energy independent. The results for a beam of 250 GeV electrons can be seen in Fig. 5.19.

[6] $\text{Energy}_{\pm 2\,\text{cm}}/\text{TotalEnergy} > 0.955$, where the cut value has been tuned with test-beam data.

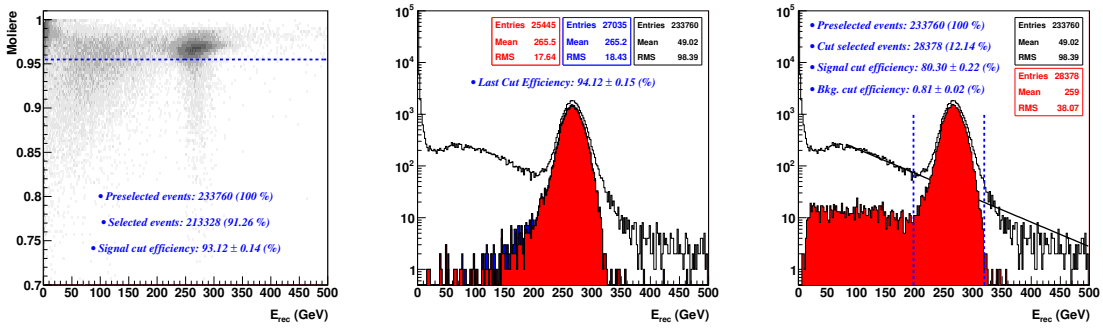

(a) (b) (c)

Fig. 5.19: *Dependence of the fraction of energy contained in a cylinder of 2 cm of radius with the energy, where the dash blue line is the Moliere cut (Fig. 5.19(a)). Distribution of the reconstructed energy of the preselected sample (black), for events after the sequence of cuts except the Moliere cut (blue), and for events after the sequence of cuts where the Moliere cut is the last cut applied (red) (Fig. 5.19(b)). Distribution of the reconstructed energy of the preselected sample (black) and of the events after the fourth step in the sequence of cuts (red). The dash blue lines defines the signal (Fig. 5.19(c)).*

5.3.1.e Matching Energy/Momentum

In addition to the set of electromagnetic cuts already applied (*ShowerMax*, *RearLeak*, *Energy/Hit* and *Moliere*), the reconstructed energy in the calorimeter must be compatible with the reconstructed momentum of the particle measured in the Tracker. The cut applied [7] in the ratio $E/|P|$ is energy independent. The results for a beam of 250 GeV electrons can be seen in Fig. 5.20(c).

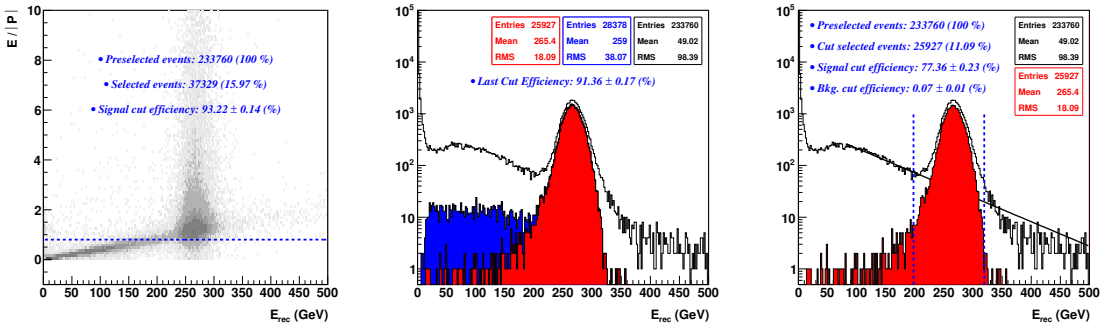

(a) (b) (c)

Fig. 5.20: *Dependence of the matching energy/momentum with the energy, where the dash blue line is the EPMatch cut (Fig. 5.20(a)). Distribution of the reconstructed energy of the preselected sample (black), for events after the sequence of cuts except the EPMatch cut (blue), and for events after the sequence of cuts where the EPMatch cut is the last cut applied (red) (Fig. 5.20(b)). Distribution of the reconstructed energy of the preselected sample (black) and of the events after the fifth step in the sequence of cuts (red). The dash blue lines defines the signal (Fig. 5.20(c)).*

[7] $E/|P| > 0.8$, where the cut value has been tuned with MC.

5.3.2 Calibration Method

The MIPs absolute calibration equalizes the channels in high gain. Besides, the low gain channels can be equalized with the ratio of high and low gain for each anode in the region where the high gain is not yet saturated. The average ratio found using the runs of block Ecal2 is 33 (Fig. 5.21(a)), in agreement with previous measurements [76].

The great advantage of using MIPs to calibrate is that the energy deposition is the same in all cells and layers along the particle path. However, this energy differs by three orders of magnitude with the energy deposited by a 250 GeV electron in the axis of the electromagnetic shower and central layers (Fig. 5.21(b)). Therefore, a subsequent calibration with electromagnetic showers can be used to equalize the energy deposition in the ECAL cells. This calibration comprises four steps: attenuation check, cells equalization, impact point correction implementation and rear leak check.

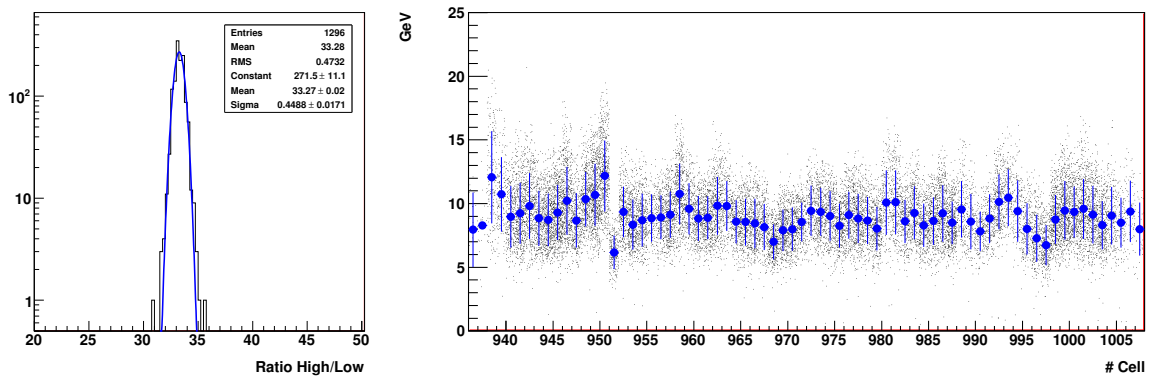

(a) (b)

Fig. 5.21: *Ratio of high and low gain for each anode (Fig. 5.21(a)). Deposited energy in cells of layer 13 along the shower axis with 250 GeV electrons (block Ecal2) (Fig. 5.21(b)).*

5.3.3 Attenuation Correction

The strategy used to check the attenuation correction with electromagnetic showers involves the comparison of the deposited energy in the same cell at different fiber lengths using opposite runs (table 5.6). The differences of energy in the external cells can reach values up to 40 %, decreasing toward the center of the ECAL (Fig. 5.22(a)). On the contrary, the MC simulation does not exhibit such behavior (Fig. 5.22(b)), showing that the attenuation effects are consistently accounted by the reconstruction.

If the energy coming from the attenuation correction α is written as a fraction of the energy without attenuation correction E^0

$$\alpha = \kappa \cdot E^0 \tag{5.2}$$

where κ is constant for a fixed position along the fiber, the energy deposited in the same cell in two opposite runs must be equal

$$E_1^0 + f \cdot \alpha_1 = E_2^0 + f \cdot \alpha_2 \quad \Rightarrow \quad E_1^0(1 + \kappa_1 \cdot f) = E_2^0(1 + \kappa_2 \cdot f) \tag{5.3}$$

TABLE 5.6: *List of pairs of runs used to check the attenuation correction. The Run1 is compared with the Run2, which share the same coordinate x (X-View) or the same coordinate y (Y-View).*

X-View				**Y-View**			
Run1 (Tag)	Run2 (Tag)	Run1 (Tag)	Run2 (Tag)	Run1 (Tag)	Run2 (Tag)	Run1 (Tag)	Run2 (Tag)
0181	01a6	018b	019c	0181	0194	018b	019e
0182	01a5	018c	019b	0182	0195	018c	019f
0183	01a4	018d	019a	0183	0196	018d	01a0
0184	01a3	018e	0199	0184	0197	018e	01a1
0185	01a2	018f	0198	0185	0198	018f	01a2
0186	01a1	0190	0197	0186	0199	0190	01a3
0187	01a0	0191	0196	0187	019a	0191	01a4
0188	019f	0192	0195	0188	019b	0192	01a5
0189	019e	0193	0194	0189	019c	0193	01a6
018a	019d			018a	019d		

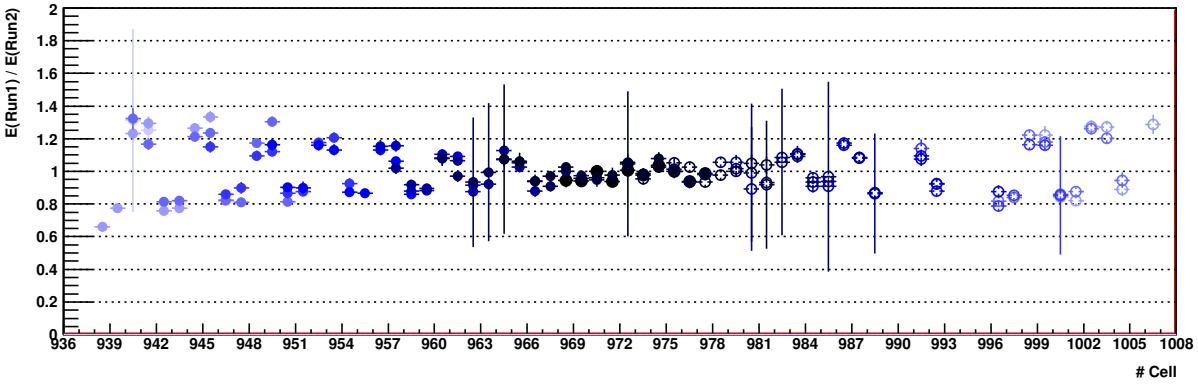

(a) Data

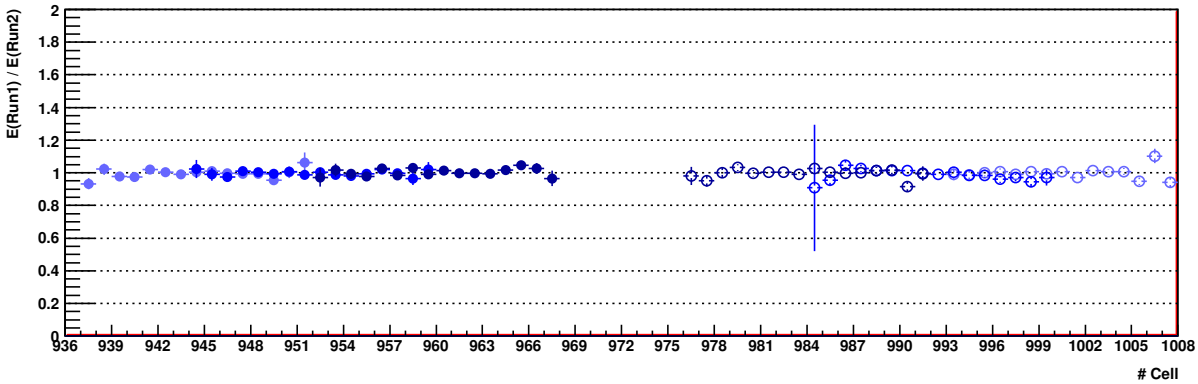

(b) MC

Fig. 5.22: *Ratio of energies deposited in the same cell using opposite runs in data (Fig. 5.22(a)) and MC (Fig. 5.22(b)) for layer 13.*

where f is an amplification factor, and the subscripts $1, 2$ means the run 1 and run 2. Defining the variable δ as

$$\delta \equiv \frac{1+\kappa_1 \cdot f}{1+\kappa_2 \cdot f} = \frac{E_2^0}{E_1^0} \quad ; \quad \frac{\sigma(\delta)}{\delta} = \sqrt{\frac{\sigma^2(E_1^0)}{(E_1^0)^2} + \frac{\sigma^2(E_2^0)}{(E_2^0)^2}} \tag{5.4}$$

the amplification f can be written as

$$f = \frac{\delta - 1}{\kappa_1 - \delta \cdot \kappa_2} \quad ; \quad \frac{\sigma(f)}{f} = \sigma(\delta) \left[\frac{\kappa_1 - \kappa_2}{(\kappa_1 - \delta\kappa_2)(\delta - 1)} \right] \tag{5.5}$$

The Fig. 5.23(a) shows the amplification factor extracted from data for layer 13 and the Fig. 5.23(b) and 5.23(c) the amplification factor for all the layers for data and MC respectively, which confirms the necessity of an attenuation re-correction using an amplification factor for each layer (Fig. 5.24). The Fig. 5.23(b) indicates a same fiber behavior at the superlayer level.

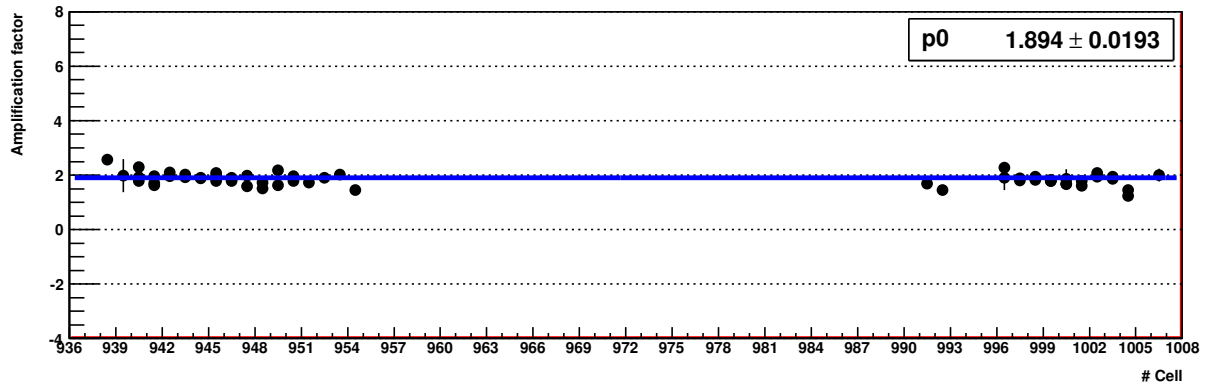

(a)

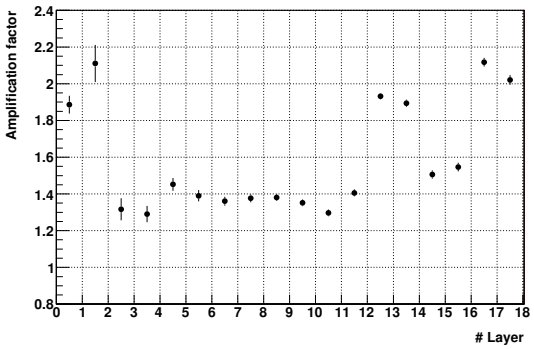

(b) TB Data

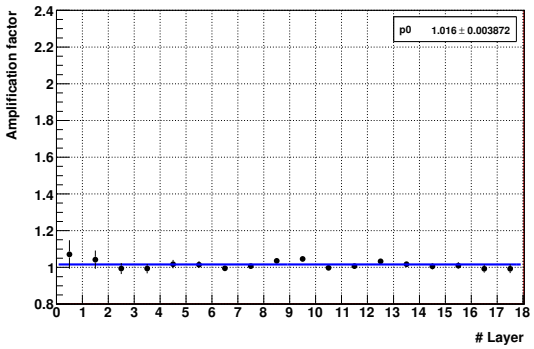

(c) MC

Fig. 5.23: *Amplification factor extracted for layer 13 (Fig. 5.23(a)). Amplification factors of all the layers for data (Fig. 5.23(b)) and MC (Fig. 5.23(c))*

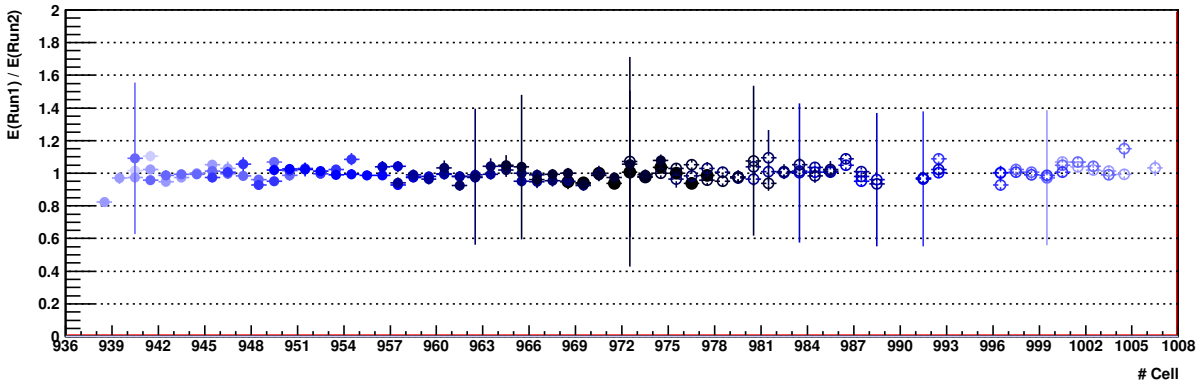

Fig. 5.24: *Ratio of energies deposited in the same cell using opposite runs in data after correction with amplification factor for layer 13.*

5.3.4 Gain Equalization

Once the attenuation has been corrected, any run of block Ecal2, independently of its position, can be used to equalize the cells. The values of the energy deposited by the shower axis in each layer have been obtained using different samples of cells:

- All the cells with the statistic of all the runs of block Ecal2.
- Cells at the center of the beam for individual runs of block Ecal2.
- Cells at 2 cm to the right of the center of the beam for individual runs.
- Cells at 2 cm to the left of the center of the beam for individual runs.

In all the cases, the average energy of the cells is fitted to a straight line after removing cells that can introduce a bias in the fit (Fig. 5.25 and 5.26). The energy of the cells in data requires an equalization, whereas the MC is equalized.

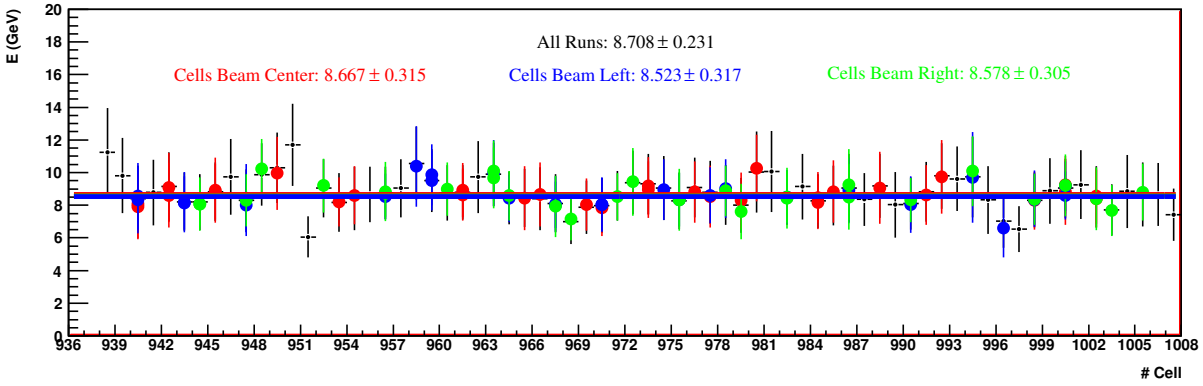

Fig. 5.25: *Deposited energy by the shower axis in the cells of layer 13, using all the statistics of block Ecal2 (black), cells at the center of the beam for individual runs (red), cells at 2 cm to the right of the center of the beam (green), and cells at 2 cm to the left of the center of the beam (blue). Real Data.*

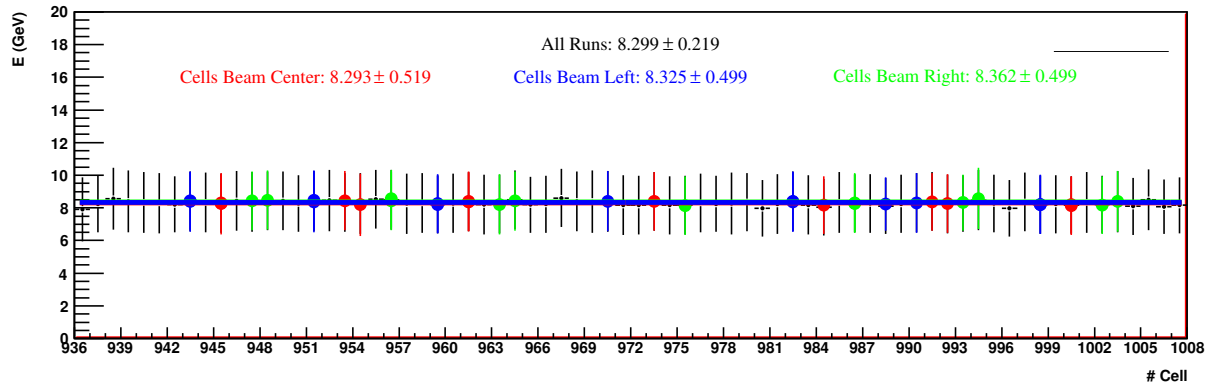

Fig. 5.26: *Deposited energy by the shower axis in the cells of layer 13, using all the statistics of block Ecal2 (black), cells at the center of the beam for individual runs (red), cells at 2 cm to the right of the center of the beam (green), and cells at 2 cm to the left of the center of the beam (blue). MC.*

The values of the energy obtained for each layer are plotted in the Fig. 5.27 and fitted to the Eq. (2.21) (pag. 18). The three cases are consistent with each other (Fig. 5.28(a)), so the values that have been chosen to equalize the cells are the energies obtained with all the statistics.

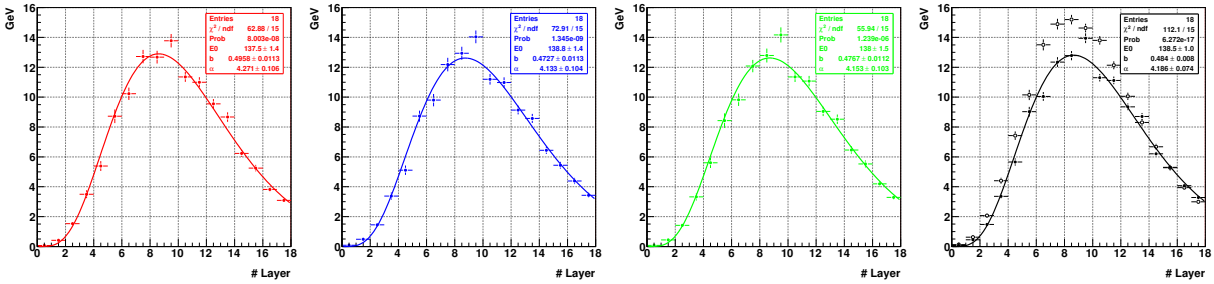

(a) Beam center (b) Beam left (c) Beam right (d) All events

Fig. 5.27: *The values of the energy obtained for each layer using cells at the center of the beam for individual runs (Fig. 5.27(a)), cells at 2 cm to the left of the center of the beam (Fig. 5.27(b)), cells at 2 cm to the right of the center of the beam (Fig. 5.27(c)), and all the statistic (Fig. 5.27(d)), where the black solid point is data and the black empty points is MC.*

The correction factors can be calculated as (Fig. 5.28(b))

$$\text{Correction Factor} = \frac{E(Layer)}{E(Cell)} \tag{5.6}$$

and once applied, the response of the cells is equalized (Fig. 5.29). For instance, the mean value of the cells energy of layer 13 is equalized at the level of 0.2 %, with an energy spread remaining stable within 8 % (Fig. 5.30).

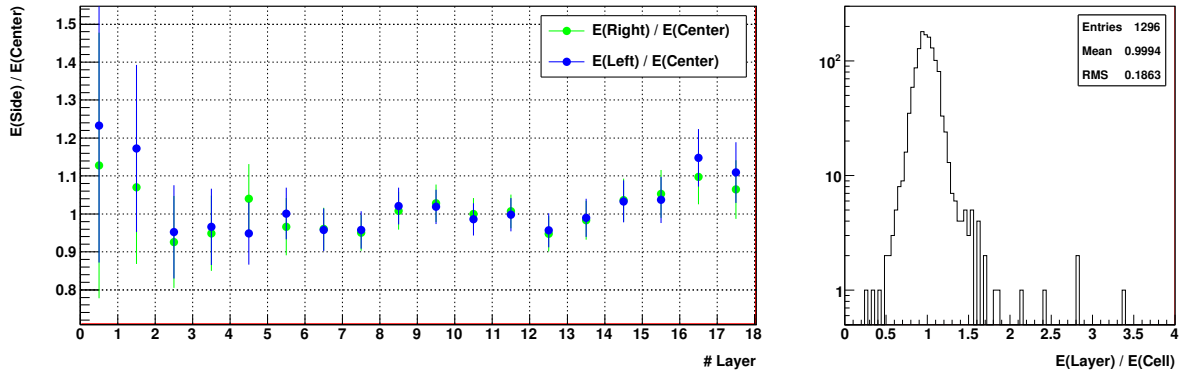

(a) (b)

Fig. 5.28: *Comparison of the energies obtained using cells at the right and left of the center with the energies obtained using the cells at the center of the beam (Fig. 5.28(a)). Distribution of the correction factors needed to equalized the energy in each layer (Fig. 5.28(b)).*

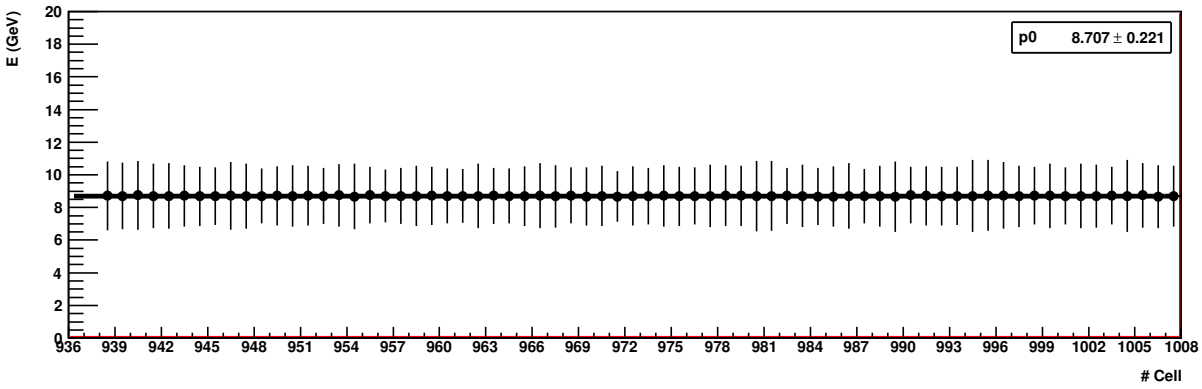

Fig. 5.29: *Energy of the cells of layer 13 after appling the correction factors.*

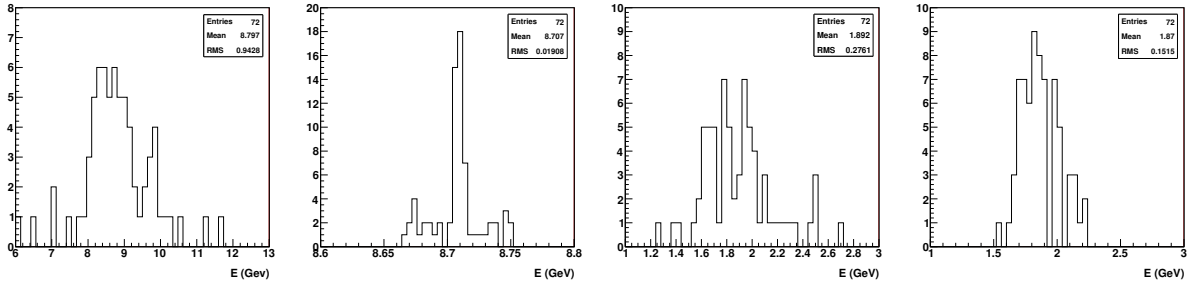

(a) (b) (c) (d)

Fig. 5.30: *Distribution of the cells energy before equalization (Fig. 5.30(a)) and after equalization (Fig. 5.30(b)) of the layer 13. Distribution of the cells energy spread before equalization (Fig. 5.30(c)) and after equalization (Fig. 5.30(d)) of the layer 13.*

5.3.4.a Inclined Runs

To check if the method used to equalize the energy of the cells is applicable to a more general case of data taking, all the procedure has been repeated with runs of 250 GeV and 5°,10°, and 15° to calculate the respective correction factors. The Fig. 5.31 shows a correlation of the correction factors at 0° with the correction factors obtained at 5, 10, and 15 degrees, remaining stable within 4 % (Fig. 5.32), which confirms that the method is not limited to events at normal incidence, but validates it up to at least 10° (Fig. 5.32(d)).

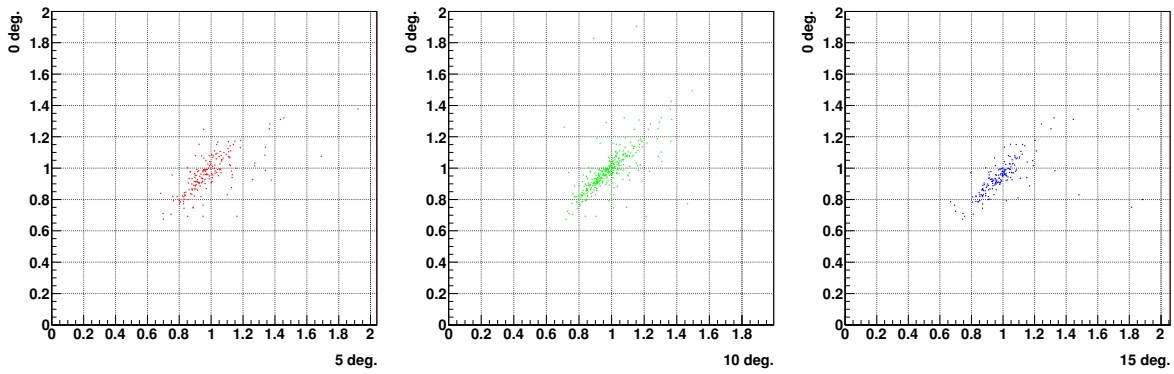

(a) (b) (c)

Fig. 5.31: *Correction factors at 0° compare with the correction factors at 5° (Fig. 5.31(a)), 10° (Fig. 5.31(b)), and 5° (Fig. 5.31(c)).*

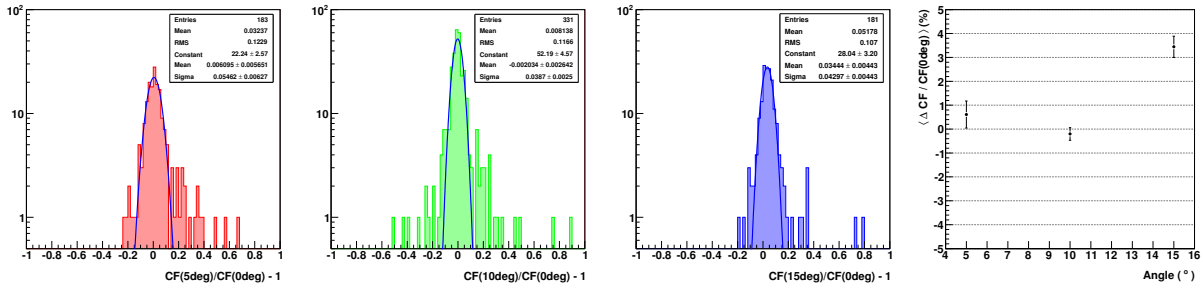

(a) (b) (c) (d)

Fig. 5.32: *Comparison of the correction factors obtained at 0° with the correction factors obtained at 5° (Fig. 5.32(a)), 10° (Fig. 5.32(b)), and 15° (Fig. 5.32(c)).*

5.3.5 Impact Position Correction

The deposited energy is sensitive to the impact point of the particle within the cell [86]. This energy dependence is corrected using the so-called S1/S3 ratio, where S1 is the energy deposited in a cell containing the shower axis, and S3 is the energy in the adjacent cells plus S1. This ratio has a great sensitivity to the impact point and its behavior is the same for different energies and angles (Fig. 5.33).

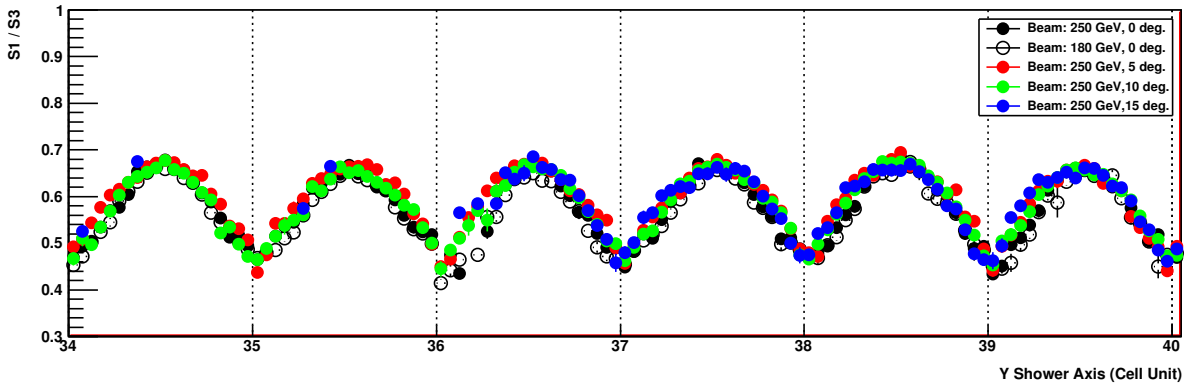

Fig. 5.33: *Sensitivity of the ratio S1/S3 to the impact position in units of cell number for differents energies and angles.*

The S1/S3 ratio can be given for a particular view if S1 and S3 are caculated using the layers in x or y. In the X-View S1/S3 has a mean value of 0.68 (Fig. 5.34(a)). Besides, it has a dependence with the energy (Fig. 5.34(b)), that can be parametrized with a hyperbolic tangent function

$$p0 \cdot (\tanh(p1 \cdot x + p2) + p3) \tag{5.7}$$

where $p0, \ldots, p3$ are parameters to fit. The left plateau ($S1/S3 < 0.5$) and the right plateau ($S1/S3 > 0.8$) correspond to the minimum and maximum energy deposition respectively. Therefore, the total deposited energy depends on the correction function $f(S1/S3)$ definition. For instance, the difference in the deposited energy for 250 GeV electrons between the minimum ($f(0) = 1$) and the maximum ($f(1) = 1$) correction is 20 GeV. The correction function that has been applied is defined with the mean of the $S1/S3$ distribution ($f(\langle S1/S3\rangle)$=1), since this value is stable at least for 250 GeV and 180 GeV electrons (Fig. 5.34(c)). This correction is applied at each layer and the resulting shower energy remains stable within 1 % with $S1/S3$ (Fig. 5.35).

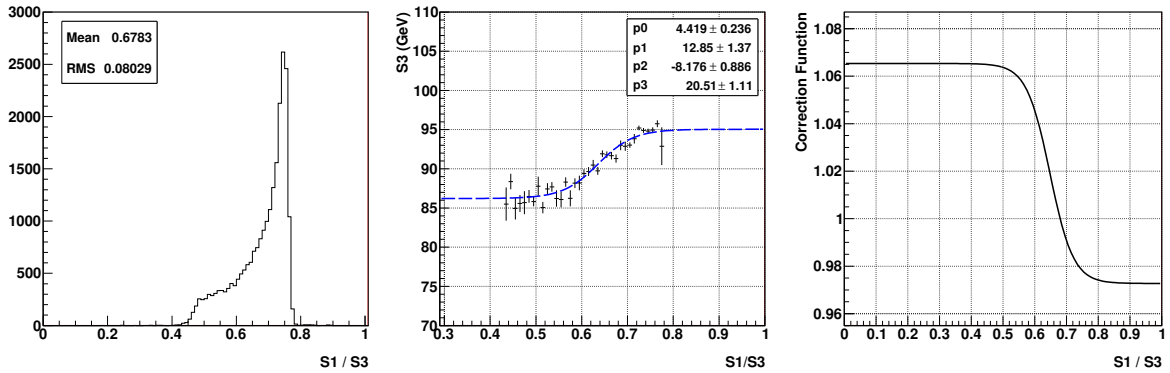

(a) (b) (c)

Fig. 5.34: *Distribution of S1/S3 in the x-view (Fig. 5.34(a)). Dependence of S1/S3 with the energy in the X-View (Fig. 5.34(b)). Correction function applied to the data (Fig. 5.34(c)).*

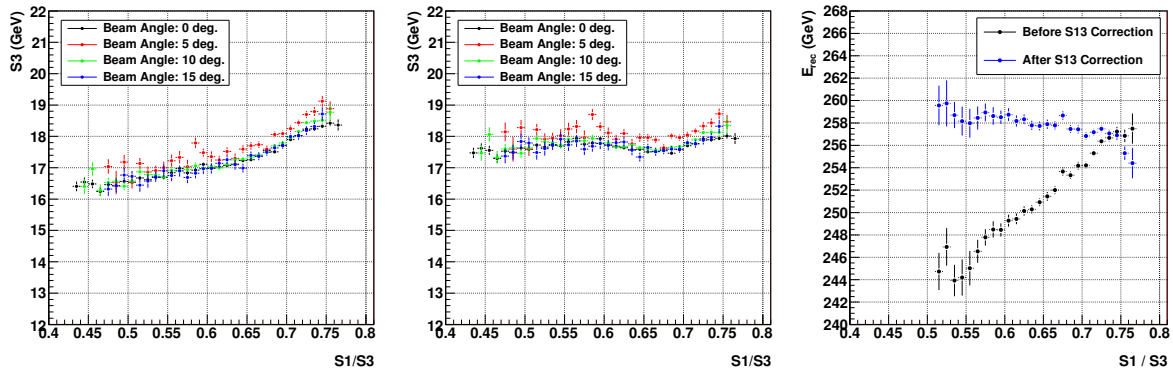

(a) Layer 11 before S1/S3 correction (b) Layer 11 after S1/S3 correction (c) Shower energy

Fig. 5.35: *Energy dependence with S1/S3 before (Fig. 5.35(a)) and after (Fig. 5.35(b)) the correction in layer 11 for different angles and beam energy 250 GeV. Reconstructed energy dependence with S1/S3 before and after correction using a normal incidence run at ECAL center (Fig. 5.35(c))*

5.3.6 Rear Leak Correction

The electromagnetic showers are not completely contained in the calorimeter, and the leakage of energy must be estimated. The rear leak correction relies on the linear dependence of the missing energy due to the longitudinal leakage with the fraction of energy deposited in the last layer [99, 100]

$$E - E_{dep} = \alpha \frac{E_{last}}{E_{dep}} \tag{5.8}$$

where E is the incident particle energy, E_{dep} is the deposited energy in the calorimeter, E_{last} is the deposited energy in the last ECAL layer and α is a constant.

The mean value of the deposited energy (without rear leak) before any correction is 230 GeV (Fig. 5.36(a)), whereas the reconstructed energy (with rear leak) is 266 GeV (Fig. 5.38(a)), which means 86 % of deposited energy and 14 % of rear leak.

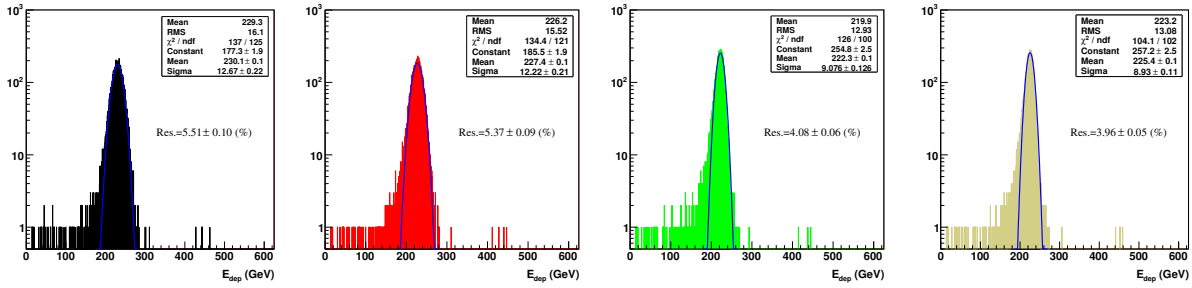

(a) (b) (c) (d)

Fig. 5.36: *Distribution of the deposited energy (without rear leak) for the runs of block Ecal2 without corrections (Fig. 5.36(a)), after the attenuation correction (Fig. 5.36(b)), after the attenuation correction plus the equalization, (Fig. 5.36(c)), and after the attenuation correction plus the equalization and impact point correction (Fig. 5.36(d)).*

Once the corrections have been applied (attenuation, equalization, and impact point), the deposited energy is 225 GeV (Fig. 5.36(d)), whereas the reconstructed energy is 260 GeV (Fig. 5.38(d)), once again 86 % of deposited energy and 14 % of rear leak.

To check if the correction is well implemented, the deposited energy (without rear leak) and the reconstructed energy (with rear leak) are plotted against the fraction of energy deposited in the last layer (Fig. 5.37(a) and 5.37(b)), which is 4 % for 250 GeV electrons (Fig. 5.37(c)). The battery of corrections applied to the recontructed data: the re-correction of the attenuation, the cells equalization, and the impact point correction, do not introduce any dependence in the reconstructed energy.

Another method to estimate the missing energy is to fit the longitudinal energy profile (Fig. 5.42(b)) to Eq. (2.21) (pag. 18). The results for 250 GeV electrons are 13.4 % of rear leak for 3.9 % energy deposition in the last layer. Therefore, the rear leak can be tuned using the fit result, due to the linear dependence of the rear leak with the last layer energy deposition (Fig. 5.37(c)).

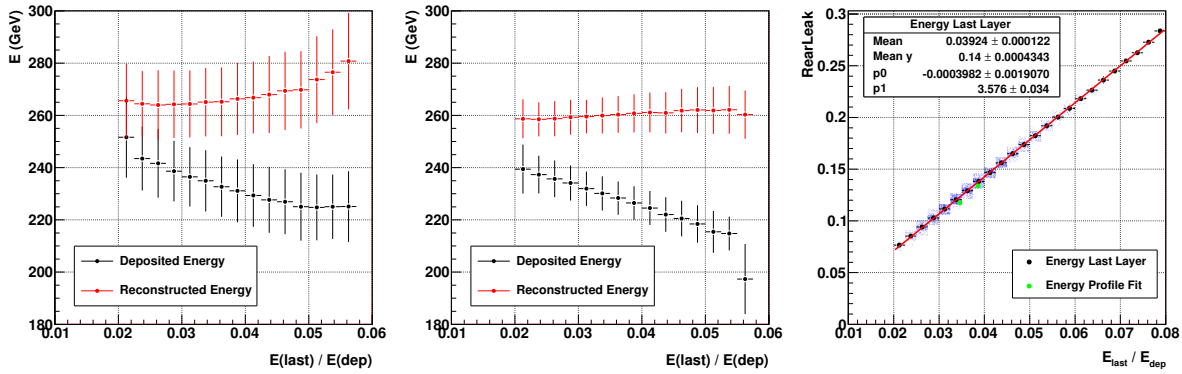

(a) Before corrections (b) After corrections (c)

Fig. 5.37: *Dependency of the deposited energy (without rear leak, black) and the reconstructed energy (with rear leak, red) with the fraction of deposited energy in the last layer, before corrections (Fig. 5.37(a)) and after corrections (attenuation, equalization, and impact point. Fig. 5.37(b)). Linear dependence of the rear leak with the energy deposited in the last layer, where the green markers come from the energy profile fit (Fig. 5.37(c)).*

5.4 ECAL Performance

5.4.1 Energy Resolution

Using the runs of block Ecal2, the energy resolution is 5 % at 250 GeV (Fig. 5.38(d)), which is a consequence of the energy dependence with the reconstruction position in the ECAL (Fig. 5.4). If the energy of the shower is recalculated after all the corrections, this value is reduced to 2.6 % (Fig. 5.38(d)). Although the improvement in the resolution is considerable, the question that arises at this point is if there is any possibility to get a better resolution, since there exists a residual structure in the energy dependence with the impact point (Fig. 5.39).

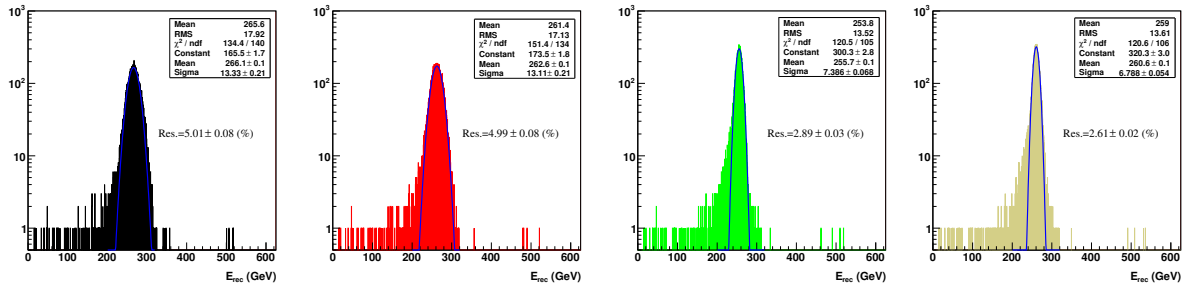

(a) (b) (c) (d)

Fig. 5.38: *Distribution of the energy for the runs of block Ecal2 without corrections (Fig. 5.38(a)), after the attenuation correction (Fig. 5.38(b)), after the attenuation correction plus the equalization, (Fig. 5.38(c)), and after the attenuation correction plus the equalization and impact point correction (Fig. 5.38(d)).*

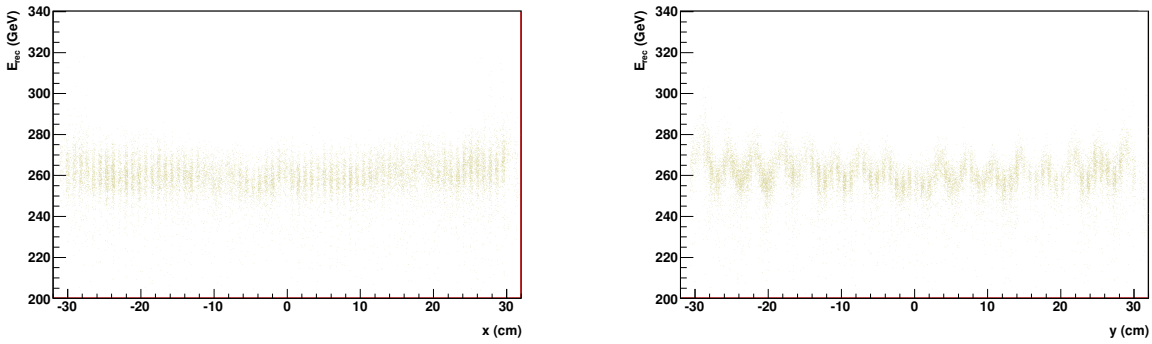

(a) (b)

Fig. 5.39: *Reconstructed energy after corrections of attenuation, equalization and impact point with the showers position along x (Fig. 5.39(a)) and y (Fig. 5.39(b)) axis using the runs of block Ecal2 and events after the preselection cuts and the set of electron selection cuts.*

5.4.1.a Beam Profile

The Fig. 5.40(a) and 5.40(b) shows the beam profile, which have a spread in x of $\sim 1.5\,\text{cm}$ and a spread in y of $\sim 2.5\,\text{cm}$. Looking into the energy profile of the beam there exists a structure in x and y that remains after the corrections (Fig. 5.40(c) and 5.40(d)). Taking into consideration only the central part of the beam ($\pm 1\,\text{cm}$) the resolution is reduced to $2.33\,\% \pm 0.05\,\%$.

5.4.1.b Angles

Another consideration to take into account is that the energy resolution improves with the angle of the beam (Fig. 5.41), since the number of radiation lengths that the particles go through increases with the incidence angle. The energy resolution goes from $2.33\,\% \pm 0.05\,\%$ at $0°$ to $1.83\,\% \pm 0.15\,\%$ at $15°$ within the beam center.

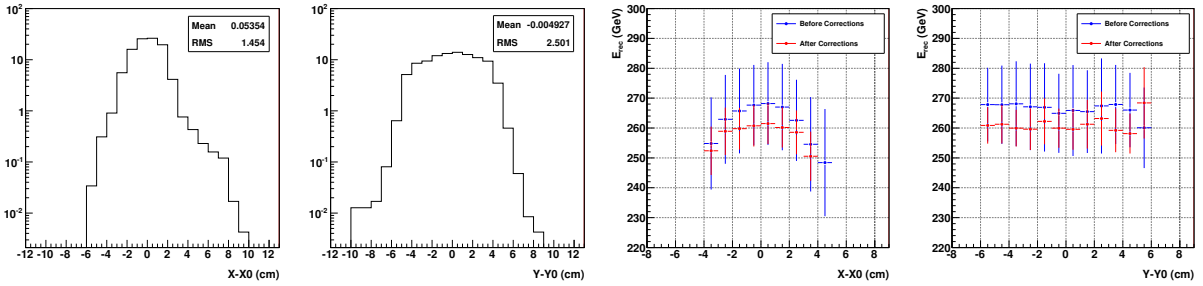

(a) (b) (c) (d)

Fig. 5.40: *Distribution of the beam profile in x (Fig. 5.40(a)) and y (Fig. 5.40(b)) normalized to 100. Energy profile before corrections (blue) and after corrections (red) in x (Fig. 5.40(c)) and y (Fig. 5.40(d)).*

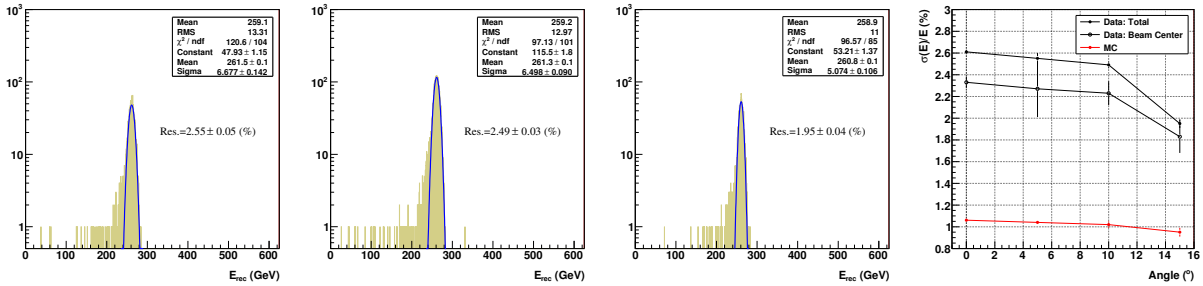

(a) 5 deg. (b) 10 deg. (c) 15 deg. (d)

Fig. 5.41: *Distribution of the reconstructed energy after corrections (attenuation, equalization, and impact point) for runs of 250 GeV and angle 5° (Fig. 5.41(a)), 10° (Fig. 5.41(b)), and 15° (Fig. 5.41(c)). Evolution of the resolution with the incidence angle (Fig. 5.41(d)), total (black solid), beam center (black empty), and MC (red).*

5.4.1.c Energy Scale

The energy resolution obtained in the MC is 1.1 % (Fig. 5.42(a)), better than resolution obtained in the data. In order to compare both, the deposited energy in each layer has been equalized to the repective value in MC (Fig. 5.42(b)), implying a multiplicative factor for each layer (Fig. 5.42(c)). The result is a deterioration of the resolution (3.2 % and 2.8 % within the beam center), that among other reasons, can be caused by correlations in the deposited energy in the different layers.

If the correlation matrix of the deposited energy in each layer is calculated as

$$\rho_{ij} = \frac{V_{ij}}{\sqrt{V_{ii}}\sqrt{V_{jj}}} \qquad i,j = 1,\ldots,18 \tag{5.9}$$

where ρ_{ij} are the elements of the matrix, V_{ij} the elements of the covariance matrix (Fig. 5.44(a))

$$V_{ij} = \langle E_i E_j \rangle - \langle E_i \rangle \langle E_j \rangle \qquad i,j = 1,\ldots,18 \tag{5.10}$$

and E_i the deposited energy in each layer, the superlayer structure is clearly visible (Fig. 5.43(a)).

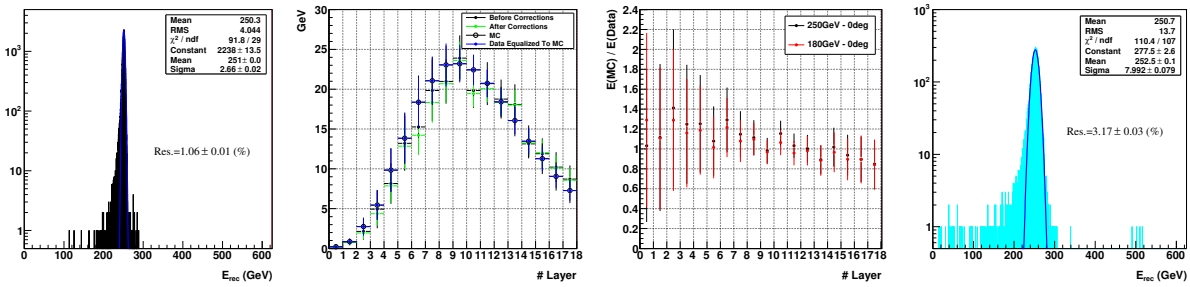

(a) (b) (c) (d)

Fig. 5.42: *Energy distribution of the MC runs of block Ecal2 generated (Fig. 5.42(a)). Energy profile for data without corrections (solid black), MC (empty black), data with corrections (green), and data equalized to MC (blue) (Fig. 5.42(b)). Ratio between the energy corrected and MC for each layer, 250 GeV (black) and 180 GeV (red) (Fig. 5.42(c)), only has been used the multiplicative factors of 250 GeV. Energy distribution after been equalized to MC (Fig. 5.42(d))*

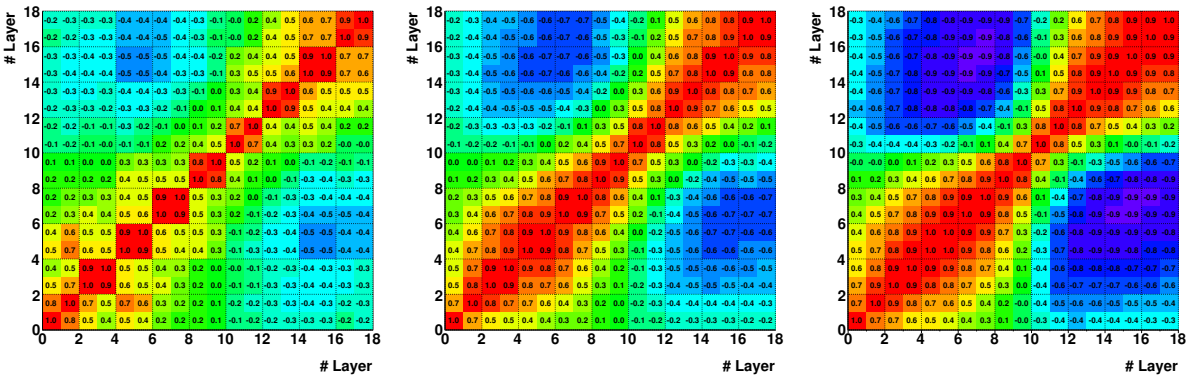

(a) Data before corrections (b) Data after corrections (c) MC

Fig. 5.43: *Correlation matrix of the deposited energy in each layer for data without corrections (Fig. 5.43(a)), data with corrections (Fig. 5.43(b)), and MC (Fig. 5.43(c)).*

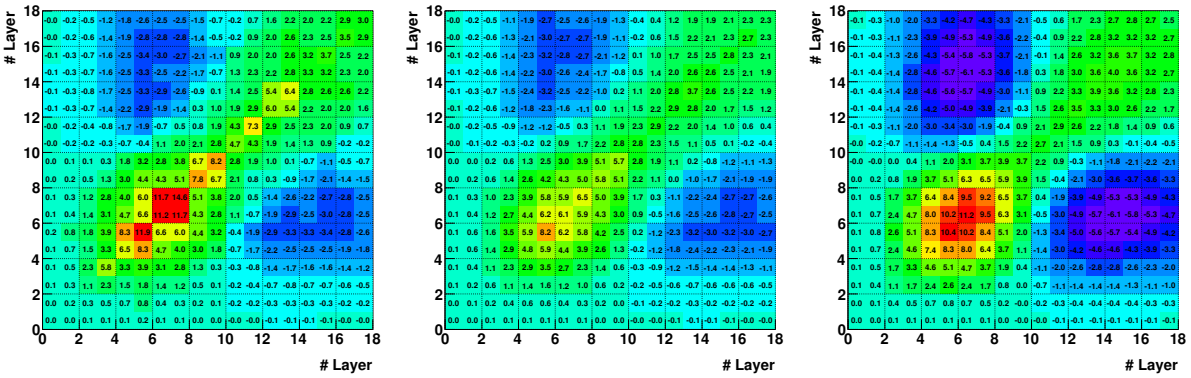

(a) Data before corrections (b) Data after corrections (c) MC

Fig. 5.44: *Covariance matrix of the deposited energy in each layer for data without corrections (Fig. 5.44(a)), data with corrections (Fig. 5.44(b)), and MC (Fig. 5.44(c)). They have the same scale.*

The energy variance $\sigma^2(E)$ can be calculated as the sum of the elements of the covariance matrix

$$\sigma^2(E) = \sum_{i,j} V_{ij} \tag{5.11}$$

which can be rewritten as the sum of the diagonal elements, the non diagonal positive elements, and the non diagonal negative elements

$$\sigma^2(E) = \sum_{i=j} V_{ij} + \sum_{i \neq j} V_{ij}(positives) - \sum_{i \neq j} |V_{ij}(negatives)| \tag{5.12}$$

The table 5.7 resumes the three sets of energy variance terms. The positive and negative non diagonal elements almost cancelled each other in MC, but not in real data. The correlations among layers are weaker in data than in MC (Fig. 5.43(c)), existing an improvement after corrections (Fig. 5.43(b)). The correlations exposed suggests the use of a global energy scale factor to correct the energy. The 250 GeV electrons need a scale factor of 4 % to adjust the shower mean energy of 260 GeV to the beam energy.

TABLE 5.7: *Energy variance* $\sigma^2(E)$.

	Diagonal (GeV^2)	Non Diagonal Positives (GeV^2)	Non Diagonal Negatives (GeV^2)	Total (GeV^2)
TB: before corrections	105.2	352.1	189.8	267.5
TB: after corrections	62.8	290.1	181.5	171.4
MC	78.7	369.4	384.8	63.3

Instead of equalize the deposited energy in each layer to the MC longitudinal energy profile, the energy can be equalized to the fit of the data longitudinal energy profile to Eq. (2.21) (pag. 18) without any deterioration in the energy resolution and mean reconstructed energy of 261 GeV. The correction factors from 180 and 250 GeV electrons are very similar, with differences below 2 %, which produced practically the same result with both sets of correction factors.

5.4.2 ECAL e/p Separation Cuts Efficiency

One of the main goals of the calorimeter is to provide an e/p separation to reduce the cosmic proton background. To maximize the electron acceptance, the preselection *Acc* cut must be revisited, since due to the backsplash at the ECAL entry the cut was set to select clean electromagnetic events to the detriment of the electron acceptance. The distribution of number of anticounters fired per event (Fig. 5.45) is different for electrons and protons. The table 5.8 collects the efficiency of the *Acc* cut for different ranges of anticounters fired, which suggest to take the range $0-4$ than represents 90 % of the events than only the first bin. This modification does not imply a substantial deviation from the results already obtained (Fig. 5.45(c)).

Additionally, a cut in the quality of the tracker track may be considered, represented for instance by the reconstructed chi-squared [8]. The table 5.9 collects the number of entries of the chi-squared distribution for different ranges. A chi-squared of 35 represents 80 % of the

[8] Reconstructed variable related to the quality of the track fit.

statistics in electrons and 89 % in protons. Taking this value as a limit will discard events with low reconstructed momentum without compromise the preselection.

TABLE 5.8: *Anticounters cut efficiency.*

# Anticounters (Maximum)	Electron 250 GeV (%)	Proton 400 GeV (%)
0	10.5	57.1
1	34.3	71.4
2	62.1	79.6
3	83.1	85.6
4	94.2	90.2
5	98.5	93.7
6	99.7	96.4
7	99.9	98.5
8	100	100

TABLE 5.9: *Chi-squared distribution entries.*

χ^2	Electron 250 GeV (%)	Proton 400 GeV (%)
5	27.9	26.9
10	53.4	56.6
15	65.8	72.2
20	72.2	80.2
25	76.1	84.6
30	78.6	87.1
35	80.2	88.7
40	81.4	89.7
45	82.3	90.4
50	83.0	90.9

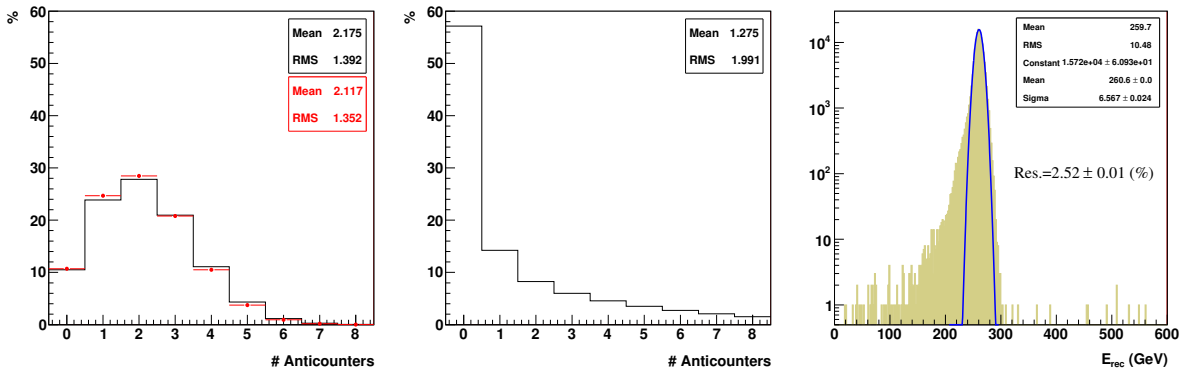

(a) 250 GeV e^- (b) 400 GeV p (c)

Fig. 5.45: *Number of anticounters fired per event for 250 GeV electrons (Fig. 5.45(a)) and 400 GeV protons (Fig. 5.45(b)). In the Fig. 5.45(a), the black line represents a sample selected with the set of cuts presented in the section 5.3.1 without the matching energy-momentum, and the red markers represents a sample with the matching energy-momentum. Energy resolution (Fig. 5.45(a)) after attenuation correction, plus equalization and impact point correction with Acc cut modified.*

Once these changes are taken into account and the selection cut parameters (see section 5.3.1, pag. 52) are tuned [9] to the calibrated data, the efficiency for 250 GeV electrons is 75 % (Fig. 5.46(b)) and 0.067 % for 400 GeV protons (Fig. 5.47(a)). The electron efficiency is obtained within a certain range of energy, after subtraction of an exponential background in this region. The table 5.10 collects the signal (electron) and background (proton) efficiencies using electromagnetic cuts and the matching between energy and momentum.

[9] *ShowerMax*: $a = \{7.803, 3.61, 2.55, 0.71\}$, $b = \{32.66, 2.300, 1.727, 0.242\}$. *RearLeak*: $a = \{0.1, 0.0209\}$. *Energy/Hit*: $a = \{9.3147 \times 10^{-2}, 2.538 \times 10^{-3}\}$. *Moliere*: $\text{Energy}_{\pm 2\,\text{cm}}/\text{TotalEner} > 0.957$. *EPMatch*: $E/|P| > 0.9$

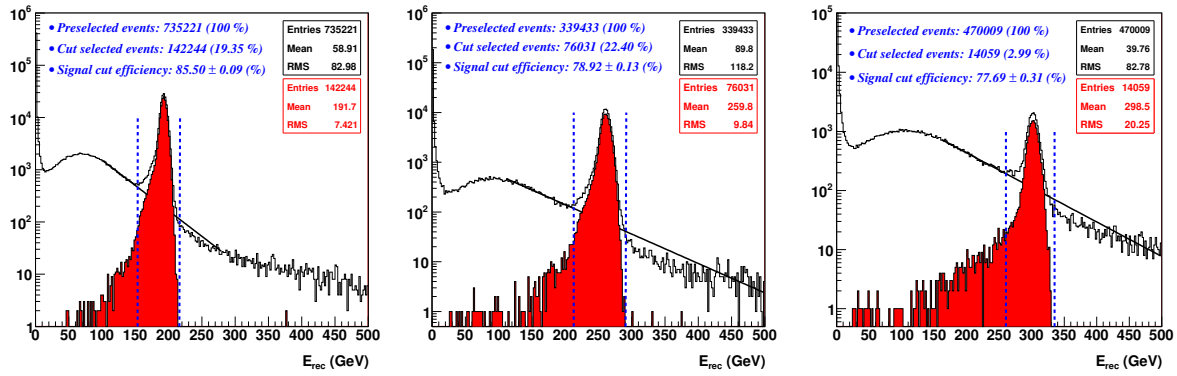

(a) 180 GeV e^- (b) 250 GeV e^- (c) 300 GeV e^-

Fig. 5.46: *Distribution of the reconstructed energy of the preselected sample (black) and the events after the sequence of cuts (red) for 180 GeV electrons (Fig. 5.46(a)), 250 GeV electrons (Fig. 5.46(b)), and 300 GeV electrons (Fig. 5.46(c)). The dash blue lines defines the signal and the solid black line represents the exponential background.*

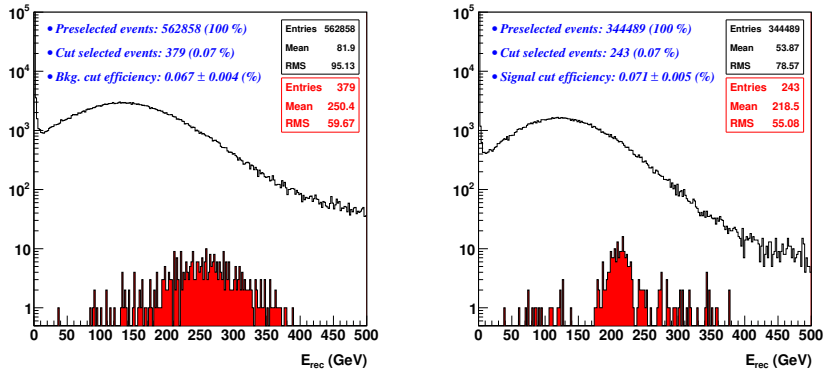

(a) TB Data: 400 GeV p (b) MC: 400 GeV p

Fig. 5.47: *Distribution of the reconstructed energy of the preselected sample (black) and the events after the sequence of cuts (red) for 400 GeV protons, test-beam data (Fig. 5.47(a)) and MC (Fig. 5.47(b)).*

TABLE 5.10: *Electron and proton selection cuts efficiencies at different energies with binomial errors using electromagnetic cuts and the matching between energy and momentum. The values are normalized to the sample of preselected events.*

	Electron 180 GeV (%)	Electron 250 GeV (%)	Electron 300 GeV (%)	Proton 400 GeV (%)
TB Data	85.50 ± 0.09	78.92 ± 0.10	77.69 ± 0.31	0.067 ± 0.004
MC	85.85 ± 0.27	80.53 ± 0.23	79.73 ± 0.32	0.071 ± 0.005

5.4.2.a ECAL e/p Separation Cuts Efficiency MC/Data Comparison

The e/p separation performance results obtained with test-beam data are compared in this section with simulated MC data from table 5.4 (pag. 48) and table 6.1 (pag. 75).

The MC and test-beam data distributions of the ECAL electromagnetic variables used to discriminate electrons from protons present a disagreement in the maximum of the shower and the rear leak that comes from the differences in the longitudinal energy profile discussed in previous sections, although it has not impact in the e/p separation. From the fit of the longitudinal energy profile to Eq. (2.21) (pag. 18), the discrepancy in the maximum of the shower is compatible to an earlier development of the electromagnetic shower in MC due to an extra amount of material equivalent to 0.25 radiation lengths. The observed MC shower maximum shift has an influence on the rear leak estimation as well, since this estimation depends on the deposited energy in the last layer. If the longitudinal energy profile is used to estimate the rear leak instead of the last layer method, the percentage of rear leak increases to 13.3 % once the extra 0.25 X_0 is taken into consideration, which is closer to the rear leak observed in data.

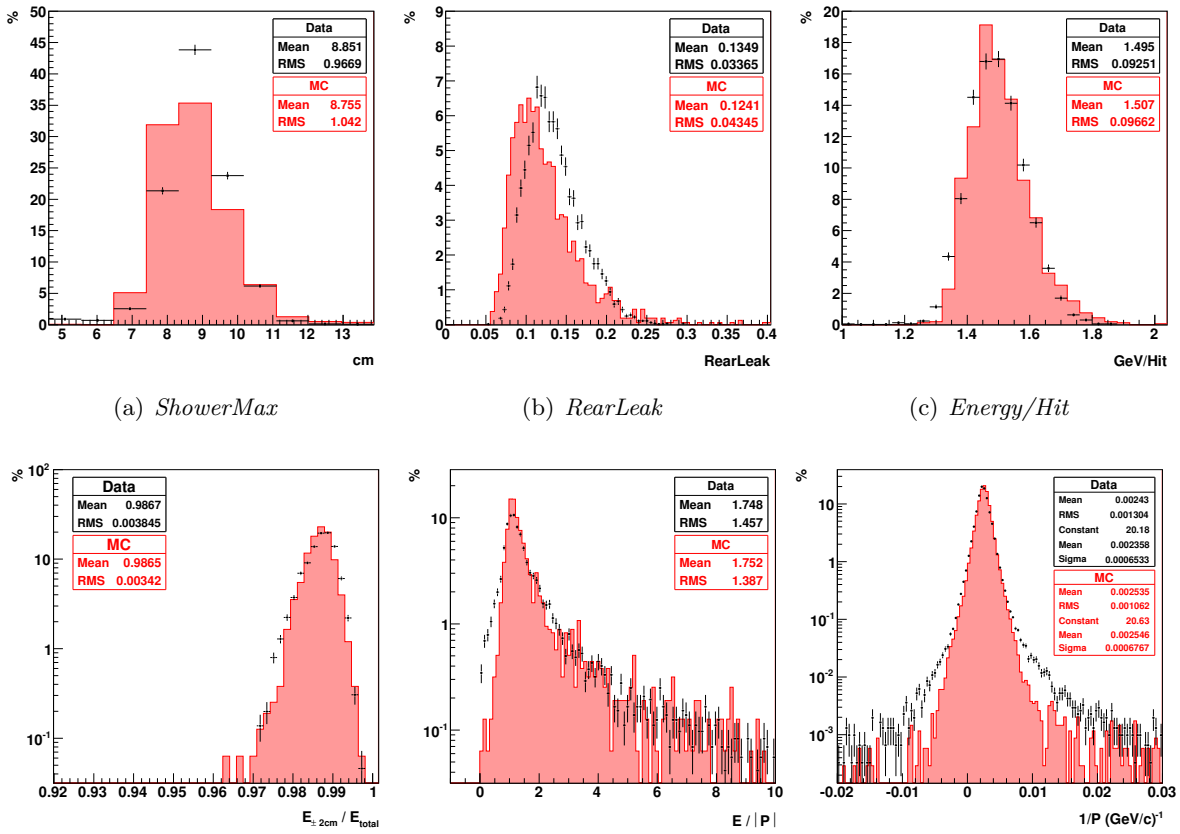

(a) *ShowerMax* (b) *RearLeak* (c) *Energy/Hit*

(d) *Moliere* (e) *EPMatch* (f) 400 GeV p

Fig. 5.48: *Distribution of the ECAL electromagnetic reconstructed variables for 250 GeV electrons at 0° (block Ecal1). The rear leak has been tuned using the longitudinal energy profile fit results. The Energy/Hit and Moliere distributions include a threshold in the hit energy ($E > 39$ MeV). Inverse of the reconstructed momentum for 400 GeV protons (Fig. 5.48(f)). Test-beam data (black markers) and MC (red line).*

On the other hand, the energy equipartition (*Energy/Hit*) and the energy contained in a cylinder of 2 cm of radius around the shower axis (*Moliere*) come to an agreement when a threshold in the hit energy is set ($E_{hit} > 39\,\text{MeV}$), which from section 5.3.1.c supposes a reduction of 45 % in the number of the shower hits but only 1 % in the shower energy. Besides, the matching between the energy and the momentum exhibits an agreement in the distribution mean (Fig. 5.48(e)), an agreement that is also observed in the momentum distribution (Fig. 5.48(f)).

Once the selection cut parameters (see section 5.3.1, pag. 52) are tuned [10] to get closer the test-beam and MC efficiencies of the cuts when they are used as first cut [11], the cumulative efficiency (table 5.10) of the sequence of cuts for 250 GeV electrons is 77 % and 0.07 % for 400 GeV protons (Fig. 5.47(b)), quite similar to the results obtained with test-beam data.

[10] *ShowerMax*: $a = \{7.803, 3.61, 2.55, 0.71\}$, $b = \{32.66, 2.143, 1.727, 0.242\}$. *RearLeak*: $a = \{0.1, 0.030\}$. *Energy/Hit*: $a = \{0.1541, 2.538 \times 10^{-3}\}$. *Moliere*: $\text{Energy}_{\pm 2\,\text{cm}}/\text{TotalEner} > 0.957$. *EPMatch*: $E/|P| > 0.9$

[11] The 250 GeV electrons at 0° (block Ecal2) have been used as reference.

6

Transition Radiation Detector

The transition radiation detector provides an additional e/p separation that contributes to reduce the proton background. The data collected in the February 2010 test-beam with the AMS-02 superconducting magnet configuration of the detector is used in this chapter to analize the TRD performance, which is compared to MC data. A good agreement between test-beam data and MC data is required to validate the cosmic ray positron analysis.

The same runs summarized in the table 5.2 (pag. 44) have been used to evaluate the TRD performance during the February 2010 test-beam and compared with the simulated MC data from table 5.4 (pag. 48) together with new simulated runs of protons and pions (table 6.1) that replicate the block Ecal1 and block Ecal2 positions. The generated events follow a Gaussian distribution centered at the beam center and with $\sigma_x = 1.5\,\text{cm}$ and $\sigma_y = 2.7\,\text{cm}$.

Table 6.1: *MC simulated runs.*

Particle	Energy (GeV)	Block	Angle (°)	# Runs	# Generated Events
Pion	180	Ecal1	0	1	40000
Pion	180	Ecal1	5	1	40000
Pion	180	Ecal1	10	1	40000
Pion	180	Ecal1	15	1	40000
Pion	300	Ecal1	0	1	40000
Pion	300	Ecal1	5	1	40000
Pion	300	Ecal1	10	1	40000
Pion	300	Ecal1	15	1	40000
Pion	250	Ecal2	0	13	260000
Proton	400	Ecal1	0	1	200000
Proton	400	Ecal1	5	1	200000
Proton	400	Ecal1	10	1	200000
Proton	400	Ecal1	15	1	200000

6.1 Data Sample Preselection

The changes introduced in the section 5.4.2 (pag. 70) to the preselection cuts have been incorporated into the TRD analysis. The Fig. 6.1 updates the Fig. 5.1 from section 5.1.2 taking into account these changes.

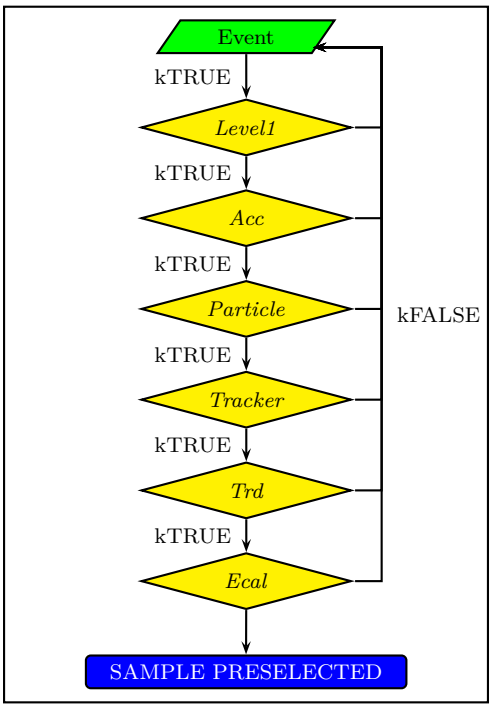

1. ***Level1*:** Level1 trigger present.
2. ***Acc*:** Number of anticounters fired ≤ 4.
3. ***Particle*:** 1 Particle reconstructed.
4. ***Tracker*:**
   (a) $0 <$ Tracker tracks reconstructed ≤ 3.
   (b) Chi-squared track (`Chi2FastFit`) ≤ 35
5. ***Trd*:** 1 TRD track reconstructed.
6. ***Ecal*:**
   (a) 1 Shower reconstructed.
   (b) $|x(track)| < 32\,\text{cm}$ (Particle track at ECAL entry).
   (c) $|y(track)| < 32\,\text{cm}$ (Particle track at ECAL entry).
   (d) $|x(track) - x(ecal)| < 1\,\text{cm}$ (Spatial matching at ECAL entry).
   (e) $|y(track) - y(ecal)| < 1\,\text{cm}$(Spatial matching at ECAL entry).

Fig. 6.1: *Preselection cuts used in the data analysis.*

The table 6.2 collects the fraction of events after each preselection cut following the sequence presented in the Fig. 6.1, for electron and proton beams. Note that the electron beam is composed by electrons and pions, therefore, the figures of the table 6.2 refer to the electron beam do not represent cut efficiencies of any particular species.

TABLE 6.2: *Fraction of events after preselection cuts.*

Beam		Level1 (%)	Acc (%)	Particle (%)	Tracker (%)	Trd (%)	Ecal (%)
Electron	(180 GeV)	100	96.2	85.8	41.6	36.0	16.3
Electron	(250 GeV)	100	87.5	75.4	35.8	30.1	14.3
Electron	(300 GeV)	100	90.7	80.9	46.2	40.1	18.1
Proton	(400 GeV)	100	90.0	81.9	61.5	56.9	33.6

6.2 TRD Calibration Verification

The readout signals from the TRD tubes constitute the lowest level pattern of the TRD track reconstruction. Besides, the amount of deposited energy in these tubes provides the signature to perform the e/p separation.

All the 5248 tubes were active during the test-beam, which can be seen in the distribution of the tubes occupancy (Fig. 6.2).

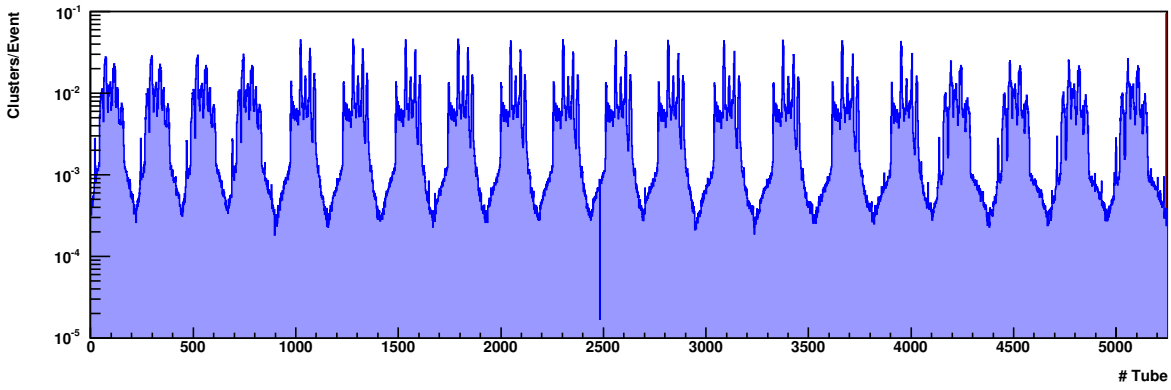

Fig. 6.2: *Tubes occupancy distribution in total clusters per event after preselection cuts and electron selection cuts (section 5.3.1) for 250 GeV electrons.*

6.2.1 TRD Track Multiplicities

The TRD track is reconstructed with the clusters (see section 4.1.2, pag. 39) that emerge from the interaction of the incident particle along the 20 layers. The used clusters represent 73 % of the total clusters for 250 GeV electrons (Fig. 6.3). The number of total clusters per track and event is 27, while the number of used clusters per track and event is 19, slightly above the MC.

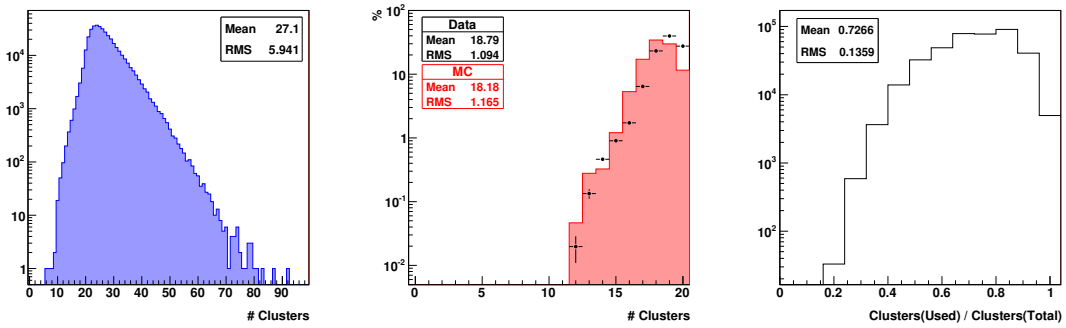

(a) 250 GeV e^- (b) 250 GeV e^- @ 5° (c) 250 GeV e^-

Fig. 6.3: *Distribution of the track cluster multiplicity in total clusters (6.3(a)) and used clusters (6.3(b)), MC (black markers) and test-beam data (red line), after preselection cuts and electron selection cuts (section 5.3.1) for 250 GeV electrons. Ratio of used clusters and total clusters (6.3(c)).*

On the other hand, for 400 GeV protons, the used clusters represent 89 % of the total clusters (Fig. 6.4). The number of total clusters per track and event is 21, while the number of used clusters per track and event is 19, slightly above the MC.

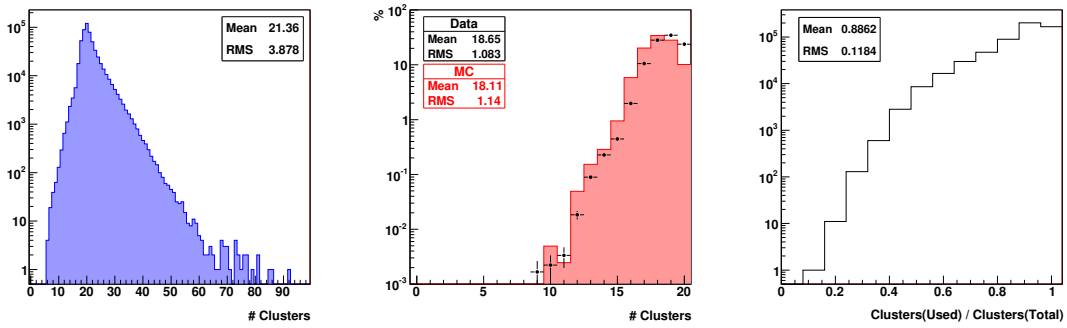

(a) 400 GeV p (b) 400 GeV p @ 5° (c) 400 GeV p

Fig. 6.4: *Distribution of the track cluster multiplicity in total clusters (6.4(a)) and used clusters (6.4(b)), MC (black markers) and test-beam data (red line), after preselection cuts for 400 GeV protons. Ratio of used clusters and total clusters (6.4(c)).*

The clusters themselves have a multiplicity in number of hits (Fig. 6.5). For 400 GeV protons 88 % of the clusters have one hit, while for 250 GeV electrons this percentage decreases to 68 % due to the presence of transition radiation.

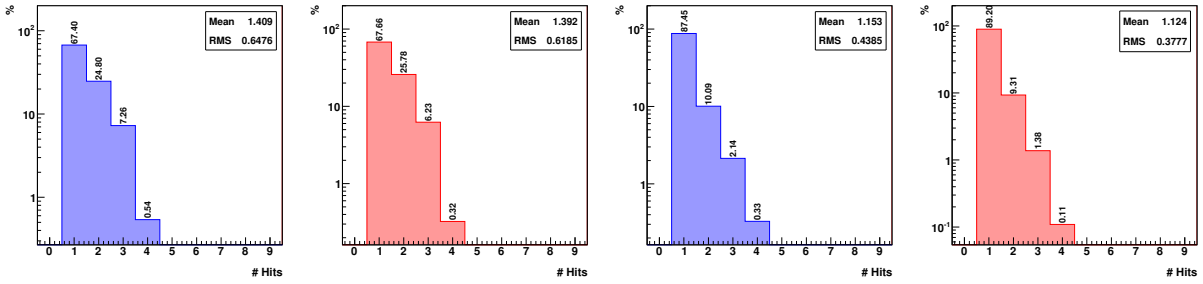

(a) 250 GeV e^- (b) 250 GeV e^- (c) 400 GeV p (d) 400 GeV p

Fig. 6.5: *Distribution of the hits multiplicity within total clusters (6.5(a) and 6.5(c)) and used clusters (6.5(b) and 6.5(d)) for 250 GeV electrons (after preselection cuts and electron selection cuts (section 5.3.1)) and 400 GeV protons (after preselection cuts).*

6.2.2 Tubes Deposited Energy

The deposited energy spectrum of the tubes can be a pure ionization spectrum or the mixture of two contributions: ionization and transition radiation, where the amount of transition radiation detected increases with the Lorentz-factor γ of the primary particle. The Fig. 6.6 shows the tubes energy spectrum for electrons, protons and pions, where the MC energy deposition has been adjusted to the test-beam data energy deposition under the assumption of no layer correlation in the energy deposition.

In the case of pions there exists an electron contamination, which is 6 % (Fig. 6.7(a)). Looking at the efficiency of a TRD cut with the energy reconstructed in the ECAL, e.g, a likelihood cut (see section 6.3.2), confirms the existence of two different species (Fig. 6.7(b)). Therefore, due to the existence of this electron contamination and to avoid a direct cut in the reconstructed energy, the measurement of a MIP signal in the ECAL (see section 5.2.1, pag. 48) will be used to select a pion sample.

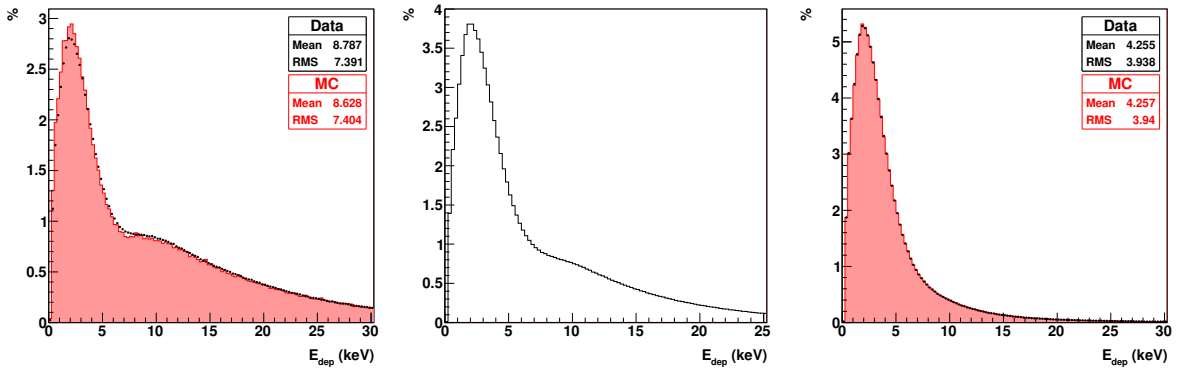

(a) 250 GeV e^- (b) 250 GeV π (c) 400 GeV p

Fig. 6.6: *Deposited energy spectrum of all the tubes for 250 GeV e^- (Fig. 6.6(a)), 250 GeV π (Fig. 6.6(b)), and 400 GeV p (Fig. 6.6(c)). The black markers represent the test-beam data and the red line the MC data.*

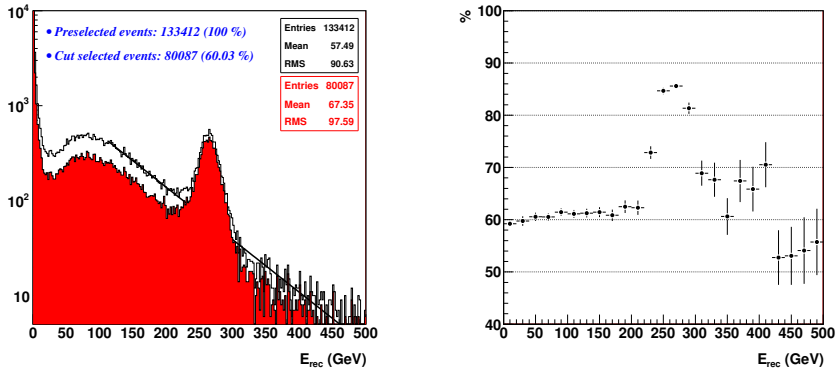

(a) 250 GeV π (0°) (b) 250 GeV π (!(EcalMIPs) 0°)

Fig. 6.7: *ECAL reconstructed energy for 250 GeV π before (black) and after the likelihood cut (red) (see section 6.3.2) (Fig. 6.7(a)). Likelihood cut efficiency with the energy reconstructed in the ECAL for 250 GeV π no MIPs selection (Fig. 6.7(b)).*

6.2.2.a Ionization and Transition Distributions

The ionization distribution can be fitted to a convoluted Landau and Gaussian function in the range [0.5,6] keV. The individual tubes have a mean MPV of 1.8 keV for 250 GeV electrons (Fig. 6.8(a)), and the MPV obtained for each layer remains stable within 3 % (Fig. 6.8(b)).

There exits a dependence of the ionization MPV with the beam angle (Fig. 6.9), and the differences between the MPV values are not greater than 13 % for electrons, and 6 % for pions and protons (table 6.3). Using the pion samples extracted from the electron beam and the cosmic muons taken during the test-beam (Fig. 6.10), the MPV can be plotted as a function of the Lorentz-factor γ (Fig. 6.8(c)).

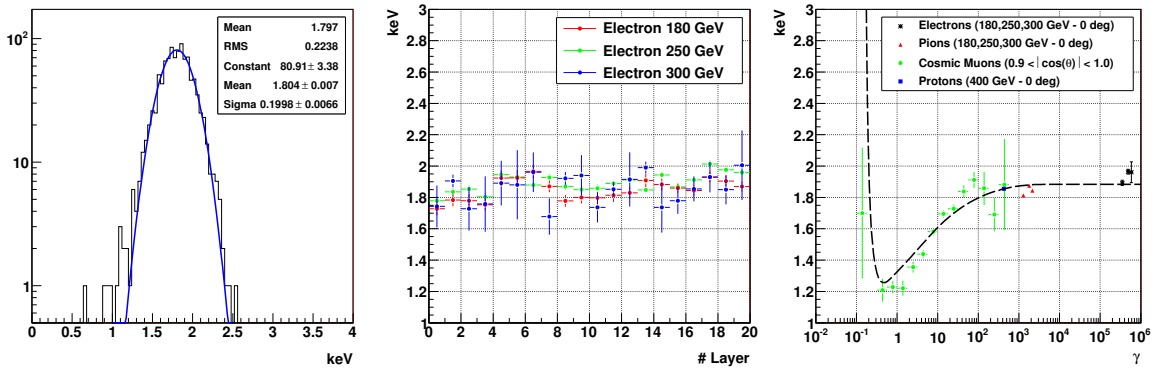

(a) (b) (c)

Fig. 6.8: *Tubes ionizatiton MPV for 250 GeV electrons (Fig. 6.8(a)). Ionization MPV within each layer for 180, 250, and 300 GeV electrons (Fig. 6.8(b)). Ionization MPV dependence with the Lorentz-factor γ (Fig. 6.8(c)).*

TABLE 6.3: *Ionization MPV and beam angles.*

Particle	Energy (GeV)	Highest MPV[IO] (keV)	Lowest MPV[IO] (keV)	$\lvert Low/High - 1\rvert$ (%)
Electron	180	1.893 @ 0°	1.745 @ 5°	7.65
	250	1.964 @ 0°	1.715 @ 5°	12.7
	300	1.989 @ 15°	1.767 @ 5°	11.2
Pion	180	1.907 @ 15°	1.793 @ 5°	5.96
	250	1.885 @ 15°	1.820 @ 5°	3.93
	300	1.880 @ 15°	1.804 @ 5°	4.04
Proton	400	1.926 @ 10°	1.813 @ 5°	5.87

From MC, the 400 GeV protons have 2 % of transition radiation emission probability using 32 GeV protons as ionization pattern. Therefore, due to the absence of better test-beam data samples, the deposited energy in all the tubes by 400 GeV protons is taken as the ionization distribution pattern. The transition distribution can be obtained subtracting the ionization pattern to the actual deposited energy, once the ionization distribution has been scaled according with its MPV dependence with γ (Fig. 6.11(a)). The resulting transition distribution has a MPV of 11 keV for 180 GeV at 0°. There exits a dependence of the transition MPV with the beam angle (Fig. 6.11(b) and 6.11(c)), and the differences between the MPV values are not greater than 8 % for electrons and 5 % for pions (table 6.4).

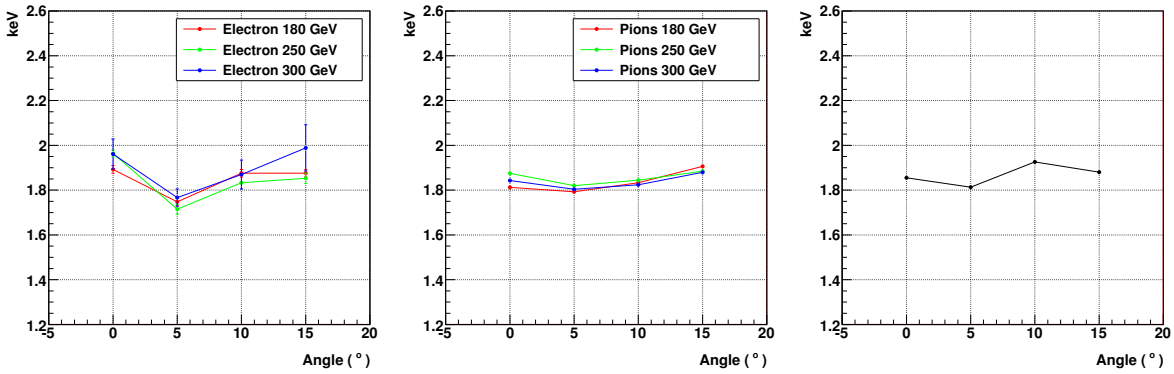

(a) e^- (b) π (c) p

Fig. 6.9: *Ionizatiton MPV dependence with beam angle for electrons (Fig. 6.9(a)), pions (Fig. 6.9(b)), and protons (Fig. 6.9(c)).*

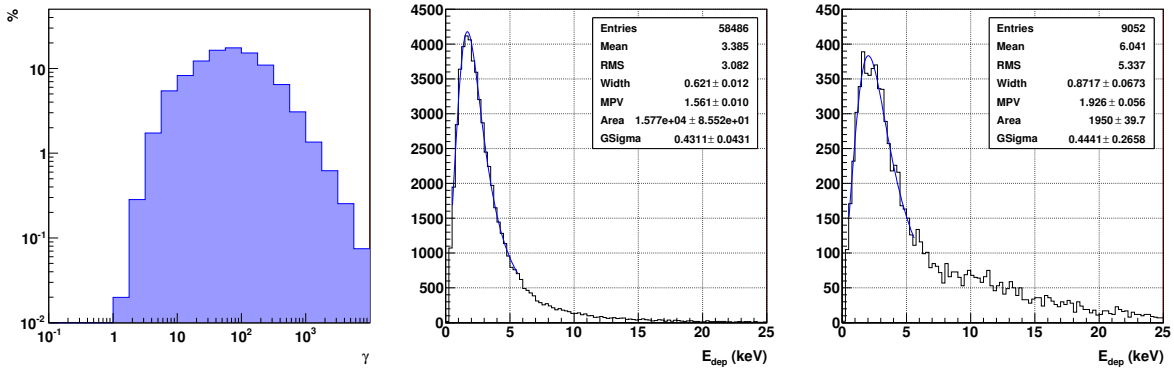

(a) (b) $3.16 < \gamma < 5.62$ (c) $100 < \gamma < 562$

Fig. 6.10: *Cosmic muons spectrum (Fig. 6.10(a)). Cosmic muons energy deposited in all the tubes for two ranges of Lorentz-factor γ (Fig. 6.10(b) and 6.10(c)).*

TABLE 6.4: *Transition MPV and beam angles.*

Particle	Energy (GeV)	Highest MPV[TR] (keV)	Lowest MPV[TR] (keV)	$\lvert Low/High - 1\rvert$ (%)
Electron	180	11.181 @ 0°	10.601 @ 10°	5.19
	250	11.275 @ 0°	10.677 @ 5°	5.30
	300	11.627 @ 15°	10.724 @ 10°	7.77
Pion	180	10.898 @ 15°	10.391 @ 5°	4.65
	250	10.753 @ 15°	10.390 @ 5°	3.38
	300	10.884 @ 15°	10.452 @ 10°	3.97

The transition emission probability Prob(TR) can be estimated from the ionization distribution, which is used to calculate the ionization probability

$$\text{Prob(IO)} = \frac{\int f_{ion}(E)\,dE}{\int f_{tot}(E)\,dE} \tag{6.1}$$

where $f_{ion}(E)$ is the ionization distribution and $f_{tot}(E)$ is the total deposited energy distribution. Therefore, the transition emission probability is

$$\text{Prob(TR)} = 1 - \text{Prob(IO)} \tag{6.2}$$

which is 42 % for $\gamma \gg$ (Fig. 6.12(a) and 6.12(b)).

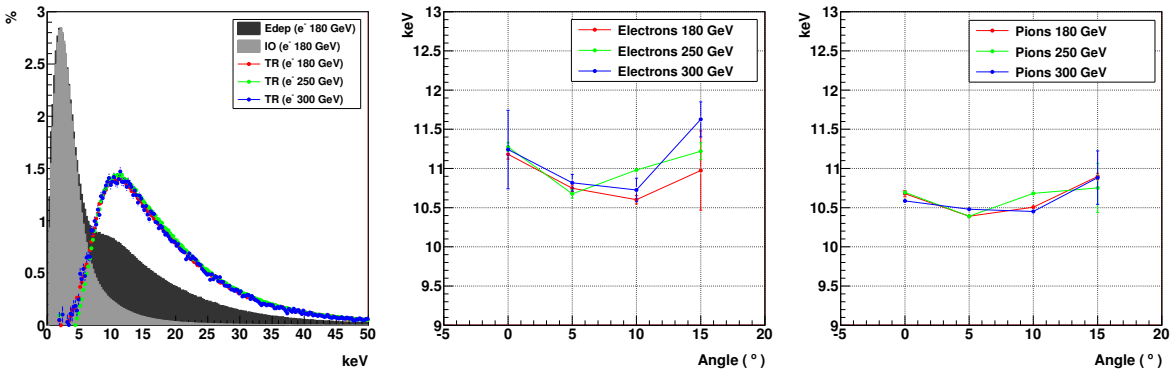

(a) (b) (c)

Fig. 6.11: *Total deposited energy in all the tubes (dark grey), ionization distribution (grey), and transition distributions (red, green, and blue markers) for electrons (Fig. 6.11(a)). Transition MPV dependence with beam angle for electrons (Fig. 6.11(b)) and pions (Fig. 6.11(c)).*

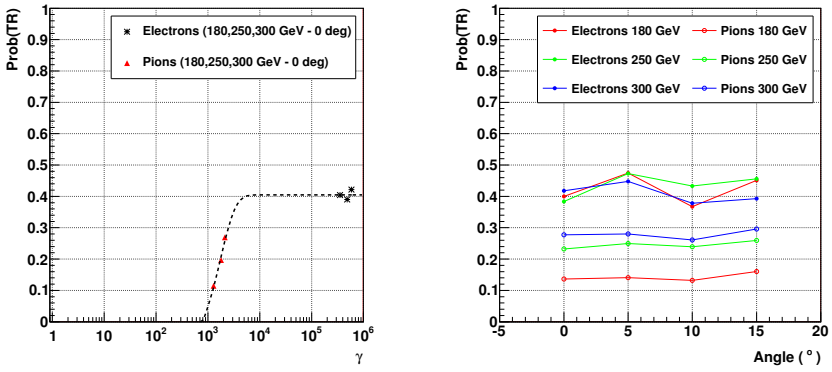

(a) (b)

Fig. 6.12: *Transition emission probability plotted as a function of the Lorentz-factor γ (Fig. 6.12(a)), where Prob(TR) is fitted to $p_0 \cdot tanh(x/p_1 + p_2)$ with $p = \{p_0, p_1, p_2\} = \{0.425, 1889, -0.346\}$. Transition emission probability dependence with the beam angle (Fig. 6.12(b)).*

6.3 TRD Performance

The TRD e/p separation is based on the dependence of the deposited energy in the tubes with the Lorentz-factor. The two most representative methods out of the several methods to carry out this separation [87] are presented in this analysis: the cluster counting method and the likelihood method.

6.3.1 Cluster Counting

The cluster counting method is based on the number of clusters with deposited energy above a threshold ($E_{dep} > 6.5\,\text{keV}$) that exists in an event (Fig. 6.13) . The events with a number of clusters greater or equal than a certain cut value are selected ($N_{cl} \geq 6$). The efficiency of this method is 97.45 % for 250 GeV electrons at 5° and 8.17 % for 400 GeV protons at 5°. The complete set of efficiencies, including the efficiencies from the adjusted MC to test-beam data, is summarized in table 6.5. The difference in the number of used clusters per event observed in section 6.2.1 between MC and data is a source for the discrepancies on the efficiency values for electrons and protons between the adjusted MC and data. There exits a dependence of the cluster counting efficiency with the beam angle (Fig. 6.14), and the differences between the efficiency values are not greater than 8 % for electrons, 20 % for pions, and 30 % for protons (table 6.6). Using all the available samples, the efficiency can be plotted as a function of γ (Fig. 6.13(c)).

TABLE 6.5: *Cluster counting efficiencies and beam angles for test-beam data and adjusted MC.*

Particle	Energy (GeV)	Block	0° Eff. (%)	5° Eff. (%)	10° Eff. (%)	15° Eff. (%)
			TB Data			
Electron	180	Ecal1	90.00 ± 0.18	97.74 ± 0.07	92.65 ± 0.14	97.72 ± 0.07
	250	Ecal1	93.17 ± 0.28	97.45 ± 0.10	94.32 ± 0.09	97.66 ± 0.09
	250	Ecal2	93.21 ± 0.07			
	300	Ecal1	93.44 ± 0.53	95.74 ± 0.24	91.93 ± 0.46	95.99 ± 0.46
Pion	180	Ecal1	51.13 ± 0.14	49.21 ± 0.15	48.44 ± 0.16	59.80 ± 0.18
	250	Ecal1	71.13 ± 0.22	73.78 ± 0.21	72.69 ± 0.13	79.63 ± 0.19
	250	Ecal2	72.24 ± 0.07			
	300	Ecal1	76.06 ± 0.15	79.44 ± 0.12	75.29 ± 0.19	83.96 ± 0.16
Proton	400	Ecal1	11.60 ± 0.09	8.17 ± 0.07	9.50 ± 0.08	9.33 ± 0.09
			MC			
Electron	180	Ecal1	93.83 ± 0.69	95.40 ± 0.28	91.70 ± 0.42	93.67 ± 0.33
	250	Ecal1	95.79 ± 0.58	95.46 ± 0.29	94.43 ± 0.19	93.53 ± 0.35
	250	Ecal2	95.82 ± 0.16			
	300	Ecal1	93.09 ± 0.75	94.95 ± 0.31	90.50 ± 0.46	94.87 ± 0.31
Pion	180	Ecal1	58.26 ± 0.77	57.90 ± 0.31	48.92 ± 0.33	53.89 ± 0.32
	250	Ecal2	79.82 ± 0.24			
	300	Ecal1	81.45 ± 0.60	83.89 ± 0.23	75.86 ± 0.28	79.41 ± 0.26
Proton	400	Ecal1	10.39 ± 0.27	8.26 ± 0.08	8.10 ± 0.08	8.76 ± 0.09

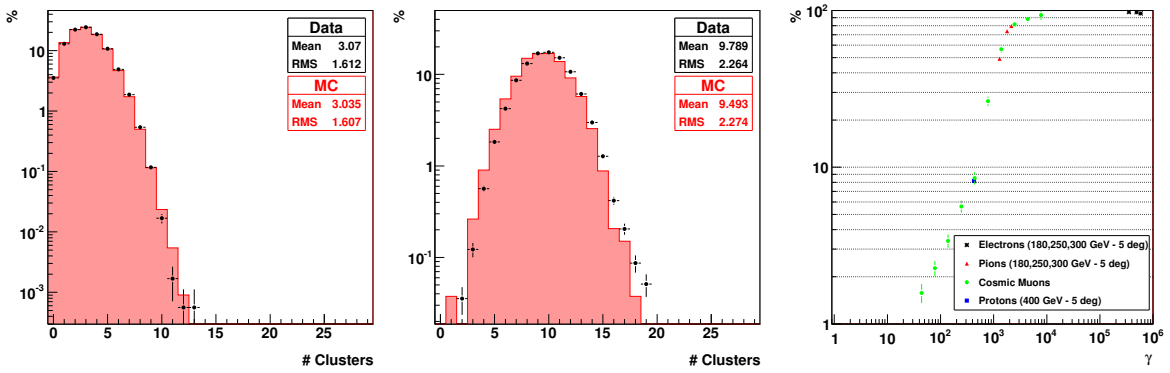

(a) 400 GeV p @ 5° (b) 250 GeV e^- @ 5° (c)

Fig. 6.13: *Distribution of the number of clusters with $E_{dep} > 6.5keV$ for 400 GeV protons at 5° (Fig. 6.13(a)) and 250 GeV electrons at 5° (Fig. 6.13(b)). Efficiency of the cluster counting method with $N_{cl} \geq 6$ plotted as a function of the Lorentz-factor γ (Fig. 6.13(c)).*

TABLE 6.6: *Cluster counting efficiencies and beam angle differences for test-beam data.*

Particle	Energy (GeV)	Highest Efficiency (%)	Lowest Efficiency (%)	$\lvert Low/High - 1\rvert$ (%)
Electron	180	97.74 @ 5°	90.00 @ 0°	7.92
	250	97.66 @ 15°	93.17 @ 0°	4.60
	300	95.99 @ 15°	91.93 @ 10°	4.23
Pion	180	59.80 @ 15°	48.44 @ 10°	20.00
	250	79.63 @ 15°	71.13 @ 0°	10.67
	300	83.96 @ 15°	75.29 @ 10°	10.33
Proton	400	11.60 @ 0°	8.17 @ 5°	29.6

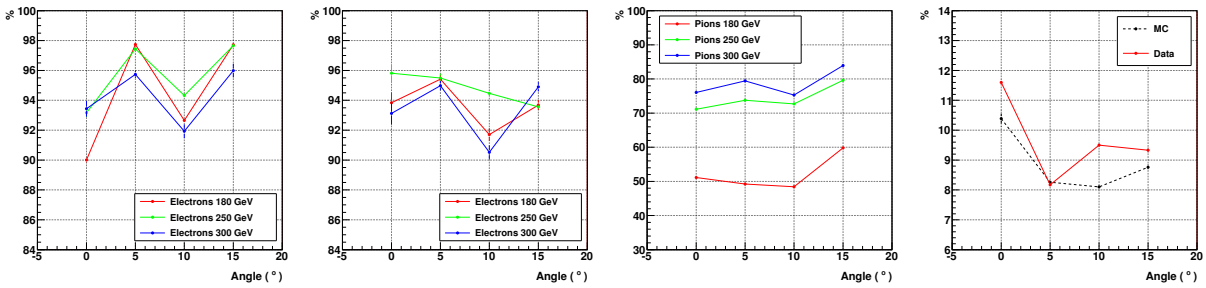

(a) test-beam e^- (b) MC e^- (c) π (d) p

Fig. 6.14: *Distribution of the cluster counting efficiency dependence with the beam angle for electrons (Fig. 6.14(a) and Fig. 6.14(b)), pions (Fig. 6.14(c)), and 400 GeV protons (Fig. 6.14(d)).*

6.3.2 Likelihood

The likelihood method is based on the likelihood ratio test, that can be used when there exist events that can occur with two different distributions and the hypothesis of events occurring with one of them must be ruled out. The likelihood ratio can be defined as [87]:

$$L = \frac{W_e}{W_e + W_p} \qquad ; \qquad W_{e,p} = \sqrt[n]{\prod_{i=1}^{n} P^i_{e,p}(E_i)} \tag{6.3}$$

where n is the number of clusters of each event, $P^i_{e,p}(E_i)$ are the probability density functions ($p.d.f.$) for electrons (e) and protons (p) and E_i the clusters energy.

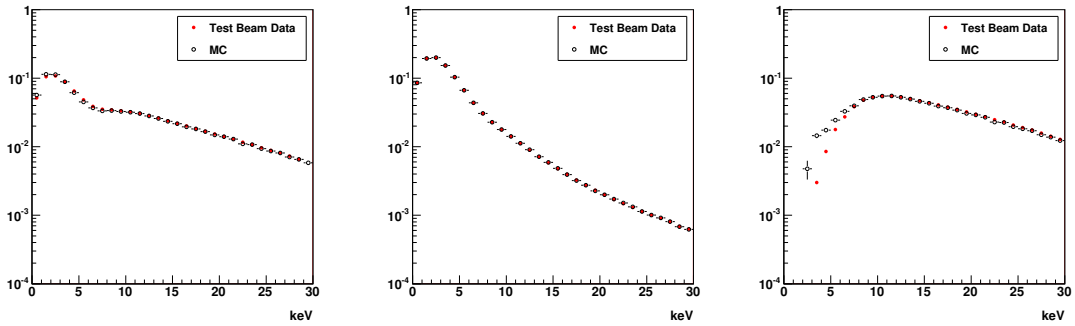

(a) Electron-like p.d.f. (b) Proton-like p.d.f. (c) Transition p.d.f.

Fig. 6.15: *Electron-like event p.d.f. from test-beam data and adjusted MC (Fig. 6.15(a)). Proton-like event p.d.f. and also ionization p.d.f. from test-beam data and adjusted MC (Fig. 6.15(b)). Transition p.d.f. from test-beam data and adjusted MC (Fig. 6.15(c)). Test-beam data is solid red circle markers and MC is empty black circle markers.*

In this analysis two different approaches using the likelihood method are presented:

1. Take into account only used clusters, with the natural logarithm of the likelihood definition (6.3) and the electron-like and proton-like $p.d.f.$ from test-beam.

2. Take into account only used clusters, with the natural logarithm of the likelihood definition (6.3) and the ionization and transition $p.d.f.$ from test-beam. For each cluster energy, the $p.d.f.$ with greater value is used to calculate W_e.

The resulting likelihood distributions are used to establish the efficiency of the method fixing a threshold likelihood. Integrating this distributions along the likelihood value determines the variation of the efficiency with the likelihood threshold (Fig. 6.16).

The table 6.7 summarizes the threshold values that have been obtained at 90 % electron efficiency and the efficiencies of the two likelihood methods at 0 degrees beam angle. From adjusted MC to test-beam data, the 400 GeV protons efficiency reproduces the data at 90 % electron efficiency (Fig. 6.17). Besides, there exits a dependence of the likelihood efficiencies with the beam angle and the differencies between the efficiency values are not greater than 9 % for electrons, 27 % for pions, and 29 % for protons (table 6.8).

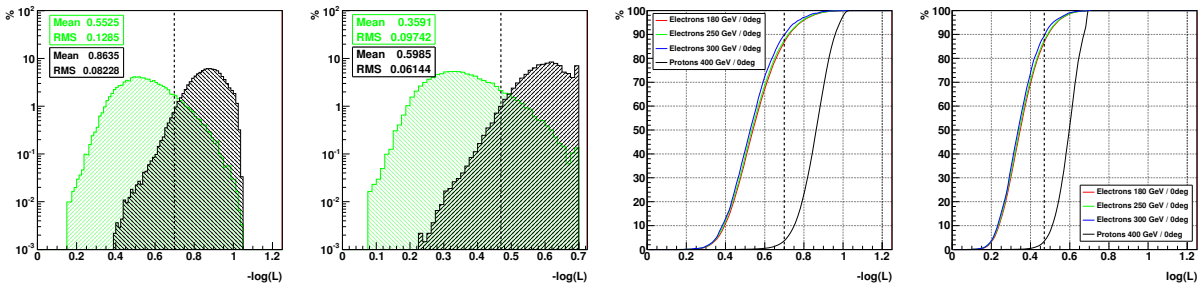

(a) Likelihood (1) (b) Likelihood (2) (c) Likelihood (1) (d) Likelihood (2)

Fig. 6.16: *Distributions of the natural logarithm of the likelihood for 250 GeV electrons (green) and 400 GeV protons (black). Both of them at 0° (Fig. 6.16(a) and 6.16(b)). Efficiency variation with the likelihood threshold for 180 GeV electrons (red), 250 GeV electrons (green), 300 GeV electrons (blue), and 400 GeV protons (black). The four of them at 0° (Fig. 6.16(c) and 6.16(d)). The vertical dash line represents the likelihood threshold value for* 90 % *electron efficiency.*

TABLE 6.7: *Likelihood threshold values and efficiencies with binomial errors at 0° for test-beam data and adjusted MC.*

Likelihood Method	Likelihood Threshold			e^- 180 GeV (%)	e^- 250 GeV (%)	e^- 300 GeV (%)	p 400 GeV (%)
TB Data							
Likelihood (1)	$-\log(L)$	$<$	0.70	87.73 ± 0.18	90.04 ± 0.33	89.23 ± 0.66	3.22 ± 0.05
Likelihood (2)	$-\log(L)$	$<$	0.47	86.58 ± 0.19	89.55 ± 0.34	88.59 ± 0.68	2.90 ± 0.05
MC							
Likelihood (1)	$-\log(L)$	$<$	0.70	91.78 ± 0.69	91.18 ± 0.48	88.65 ± 0.82	3.19 ± 0.14
Likelihood (2)	$-\log(L)$	$<$	0.47	91.45 ± 0.70	90.61 ± 0.49	88.45 ± 0.82	3.25 ± 0.14

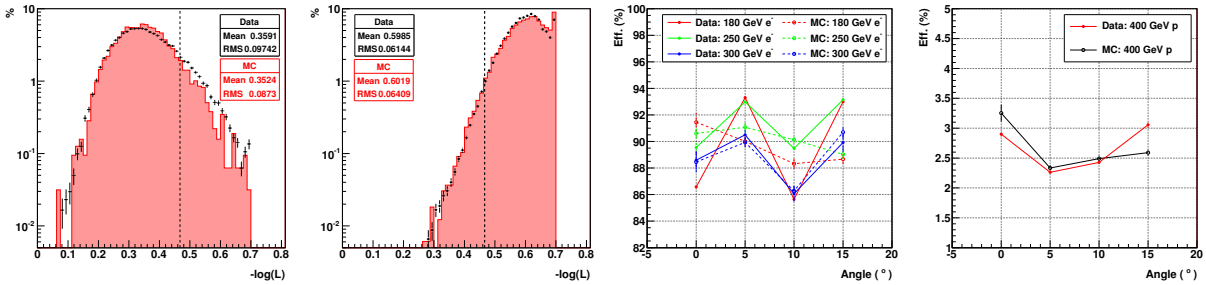

(a) 250 GeV e^- @ 0° (b) 400 GeV p @ 0° (c) Likelihood (2) (d) Likelihood (2)

Fig. 6.17: *Distribution of the natural logarithm of the likelihood method (2) for 250 GeV electrons at 0° (Fig. 6.17(a)) and 400 GeV protons at 0° (Fig. 6.17(b)), the black markers represent the test-beam data and the red line the adjusted MC. Likelihood method (2) efficiency dependence with the beam angle for electrons (Fig.6.17(c)) and 400 GeV protons (Fig. 6.17(d)). Solid markers and solid line represent the test-beam data and the empty markers and dash line the adjusted MC.*

TABLE 6.8: *Likelihood efficiencies and beam angles.*

Particle	Energy (GeV)	Likelihood Method	Highest Efficiency (%)	Lowest Efficiency (%)	$\lvert Low/High - 1\rvert$ (%)
Electron	180	(1)	93.86 @ 5°	87.72 @ 10°	6.44
		(2)	93.31 @ 5°	85.65 @ 10°	8.21
	250	(1)	93.63 @ 15°	89.91 @ 10°	3.97
		(2)	93.15 @ 15°	89.48 @ 10°	3.94
	300	(1)	91.06 @ 5°	87.27 @ 10°	4.16
		(2)	90.50 @ 5°	86.07 @ 10°	4.90
Pion	180	(1)	44.64 @ 15°	32.71 @ 0°	26.7
		(2)	43.48 @ 15°	31.95 @ 0°	26.5
	250	(1)	67.38 @ 15°	54.01 @ 0°	19.8
		(2)	66.28 @ 15°	53.30 @ 0°	19.6
	300	(1)	73.56 @ 15°	63.84 @ 10°	13.2
		(2)	72.30 @ 15°	62.64 @ 10°	13.4
Proton	400	(1)	3.25 @ 15°	2.32 @ 5°	28.6
		(2)	3.06 @ 15°	2.26 @ 5°	26.1

Using the pion samples extracted from the electron beam and the cosmic muons taken during the test-beam, the efficiency can be plotted as a function of the Lorentz-factor γ (Fig. 6.18), taking into account the likelihood threshold values obtained at 90 % electron efficiency.

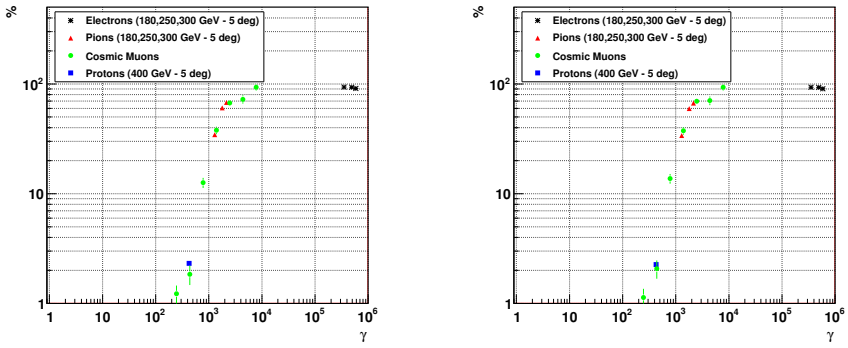

(a) Likelihood (1) (b) Likelihood (2)

Fig. 6.18: *Likelihood method efficiency plotted as a function of the Lorentz-factor γ, taking into account the likelihood threshold values obtained for 90 % of electron efficiency.*

6.3.3 TRD-ECAL correlations

The efficiencies for 400 GeV protons using only the TRD cuts presented in the section 6.3 are within the range $[2.6, 10]$ % (Fig. 6.19). If there exist no correlations between the TRD and

the ECAL, the product of the two individual efficiencies must be equal to the efficiency obtained applying the two sets of cuts. The results presented in the table 6.9 for test-beam data and adjusted MC do not show any hint of the existence of correlations, since the values are consistent within the error bars.

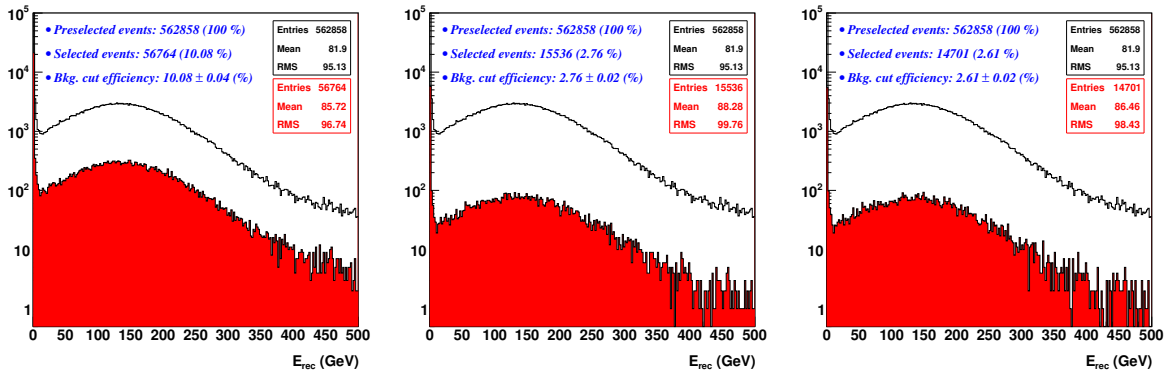

(a) 400 GeV p: Cl. Counting (b) 400 GeV p: Likelihood (1) (c) 400 GeV p: Likelihood (2)

Fig. 6.19: *Distribution of the ECAL reconstructed energy of the preselected sample (black) and of the events after TRD cuts (red), for differents TRD methods and 400 GeV protons.*

TABLE 6.9: *Proton selection cuts efficiencies with binomial errors for test-beam data and adjusted MC. The values are normalized to the sample of preselected events.*

		ϵ_{ecal} (%)	ϵ_{trd} (%)	$\epsilon_{ecal} \cdot \epsilon_{trd}$ (%)	$\epsilon_{ecal+trd}$ (%)
TB Data	Cluster Counting	0.067 ± 0.004	10.08 ± 0.04	0.0068 ± 0.0004	0.0055 ± 0.0010
	Likelihood (1)		2.76 ± 0.02	0.0019 ± 0.0001	0.0021 ± 0.0006
	Likelihood (2)		2.61 ± 0.02	0.0018 ± 0.0001	0.0018 ± 0.0006
MC	Cluster Counting	0.071 ± 0.005	7.82 ± 0.05	0.0056 ± 0.0003	0.0044 ± 0.0011
	Likelihood (1)		2.43 ± 0.03	0.0017 ± 0.0001	0.0017 ± 0.0007
	Likelihood (2)		2.48 ± 0.03	0.0018 ± 0.0001	0.0020 ± 0.0008

Besides, the TRD efficiency do not present any special feature when it is plotted for different energy bins, instead of integrated over the entire energy range, in test-beam data (Fig. 6.20(a)) and MC (Fig. 6.20(b)). Using the ECAL MIPs selection (see section 5.2.1, pag. 48), the total events can be split in two samples: MIPs and no MIPs. The distribution of the number of anticounters fired per event for protons that develop an hadronic shower in the ECAL (tagged as no MIPs) shows an increase in the number of anticounters due to the existence of backsplash at the ECAL entry (Fig. 6.21(a)).

This two samples, after TRD cuts, contain the same amount of transition radiation that can be seen, e.g., in the number of clusters with $E_{dep} > 6.5\,\text{keV}$, integrated over the beam angle (Fig. 6.21(b)) or for individual beam angles (Fig. 6.21(c)). The efficiency of both samples are compatible within the error bars (Fig. 6.20(c) and 6.20(d)).

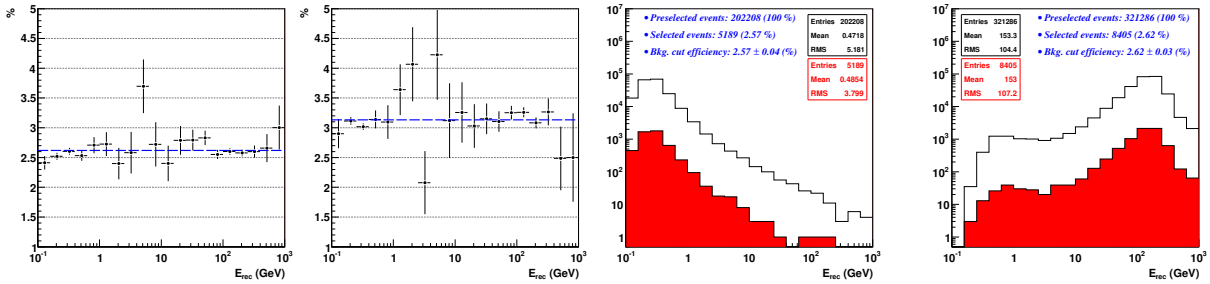

(a) TB 400 GeV protons: Likelihood (2)

(b) MC 400 GeV protons: Likelihood (2)

(c) Ecal MIPs selection

(d) [!(Ecal MIPs) selection

Fig. 6.20: *Likelihood (2) efficiency for different ECAL reconstructed energy bins (Fig. 6.20(a) and 6.20(b)) for 400 GeV protons, where the dash blue line represents the total efficiency integrated over energy. Distribution of the ECAL reconstructed energy of the preselected sample (black) and of the events after the likelihood (2) cut (red), for the MIPs sample (Fig. 6.20(c)) and the no MIPs sample (Fig. 6.20(d)).*

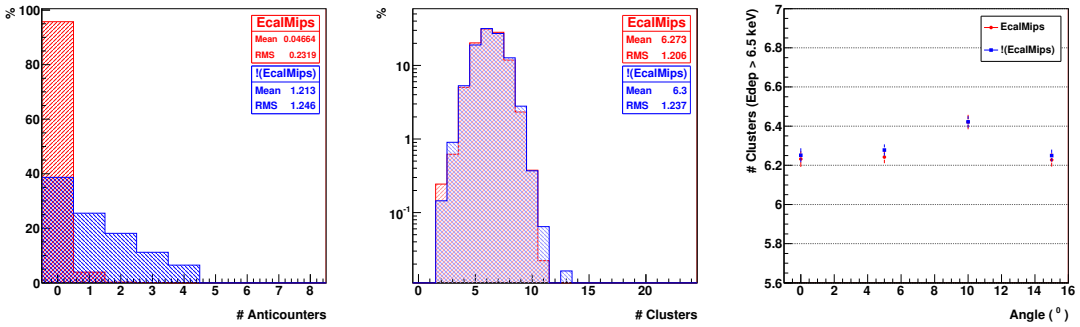

(a) 400 GeV p

(b) 400 GeV p

(c) 400 GeV p

Fig. 6.21: *Number of anticounters fired per event after the likelihood (2) cut (Fig. 6.21(a)). Number of clusters with $E_{dep} > 6.5\,keV$ per event after the likelihood (2) cut (Fig. 6.21(b)). Mean number of clusters with $E_{dep} > 6.5\,keV$ per event after the likelihood (2) cut for different beam angles (Fig. 6.21(c)).*

6.4 AMS-02 SCM Configuration Proton Rejection Factor

The rejection factor is defined as the ratio of the signal (electron) acceptance and the background (proton) acceptance

$$R(E) = \frac{A_{sig}(E)}{A_{bkg}(E)} \tag{6.4}$$

where the acceptance A can be written as the product of the trigger acceptance, the preselection cuts efficiency, and the selection cuts efficiency (section 5.3.1)

$$A = A_{trig} \cdot \epsilon_{pre} \cdot \epsilon_{sel} \tag{6.5}$$

This acceptance must be corrected for protons in real data-taking, since the reconstructed energy is lower than the real one, and the background contribution at certain energy E comes from a

cosmic proton spectrum region with lower flux. The section 8.2.2 (pag. 107) will get back to this subject.

6.4.1 Preselection Cuts Efficiency

For the test-beam 400 GeV protons, the set of preselection cuts (Fig.6.1) has an efficiency of 34 %, which comes from the ratio of the number of events after preselection cuts and the number of processed events (Fig. 6.22(b)). In the case of test-beam electrons, the preselection cuts efficiency is 42 % (250 GeV), and comes from the quotient of the number of events within a range of energy after selection cuts (section 5.3.1, pag. 52) without the energy/momentum matching and the number of events within the same range of energy after selection cuts (without the energy/momentum matching) and preselection cuts (Fig. 6.22(a)). The table 6.10 summarizes the efficiency of the preselection cuts sequence for test-beam data and MC.

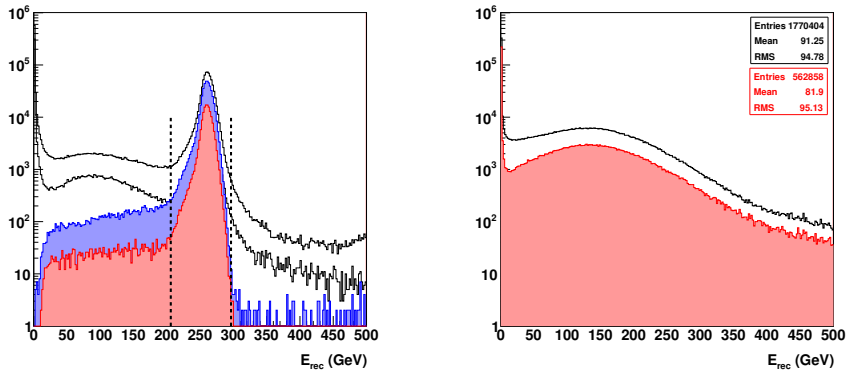

(a) 250 GeV e^- (b) 400 GeV p

Fig. 6.22: ***6.22(a):*** *Reconstructed energy distribution (250 GeV electron runs) for events with one shower reconstructed (bold black line), events after preselection cuts (thin black line), events after selection cuts (section 5.3.1) without the energy/momentum matching (blue), and events after selection cuts (without the energy/momentum matching) and preselection cuts (red).* ***6.22(b):*** *Reconstructed energy distribution (400 GeV proton runs) for events processed (bold black line) and events after preselection cuts (red).*

TABLE 6.10: *Preselection cuts efficiencies at different energies with binomial errors.*

	Electron 180 GeV (%)	Electron 250 GeV (%)	Electron 300 GeV (%)	Proton 400 GeV (%)
TB Data	42.33 ± 0.10	42.14 ± 0.15	35.21 ± 0.24	33.57 ± 0.04
MC	42.50 ± 0.25	40.48 ± 0.25	34.80 ± 0.28	38.68 ± 0.06

6.4.2 ECAL+TRD e/p Separation Cuts Efficiency

The efficiency of the set of ECAL electromagnetic cuts and the matching between energy and momentum (section 5.3.1, pag 52) plus TRD cuts is within the range $[0.002, 0.006]$ % for 400 GeV

protons, and within the range $[72, 76]\,\%$ for 250 GeV electrons (Fig. 6.23). In the case of test-beam electrons, the events within a certain range of energy, after subtraction of an exponential background in this region, are considered as signal. On the other hand, the MC efficiencies are within the range $[74, 75]\,\%$ for 250 GeV electrons and within the range $[0.002, 0.004]\,\%$ for 400 GeV protons (Fig. 6.23(f)). The table 6.11 summarizes the signal (electron) and background (proton) efficiencies for test-beam data and MC where the background efficiencies that have been obtained are consistent within the error bars for a similar signal efficiency.

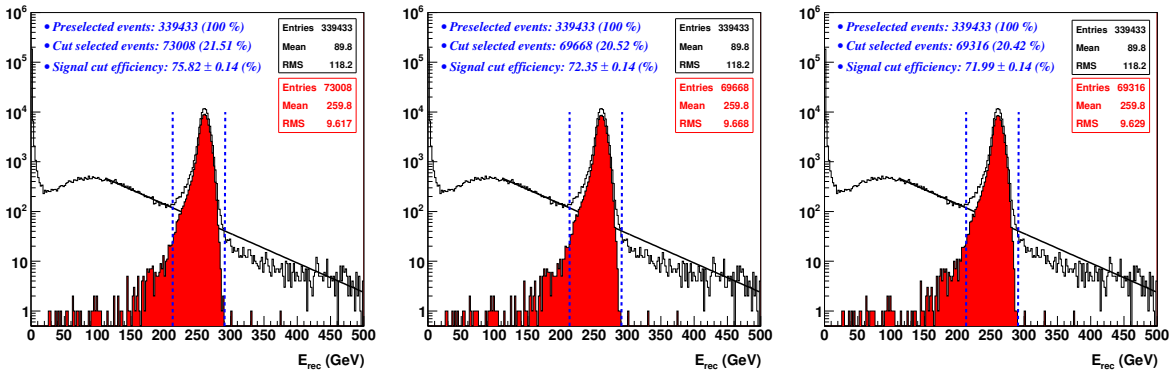

(a) TB 250 GeV e^-: Cluster Counting

(b) TB 250 GeV e^-:Likelihood (1)

(c) TB 250 GeV e^-:Likelihood (2)

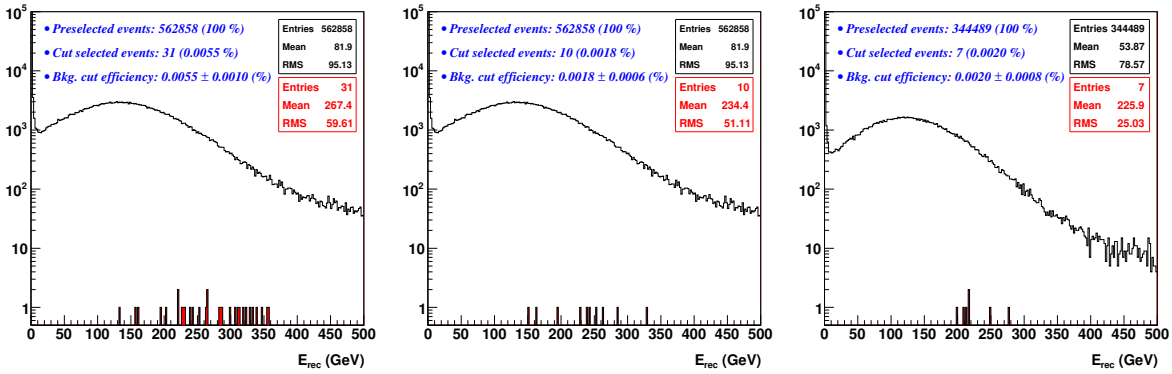

(d) TB 400 GeV p: Cluster Counting

(e) TB 400 GeV p:Likelihood (2)

(f) MC 400 GeV p:Likelihood (2)

Fig. 6.23: *Distribution of the ECAL reconstructed energy of the preselected sample (black) and of the events after ECAL+EPMatch+TRD cuts (red), for differents TRD methods. The black solid line represents the exponential bakground subtracted from the signal within the range of the two vertical blue dash lines.*

TABLE 6.11: *Electron and proton selection cuts efficiencies at different energies with binomial erros. The values are normalized to the sample of preselected events.*

			e^- 180 GeV (%)	e^- 250 GeV (%)	e^- 300 GeV (%)	p 400 GeV (%)
ECAL+EPMatch	TB Data		85.50 ± 0.09	78.92 ± 0.13	77.69 ± 0.31	0.067 ± 0.004
	MC		85.85 ± 0.27	80.53 ± 0.23	79.73 ± 0.32	0.071 ± 0.005
ECAL+EPMatch+TRD	TB Data	Cluster Counting	81.43 ± 0.10	75.82 ± 0.14	73.99 ± 0.33	0.0055 ± 0.0010
		Likelihood (1)	77.29 ± 0.10	72.34 ± 0.15	70.58 ± 0.34	0.0021 ± 0.0006
		Likelihood (2)	76.76 ± 0.10	71.99 ± 0.15	69.99 ± 0.35	0.0018 ± 0.0006
	MC	Cluster Counting	79.28 ± 0.31	75.37 ± 0.25	72.24 ± 0.36	0.0044 ± 0.0011
		Likelihood (1)	77.37 ± 0.32	73.89 ± 0.26	69.67 ± 0.37	0.0017 ± 0.0007
		Likelihood (2)	77.14 ± 0.32	73.74 ± 0.26	69.39 ± 0.37	0.0020 ± 0.0008

Part IV

AMS-02 Permanent Magnet Configuration Capabilities

7

AMS-02 SCM and PM Configurations Comparison

The permanent magnet configuration is the AMS-02 flight configuration. The data collected in the February 2010 test-beam with the AMS-02 superconducting magnet configuration of the detector is compared with the August test-beam data, taken with the AMS-02 flight configuration. A good agreement between both configurations, together with the Monte Carlo comparison carried out in previous chapters, validates the cosmic ray positron analysis.

The AMS-02 detector was tested with a beam of protons, electrons and positrons during August 2010 at the CERN facilities with the flight configuration, ie., the permanent magnet (PM) configuration (section 3.2.2, pag. 34). The replacement of the superconducting magnet by the permanent magnet and the re-arrangement of the Tracker planes should not affect the intrinsic performance of the calorimeter and the transition radiation detector since the new layers on top of both subsystems do not represent a substantial increment in the amount of material that the particles go through along the detector. Therefore, a cross-check of the February test-beam data with the August test-beam data must validate the results obtained in the chapters 5 and 6.

7.1 Electromagnetic Calorimeter

The August test-beam positions do not include the block Ecal2 from February test-beam (see section 5.1.1, pag. 43). Therefore, not all the cells along the 18 layers have recorded signals for an impinging electron beam at the ECAL entry, since the block Ecal2 offers two samples of the same cell at different fiber positions, which makes possible the attenuation study carried out in the section 5.3.3 (pag. 57) with the February data.

To compare the ECAL performance between the February and August test-beam, 180 GeV electrons and 400 GeV protons data samples have been used (table 5.2 (pag. 44)).

7.1.1 ECAL Calibration Verification

The distribution of the cells occupancy of the Fig. 7.1(a) shows that the 100 % of the cells were active during the August test-beam. The fraction of used hits is 82 % in the last layers using 180 GeV electrons, which is in good agreement with February test-beam data (Fig. 7.1(b)). On the other hand, the number of total and used hits per layer and event is practically the same in February and August data (Fig. 7.2(a) and 7.2(b)), with a difference lower than 1 % for most of the layers (Fig. 7.2(c)).

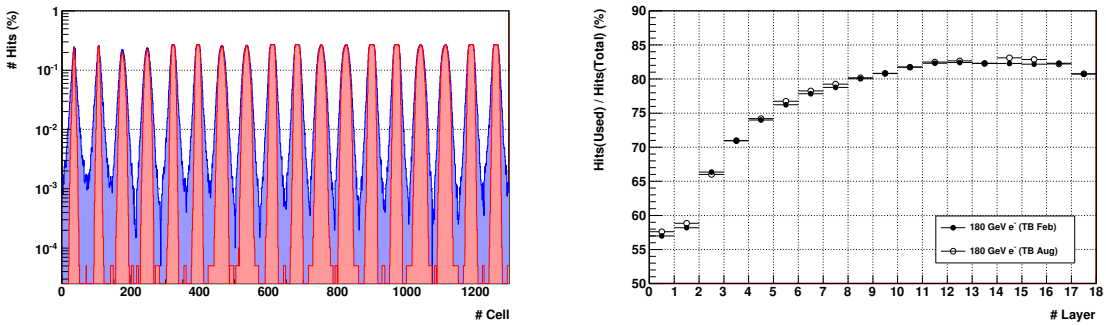

(a) 180 GeV e^- (b) 180 GeV e^-

Fig. 7.1: *Distribution of cells occupancy (Fig. 7.1(a)) in total hits (blue) and used hits (red) after preselection cuts and electron selection cuts, using 180 GeV electrons from August test-beam. Ratio of used hits and total hits for each layer (Fig. 7.1(b)) using 180 GeV electrons from February (solid markers) and August (empty markers). The cell number increases from top layer to the bottom layer.*

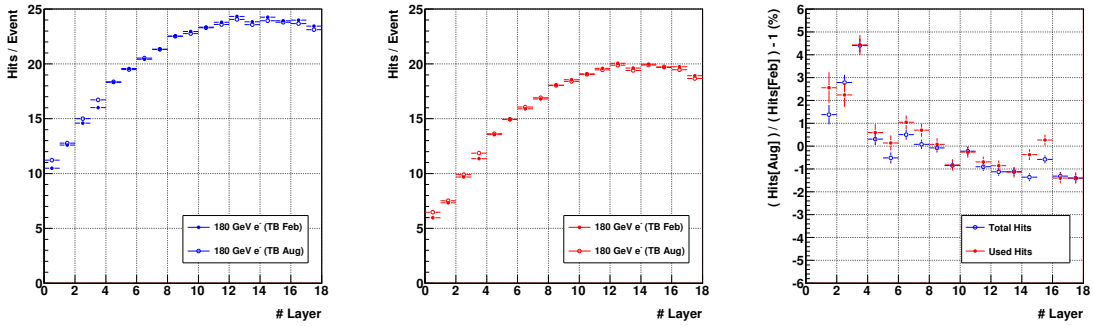

(a) Total hits (180 GeV e^-) (b) Used hits (180 GeV e^-) (c) 180 GeV e^-

Fig. 7.2: *Number of total hits per layer and event (Fig. 7.2(a)) for February (solid markers) and August (empty markers) 180 GeV electrons. Number of used hits per layer and event (Fig. 7.2(b)) for February (solid markers) and August (empty markers) 180 GeV electrons. Comparison of the number of hits, total (blue empty markers) and used (red solid makers), between February and August (Fig. 5.6(c)).*

7.1.1.a ECAL Calibration Cross-Check with MIPs

The ADC signal of the hits is converted to energy with a channel calibration factor that relates the ADC counts response of the PMT channels in high gain to MIPs, with deposited energy in MeV (Fig. 5.12(a), pag. 51). This straightforward conversion, ADC to MeV, remains valid until the high gain is saturated. Once saturated the high gain, the ADC counts in low gain are scaled with the ratio of high and low gain in the region where the high gain is not yet saturated.

The MIPs selection cut presented in section 5.2.1 (pag. 48) has been applied to August test-beam data in order to select MIP events. A truncated Landau fit to the distribution of the signal amplitude in ADC counts shows that the distribution of the MPVs for the 1296 channels peaks at 28 ADC counts (Fig. 7.3(a)) and it has a width of 16 %. The comparison of the channels' MVP[ADC] between the February and August test-beam shows a correlation (Fig. 7.3(b)), with

a MPV[ADC] values 2 % higher in August an spread of 10 % (Fig. 7.3(c)). On the other hand, from a fit to a Landau function channel by channel in the distribution of the hits energy, the distribution of the MPVs peaks at 12.9 MeV, 2 % lower than in February, and has a width of 2.7 %.

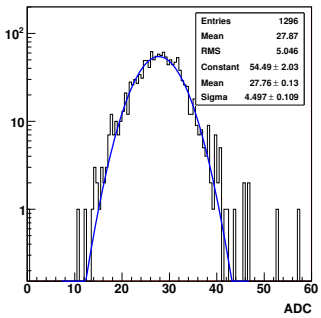

(a) ADC MPV (TB Aug)

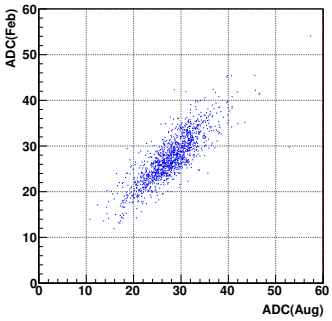

(b)

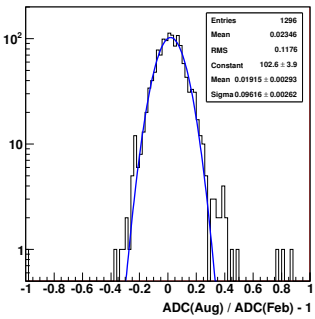

(c)

Fig. 7.3: *Distribution of the MPV values in ADC counts for all the channels (7.3(a)). Comparison of the channels' MPV obtained in February and August (Fig. 7.3(b) and 7.3(c)).*

7.1.2 ECAL Performance

If the energy is re-reconstructed from the hit ADC counts using the February calibration factors that converts the ADC counts collected into deposited energy (Fig. 5.12(a), pag. 51), a low to high gain ratio of 33.5 for all the channels, and taking into account the battery of corrections presented in the section 5.3 (pag. 51): the amplification factors of the attenuation correction (Fig. 5.23(b), pag. 59), the correction factors of the gain equalization (Fig. 5.28(b), pag. 62), and the impact point correction (see section 5.3.5, pag. 63), the energy resolution obtained for 180 GeV electrons at 0° in the February test-beam is 1.97 ± 0.03 % (Fig. 7.4(a)), in good agreement with the energy resolution obtained in the August test-beam, which is 1.91 ± 0.03 % (Fig. 7.4(b)).

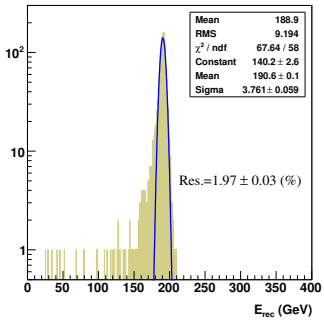

(a) TB February

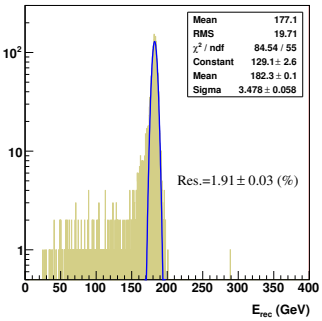

(b) TB August

Fig. 7.4: *Distribution of the reconstructed energy for 180 GeV electrons at 0° in February (Fig. 7.4(a) and in August (Fig. 7.4(b)) .*

7.1.2.a ECAL e/p Separation Cuts Efficiency

The ECAL selection cuts (see section 5.4.2, pag. 70) based on ECAL electromagnetic variables, ie., *ShowerMax*, *RearLeak*, *Energy/Hit* and *Moliere*, have a similar cumulative efficiency for 400 GeV protons in February (1.3 %) and August (1.4 %) test-beam data, while the efficiency for 180 GeV electrons is above 80 % (Fig. 7.5). The results are summarized in table 7.1

TABLE 7.1: *Electron and proton selection cuts efficiencies with binomial errors. The values are normalized to the sample of preselected events.*

Particle	TB	ShowerMax (%)	RearLeak (%)	Energy/Hit (%)	Moliere (%)
180 GeV e^-	Feb	96.27 ± 0.15	94.78 ± 0.17	93.61 ± 0.19	86.53 ± 0.27
	Aug	95.64 ± 0.41	94.26 ± 0.41	92.08 ± 0.40	80.01 ± 0.38
400 GeV p	Feb	47.89 ± 0.07	25.73 ± 0.06	3.96 ± 0.03	1.30 ± 0.02
	Aug	49.19 ± 0.06	20.40 ± 0.04	4.51 ± 0.02	1.41 ± 0.01

The momentum resolution degradation within the PM configuration (see section 3.2.2.b, pag. 35) affects the *EPMatch* cut. For a practically same efficiency of 13 % for 400 GeV protons when it is used as first cut, the 180 GeV electron efficiency goes from 94 % in February to 84 % in August (Fig. 7.6).

Instead of use a set of electromagnetic cuts, there is another approach to maximize the ECAL e/p rejection factor which involves multivariate analysis [101]. Using real-flight data, there exits an improvement of a factor of 3 in the proton efficiency at 100 GV and 90 % electron efficiency when the multivariate analysis is used instead of the electromagnetic cuts presented in this analysis.

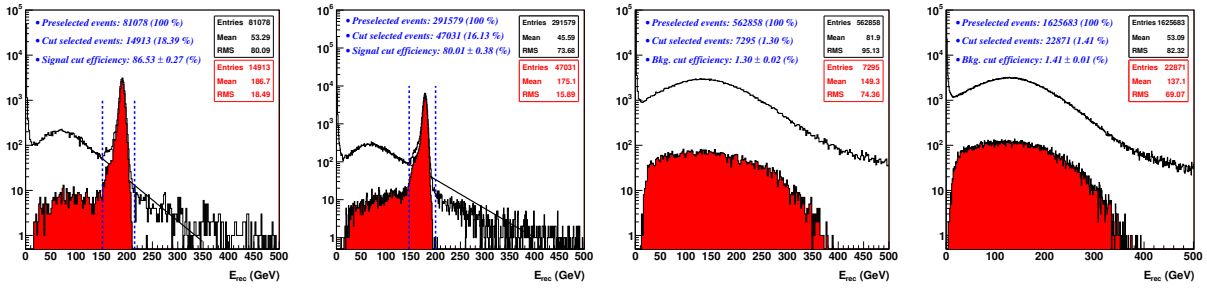

(a) 180 GeV e^- (TB Feb) (b) 180 GeV e^- (TB Aug) (c) 400 GeV p (TB Feb) (d) 400 GeV p (TB Aug)

Fig. 7.5: *Distribution of the reconstructed energy of the preselected sample (black) and the events after the sequence of cuts without EPMatch (red) for 180 GeV electrons at 0°, February test-beam (Fig. 7.5(a)) and August test-beam (Fig. 7.5(b)), and 400 GeV protons, February test-beam (Fig. 7.5(c) and August test-beam (Fig. 7.5(d)).*

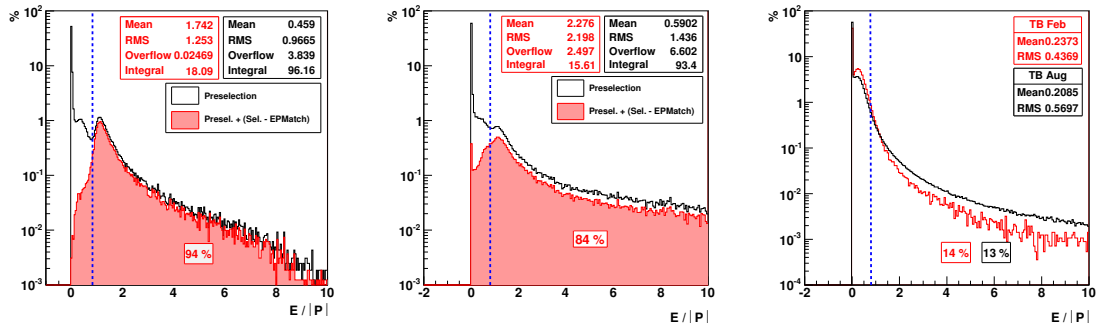

(a) 180 GeV e^- (TB Feb) (b) 180 GeV e^- (TB Aug) (c) 400 GeV p

Fig. 7.6: *Distribution of the quotient $E/|P|$ for 180 GeV electrons in February (7.6(a)), 180 GeV electrons in August (7.6(b)), and 400 GeV protons in February and August (Fig. 7.6(c)). The red distribution in the electron runs contains events after the ECAL selection cuts without the EPMatch cut. The number in each figure represents the efficiency of the EPMatch cut as first cut.*

7.2 Transtition Radiation Detector

To compare the TRD performance between the February and August test-beam, 180 GeV electrons and 400 GeV protons samples have been used from table 5.2 (pag. 44), together with 180 GeV electrons and 400 GeV protons from August test-beam.

7.2.1 TRD Calibration Verification

The distribution of the tubes occupancy of the Fig. 6.2 (pag.77) shows that the 100 % of the 5248 tubes were active during the February test-beam. The same tubes occupancy distribution shows that in the August test-beam there were 5247 (99.98 %) tubes active and one tube with no collected signal (Fig. 7.7).

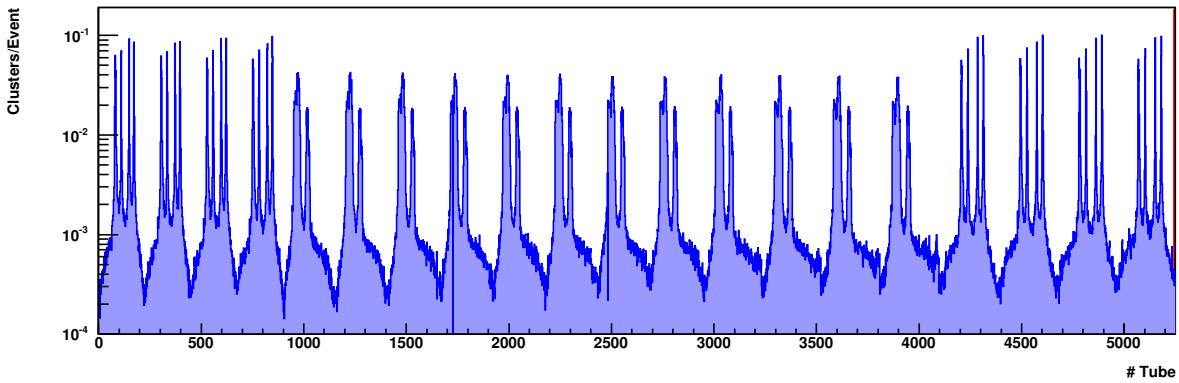

Fig. 7.7: *Tubes occupancy distribution in total clusters per event after preselection cuts and electron selection cuts (section 5.3.1) for 180 GeV electrons.*

7.2.1.a TRD Track Multiplicities

The deposited energy of the reconstructed clusters from the tubes readout signals is behind the TRD e/p separation. Therefore, the TRD cluster multiplicity distributions of Fig. 6.3 and Fig. 6.4 (pag. 77) must be compared between the February and the August test-beam data. The number of total clusters per track and event is 25 for 180 GeV electrons, while the number of used clusters is 19, which represents a ratio of 76 % (Fig. 7.8). On the other hand, the number of total clusters per track and event is 21 for 400 GeV protons with 19 used clusters, which represents a ratio of 89 % (Fig. 7.9).

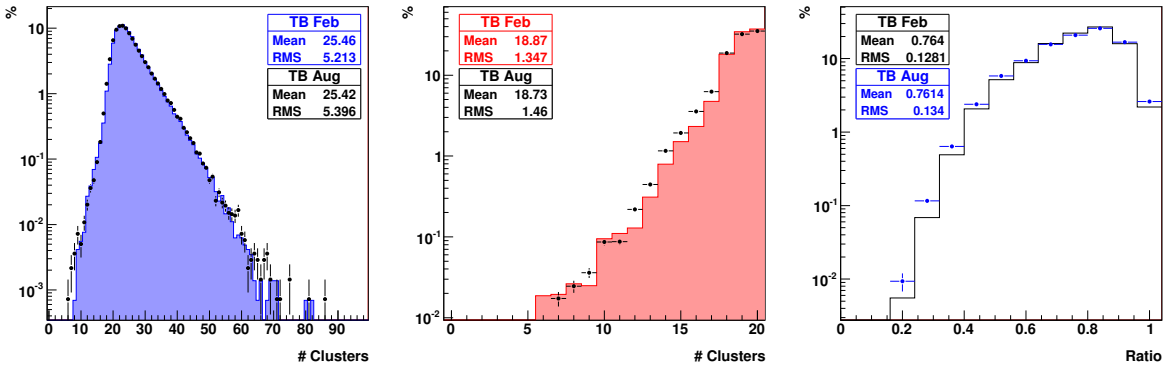

(a) 180 GeV e^- (b) 180 GeV e^- (c) 180 GeV e^-

Fig. 7.8: *Distribution of the track cluster multiplicity in total clusters (Fig. 7.8(a), August (black markers) and February (blue line)) and used clusters (Fig. 7.8(b), August (black markers) and February (red line)), after preselection cuts and electron selection cuts (section 5.3.1) for 180 GeV electrons. Ratio of used clusters and total clusters (Fig. 7.8(c), August (blue markers) and February (black line)).*

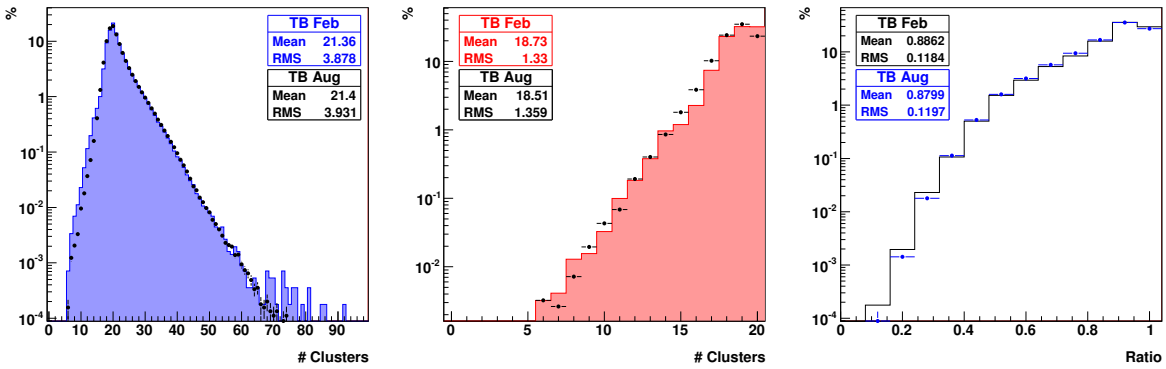

(a) 400 GeV p (b) 400 GeV p (c) 400 GeV p

Fig. 7.9: *Distribution of the track cluster multiplicity in total clusters (Fig. 7.9(a), August (black markers) and February (blue line)) and used clusters (Fig. 7.9(b), August (black markers) and February (red line)), after preselection cuts for 400 GeV protons. Ratio of used clusters and total clusters (Fig. 7.9(c), August (blue markers) and February (black line)).*

7.2.1.b Tubes Deposited Energy

The distribution of the energy deposited in the tubes for 180 GeV electrons is shown in Fig. 7.10(a)), where the spectra ratio holds below 5 %. However, in the case of protons (Fig. 7.10(b)), the spectra matching is not at the same level of the electron agreement, with a difference of 15 % at 15 keV in the spectra quotient due to a lower amount of deposited energy in the August sample. The fit to a convoluted Landau and Gaussian function in the range [0.5,6] keV of the deposited energy spectra, provides an ionization MPV of 1.8 keV for 180 GeV electrons. The MPV obtained for each layer remains stable within 3 % (Fig. 7.10(c)).

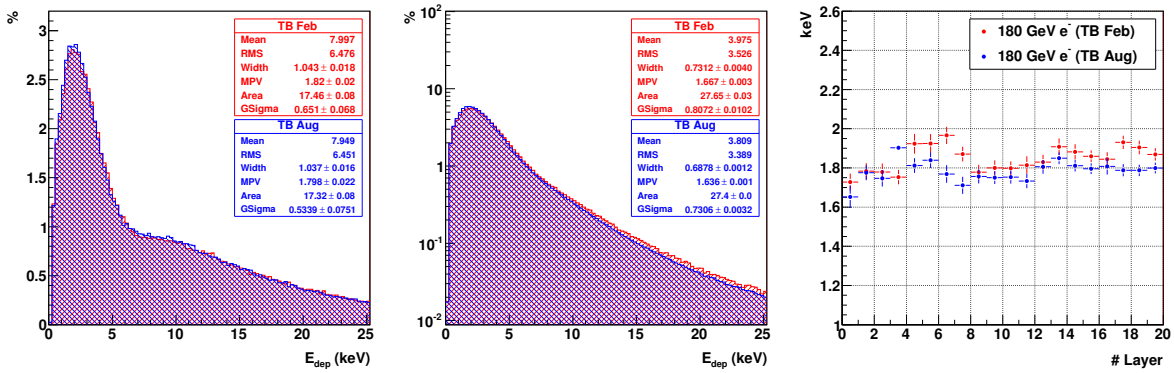

(a) 180 GeV e^- (b) 400 GeV p (c) 180 GeV e^-

Fig. 7.10: *Deposited energy spectrum of the tubes for 180 GeV electrons (Fig. 7.10(a)) and 400 GeV protons (Fig. 7.10(b)). Ionization MPV within each layer for 180 GeV electrons (Fig. 7.10(c)). August (blue) and February (red)).*

7.2.2 TRD Performance

In section 6.3 (pag. 83) two methods were introduced to perform the TRD e/p separation: the cluster counting method and the likelihood method. The cluster counting method is a straightforward method, since a cut in the number of clusters per event ($N_{cl} \geq 6$) with energy above a threshold, separates particles with different Lorentz-factor γ.

TABLE 7.2: *Modified cluster counting and likelihood efficiencies with binomial errors at 5°.*

Particle	TB	Modified Cluster Counting (%)	Likelihood (1) (%)	Likelihood (2) (%)
180 GeV e^-	Feb	91.10 ± 0.14	91.82 ± 0.13	91.06 ± 0.13
	Aug	91.47 ± 0.34	90.77 ± 0.37	89.89 ± 0.38
400 GeV p	Feb	7.12 ± 0.07	2.02 ± 0.03	1.97 ± 0.03
	Aug	7.18 ± 0.03	2.13 ± 0.02	1.95 ± 0.02

On the other hand, the likelihood method requires as input two probability density functions ($p.d.f.$) in order to test two hypothesis. The Fig. 7.11 shows the $p.d.f.$ obtained from the

February and August test-beam data. The transition distributions obtained with both data sets (Fig 7.11(c)) are quite similar, with a MPV of 11 keV for 180 GeV electrons.

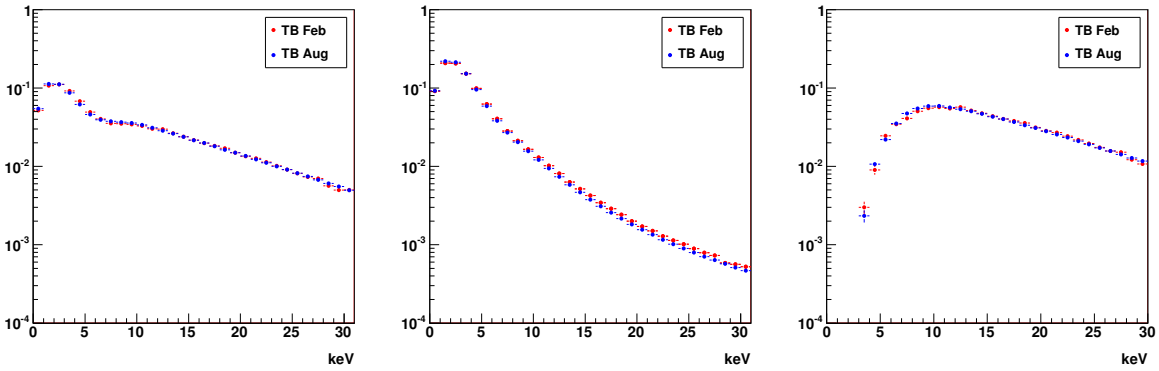

(a) Electron-like p.d.f. (b) Proton-like p.d.f. (c) Transition p.d.f.

Fig. 7.11: *Electron-like event p.d.f. (Fig. 7.11(a)), proton-like event p.d.f. and also ionization p.d.f. (Fig. 7.11(b)), and transition p.d.f. (Fig. 7.11(c)) from February test-beam data (solid red circle marker) and August test-beam data (solid blue circle marker).*

The number of clusters tagged as transition clusters when the second likelihood method is applied will be used to compare the February and August data samples instead of the number of clusters with deposited energy above 6.5 keV. This modified cluster counting is based on the comparison of the ionization and transition *p.d.f.* values at each cluster energy. The distribution of the number of transition clusters per event for 180 GeV electrons and 400 GeV protons at 5° has a similar mean and spread for the February and August data sets (Fig. 7.12). A cut in the number of transition clusters per event ($N_{cl} \geq 6$) gives an efficiency of 7 % for protons and 91 % for electrons (table 7.2).

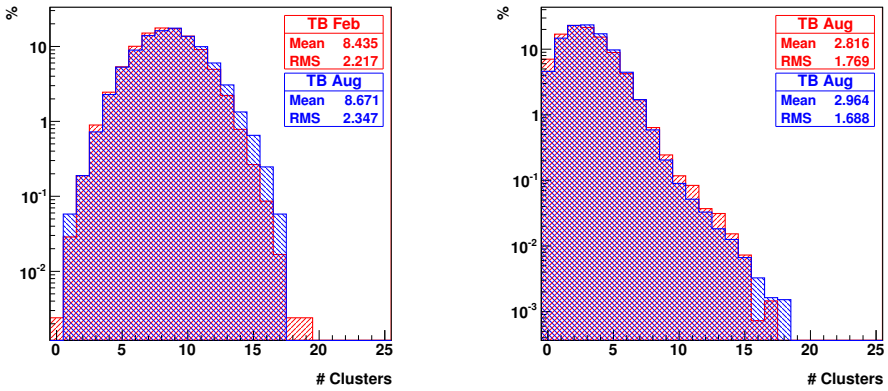

(a) 180 GeV e^- @ 5° (b) 400 GeV p @ 5°

Fig. 7.12: *Distribution of the number of transition clusters per event for 180 GeV electrons at 5° (Fig. 7.12(a)) and 400 GeV protons at 5° (Fig. 7.12(b)). August test-beam data is in blue and February test-beam data in red.*

The probability density functions from Fig 7.11 are used in the two likelihood methods introduced in the section 6.3.2 (pag. 85). The distributions of the natural logarithm of the likelihood are shown in Fig. 7.13, where the efficiency obtained for 400 GeV protons is 2 % while the electron efficiency is close to 90 % (table 7.2).

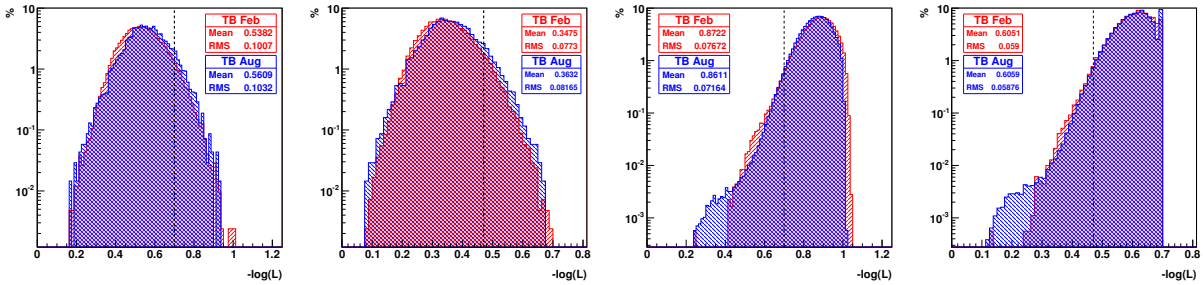

(a) e^-: Likelihood (1) (b) e^-: Likelihood (2) (c) p: Likelihood (1) (d) p: Likelihood (2)

Fig. 7.13: *Distributions of the natural logarithm of the likelihood for 180 GeV electrons at 5° (Fig. 7.13(a) and 7.13(b)) and 400 GeV protons at 5° (Fig. 7.13(c) and 7.13(d)). August test-beam data is in blue and February test-beam data in red. The vertical dash line represents the likelihood threshold value for ≈ 90 % electron efficiency, and has been tuned in February to get close the efficiencies.*

8

AMS-02 Capabilities for CR Positron Measurements

The results obtained in both test-beams demonstrate that the ECAL and TRD performances remain the same despite the latest detector upgrade. However, the proton suppression obtained from test-beam data is limited to one energy point. Therefore, a Monte Carlo simulation of the detector in its flight configuration is used to extend the rejection factor to other energies in order to exclude a proton contamination in the estimation of the positron signal detected by AMS-02.

Once AMS-02 underwent the test-beam with the flight configuration in August 2010, the AMS software has been updated to have an event reconstruction with calibrated subsystems and a realistic Monte Carlo simulation. This updated version has been used to simulate protons an electrons in order to estimate the rejection power at different energies and thereby determine an upper limit for the positron measurement.

8.1 Monte Carlo Data Sample

The generation range for protons and electrons was split into three sub-ranges, namely (0.5,10), (10,200), and (200,4000) GeV. The events in each range were generated isotropically following a logarithmic spectrum in momentum and the total statistics add up 2.6×10^{10} events in the case of protons and 3.9×10^{8} events in the case of electrons (table 8.1).

Table 8.1: *Proton and electron MC statistics.*

Particle	Energy Range (GeV)	# Generated Events
Proton	0.5–10	1.95×10^{10}
	10–200	5.92×10^{9}
	200–4000	2.92×10^{8}
Electron	0.5–10	9.99×10^{7}
	10–200	9.59×10^{7}
	200–4000	1.97×10^{8}

8.2 AMS-02 e/p Separation Performance

The detector upgrade, which basically consisted in the replacement of the superconducting magnet and the re-arrangement of the Tracker planes, does not interfere with the ECAL and TRD intrinsic capabilities to suppress the proton background since the e/p separation performance of both subsystems remains the same as the previous chapter demonstrates. However, when the energy and momentum matching is introduced, the AMS-02 efficiency for 400 GeV protons differs by a factor 3 between both configurations due to the degradation in the momentum resolution. To extend the AMS-02 e/p separation performance to other energies, the electromagnetic cuts were tuned independently to match the result obtained with data at 400 GeV. The agreement between data and MC can be seen in Fig. 8.1 when the complete set of cuts is applied.

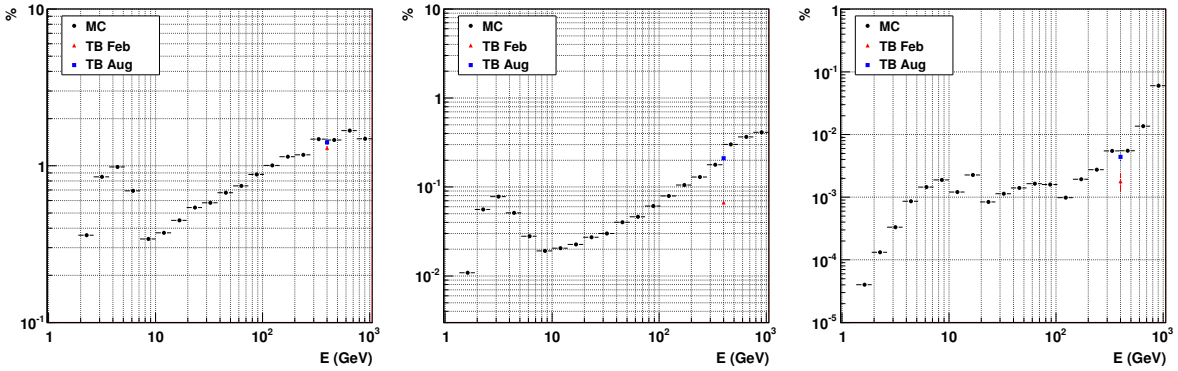

(a) *ECAL* (b) *ECAL + EPMatch* (c) *ECAL + EPMatch + TRD*

Fig. 8.1: *ECAL electromagnetic cuts (Fig. 8.1(a)), plus matching between energy and momentum (Fig. 8.1(b)), plus TRD likelihood cut (Fig. 8.1(c)) efficiency for protons from MC simulation compare with test-beam data results at 400 GeV.*

8.2.1 AMS-02 Acceptance

An acceptance in m^2 sr units must be calculated in order to obtain a detection rate, ie., number of events detected per second, from a particle flux. The acceptance is obtained from MC multiplying the detection efficiency N_{cut}/N_{gen} by the generated acceptance A_{gen}

$$A(E) = \frac{N_{cut}(E)}{N_{gen}(E)} \cdot A_{gen}(E) \tag{8.1}$$

where N_{cut} is the number of events after cuts at certain energy and N_{gen} is the number of generated events at certain energy. The generated acceptance is $A_{gen} = \pi L^2$, which results from generating particles on the top plane of a cube which is concentric and coaxial with AMS-02. The cube edge length L has a value of 3.9 m to match the 45° of field of view of AMS-02 around the zenith direction [94]. Fig. 8.2 shows the protons and electrons acceptance after preselection and selection cuts.

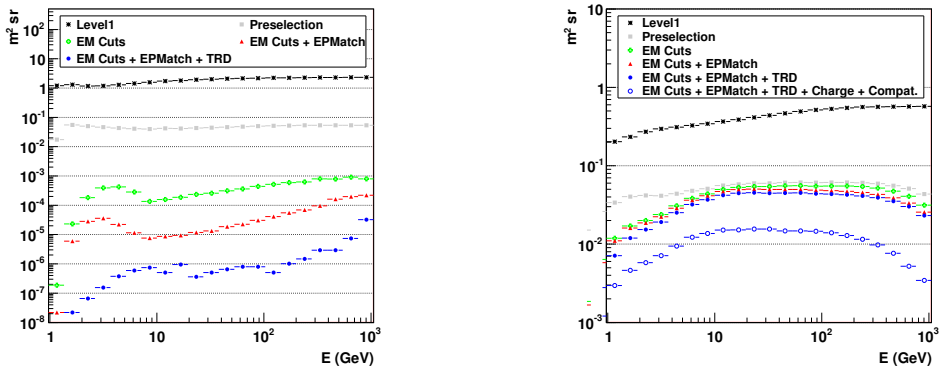

(a) protons (b) electrons

Fig. 8.2: *Acceptance for protons (Fig. 8.2(a)) and electrons (Fig. 8.2(b)), using electromagnetic cuts, the TRD likelihood cut and the matching between energy and momentum, where the cut Charge selects particles reconstructed with a negative sign of the charge, and the cut Compat establishes compatibility between the rigidity reconstructed with different combinations of Tracker planes.*

8.2.2 AMS-02 Proton Rejection Factor

The cosmic ray proton flux is 10^3–10^5 greater than the positron flux (section 1.5, pag. 10). Therefore, a rejection factor against protons of 10^4–10^6 is needed to properly identify positrons, plus an accurate measurement of the charge sign to reject electrons. The positron signal detection rate $\dot{n}_{sig}$, at certain energy, is calculated with the equation

$$\dot{n}_{sig}(E) = A_{sig}(E) \cdot \phi_{sig}(E) \cdot \Delta E \tag{8.2}$$

where A is the acceptance in $\mathrm{m}^2\,\mathrm{sr}$ units and ϕ is the particle flux in $(\mathrm{m}^2\,\mathrm{sr}\,\mathrm{GeVs})^{-1}$ units. In the case of protons (background), the reconstructed ECAL energy is lower than the actual value and the background contribution at certain energy E comes from a cosmic proton spectrum region with lower flux. Therefore, the number of background events per second is calculated with the equation

$$\dot{n}_{bkg} = \int_{E'} A_{bkg}(E') \cdot P_{bkg}\left(E' \rightarrow (E, E+\Delta E)\right) \cdot \phi_{bkg}(E')\, dE' \tag{8.3}$$

where $P_{bkg}(E' \rightarrow (E, E+\Delta E))$ is the probability that a proton with energy E' be reconstructed with energy within the range $(E, E+\Delta E)$. Besides, if a corrected acceptance $\tilde{A}_{bkg}$ is introduced, $\dot{n}_{bkg}$ can also be written as

$$\dot{n}_{bkg}(E) = \tilde{A}_{bkg}(E) \cdot \phi_{bkg}(E) \cdot \Delta E \tag{8.4}$$

where $\tilde{A}_{bkg}$ is

$$\tilde{A}_{bkg}(E) = \int_{E'} A_{bkg}(E') \cdot \frac{P_{bkg}\left(E' \rightarrow (E, E+\Delta E)\right)}{\Delta E} \cdot \frac{\phi_{bkg}(E')}{\phi_{bkg}(E)}\, dE' \tag{8.5}$$

Finally, the rejection factor is defined as the quotient of the signal acceptance and the background acceptance

$$R(E) = \frac{A_{sig}(E)}{A_{bkg}(E)} \tag{8.6}$$

which from Eq. (8.2) and (8.4) can be rewritten with the corrected acceptance $\tilde{A}_{bkg}$

$$\tilde{R}(E) = \frac{A_{sig}(E)}{\tilde{A}_{bkg}(E)} = \left(\frac{\dot{n}_{sig}(E)}{\dot{n}_{bkg}(E)}\right) \cdot \left(\frac{\phi_{bkg}(E)}{\phi_{sig}(E)}\right) \tag{8.7}$$

In order to estimate the number of cosmic ray positrons collected by AMS-02 and the proton background in a period of time from Eq. 8.2 and 8.3, a propagation model [26, 47] has been used to evaluate the positron and proton fluxes at low Earth orbit (Fig. 1.8(a), pag. 12). An effective transfer function has been introduced as well to account for the vertical rigidity cut-off (section 1.3.1) at the ISS orbit, which goes from 5 % at 1 GeV to 100 % at 20 GeV and beyond. Besides, in the case of protons, a migration matrix has been used to take into account the lower reconstructed energy in the calorimeter. This migration matrix, which represents the number of generated events within a set of energy ranges and the number of events reconstructed within the same energy ranges, is normalized to obtain the probability that a proton generated with energy E' be reconstructed with energy within the range $(E, E + \Delta E)$. The probabilities of all the possible reconstructed energies for a certain generated energy add up 1 (Fig. 8.3).

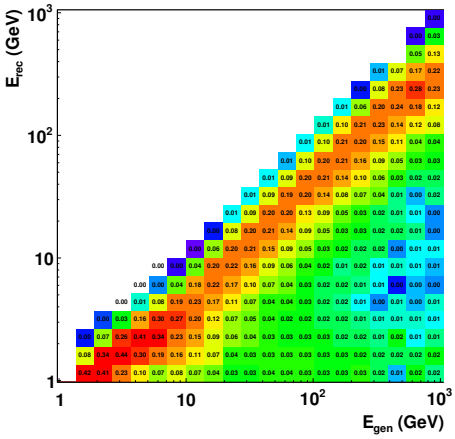

Fig. 8.3: *Protons probability matrix after electromagnetic cuts.*

The Fig. 8.4 shows the number of positrons [1] and background of protons that AMS-02 would collect in 5 years using the acceptance after selection cuts ($ECAL + EPMatch + TRD$) obtained in the previous section. The background of protons represents a fraction of the signal below 10 % up to 400 GeV and the rejection factor is above 10^5 up to 400 GeV when a reconstructed positive charge sign is demanded as well as rigidity compatibility between different Tracker planes combinations. In the case of electrons, the flux of electrons is 4–200 times greater than the flux of positrons in the energy range 1–1000 GeV. Therefore, the rejection factor due to charge confusion can be lower than the rejection factor against protons. The charge confusion holds below 0.1 % up to 400 GeV when a rigidity compatibility between different Tracker planes combinations is imposed.

[1] No primary source of positrons has been introduced in the propagation model.

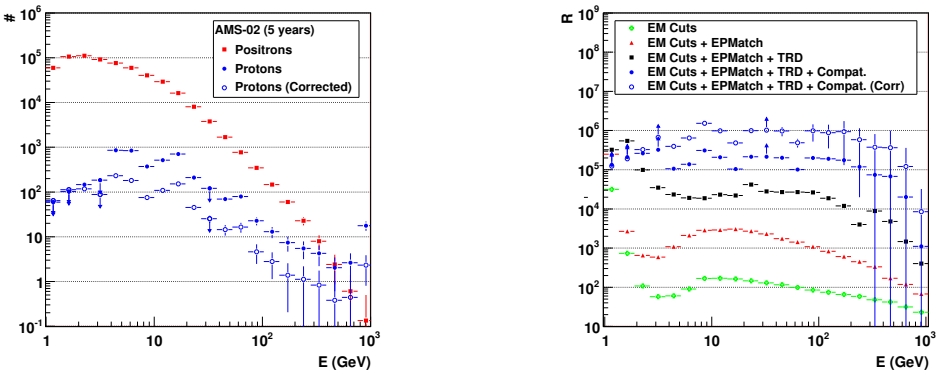

(a) (b)

Fig. 8.4: *Estimation of the number of positrons and protones detected by AMS-02 in 5 years (Fig. 8.4(a)), using the acceptances after the selection cuts (ECAL+EPMatch+TRD), plus the charge sign and the rigidity compatibility, the protons migration matrix, and a propagation model which does not include a primary source of positrons. Rejection factor against protons (Fig. 8.4(b)).*

8.3 AMS-02 Cosmic Ray Positrons Signal Estimation

The results from other experiments [39–42] indicate an excess of positrons with respect to a standard propagation model above 10 GeV (Fig. 1.7(a), pag.11). This increase requires a new source of primary positrons whose nature has been widely discussed, and goes from nearby *pulsars* [43] to dark matter annihilation in the galactic halo [44]. The positron fraction is defined as follows

$$\frac{e^+}{e^+ + e^-} = \frac{N_{e^+}}{N_{e^+} + N_{e^-}} \tag{8.8}$$

where $N_{e^+,^-}$ is the number of electrons and positrons calculated from the detection rate (Eq. 8.2) during a period of time. Both, electrons and positrons, share the same acceptance plotted in Fig. 8.2(b). If there is not contamination in the positron and the combined spectrum ($e^+ + e^-$) measurements, the resulting positron fraction is unbiased and does not diverge from the standard propagation model [2] at any energy (Fig. 8.5(a)). However, there exists a residual background of protons B_p and electrons B_{e^-} in the positron measurement and a background of protons in the combined spectrum. Therefore, in order to be reproduced with MC, the positrons fraction can be rewritten as

$$\frac{e^+}{e^+ + e^-} = \frac{N_{e^+} + B_p + B_{e^-}}{N_{e^+} + N_{e^-} + B_p + B_{e^-} + B_{e^+}} \tag{8.9}$$

where B_p is the number of protons calculated in the previous section after the sequence of cuts ($ECAL + EPMatch + TRD$) plus the charge and rigidity compatibility cuts.

The positron fraction is measured up to 400 GeV with a background of protons properly reduced, and a background of electrons/positrons $B_{e^-,^+}$, due to charge confusion, low enough to do not distort the positron measurement (Fig. 8.5). Besides, when a primary source of

[2] No primary source of positrons has been introduced in the propagation model.

positrons [102] is introduced in the propagation model to reproduce the results obtained by other experiments, the energy range can be extended beyond 500 GeV (Fig. 8.6).

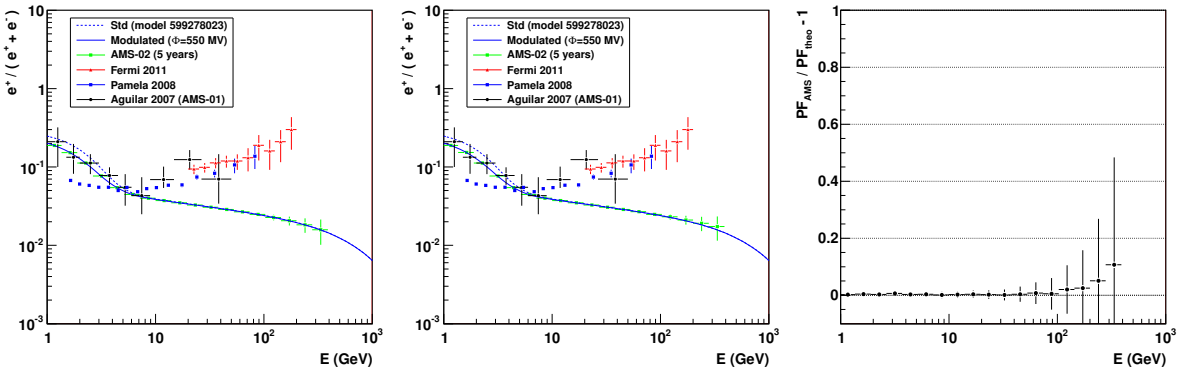

(a) (b) (c)

Fig. 8.5: *Estimation of the positron fraction (green markers) without proton (Fig. 8.5(a)) and with proton contamination (Fig. 8.5(b)) in the positron measurement. The blue line represents a standard propagation model which does not include a primary source of positrons. Ratio between the theoretical positron fraction and the AMS-02 estimation (Fig. 8.5(c)).*

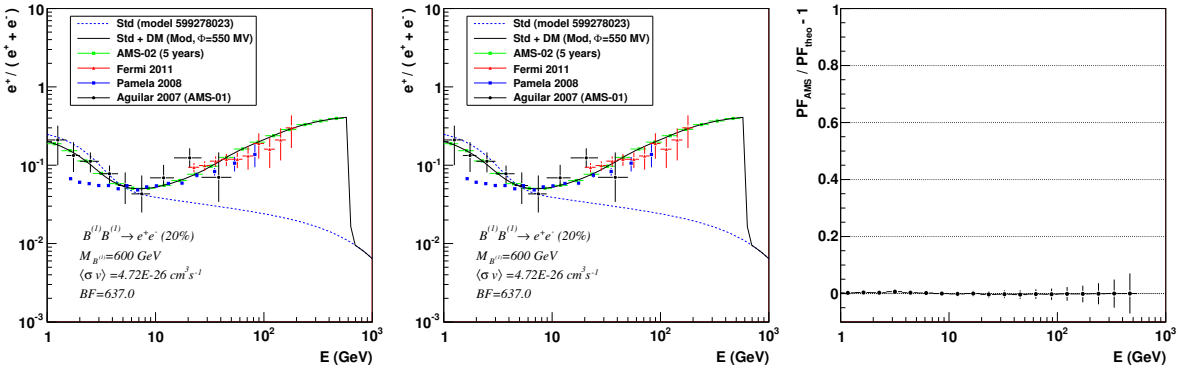

(a) (b) (c)

Fig. 8.6: *Estimation of the positron fraction (green markers) without proton (Fig. 8.6(a)) and with proton contamination (Fig. 8.6(b)) in the positron measurement. The dash blue line represents a standard propagation model which does not include a primary source of positrons and the black line represents a propagation model which includes a primary source of positrons [102] that reproduce the results obtained by other experiments. Ratio between the theoretical positron fraction and the AMS-02 estimation (Fig. 8.6(c)).*

Summary and Conclusions

Since AMS-02 underwent two test-beams at the CERN facilities in 2010, a lot of work has been put into the AMS software to have an event reconstruction with calibrated subsystems and a realistic Monte Carlo simulation. The bulk of the work presented in this document takes place at the first test-beam epoch and it constitutes the groundwork of the following software upgrades related mainly with the calorimeter.

The document is focused on the cosmic ray positron measurement, covering all the angles related with the topic but the physics behind the excess of positrons observed above 10 GeV, since the first step is to evaluate the capability of the detector to get an unbiased positron signal measurement due to proton contamination.

Once the theoretical introduction motivates the study of the positron signal and explains the physics behind the detector, the document deals with the performance of the electromagnetic calorimeter and the transition radiation detector, both key subsystems in the suppression of the background of protons, using data from test-beam at fixed energies. A set of electromagnetic cuts in the case of the calorimeter and a likelihood method in the case of the transition detector were used to obtain the electron/proton separation performance of both subsystems. The results demonstrate that the detector upgrade do not interfere in their performance. Besides, a calorimeter calibration method was developed. Finally, a MC simulation of the flight detector configuration, which benefits from the latest software updates, was used to extend the results of the proton suppression to other energies in order to determine and upper limit in the positron measurement without being compromise by any contamination. A detailed summary of the work concerning the calorimeter, the transition detector and the positron measurement comes next:

Electromagnetic calorimeter A calibration method was developed using the test-beam data taken with the AMS-02 superconducting configuration instead of the flight configuration since there were specific detector arrangements devoted to the ECAL study. Besides, the e/p separation performance of the calorimeter was not affected by the detector upgrade.

Calibration The calibration method is based on a previous absolute calibration obtained with minimum ionizing particles (MIP) and a subsequent calibration with electromagnetic showers. In order to verify the existing channels equalization, a MIPs sample was used to check the attenuation correction and the high gain signal, since the PMT response to MIPs, which must be corrected due to the light attenuation in the fibers, is used to equalize the channels in high gain.

To validate the attenuation correction on MIPs, the corrected ADC counts collected according to the impact point in the fiber by each channel was fitted to a straight line using

the ADC distribution mean at each point. The distribution of slopes was centered at 0 and with a width of 3.8 %, which confirms that the attenuation effects are consistently accounted on MIPs. However, the ADC distribution presents an inherent uncertainty due to the proximity of the electronic threshold to the maximum of the distribution. Therefore, the Landau truncated mean and the Landau most probable value (MPV) of the ADC distribution were used obtaining similar results.

To check the existing channels' equalization with MIPs, the ADC distribution of each PMT channel was fitted to a Landau function. The distribution of the channels' MPV peaked at 28 ADC counts with a width of 17 % due to an intrinsic spread inside the PMTs. However, the channels' ADC counts read-out signal is converted into a measurement of the deposited energy with a calibration factor. The distribution of the channels' MPV peaked at 13 MeV with a width of 3 %, which validates the existing calibration. The great advantage of using MIPs to calibrate is that the energy deposition is the same in all cells and layers along the particle path. However, this energy differs by three orders of magnitude with the energy deposited by a electron in the shower axis and central layers at test-beam energies. Therefore, a subsequent calibration with electromagnetic showers was used to equalize the energy deposition in the ECAL cells considering two constraints: the transverse profile of the energy forces to use only cells along the shower axis, and the longitudinal profile of the energy depositions requires a layer by layer equalization. This calibration comprised an attenuation check, a cells equalization, an impact point correction implementation and a rear leak check:

1. The use of electromagnetic showers to check the attenuation correction revealed the necessity to use an amplification factor for each layer to equalize the energy deposited in the cells along the fibers since there existed differences up to 40 % in the energy deposited between the fiber ends of the same cells. The values of these amplification factors indicate a same fiber behavior at the superlayer level due to different fiber batches.

2. Once the attenuation was corrected, the cells were equalized to the average energy deposited by the shower axis in each layer. The correction factors obtained at different angles up to 15 degrees remain stable within 4 % which confirms that the method is not limited to events with normal incidence.

3. Although the energy deposition was equalized to the same value in each layer, the energy deposited in each cell has a dependence with the impact point of the particle within the cell that was corrected with the $S1/S3$ ratio. This ratio has an energy dependence that was parametrized with a hyperbolic tangent function, where the left plateau and the right plateau correspond to the minimum and maximum energy deposition respectively. The correction function applied was defined with the mean of the $S1/S3$ distribution ($f(\langle S1/S3\rangle)=1$), since this value was stable at least for the energies used in the test-beam. Once the correction was applied, the variation of the shower energy with $S1/S3$ was reduced from 5 % to 1 %.

4. The electromagnetic showers at the test-beam energies are no completely contained in the calorimeter, and the leakage of energy must be estimated. The rear leak correction relies on the linear dependence of the missing energy due to the longitudinal leakage with the fraction of energy deposited in the last layer. Another method to estimate the missing energy is to fit the longitudinal energy profile, whose results are compatible with the last layer method (14 % of rear leak for 250 GeV electrons).

Once calibrated, the energy resolution for 180 GeV electrons is below 2 % in both configurations, the superconducting magnet and the flight configuration. However, the comparison of the test-beam data with simulated Monte Carlo of the superconducting magnet configuration showed differences in the longitudinal energy profile and the number of hits per layer, which are behind the discrepancies observed in the electromagnetic quantities used to discriminate electrons from protons. The differences in the energy profile affects the shower maximum and the rear leak. The discrepancy in the maximum of the shower is compatible to an earlier development of the electromagnetic shower in MC due to an extra amount of material equivalent to 0.25 radiation lengths. This shift in the shower maximum affects the rear leak estimation as well, since this estimation depends on the deposited energy in the last layer, i.e., the rear leak is underestimated. On the other hand, the energy contained in a cylinder 2 cm of radius around the shower axis came to an agreement when a threshold in the energy of the hit was set to 39 MeV, which supposes a reduction of 45 % in the number of the shower hits but only 1 % in the shower energy. Although these differences has no impact in the electron/proton separation, they must be taken into account in order to get a realistic MC.

Electron/proton separation One of the main goals of the calorimeter is to provide an e/p separation to reduce the cosmic proton background. The selection of electromagnetic events was made with a set of cuts based on electromagnetic quantities with an efficiency in 400 GeV protons close to 1.3 % and an efficiency in 180 GeV electrons above 80 % for both detector configurations. Therefore, the detector upgrade did not affect the intrinsic performance of the ECAL. Besides, the addition of the matching between the energy and the reconstructed momentum helped to increase the proton rejection, reducing the efficiency in 400 GeV protons to 0.067 %. However, due to the momentum resolution degradation from the magnet swap, the efficiency in protons differs by a factor 3 between both configurations at the same time that the efficiency in electrons is reduced to 65 % in the flight configuration at 180 GeV.

There is an open line of work in order to maximize the ECAL e/p rejection using alternative methods. For instance, the use of multivariate analysis instead of a set of electromagnetic cuts represents an improvement of a factor of 3 in the proton efficiency at 100 GV and 90 % electron efficiency using real-flight data.

Transition radiation detector The existing TRD calibration was validated in order to obtain the e/p separation performance with both configurations. The result was that the replacement of the superconducting magnet by the permanent magnet and the re-arrangement of the Tracker planes did not affect the TRD e/p separation.

Calibration The existing calibration was validated inspecting the tubes deposited energy, since the amount of deposited energy in the tubes provides the signature to perform the e/p separation. Besides, a TRD track is reconstructed with clusters that emerge from the interaction of the incident particle along the 20 layers. The number of used clusters for electrons and protons is 19 in both configurations, which was slightly above the simulated MC.

The energy distribution can be a pure ionization spectrum or the mixture of two contributions: ionization and transition radiation, where the amount of transition radiation detected increases with the Lorentz-factor γ of the primary particle. The ionization distribution was fitted to a convoluted Landau and Gaussian function in the range [0.5,6] keV. The individual tubes have a mean MPV of 1.8 keV for 250 GeV electrons and the MPV obtained for each layer remains stable within 3 % for both configurations, which validates the tubes equalization.

Besides, the ionization MPV has a dependence with the Lorentz-factor γ as expected from the Bethe-Block formula. On the other hand, the transition distribution was obtained subtracting an ionization pattern to the actual deposited energy, once the ionization distribution was scaled according with its MPV dependence with γ. The resulting transition distribution has a MPV of 11 keV on both configurations and the transition emission probability is 42 % at $\gamma \gg$.

Electron/proton separation The transition radiation detector provides an additional e/p separation that contributes to reduce the proton background. The TRD e/p separation performance was obtained with two different methods. On one hand, the cluster counting method, which is a straightforward method since a cut in the number of clusters per event with energy above a threshold separates particles with different Lorentz-factor γ. On the other hand, the likelihood method, which requires as input two probability density functions ($p.d.f.$) in order to test two hypothesis and it offers the best results. The efficiency obtained for 400 GeV protons was 2 % for both configurations at 90 % electron efficiency.

AMS-02 capabilities for cosmic ray positron measurements To properly identify positrons, a rejection factor of 10^4–10^6 is needed to suppress the vast background of protons plus an accurate measurement of the charge sign to reject electrons. A MC simulation of the flight detector configuration, which benefits from the latest software updates, was used to extend the results of the proton suppression to other energies in order to determine and upper limit in the positron measurement without being compromise by any contamination.

It has been established along the document, that the detector upgrade did not interfere with the ECAL and TRD intrinsic capabilities to suppress the proton background. However, the addition of the energy and momentum matching implies a factor 3 of difference in the efficiency for 400 GeV protons between both configurations due to the degradation in the momentum resolution. Although it can be overcome using alternative methods to improve the ECAL e/p separation performance instead of cuts in electromagnetic quantities.

The rejection factor against protons obtained with cuts in electromagnetic quantities in the calorimeter, the likelihood method in the TRD and the matching between the energy and the momentum is above 10^5 up to 400 GeV when a reconstructed positive charge sign is demanded as well as rigidity compatibility between different Tracker planes combinations, which represents a residual background of protons below 10 % up to 400 GeV. In the case of electrons, the charge confusion holds below 0.1 % up to 400 GeV when a rigidity compatibility between different Tracker planes combinations is imposed. With this level of contamination in the positron measurement, the positron fraction is measured up to 400 GeV with a background of protons properly reduced, and a background of electrons due to charge confusion, low enough to do not distort the positron measurement. Besides, when a primary source of positrons is introduced in the propagation model to reproduce the results obtained by other experiments, the energy range can be extended beyond 500 GeV.

Acknowledgments

An international collaboration like AMS implies dozens of people involved in the detector construction, logistics, and software development. Therefore, I want to express my gratitude to all the members of the collaboration, since without them this thesis could not be a reality.

La realización de esta tesis doctoral ha sido posible gracias a una beca de formación de personal investigador (FPI) concedida por el Centro de Investigaciones Científicas, Tecnológicas y Medioambientales (CIEMAT), por lo que primero de todo quiero agradecer al centro todos estos años de formación investigadora, haciendo extensible este agradecimiento tanto al director del Departamento de Investigación Básica, Manuel Aguilar, como al jefe de la División de Astrofísica de Partículas, Javir Berdugo.

Era el mes de septiembre de 2006 cuando recibí una llamada del CIEMAT en la que se me informaba que se me había concedido una beca predoctoral de cuatro años de duración. Por aquel tiempo me encontraba trabajando en el Departamento de Metrología del Instituto de Física Aplicada del CSIC, en el cual había sido muy bien acogido. Quiero dar las gracias a Joaquín Campos y Alicia Pons por darme la oportunidad de iniciarme en el mundo de la investigación. En mi primera visita al CIEMAT, Marcos Cerrada fue la primera persona con la que tuve contacto y a la que quiero agradecer su buen trato desde entonces. En aquella primera visita todavía no estaba claro a que experimento me iba a incorporar, por lo que tuve un ronda de contactos con Carlos Maña e Inés Gil para que me contasen un poco sus respectivos experimentos. Gracias Inés por abrirme las puertas de Double Chooz en un momento de incertidumbre en AMS tras la finalización del DEA. Al final, como es sabido, AMS fue el elegido.

El primer año estuvo dedicado a la obtención del DEA y desde el primer momento Jorge Casaus estuvo a mi lado para sacar el trabajo adelante. Gracias Jorge por tu dedicación, la verdad es que he aprendido mucho contigo. Durante todos estos años que he estado en el grupo de AMS, he tenido la suerte de trabajar con personas como Javier Berdugo, Carlos Maña, Carlos Delgado, Carlos Díaz, Francesca, Eduardo Cortina, Carmen Palomares, Jesús Marín y por supuesto mi director de tesis Jorge Casaus. Dejo para el final a mis compañeros doctorandos Cristina y Nacho, con los que he compartido tanto los buenos como los malos momentos. Todo ha sido más fácil con vosotros como compañeros de viaje. Gracias Cristina por estar ahí y no rendirte nunca. Gracias Nacho por el tiempo dedicado para que pudiera terminar la tesis. No me olvido tampoco de las nuevas incorporaciones al grupo Bruno e Isabel, mucha suerte.

Dejando el círculo de trabajo, primero de todo quiero dar las gracias a toda la gente del departamento por el buen trato que siempre he recibido. Además, he tenido la suerte de estar rodeado siempre de un gran ambiente con compañeros de despacho como Carlos Villanueva,

María Aldaya, José Caballero, Paco Clemente, María Cepeda, Carmen, Aurelio, Cristina y Nacho y con todos los demás, Francisco Valdivia (Mi Paco), Miguel, Tino, Javi, Julia, María, Nacho Sevilla, Juanjo, Carlos Díaz, Antonio, Jesús Puerta y toda la gente nueva que ha ido llegando. No me quiero olvidar tampoco de mis compañeros en el CSIC en mis primeros pasos en esta etapa del doctorado, José Francisco, Alejandro, Rodrigo y sobre todo Celia, que con el tiempo se convertiría en mi compañera vital, estando a mi lado durante todos estos años. Un abrazo a todos, os deseo lo mejor.

Nun quisiera finar estes llínies ensin facer alcordanza de la mio xente. Esta tesis dedíco-yla a tola mio familia, n' especial a mio madre, a la mio hermana, a Celia y a los mios güelos, faciendo una mención especial a güelito Víctor (DEP) y a mio tíu Graciano (DEP). Del mesmu mou, tampoco quiero escaeceme de los mios collacios. Un abrazu a toos.

Glossary

A

active galactic nuclei Galaxies with a central core that produces more radiation than the entire rest of the galaxy, p. 6.

axisymmetric spiral model In a galactocentric cylindrical coordinates (r, θ, z), the large-scale magnetic field radial ($B_r = 0$) and azimuthal (B_θ) components are both independent of θ and vary only with r ($B_r = B_r(r)$, $B_\theta = B_\theta(r)$) [6], p. 4.

B

bisymmetric spiral model In a galactocentric cylindrical coordinates (r, θ, z), the large-scale magnetic field radial ($B_r = 0$) and azimuthal (B_θ) components have a simple sinusoidal dependence on θ ($B_r = b_r \sin(\theta - \phi(r))$, $B_\theta = b_\theta \sin(\theta - \phi(r))$) [6], p. 4.

C

clarity Parameter related with the Rayleigh scattering length ($L = \lambda^4/C$). It gives an estimation of Rayleigh scattering in a material sample, p. 16.

coronal mass ejection Huge bubbles of gas threaded with magnetic field lines that are ejected from the Sun over the course of several hours, p. 5.

critical energy The energy at which the energy loss of electrons by bremsstrahlung is equal to the energy loss by ionization, p. 17.

F

Faraday rotation The plane of polarization of an electromagnetic wave is rotated under the influence of a magnetic field parallel to the direction of propagation [103], p. 4.

flares Short duration outburst from stars in various spectral ranges [15], p. 3.

G

gamma ray burst Short-lived bursts of gamma-ray photons associated to supernova explosions, p. 6.

GEANT A toolkit for the simulation of the passage of particles through matter. Its areas of application include high energy, nuclear and accelerator physics, as well as studies in medical and space science [92], p. 37.

I

interaction length Characteristic collision length for strongly interacting particles in matter [15], p. 9.

M

Moliere radius Transverse distance that a particle at the critical energy goes in traversing the last radiation length before it dies off [60], p. 19.

N

neutron star Star of extremely high density consisting predominantly of neutrons. Neutron stars are remmants of supernova explosions where the gravitational pressure in the remmant star is so large that the electrons and protons are merged to neutrons and neutrinos. Neutron stars have a diameter of typically 20 km [15], p. 118.

P

planetary nebula A shell of expanding ionized gas ejected from certain types of stars at the end of their lifes, p. 3.

plasma frequencies The maximum frequency of internal oscillation of a plasma. The plasma energy can be written as

$$\omega_p = \sqrt{4\pi N_e r_e^3}\frac{m_e c^2}{\alpha}$$

where N_e is electron density and r_e the classical electron radius, p. 16.

pulsars Rotating *neutron star* with characteristic pulsed emission in different spectral ranges (radio, optical, X-ray, gamma-ray) [15], p. 11.

R

radiation length Characteristic attenuation lenght for high-energy electrons anf gamma rays. It is both: (a) the mean distance over which a high-energy electron loses all but 1/e of its energy by bremsstrahlung, and (b) 7/9 of the mean free path for pair production by a high-energy photon. [55], p. 9.

Rayleigh scattering Elastic scattering of electromagnetic radiation by particles much smaller than the wavelength of the radiation. It has a wavelength dependence (λ^{-4}), i.e., shorter wavelengths are scattered stronger than longer wavelengths, p. 15.

ring model In a galactocentric cylindrical coordinates (r, θ, z), the large-scale magnetic field radial component vanishes ($B_r = 0$) and the azimuthal component (B_θ) is independent of θ but it can vary with r ($B_\theta = B_\theta(r)$) [6], p. 4.

ROOT An object-oriented framework with all the functionality needed to handle and analyse large amounts of data in a very efficient way [93], p. 37.

S

silica aerogel Aerogels consists of grains of amorphous SiO_2 forming a porous structure with bubbles of air. Silica aerogels can be produced with densities between $0.1\,g/cm^3$ and $0.6\,g/cm^3$ [54], p. 15.

solar corona Outer layer of the Sun's atmosphere., p. 9.

sunspots A disturbance of the solar surface which appears as a relatively dark center surrounded by less dark area. Sunspots appear dark because part of the thermal energy is transformed into magnetic field energy [15], p. 5.

supernova Star explosion initiated by a gravitational collapse, if a star has exhausted its hydrogen and helium supply and collapses under its own gravity [15], p. 5.

synchrotron Electromagnetic radiation emitted by an accelerated charged particle in a magnetic field [15], p. 4.

T

termination shock Heliosphere region where the solar wind slows abruptly and becomes denser and hotter, p. 5.

Z

Zeeman splitting Splitting of the spectral lines emitted by atoms into several components in the presence of a magnetic field, p. 4.

Bibliography

[1] Cronin, J. W.: *Cosmic Rays: the Most Energetic Particles in the Universe.* Reviews of Modern Physics Supplement, 71:165–+, March 1999.

[2] Schlickeiser, R.: *Cosmic Ray Astrophysics.* Springer, 2002. Second Corrected Printing 2003.

[3] Strong, A. W. and I. V. Moskalenko: *Propagation of Cosmic-Ray Nucleons in the Galaxy.* The Astrophysical Journal, 509:212–228, December 1998.

[4] Moskalenko, I. V., A. W. Strong, J. F. Ormes, and M. S. Potgieter: *Secondary Antiprotons and Propagation of Cosmic Rays in the Galaxy and Heliosphere.* The Astrophysical Journal, 565:280–296, January 2002.

[5] `http://galprop.stanford.edu`.

[6] Men, H., K. Ferrière, and J. L. Han: *Observational Constraints on Models for the Interstellar Magnetic Field in the Galactic Disk.* Astronomy and Astrophysics, 486:819–828, August 2008.

[7] Dorman, L. I., D. Venkatesan, and L. I. Dorman: *Solar Cosmic Rays.* Space Science Reviews, 64:183–+, January 1993.

[8] McDonald, F. B., B. J. Teegarden, J. H. Trainor, and W. R. Webber: *The Anomalous Abundance of Cosmic-Ray Nitrogen and Oxygen Nuclei at Low Energies.* The Astrophysical Journal, 187:L105–L108, February 1974.

[9] Cummings, A. C. and E. C. Stone: *Elemental Composition of the Anomalous Cosmic-Ray component.* In *Proceedings of the 20th International Cosmic Ray Conference Moscow*, volume 3, pages 413–+, 1987.

[10] Fisk, L. A., B. Kozlovsky, and R. Ramaty: *An Interpretation of the Observed Oxygen and Nitrogen Enhancements in Low-Energy Cosmic Rays.* The Astrophysical Journal, 190:L35–L37, May 1974.

[11] Pesses, M. E., D. Eichler, and J. R. Jokipii: *Cosmic Ray Drift, Shock Wave Acceleration, and the Anomalous Component of Cosmic Rays.* Astrophysical Journal Letters, 246:L85–L88, June 1981.

[12] Uchiyama, Y., F. A. Aharonian, T. Tanaka, T. Takahashi, and Y. Maeda: *Extremely Fast Acceleration of Cosmic Rays in a Supernova Remnant.* Nature, 449:576–578, October 2007.

[13] Wong, Samuel S.M.: *Introductory Nuclear Physics.* John Wiley & Sons, 2nd edition, 1998.

[14] Perkins, Donald: *Particle Astrophysics.* Oxford University Press, 2003.

[15] Grupen, Claus: *Astroparticle Physics.* Springer, 2005.

[16] Abbasi, R. U. and et al.: *First Observation of the Greisen-Zatsepin-Kuzmin Suppression.* Physical Review Letters, 100(10):101101–+, March 2008.

[17] The Pierre AUGER Collaboration, J. Abraham, and et al.: *Correlation of the Highest-Energy Cosmic Rays with the Positions of Nearby Active Galactic Nuclei.* Astroparticle Physics, 29:188–204, April 2008.

[18] Sokolsky, P. and G. B. Thomson: *Highest Energy Cosmic-Rays and Results from the HiRes Experiment.* Journal of Physics G Nuclear Physics, 34:401–+, November 2007.

[19] Berezinsky, V.: *Ultra High Energy Cosmic Ray Protons: Signatures and Observations.* Nuclear Physics B Proceedings Supplements, 188:227–232, March 2009.

[20] Egorova, V. P. and et al.: *The Spectrum Features of UHECRs below and Surrounding GZK.* Nuclear Physics B Proceedings Supplements, 136:3–11, November 2004.

[21] Shinozaki, K. and M. Teshima: *Agasa results.* Nuclear Physics B Proceedings Supplements, 136:18–27, November 2004.

[22] Roulet, E.: *Latest Results from the Pierre Auger Observatory.* ArXiv e-prints, January 2011.

[23] Farrar, G. R. and A. Gruzinov: *Giant AGN Flares and Cosmic Ray Bursts.* The Astrophysical Journal, 693:329–332, March 2009.

[24] Simpson, J. A.: *Elemental and Isotopic Composition of the Galactic Cosmic Rays.* Annual Review of Nuclear and Particle Science, 33:323–382, 1983.

[25] Gaisser, Thomas K.: *Cosmic Rays and Particle Physics.* Cambridge University Press, 1st edition, 1990.

[26] Strong, A. W., I. V. Moskalenko, and V. S. Ptuskin: *Cosmic-Ray Propagation and Interactions in the Galaxy.* Annual Review of Nuclear and Particle Science, 57:285–327, November 2007.

[27] Smart, D. F. and M. A. Shea: *A review of Geomagnetic Cutoff Rigidities for Earth-Orbiting Spacecraft.* Advances in Space Research, 36:2012–2020, 2005.

[28] Korte, M. and et al.: *New geomagnetic field observations in the south atlantic anomaly region.* Annals of Geophysics, 52(1), 2010.

[29] Fürst, F. and et al.: *Temporal Variations of Strength and Location of the South Atlantic Anomaly as Measured by RXTE.* Earth and Planetary Science Letters, 281:125–133, May 2009.

[30] Parker, E. N.: *The Passage of Energetic Charged Particles Through Interplanetary Space.* Planetary and Space Science, 13:9–+, January 1965.

[31] Potgieter, M. S.: *The Modulation of Galactic Cosmic Rays in the Heliosphere: Theory and Models.* Space Science Reviews, 83:147–158, January 1998.

[32] Gleeson, L. J. and W. I. Axford: *Solar Modulation of Galactic Cosmic Rays.* The Astrophysical Journal, 154:1011–1026, December 1968.

[33] Maestro, P.: *Indirect Search for Dark Matter by Measurements of the Cosmic Ray Positron Spectrum with the AMS-02 Experiment.* PhD thesis, Università degli studi di Siena, September 2003.

[34] Garcia-Munoz, M., P. Meyer, K. R. Pyle, J. A. Simpson, and P. Evenson: *The Dependence of Solar Modulation on the Sign of the Cosmic Ray Particle Charge.* Journal of Geophysical Research, 91:2858–2866, March 1986.

[35] Clem, J. M., D. P. Clements, J. Esposito, P. Evenson, D. Huber, J. L'Heureux, P. Meyer, and C. Constantin: *Solar Modulation of Cosmic Electrons.* The Astrophysical Journal, 464:507–+, June 1996.

[36] Kobayashi, T., Y. Komori, K. Yoshida, and J. Nishimura: *The Most Likely Sources of High-Energy Cosmic-Ray Electrons in Supernova Remnants.* The Astrophysical Journal, 601:340–351, January 2004.

[37] Golden, R. L. and et al.: *A Measurement of the Absolute Flux of Cosmic-Ray Electrons.* The Astrophysical Journal, 287:622–632, December 1984.

[38] Golden, R. L. and et al.: *Measurement of the Positron to Electron Ratio in Cosmic Rays above 5 GeV.* The Astrophysical Journal Letters, 457:L103+, February 1996.

[39] Adriani, O. and et al.: *An Anomalous Positron Abundance in Cosmic rays with Energies 1.5-100 GeV.* Nature, 458:607–609, April 2009.

[40] Ackermann, M. and et al.: *Measurement of Separate Cosmic-Ray Electron and Positron Spectra with the Fermi Large Area Telescope.* ArXiv e-prints, September 2011.

[41] Beatty, J. J. and et al.: *New Measurement of the Cosmic-Ray Positron Fraction from 5 to 15 GeV.* Physical Review Letters, 93(24):241102–+, December 2004.

[42] Aguilar, M. and et al.: *Cosmic-Ray Positron Fraction Measurement from 1 to 30 GeV with AMS-01.* Physics Letters B, 646:145–154, March 2007.

[43] Hooper, D., P. Blasi, and P. Dario Serpico: *Pulsars as the sources of High Energy Cosmic Ray Positrons.* Journal of Cosmology and Astroparticle Physics, 1:25–+, January 2009.

[44] Cholis, I., L. Goodenough, D. Hooper, M. Simet, and N. Weiner: *High energy positrons from annihilating dark matter.* Physical Review D, 80(12):123511–+, December 2009.

[45] Barwick, S. W. and et al.: *Measurements of the Cosmic-Ray Positron Fraction from 1 to 50 GeV.* The Astrophysical Journal Letters, 482:L191+, June 1997.

[46] Boezio, M. and et al.: *The Cosmic-Ray Electron and Positron Spectra Measured at 1 AU during Solar Minimum Activity.* The Astrophysical Journal, 532:653–669, March 2000.

[47] Moskalenko, I. V. and A. W. Strong: *Production and Propagation of Cosmic-Ray Positrons and Electrons.* The Astrophysical Journal, 493:694–+, January 1998.

[48] Chang, J. and et al.: *An Excess of Cosmic Ray Electrons at Energies of 300-800 GeV.* Nature, 456:362–365, November 2008.

[49] Yoshida, K. and et al.: *Cosmic-Ray Electron Spectrum Above 100 GeV from PPB-BETS Experiment in Antarctica.* Advances in Space Research, 42:1670–1675, November 2008.

[50] Ackermann, M. and et al.: *Fermi LAT Observations of Cosmic-Ray Electrons from 7 GeV to 1 TeV.* Physical Review D, 82(9):092004–+, November 2010.

[51] Adriani, O. and et al.: *Cosmic-Ray Electron Flux Measured by the PAMELA Experiment between 1 and 625 GeV.* Physical Review Letters, 106(20):201101–+, May 2011.

[52] Barwick, S. W. et al.: *The Energy Spectra and Relative Abundances of Electrons and Positrons in the Galactic Cosmic Radiation.* The Astrophysical Journal, 498:779–+, May 1998.

[53] Sanuki, T. and et al.: *Precise Measurement of Cosmic-Ray Proton and Helium Spectra with the BESS Spectrometer.* The Astrophysical Journal, 545:1135–1142, December 2000.

[54] Grupen, Claus and Boris Shwartz: *Particle Detectors.* Cambridge University Press, 2nd edition, 2008.

[55] Hagiwara, K. and et al.: *Review of Particle Properties.* Physical Review D, 66(1):010001, Jul 2002.

[56] Nappi, E.: *RICH Detectors.* In *American Institute of Physics Conference Series*, volume 536 of *American Institute of Physics Conference Series*, pages 60–86, September 2000.

[57] Nappi, E.: *Aerogel and its Applications to RICH Detectors.* Nuclear Physics B Proceedings Supplements, 61:270–276, February 1997.

[58] Dolgoshein, B.: *Transition Radiation Detectors.* Nuclear Instruments and Methods in Physics Research A, 326:434–469, March 1993.

[59] Cherry, M. L., D. Mueller, T. A. Prince, and G. Hartmann: *Transition Radiation from Relativistic Electrons in Periodic Radiators.* Physical Review D, 10:3594–3607, December 1974.

[60] Green, Dan: *The Physics of Particle Detectors.* Cambridge University Press, 2000.

[61] Ahlen, S. and et al.: *An Antimatter Spectrometer in Space.* Nuclear Instruments and Methods in Physics Research A, 350:351–367, October 1994.

[62] Aguilar, M. and et al.: *Alpha Magnetic Spectrometer (AMS) on the International Space Station: Part I - Results from the Test Flight on the Space Shuttle.* Physics Reports, 366:331–405, 2002.

[63] Alcaraz, J. and et al.: *Search for Antihelium in the Cosmic Rays.* Physics Letters B, 461:387–396, September 1999.

[64] Alcaraz, J. and et al.: *Protons in Near Earth Orbit.* Physics Letters B, 472:215–226, January 2000.

[65] Alcaraz, J. and et al.: *Cosmic Protons.* Physics Letters B, 490:27–35, September 2000.

[66] Alcaraz, J. and et al.: *Leptons in Near Earth Orbit.* Physics Letters B, 484:10–22, June 2000.

[67] AMS-01 Collaboration: *Cosmic-Ray Positron Fraction Measurement from 1 to 30 GeV with AMS-01.* Physics Letters B, 646:145–154, March 2007.

[68] Alcaraz, J. and et al.: *Helium in near earth orbit.* Physics Letters B, 494:193–202, November 2000.

[69] Lamanna, G. and The AMS Collaboration: *Measurement of the Deuteron Spectra in Low Earth Orbit with AMS.* In *International Cosmic Ray Conference*, volume 5 of *International Cosmic Ray Conference*, pages 1614–1617, 2001.

[70] Aguilar, M. and et al.: *Relative Composition and Energy Spectra of Light Nuclei in Cosmic Rays: Results from AMS-01.* The Astrophysical Journal, 724:329–340, November 2010.

[71] Aguilar, M. and et al: *Isotopic composition of light nuclei in cosmic rays: Results from ams-01.* The Astrophysical Journal, 736(2):105, 2011.

[72] Doetinchem, P. V. and et al.: *Performance of the AMS-02 Transition Radiation Detector.* Nuclear Instruments and Methods in Physics Research A, 558:526–535, March 2006.

[73] Amati, L. and et al.: *The TOF Counters of the AMS-02 Experiment: Space Qualification Tests and Beam Test Results.* Nuclear Physics B Proceedings Supplements, 150:276–280, January 2006.

[74] Alcaraz, J. and et al.: *The Alpha Magnetic Spectrometer Silicon Tracker: Performance Results with Protons and Helium Nuclei.* Nuclear Instruments and Methods in Physics Research A, 593:376–398, August 2008.

[75] Arruda, L., F. Barão, P. Gonçalves, and R. Pereira: *The Ring Imaging Cherenkov Detector of the AMS Experiment: Test Beam Results with a Prototype.* Nuclear Physics B Proceedings Supplements, 172:32–35, October 2007.

[76] Falco, S. D.: *Results of 2007 Test Beam of AMS-02 Electromagnetic Calorimeter.* Advances in Space Research, 45:112–122, January 2010.

[77] Blau, B., S. M. Harrison, H. Hofer, S. R. Milward, J. S. H. Ross, S. C. C. Ting, J. Ulbricht, and G. Viertel: *The Superconducting Magnet of AMS-02.* Nuclear Physics B Proceedings Supplements, 113:125–132, 2002.

[78] Battiston, R.: *The Anti Matter Spectrometer (AMS-02):. a Particle Physics Detector in Space.* In C. Leroy, P.-G. Rancoita, M. Barone, A. Gaddi, L. Price, & R. Ruchti (editor): *Astroparticle, Particle and Space Physics, Detectors and Medical Physics Applications*, pages 741–750, April 2010.

[79] McIntyre, P.: *Integration and Testing of the Superconducting Magnet and Cryogenics for AMS*. IEEE Transactions on Applied Superconductivity, 20:2010–2014, June 2010.

[80] Hauler, F. and et al.: *The AMS-02 TRD for the International Space Station*. IEEE Transactions on Nuclear Science, 51:1365–1372, August 2004.

[81] Bindi, V. and et al.: *The Scintillator Detector for the Fast Trigger and Time-of-Flight (TOF) Measurement of the Space Experiment AMS-02*. Nuclear Instruments and Methods in Physics Research A, 623:968–981, November 2010.

[82] Zuccon, P. and the AMS Tracker collaboration: *The AMS Silicon Tracker: Construction and Performance*. Nuclear Instruments and Methods in Physics Research A, 596:74–78, October 2008.

[83] Alpat, B. and et al.: *Charge Determination of Nuclei with the AMS-02 Silicon Tracker*. Nuclear Instruments and Methods in Physics Research A, 540:121–130, March 2005.

[84] Alpat, B. and et al.: *The Internal Alignment and Position Resolution of the AMS-02 Silicon Tracker Determined with Cosmic-Ray Muons*. Nuclear Instruments and Methods in Physics Research A, 613:207–217, February 2010.

[85] Pereira, R.: *The AMS-02 RICH Detector: Performance During Ground-Based Data Taking at CERN*. Nuclear Instruments and Methods in Physics Research A, 639(1):37–41, May 2011. Proceedings of the Seventh International Workshop on Ring Imaging Cherenkov Detectors.

[86] Goy, C. and the AMS calorimeter group: *The AMS-02 3D-imaging calorimeter: A tool for cosmic rays in space*. Journal of Physics Conference Series, 160(1):012041–+, April 2009.

[87] von Doetinchem, P., W. Karpinski, T. Kirn, K. Lübelsmeyer, S. Schael, and M. Wlochal: *The AMS-02 Anticoincidence Counter*. Nuclear Physics B Proceedings Supplements, 197:15–18, December 2009.

[88] Kounine, A.: *Status of the AMS Experiment*. ArXiv e-prints, September 2010.

[89] *Public Law 111-167 October 11, 2010*. `http://legislative.nasa.gov/PL%20111-267.pdf`.

[90] K., Lübelsmeyer and et al.: *Upgrade of the Alpha Magnetic Spectrometer (AMS-02) for Long Term Operation on the International Space Station (ISS)*. Nuclear Instruments and Methods in Physics Research Section A: Accelerators, Spectrometers, Detectors and Associated Equipment, 654(1):639–648, 2011.

[91] Haino, S. and AMS-02 Tracker Collaboration: *The AMS-02 Silicon Tracker*. In *Proceedings of the 12th ICATPP Conference*, October 2010.

[92] `http://geant4.cern.ch`.

[93] `http://root.cern.ch`.

[94] Caraffini, D.: *Anti-proton Flux Detection and Indirect Search for Dark Matter with the AMS-02 Experiment*. PhD thesis, Università degli studi di Perugia, 2004.

[95] `http://ams.cern.ch/AMS/Analysis/hpl3itp1/root02_v5/html/index.html`.

[96] Pilo, F.: *Diffuse Gamma Ray Emission Detection with the AMS-02 Electromagnetic Calorimeter*. PhD thesis, Università degli studi di Siena, 2005.

[97] Giovacchini, F.: *Cosmic Rays Anti-Deuteron Flux Sensitivity of the AMS-02 Detector* . PhD thesis, Università di Bologna, 2007.

[98] Brun, P.: *Equalization of the AMS Electromagnetic Calorimeter with MIPs Using Test Beam Data*. AMS Note, June 2008.

[99] Falchini, E.: *AMS-02 Dark Matter Search Inspecting Cosmic Ray Positron Spectrum*. AMS Note, December 2004.

[100] Goy, C. and S. Rosier: *The AMS Calorimeter Performance Studies with the 2007 Test Beam Data*. AMS Note, July 2008.

[101] Fiasson, A.: *e/p Rejection Study with the ECAL Esing Multivariate Approach on Test Beam Data*. AMS Note, January 2011.

[102] Hooper, D. and S. Profumo: *Dark matter and collider phenomenology of universal extra dimensions*. Physics Reports, 453:29–115, December 2007.

[103] Cabrera, J. M., F. Agulló y F. J. López: *Óptica Electromagnética Vol. II: Materiales y Aplicaciones*. Addison-Wesley, 2000.

Index

W

Y

Z

Universidad Complutense de Madrid

Departamento de Física Atómica, Molecular y Nuclear

Programa de Doctorado de Física Nuclear

Resumen en español de la memoria de tesis doctoral presentada para optar al título de Doctor en Ciencias Físicas

Prestaciones del detector AMS-02 para el estudio del canal de positrones de los rayos cósmicos

AMS-02 detector capabilities for cosmic ray positron measurements

David Crespo Roces

Tesis Doctoral dirigida por

Dr. Jorge Casaus Armentano

Curso académico 2011/2012

Introducción

AMS es una colaboración internacional de la que forman parte universidades e institutos de investigación de América, Europa y Asia cuyo objetivo fue el de construir y poner en órbita en espectrómetro magnético. El lanzamiento de AMS-02 a bordo del transbordador espacial Endeavour y su instalación posterior en la Estación Espacial Internacional (ISS), supuso la culminación del trabajo iniciado en la década de los años 90. A partir de ahora, quedan más de diez años hasta el final de la vida de la ISS para medir y analizar la composición y espectro de los rayos cósmicos.

El objetivo de este trabajo es el de obtener la señal de los positrones cósmicos con una simulación Monte Carlo (MC) del detector AMS-02 con la configuración de vuelo. Para validar este resultado, se dispone de los datos de una prueba de haz del detector con una configuración previa, de los datos de una prueba de haz del detector con la configuración de vuelo y de la propia simulación MC. El trabajo parte de la primera prueba de haz para obtener las prestaciones del detector, ya que ésta ofrece la mejor muestra de datos para calibrar el calorímetro electromagnético, un subdetector clave en la supresión del fondo de protones cósmicos. Los resultados de esta prueba de haz se compararán con la prueba de haz del detector con la configuración de vuelo y con la simulación MC, para constatar que la última actualización del detector no supuso un cambio en las prestaciones de los subdetectores involucrados en la supresión de protones.

La tesis se divide en cuatro partes. La primera parte constituye la introducción teórica que proporciona la motivación del estudio de la señal de positrones cósmicos y cómo AMS-02 hace posible esta medida. La segunda parte se dedica al experimetno, desde sus comienzos hasta el lanzamiento de AMS-02, incluyendo tanto una descripción del detector como del software. La tercera parte comprende el análisis del calorímetro electromagnético y del detector de radiación de transición usando datos de la primera prueba de haz del detector. La última parte se adentra en las capacidades del detector para estudiar la señal de positrones usando una simulación MC del detector con la configuración de vuelo, la cual es validada al comparar los resultados de los capítulos anteriores con los datos de la prueba de haz con la configuración de vuelo.

En este resumen en español de la tesis se ha concentrado la esencia del trabajo así como una introducción a los rayos cósmicos y al detector. A continuación se describen brevemente los tres capítulos de los que consta este resumen:

Capítulo 1: Este capítulo realiza una introducción al origen y propagación de los rayos cósmicos así como a los efectos geomagnéticos y solares que afectan al espectro de los rayos cósmicos a baja energía. Para finalizar, el capítulo se centra en la componente de los positrones cósmicos y en los resultados de otros experimentos.

Capítulo 2: Este capítulo realiza una descripción de AMS-02 y de sus subdetectores, tanto de la configuración con imán superconductor como de la configuración con imán permanente o de vuelo. Para finalizar, el capítulo introduce brevemente la identificación de partículas con AMS-02 y el software de AMS.

Capítulo 3: Tanto el calorímetro electromagnético como el detector de radiación de transición proporcionan una separación electrón/protón necesaria para reducir el fondo de protones cósmicos. Los datos tomados en la primera prueba de haz del detector se usan en este capítulo para desarrollar un método de calibración del calorímeetro y para evaluar las prestaciones en la separación electrón/protón de ambos subdetectores. Los resultados obtenidos se comparan con los datos de la prueba de haz del detector con la configuración de vuelo así como con una simulación MC. Un buen acuerdo entre ambas configuraciones, junto con la comparación con la simulación MC valida el análisis de la señal de positrones cósmicos.

Capítulo 4: Debido a que el resultado que se obtiene con la prueba de haz en la supresión de protones está limitado a un punto de energía, se utiliza una simulación MC del detector con la configuración de vuelo para extender el factor de rechazo a otras energías y así determinar una cota superior de energía para la medida de positrones donde ésta no se vea comprometida por el fondo de protones.

Índice general

1

Rayos cósmicos

Los rayos cósmicos son en su mayor parte núcleos atómicos totalmente ionizados con un amplio rango de energía y origen diverso. En función de este origen los rayos cósmicos se pueden clasificar en tres tipos: solares, anómalos y galácticos.

1.1 Rayos cósmicos solares

Tienen su origen en las erupciones y eyecciones de masa de la corona solar, ambas debidas a la alta actividad magnética presente en las manchas solares. Las partículas cargadas que son expulsadas del Sol (protones en su mayor parte) forman el llamado viento solar, el cual lleva consigo el campo magnético solar [1, 2].

1.2 Rayos cósmicos anómalos

En la década de los 70 [1, 3] se detectó un incremento anómalo en el espectro de baja energía de elementos químicos como el O, N, He y Ne. Posteriormente, en los años 80 [4], estas medidas se confirmaron con las observaciones realizadas por la sonda Voyager. Los rayos cósmicos anómalos tienen su origen en los átomos neutros que llegan del medio interestelar a la heliosfera, donde se ionizan al entrar en contacto con el viento solar para luego ser acelerados a energías de 1-100 MeV/nucleón [5, 6].

1.3 Rayos cósmicos galácticos

Su origen se encuentra en los procesos más energéticos del Universo, como son las supernovas, para ser luego acelerados por las ondas de choque que se forman en la expansión de los remanentes de supernova en el medio interestelar [7]. Dentro de los rayos cósmicos galácticos se distinguen dos clases, los primarios, que son aquellos que llegan directamente desde la fuente, y los secundarions, que son el producto de la espalación (fragmentación) de los primarios en el medio interestelar.

La radiacion cósmica que llega a la heliosfera está formada por nucleones (98 %) y electrones y positrones (2 %). En el rango de energía entre 10^8–10^{10} eV/nucleón, la componente nuclear está formada por ~ 87 % de hidrógeno, ~ 12 % de helio y ~ 1 % de núcleos más pesados [1]. El espectro de los rayos cósmicos galácticos sigue una ley de potencias

$$\frac{dN}{dE}(E) = kE^{-\gamma} \tag{1.1}$$

El índice espectral γ tiene un valor de 2.7 hasta 10^{15} eV/nucleón. Por encima de esta energía, la pendiente del espectro se acentúa hasta $\gamma \sim 3$ (rodilla). La existencia de esta rodilla se atribuye a la salida de rayos cósmicos de la galaxia [8,9] junto al hecho de que 10^{15} eV/nucleón es la energía máxima que puede proporcionar una explosión de supernova [9]. A partir de los $5{\times}10^{18}$ eV la pendiente disminuye otra vez (tobillo), debido probablemente a la aparición de una componente más dura de origen extragaláctico que sobresale por encima de la componente galáctica [8,9]. Por encima de $4{\times}10^{19}$ eV, los protones pierden energía debido a la interacción con el fondo cósmico de microondas (CMB) [9]:

$$p + \gamma \longrightarrow p + \pi^0 \qquad , \qquad p + \gamma \longrightarrow n + \pi^+ \tag{1.2}$$

Este corte, conocido como GZK (Greisen, Zatsepin y Kulzmin), ha sido confirmado por el experimento HiRes [10] y por el experimento Auger [11], lo que pone de manifiesto el domino de la componente de protones [12]. Otra característica de los protones extragalácticos es la depresión en el espectro (*dip*) [13]

$$p + \gamma \longrightarrow p + e^+ + e^- \tag{1.3}$$

vista en los datos de Yakutsk [14], AGASA [15], HiRes [10] y Auger [16]. Este buen acuerdo debe considerarse como una prueba de la gran cantidad de protones en el espectro [13]. Por otra parte, los candidatos más probables a fuentes de sucesos registrados con energías por encima de 10^{20} eV son núcleos de galaxia activos (AGN) y chorros de rayos gamma (GRB) [11, 17].

1.3.1 Propagación de los rayos cósmicos galácticos

La ecuación de propagación de los rayos cósmicos para una especie en particular de partículas se puede escribir de forma general como:

$$\begin{aligned}\frac{\partial\psi(\vec{r},p,t)}{\partial t} &= q(\vec{r},p,t) + \nabla\cdot(D\nabla\psi - \vec{V}\psi) \\ &\quad + \frac{\partial}{\partial p}p^2 D_{pp}\frac{\partial}{\partial p}\frac{1}{p^2}\psi - \frac{\partial}{\partial p}\left[\dot{p}\psi - \frac{p}{3}(\nabla\cdot\vec{V})\psi\right] - \frac{1}{\tau_f}\psi - \frac{1}{\tau_r}\psi\end{aligned} \tag{1.4}$$

donde $\psi(\vec{r},p,t)$ es la densidad de rayos cósmicos por unidad de momento total p de la partícula en la posición $\vec{r}$ ($\psi(p)dp = 4\pi p^2 f(\vec{p})dp$ en términos de la densidad del espacio de fases $f(\vec{p})$). $q(\vec{r},p)$ es el término fuente, que incluye tanto las contribuciones de los primarios, de la espalación y la desintegración. D_{xx} es el coeficiente de difusión espacial. $\vec{V}$ es la velocidad de convección. D_{pp} es el coeficiente por el que se calcula la difusión en el espacio de momentos, la cual describe la reaceleración difusiva. $\dot{p} \equiv dp/dt$ es la razón de momento ganado o perdido. τ_f es el periodo de tiempo para la pérdida por fragmentación y τ_r es el periodo de tiempo para la desintegración radioactiva.

1.3.2 Efectos solares y geomagnéticos

Tanto el campo magnético de la Tierra como el viento solar modifican el espectro de los rayos cósmicos por debajo de los 10 GeV/nucleón.

1.3.2.a Rigidez de corte

El campo magnético terrestre actúa como una barrera ante los rayos cósmicos con una baja rigidez por las pérdidas de energía que estos sufren al seguir trayectorias espirales a lo largo de las líneas del campo magnético. La rigidez ($R = pc/|Z|e$) mínima requerida para que una partícula atraviese el campo magnético terrestre, conocida como rigidez de corte, se puede calcular usando la ecuación de Størmer [18, 19]

$$R = M\frac{\cos^4\lambda}{r^2\left(1+\sqrt{1-\sin\theta\cos^3\lambda}\right)^2} \tag{1.5}$$

si el campo magnético se aproxima por un campo dipolar. En la ecuación 1.5 r es la distancia desde el centro del dipolo expresada en radios de la Tierra, λ es la latitud geomagnética, θ es la ángulo azimutal de la partícula incidente y el momento dipolar M tiene un valor de $\sim 58\,\mathrm{GV}$ para el modelo de campo magnético IGRF [1] 2000 [19]. El ángulo θ se considera positivo para partículas que se mueven de este a oeste, mientras que se considera negativo para partículas moviéndose en la dirección contraria. Para partículas con incidencia normal ($\theta = 0$) la rigidez de corte se reduce a

$$R = 14.5\,\mathrm{GV}\frac{\cos^4\lambda}{r^2} \tag{1.6}$$

Usando la ecuación 1.6, la rigidez de corte en el ecuador magnético ($\lambda = 0$) y a una distancia del centro del dipolo igual al radio de la Tierra ($r = 1$) es 14.5 GV. Usando la ecuación 1.5, para partículas que llegan desde el horizonte oriental ($\sin\theta = +1$) a la altura del ecuador magnético ($\lambda = 0$) y $r = 1$, la rigidez de corte es 58 GV, mientras que para partículas que llegan desde el horizonte occidental ($\sin\theta = -1$) es 9.95 GV. Esta asimetría este-oeste se observa a todas las altitudes y se conoce como efecto este-oeste.

El campo magnético de la Tierra no es un dipolo perfecto, por lo que para determinar de forma precisa la rigidez de corte se requiere un modelo detallado del campo geomagńetico junto con un método computacional para calcular las trayectorias permitidas.

1.3.2.b Anomalía del Atlántico Sur

El campo magnético terrestre es más débil en la region situada encima del Atlántico Sur [20]. Esto permite a los rayos cósmicos penetrar más abajo en la atmósfera, incrementándose el flujo local. La existencia de esta anomalía del Atlántico Sur (SAA), la cual se desplaza hacia el oeste [21], interfiere en la comunicación con satélites.

1.3.2.c Modulación solar

El plasma de protones y electrones expulsado de la corona solar al medio interplanetario se conoce como viento solar, el cual lleva incrustado el campo magnético del Sol. El resultado, es un campo magnético a gran escala en forma de espiral de Arquímedes unido a pequeñas irregularidades debidas a la turbulencia e inestabilidades presentes en el medio interplanetario. Los rayos cósmicos cargados extrasolares con rigidez $\lesssim 10\,\mathrm{GV}$ se mueven a lo largo del campo magnético a gran escala y se dispersan en las pequeñas irregularidades, dando como resultado una menor densidad de rayos cósmicos extrasolares observados desde la Tierra [1].

[1] *International Geomagnetic Reference Field.*

Los modelos de modulación solar se basan en la ecuación de transporte de los rayos cósmicos formulada por Parker [22], la cual describe la propagación de los rayos cósmicos a través de la heliosfera teniendo en cuenta procesos convectivos, difusivos, cambios de energía adiabáticos y fuentes [23]. Gleeson y Axford [24] encontraron una aproximación de la ecuación donde el flujo modulado $F(r, R, t)$ a una distancia radial r desde el Sol, en un tiempo t y para partículas de energía E está relacionada con el flujo interestelar $F(\infty, E)$, independiente del tiempo, por la función [25]

$$F(r, E, t) = \frac{E^2 - E_0^2}{(\Phi(t) + E^2) - E_0^2} F(\infty, \Phi(t) + E) \tag{1.7}$$

$\Phi(t)$ es un parámetro que puede se interpretado como la pérdida de energía sufrida por las partículas en su camino a la Tierra desde el exterior de la heliosfera. El parámetro Φ está relacionado con el parámetro de la modulación solar ϕ a través de la relación $\Phi = |Z|e\phi$.

Es conocido que la modulación solar depende del signo de la carga de las partículas [26]. La orientación del campo magnético del sol provoca que la polaridad magnética se invierta en ciclos solares consecutivos (11 años para cada polaridad) y modelos más precisos tienen en cuenta este efecto [27].

1.4 Positrones cósmicos

Los electrones y positrones de los rayos cósmicos interactúan con el medio interestelar sólo a través de procesos electromagnéticos. Los procesos que dominan hasta energías de unos pocos GeV son la ionización y el *bremsstrahlung*, siendo la radiación de sincrotrón y el efecto Compton inverso los procesos dominantes a energías mayores.

Las medidas del espectro conjunto de electrones y positrones $(e^- + e^+)$ [28] constatan quel flujo es ~ 1 % del flujo de protones a 10 GeV, y que el índice γ de la ecuación 1.1 del espectro de electrones por encima de 10 GeV es ~ 3.0, mientras que para protones es de ~ 2.7.

Las interacciones hadrónicas entre los núcleos de los rayos cósmicos y los núcleos del medio interestelar es una fuente secundaria de electrones y positrones aproximadamente en igual número, aunque la fracción de positrones observada $e^+/(e^- + e^+)$ en la parte alta de la atmósfera es ~ 10 % a unos pocos GeV [29] con un incremento por encima de los 10 GeV (figura 1.1(a). Este incremento fue medido por PAMELA [30], y más recientemente por FERMI [31], confirmando medidas anteriores de HEAT [32] y AMS-01 [33]. Por lo tanto, la mayoría de electrones tiene que ser de origen primario, a la vez que el incremento de la fracción de positrones por encima de 10 GeV sugiere la existencia de una nueva fuente primaria de positrones, cuya naturaleza ha sido ampliamente discutida con propuestas que van desde púlsares cercanos [34] a la aniquilación de materia oscura en la halo galáctico [35].

Las medidas realizadas por ATIC [36] y PPB-BETS [37] hace unos años mostraron un incremento en el espectro conjunto de electrones y positrones a unos 600 GeV (figura 1.1(b)), que podría ser un indicio de la presencia de una fuente primaria cercana de electrones y positrones. Sin embargo, medidas más recientes de FERMI [31, 38] y PAMELA[2] [39] no muestran tal incremento y los datos se pueden interpretar en términos de modelos de propagación difusivos convencionales, aunque son también consistentes con modelos que incluyen nuevas fuentes que pudieran explicar el aumento en la fracción de positrones.

[2] La referencia sólo incluye el flujo de electrones.

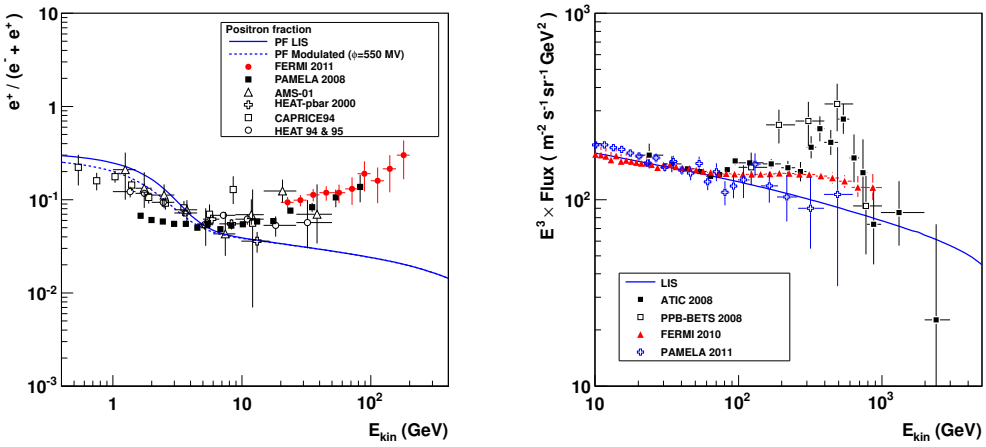

(a) $e^+/(e^- + e^+)$ (b) $e^- + e^+$

Figura 1.1: *Medidas de la fracción de positrones por parte de los experimentos HEAT [32,40], CAPRICE [41], AMS-01 [33], PAMELA [30] y FERMI [31] junto con un modelo de propagación que sólo tiene en cuenta una producción secundaria de positrones y una producción primaria y secundaria de electrones (línea azul) a partir de [42,43] (figura 1.1(a)). Espectro conjunto de electrones y positrones a partir de los datos de ATIC [36], PPB-BETS [37], FERMI [38] y el espectro de electrones medido por PAMELA [39], junto con un modelo de propagación que sólo tiene en cuenta una producción secundaria de positrones y una producción primaria y secundaria de electrones (línea azul) a partir de [42,43] (figura 1.1(b)).*

Debido a la baja intensidad de las señales de $e^{\pm}$ en comparación con el gran fondo de protones (figura 1.2(a)), cuyo flujo es 10^3–10^5 mayor que el de positrones (figura 1.2(b)), se necesita una factor de rechazo frente a protones del orden de 10^4–10^6 para realizar medidas de positrones, junto a una medida precisa del signo de la carga para distinguirlos de los electrones. AMS-02 es un espectrómetro magnético con gran aceptancia, gran tiempo de exposición y una excelente separación e/p, que le permitirá extender el conocimiento que se tiene de los positrones de los rayos cósmicos actualmente.

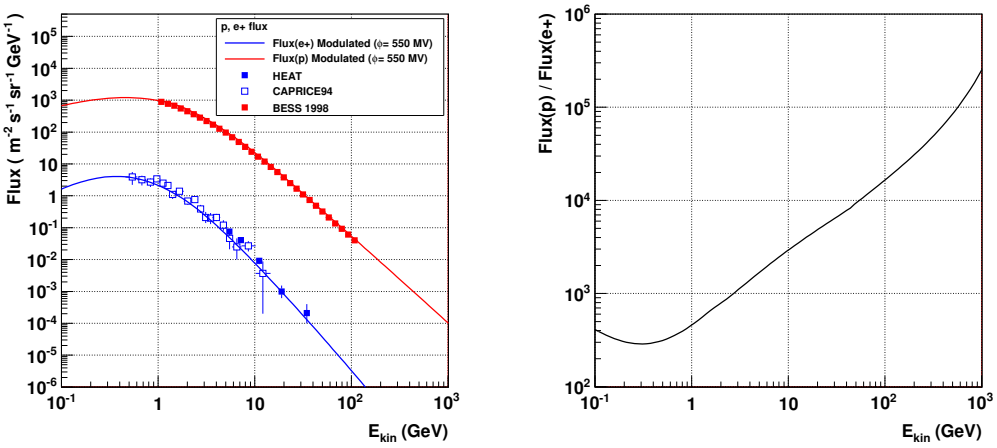

(a) (b)

Figura 1.2: *Medidas del flujo de positrones de HEAT [44] y CAPRICE [41], del flujo de protones medido por BESS [45], junto con un modelo de propagación para positrones (línea azul) a partir de [43] y un modelo de propagación de protones (línea roja) a partir de [46] (figura 1.2(a)). Ratio de los flujos de protones y positrones (figura 1.2(b)).*

2

El experimento AMS

AMS (*Alpha Magnetic Spectrometer*) es una colaboración internacional integrada por universidades e institutos de investigación de América, Europa y Asia cuyo objetivo era la construcción y puesta en órbita alrededor de la Tierra de un espectrómetro magnético para poder medir con precisión el espectro y composición de los rayos cósmicos, siendo la Estación Espacial Internacional (ISS) un laboratorio ideal donde instalar un detector de partículas para un experimento de larga duración como AMS.

Los primeros estudios para enviar un espectrómetro magnético al espacio aparecieron publicados en 1994 [47]. En abril de 1995, AMS fue aprobado por el departamento de energía de los EE.UU y en ese mismo año comenzó la construcción de un primer detector para comprobar la viabilidad del proyecto. En junio de 1998, el detector AMS-01 voló abordo del transbordador espacial Discovery durante 10 días dentro de la misión STS-91 de la NASA. El éxito de la misión dio lugar al nacimiento de AMS-02, un nuevo detector que iba a ser instalado en la ISS. AMS-02 voló abordo del transbordador espacial Endeavour en Mayo de 2011 dentro de la misión STS-134 de la NASA para ser instalado en la Estación Espacial Internacional.

2.1 El detector AMS-02

Desde mayo de 2011 AMS-02 está orbitando alrededor de la Tierra a una altitud de unos 350 km. El detector, con un peso de 8500 kg, un volumen de 64 m^3 y un consumo eléctrico de 2.5 kW, no retornará a la Tierra. La duración de la misión se alargará hasta el final de la vida de la ISS, año 2020–2028.

AMS-02 consta de varios subdetectores: el imán, el detector de radiación de transición (TRD), el sistema de tiempo de vuelo (TOF), el detector de trazas de silicio (Tracker), el detector de anillos Cherenkov (RICH), el calorímetro electromagnético (ECAL) y el contador de anticoincidencias (ACC). La colaboración ha desarrollado dos imanes para ser usados en el espacio: un imán permanente (PM) y un imán superconductor (SCM). El imán permanente fue utilizado en AMS-01, mientras que el imán superconductor se empezó a construir a raíz del éxito de esta primera misión. Tanto el imán permanente como el superconductor tienen el mismo diámetro interior y todos los subdetectores de AMS-02 han sido diseñados con unas conexiones compatibles con ambos imanes.

AMS es un experimento de larga exposición, con una gran aceptancia, excelente indentificación de partículas y una precisa medida de la rigidez y la carga. Esto hace posible que se puedan

medir las componentes más débiles de los rayos cósmicos, como son los positrones, a pesar del gran fondo de protones. Esta supresión del fondo de protones se consigue gracias al calorímetro, al detector de radiación de transición y al detector de trazas.

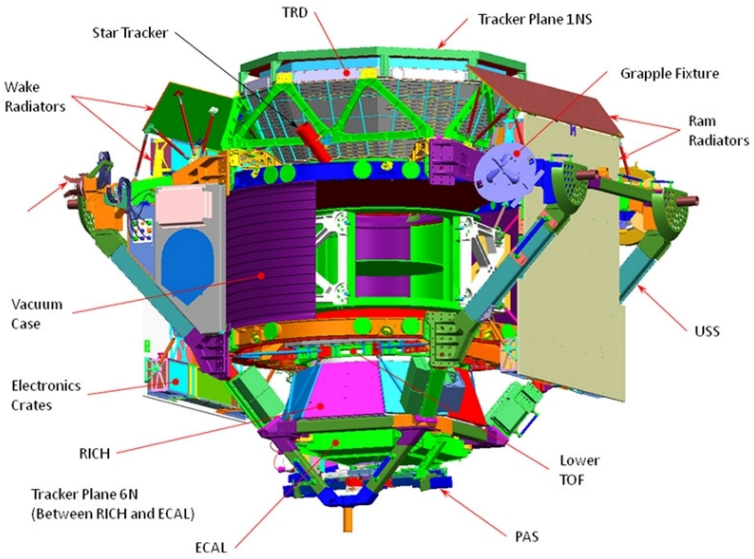

Figura 2.1: *Diseño del detector AMS-02 con su configuración de vuelo.*

2.1.1 La configuración con imán superconductor

AMS-02 fue construído para una misión de 3 años en la ISS, y el imán superconductor era la opción ideal para este escenáreo. Los diferentes subdetectores de AMS-02 pasaron diferentes pruebas de calificación de vuelo así como pruebas de haz antes del emsamblaje final llevado acabo en las instalaciones del CERN entre los años 2008 y 2009. En febrero de 2010, AMS-02 con el imán superconductor se probó con un haz de protones y otro de electrones.

2.1.1.a El imán superconductor

El sistema del imán superconductor está formado por un conjunto de bobinas superconductoras, un contenedor de helio superfluido y un sistema criogénico, todo ello encerrado en una cámara de vacío [48, 49]. La cámara de vacío tiene una forma toroidal con un diámetro interno de 1.1 m y un diámetro externo de 2.7 m. El imán opera a una temperatura de 1.8 K gracias a la refrigeración aportada por el helio superfluido.

El sistema de bobinas está formado por 14 bobinas superconductoras, todas ellas dispuestas en una configuración circular. Un par de bobinas genera el campo magnético dipolar, cuya dirección define el eje x del experimento. El eje z viene dado por la dirección paralela al eje de giro de la propia estructura toroidal, mientras que el eje y es perpendicular al plano $x - z$. Las 12 bobinas restantes reducen el campo magnético residual al mismo tiempo que contribuyen al campo dipolar. En el centro geométrico del sistema se alcanza una densidad de flujo magnético de 0.8 T.

2.1.1.b El detector de radiación de transición (TRD)

El detector de radiación de transición [50] proporciona una separación electrón/hadrón al experimento. Está situado encima de la cámara de vacío del imán superconductor y está compuesto por 20 capas de módulos de tubos de deriva y radiadores de fibra de polipropileno montadas en una estructura cónica octogonal. Las 4 capas superiores y las 4 inferiores están orientadas paralelamente al eje x de AMS-02, mientras que las 12 capas restantes son ortogonales a estas últimas, orientadas paralelamente al eje y. Los tubos de deriva están rellenos con una mezcla de gas Xe : CO_2 (80:20) y tienen una diámetro de 6 mm.

El TRD tiene una factor de rechazo en la separación e/p en el rango de energía 1.5–300 GeV de 10^2–10^3 para el 90 % de efficiencia en la señal [51].

2.1.1.c El contador de tiempo de vuelo (TOF)

El contador de tiempo de vuelo [52] proporciona la señal de disparo rápido (*fast trigger*) a la electrónica de lectura de AMS (el primer nivel en la cadena de adquisición de datos), una medida de la velocidad de las partículas (distinguiendo entre partículas que se mueven hacia abajo de partículas que se mueven hacia arriba al nivel del 10^9) y una medida del valor absoluto de la carga por pérdidas de energía.

El TOF está formado por 4 planos de plástico centelleador (dos por encima y dos por debajo del imán), con 8, 8, 10 y 8 contadores cada uno. Los contadores de planos adyacentes son ortogonales entre sí, proporcionando de esta manera una granularidad de aproximadamente $12 \times 12\,\mathrm{cm}^2$. Dos fotomultiplicadores colocados en los extremos de cada plano centelleador, conectados por guías de luz, son los encargados de la lectura.

El TOF tiene una resolución temporal de 160 ps (1 ps = 10^{-12} s) y una resolución en la velocidad β ($\beta = v/c$) del 4 % para partículas con $\beta \sim 1$. Además se pueden identificar núcleos hasta $Z \approx 15$ con una resolución en β cercana al 2 % [52].

2.1.1.d El detector de trazas de silicio (STD)

El detector de trazas [53] está formado por 5 planos. Los dos planos externos están equipados con detectores de silicio por una sola cara, mientras que los tres planos interiores están equipados con detectores de silicio por ambas caras. Estas 8 capas de detectores de silicio son las que proporcionan la medida de la trayectoria de la partícula en el interior del imán.

Las prestaciones de los detectores de silicio han sido medidas en haces de protones e iones. La rigidez máxima detectable estimada para protones y helio es de 2.2 y 3.7 TV respectivamente con una resolución en la rigidez del 1–3 % en el rango 1–50 (1–100) GV para protones (nucleos de helio) [54]. Las pérdidas de energía en las diferentes capas permiten distinguir partículas hasta $Z = 26$ [55]. Durante la fase de preensamblaje de AMS-02 (años 2007–2008 sin imán) la resolución en la medida de la posición con muones de rayos cósmicos fue de 12.5 mm en el plano de curvatura ($y - z$) y de 35 mm en el plano de no curvatura ($x - z$) [56], que es compatible con los resultados que se obtuvieron con el haz de protones.

2.1.1.e El contador de anticoincidencias (ACC)

El detector de trazas de AMS-02 está rodeado por una pantalla centelleadora de alta eficiencia [57]. Esta es usada para descartar aquellas trazas que no se encuentran dentro de la aceptancia del detector para así evitar una distorsión en la medida del signo de la carga.

El contador de anticoincidencias está formado por 16 paneles centelleadores colocados en la parte interior de la cámara de vacío a menos de 8 *cm* de la superficie de las bobinas del imán superconductor. La luz de los centelleadores es canalizada en ambos extremos a través de fibras ópticas hasta unos fotomultiplicadores situados en la parte superior e inferior de la cámara de vacío.

Con una ineficiencia por debajo de 10^{-4} (ratio de trazas perdidas y del número total de trazas que atraviesan el ACC) [57], el ACC garatiza que una señal de antimateria no será simulada debido a partículas que entran por los laterales.

2.1.1.f El detector de anillos Cherenkov (RICH)

El detector de anillos Cherenkov [58] proporciona una medida precisa de la velocidad ($\sigma_\beta/\beta \sim 1.0\times10^{-3}$) y del valor absoluto de la carga ($Z < 26$ con una probabilidad de equivocación en la carga de 10^{-2}). Se encuentra en la parte inferior del espectrómetro, entre el TOF y el ECAL, tiene una forma cónica truncada con un radio superior de 60 cm, un radio inferior de 67 cm. La distancia de expansión (distancia entre el radiador y el plano de detección) es de 46.8 *cm*. El RICH cubre el 90 % de la aceptancia del imán de AMS-02.

El radiador está formado por 92 losetas de aerogel de sílice ($n = 1.05$) con 2.5 cm de grosor y 16 losetas centrales de NaF ($n = 1.334$) con 0.5 cm de grosor. La parte central de NaF tiene como misión incrementar la eficiencia en la detección de fotones para aquellas partículas que atraviesan la parte central del plano detector, ya que al tener un índice de refracción mayor, el ángulo de emisión también es mayor. Además, debido a ese mayor índice de refracción, se aumenta el rango dinámico del detector, al tener una velocidad umbral de $\beta_{umbral} = 0.75$.

El plano de detección, el cual tiene una hueco central de $64\times64\,\mathrm{cm}^2$ para evitar interacciones en las partículas que están dentro de la aceptancia geométrica del ECAL, está formado por un conjunto de 680 guías de luz y fotomultiplicadores multiánodo con 4×4 píxeles de $4\times4\,\mathrm{mm}^2$ que suman en total 10880 canales.

El RICH de AMS-02 cuenta además con un reflector rodeando toda la estructura para aumentar así la aceptancia, ya que aproximadamente el 33 % de los fotones son reflejados y redireccionados al plano detector. Este tiene una forma cónica truncada con un diámetro superior de 120 cm y un diámetro inferior de 134 cm. La superficie interna está recubierta por una fina capa reflectiva hecha de 100 nm de aluminio y 300 nm de SiO_2 que hace que la reflectividad sea del 85 % para longitudes de onda de 420 nm.

2.1.1.g El calorímetro electromagnético (ECAL)

El calorímetro electromagnético [59] proporciona una medida de la energía de partículas electromagnéticas a la vez que proporciona un rechazo frente hadrones.

El ECAL está formado por 9 supercapas hechas de láminas de plomo de 1 mm de espesor y fibras centelleadoras de 1 mm de diámetro con una densidad media final de $6.83 \pm 0.08\,\mathrm{g/cm}^3$. La orientación de las fibras cambia en cada supercapa para tener de esta manera una lectura bidireccional. Las fibras de cada capa son leídas por fotomultiplicadores multiánodo de 4 píxeles, los cuales están dispuestos de forma alterna en cada lado. Cada píxel cubre un área de $9\times9\,\mathrm{mm}^2$ y 35 fibras, lo cual defina la región llamada celda y divide el calorímetro en 18 capas. Esto permite que el perfil longitudinal de la cascada electromagnética sea muestreado por 18 medidas independientes.

El calorímetro tiene un gran rango dinámico, ya que debe detectar señales que van desde los pocos photoelectrones de las partículas de mímina ionización, a los aproximadamente 10^5

fotoelectrones de las cascadas electromagnéticas en el rango de los TeV. Por lo tanto la electrónica está diseñada con dos ganancias y un ratio de alta a baja ganancia de 33 en media.

Se ha medido una resolución en energía de 2.5–3 % para electrones de 100–300 GeV, una resolución angular de $\sim 1^\circ$ y un fator de rechazo frente hadrones de $\sim 10^4$ para $E < 1\,\mathrm{TeV}$ [59, 60].

2.1.2 La configuración con imán permanente

Después de la pruebaz de haz de febrero de 2010, AMS-02 se transladó al centro europeo de tecnología e investigación espacial (ESTEC), situado en Noordwijk (Países Bajos). Durante marzo y abril de 2010, AMS-02 pasó una prueba térmica de vacío en el gran simulador espacial. Los resultados de la prueba situaban la vida del imán superconductor en 28 ± 6 meses [61].

El 11 de marzo de 2010, las agencias espaciales que participan en la ISS anunciaron sus intenciones de prolongar la vida de la ISS hasta el año 2020 como mímino, retrasando la reentrada en la atmośfera terrestre que estaba programada para el año 2015. Este hecho, junto con la duración del imán superconductor y la cancelación del programa de transbordadores espaciales de la NASA, constituyó el punto de inflexión para un nuevo escenario donde el imán superconductor fue replazado por el imán permanente de AMS-01. Esta nueva configuración se probó con un haz de protones, electrones y positrones en agosto de 2010.

2.1.2.a El imán permanente

El imán permanente tiene una forma cilíndrica, con una longitud de 80 cm, un diámetro interior de 111.5 cm y uno exterior de 129.8 cm. Consta de 64 sectores de Nd–Fe–B y cada sector está compueseto de 100 bloques (5.08 cm × 5.08 cm × 2.54 cm). El campo magnético es directamente ortogonal al eje longitudinal del cilindro y la densidad de flujo magnético en el centro geométrico tiene un valor de 0.15 T. El campo fuera del imán a una distancia de 2 m desde el centro del imán es menor de 3 G [1].

Después del vuelo de AMS-01 en junio de 1998, el imán se almacenó en una sala limpia. Las medidas del campo realizadas en 1997 y en abril de 2010 concuerdan dentro del 1 % de precisión del aparato de medida, lo que verifica la estabilidad en el tiempo del campo magnético.

Aunque el imán permanente tenga un campo magnético 5 veces inferior al del imán superconductor, éste tiene una vida ilimitada. Además, el menor poder de curvatura se puede compensar con una configuración diferente de los planos del detector de trazas.

2.1.2.b El detector de trazas de silicio

La nueva configuración de los planos del detector de trazas amplía el brazo de palanca al transladar el primer plano encima del TRD y la colocación de un nuevo plano entre el RICH y el ECAL. Esta nueva configuración hace posible que la rigidez máxima detectable (MDR [2]) de AMS-02 no se vea afectada (2.14 TV para protones y 3.75 TV para nucleos de He) [61].

2.1.2.c La actualización y mejora de AMS-02

Las modificaciones realizadas en AMS-02 para alargar la vida del experimento en la ISS no afectan a la aceptancia de AMS-02 en la mayoría de los estudios de física, incluyendo la búsqueda

[1] 1 T=10000 G.

[2] La MDR se corresponde con un error en la medida de la rigidez del 100 %.

de materia oscura, para partículas con una rigidez de hasta 400 GV. Por encima de este valor y hasta los 2.2 TV, la aceptancia se reduce por un factor entre 1.5 y 2 [62]. Sin embargo, la precisión estadística se recupera al tener un mayor tiempo de exposición.

Para asegurar la funcionabilidad de AMS-02 a lo largo de la vida útil de la ISS se han hecho evaluaciones a todos los componentes, incluyendo [62]:

- La vida útil del los tubos de deriva del TRD. La tasa de fuga del CO_2 es de unos 5 µg/s para todo el TRD. Un tanque relleno de 5 kg de CO_2 instalado en el TRD asegura una vida útil de 30 años.
- La vida útil del imán. A partir de las medidas del campo magnético que arrojaron una degradación dentro del margén del 1 % en 12 años, se infiere que el campo permanecerá igual por los siguientes 20 años.

El cambio de imán trae consigo además una redución en el campo magnético residual al que están expuestos los diferentes subdetectores, lo cual beneficia a su rendimiento. Además, con la ausencia del sistema criogénico y el tanque de helio, AMS-02 es técnicamente más sencillo.

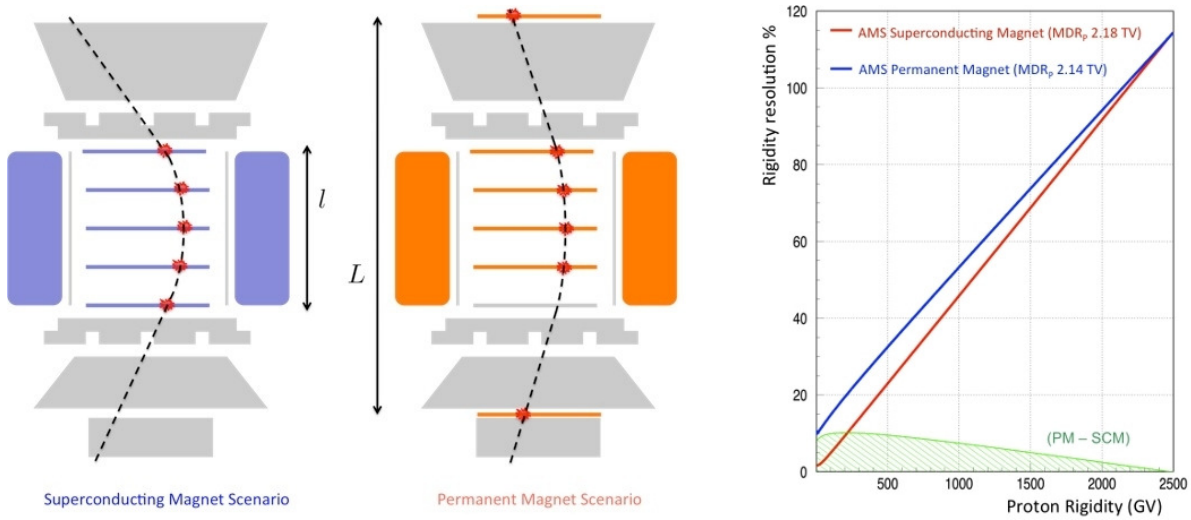

(a) (b)

Figura 2.2: *Vista esquemática de las configuraciones del detector de trazas con el imán superconductor y permante (figura 2.2(a)). Resolución en la rigidez de la configuración con imán superconductor (rojo), de la configuración con imán permanente (azul) y la diferencia entre ambas (verde) (figura 2.2(b)).*

2.2 Identificación de partículas con AMS-02

Para poder identificar una partícula es necesario deteminar su masa y su carga eléctrica. La desviación de la trayectoria de una partícula con un radio de curvatura r en un campo magnético B, se puede determinar usando un detector de trazas para medir la rigidez R ($R = rBc$). Una vez la rigidez es conocida, el momento se puede calcular a partir de la ecuación:

$$p = ZeR \tag{2.1}$$

si la carga Ze se ha medido. El valor absoluto de la carga se puede determinar a partir de la energía perdida por ionización en partes activas del dectector o con un detector Cherenkov. Por otra parte, el signo de la carga se puede obtener a partir del signo de la curvatura junto a la dirección de la partícula proporcionada por el TOF. Finalmente, si la velocidad β ha sido también medida, la masa de las partícula se puede calcular a partir de la ecuación

$$p = mc\gamma\beta \tag{2.2}$$

donde la velocidad se puede medir a través del tiempo de vuelo o a partir del ángulo Cherenkov.

AMS-02 mide el signo y el valor absoluto de la carga, la velocidad y la rigidez de las partículas. Además, para reducir la probabilidad de errar en la identificación, la velocidad y el valor absoluto de la carga es proporcionado por varios subdetectores. La velocidad se mide con el TOF y el RICH. El valor absoluto de la carga se mide con el TOF, el detector de trazas y el RICH. Además el TOF puede distinguir partículas que van hacia arriba de las que van hacia abajo. La inclusión del ECAL y del TRD propociona una separación electrón/protón.

2.3 El software de AMS

El software de AMS proporciona al experimento las herramientas necesarias para simular la respuesta del detector al paso de las partículas y para reconstruir los sucesos almacenados:

- El software de simulación está basado en el paquete GEANT [63], el cual hace uso de la geometría del detector para simular la energía depositada y las interacciones de las partículas en los diferentes subdetectores.
- El software de reconstrucción, que puede ser alimentado con datos reales o simulados, procesa los sucesos almacenados para generar un fichero de salida en formato ROOT con una serie de objetos C++. Por lo tanto, la forma más directa para analizar estos ficheros de datos, es usar el lenguaje C++ dentro del entorno ROOT [64].

2.3.1 Reconstrucción de sucesos

El primer paso en la cadena de reconstrucción es el de la búsqueda de señales en los datos sin procesar de los diferentes subdetectores, es decir, canales de lectura por encima de un umbral, para así poder identificar patrones. Estos patrones son almacenados en un objeto C++ con la información pertinente y usada a continuación para identificar otros patrones a un nivel superior y específicos para cada subdetector. El resultado es unos datos procesados que están organizados de forma jerárquica (figura 2.3 [65]), lo que permite por ejemplo, volver a reconstruir la información de más alto nivel a partir de la información de más bajo nivel [65, 66].

Una vez se han reconstruído las estructuras de más alto nivel para cada subdetector, `TrdTrackR` para el TRD, `TrTrackR` para el detector de trazas, `RichRingR` para el RICH y `EcalShowerR` para el ECAL, otras estructuras son construídas, `BetaR`, `ChargeR`, `ParticleR` y `AMSEventR`:

- El objeto `BetaR` contiene la velocidad de la partícula reconstruída usando información del TOF y la longitud de `TrTrackR`.
- El objeto `ChargeR` contiene el valor absoluto de la carga de la partícula reconstruída a partir del TOF, del detector de trazas y del RICH.

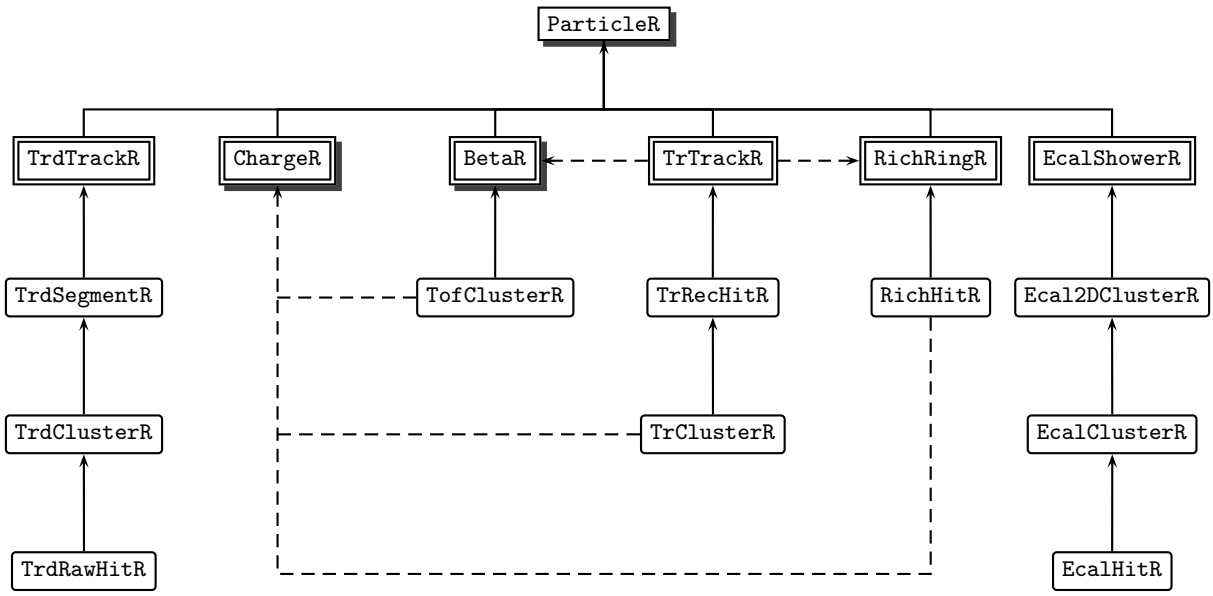

Figura 2.3: *Diagrama de arbol simplificado de las jerarquías entre los objetos C++ dentro de un suceso reconstruído.*

- El objeto `ParticleR` es la estructura de más alto nivel de la reconstrucción, la cual contiene información acerca de la velocidad, la carga, el momento y la masa de la partícula.
- El objeto `AMSEventR` con el que se tiene acceso a todas las estructuras de datos.

3

Prestaciones de AMS-02 en la separación e/p

El objetivo de este trabajo es la obtención de la señal de positrones cósmicos utilizando una simulación Monte Carlo (MC) del detector en su configuración de vuelo. Para validar tal estudio se dispone de los datos tomados en la prueba de haz de febrero de 2010 con la configuración del imán superconductor, los datos tomados en la prueba de haz de agosto de 2010 con la configuración del imán permanente y la propia simulación MC. Los datos que se han tomado como referencia en este trabajo son los pertenecientes a la prueba de haz de febrero de 2010, ya que fueron tomados con unas configuraciones específicas de la posición del detector respecto al haz para el estudio del calorímetro. La tabla 3.1 resume las tres muestras de datos utilizadas en este trabajo.

TABLA 3.1: *Muestras de datos utilizadas en este trabajo.*

Muestra	**Partícula**	**Energía (GeV)**	**Número de sucesos**
TB febrero	Electrón	180	4.6×10^6
		250	1.2×10^7
		300	2.7×10^6
	Protón	400	1.8×10^6
TB agosto	Electrón	180	4.4×10^6
	Protón	400	2.1×10^7
MC	Electrón	180	4.0×10^4
		250	2.3×10^5
		300	4.0×10^5
	Protón	400	8.0×10^5

3.1 El calorímetro electromagnético

El calorímetro electromagnético proporcionada una separación electrón/protón (e/p) necesaria para reducir el fondo de protones cósmicos. Los datos tomados en la prueba de haz llevada

a cabo en febrero de 2010 con el detector con imán supercorductor se han usado para desarrollar un método de calibración del calorímetro así como obtener las prestaciones del mismo en la separación e/p.

3.1.1 Calibración del calorímetro electromagnético

El método de calibración desarrollado en este trabajo parte de una calibración de referencia realizada con partículas de mínima ionización (MIPs), para realizar a posteriori una calibración con cascadas electromagnéticas. En análisis previos ya se han utilizado cascadas electromagnéticas para ecualizar la respuesta de los canales del calorímetro [67], aunque la implementación utilizada en el método desarrollado en este trabajo difiere de las anteriores.

3.1.1.a Calibración de referencia con partículas de mínima ionización

Las partículas hadrónicas que no desarrollan una cascada atraviesan el calorímetro como partículas de mínima ionización. Para la selección de MIPs se ha utilizado tanto el haz de protones como el haz de electrones, ya que este último presenta una contaminación de piones. Los cortes que se han aplicado son los siguientes:

1. Sucesos con prácticamente toda la energía en el eje de la cascada [1].
2. Sucesos con una baja multiplicidad en el número de señales usadas por capa [2].

La muestra de sucesos seleccionados como MIPs supone el 66.6 % de la preselección, con una energía media de 460 MeV y 14 señales usadas (figura 3.1).

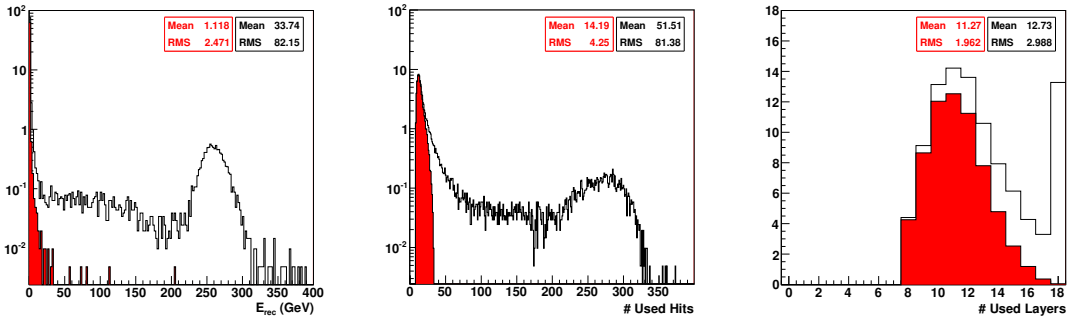

(a) (b) (c)

Figura 3.1: *Distribuciones normalizadas de la energía reconstruída (figura 3.1(a)), del número de señales usadas(figura 3.1(b)) y del número de capas con señales usadas (figura 3.1(c)) para una muestra del haz de electrones y donde las distribuciones en rojo muestran la selección de MIPs (RunId 1265493420, Tag 01c6, 250 GeV).*

La respuesta del calorímetro no es la misma para partículas que inciden en diferentes posiciones a los largo de las fibras debido a la atenuación de la luz en las mismas. Por lo tanto, para verificar la ecualización existente de los canales realizada con MIPs, es necesario verificar

[1] Corte aplicado: `Energy3C[0]` > 0.999, variable reconstruída de `EcalShowerR` que almacena la energía depositada en un cilindro de 2 cm de radio.

[2] Corte aplicado: `Hits/Plane` < 2

también la implementación de la corrección por atenuación en la reconstrucción. Esta atenuación se parametriza con una doble exponencial, ya que existen dos longitudes de atenuación, larga y corta. La corrección final se normaliza al centro de la fibra y se tiene en cuenta tanto la componente directa de la luz como la reflejada.

Para verificar la implementación de esta corrección en la reconstrucción, la señal en cuentas ADC (sin procesar y corregida) de los diferentes canales a lo largo de las fibras se puede ajustar a una línea recta en primera aproximación (figura 3.2). La pendiente de este ajuste da una idea de la bondad de la corrección, ya que cuando el ajuste se realiza sobre las cuentas ADC sin procesar, existen dos conjuntos de pendientes, negativas y positivas (figura 3.3(a)), que tan sólo reflejan la estructura mecánica del calorímetro, ya que los fotomultiplicadores están colocados de forma alterna, mientras que cuando el ajuste se realiza sobre la cuentas ADC corregidas la distribución de las pendientes del ajuste está centrada en cero con una anchura del 4 % (figura 3.3(b)), lo que valida la corrección por atenuación en MIPs.

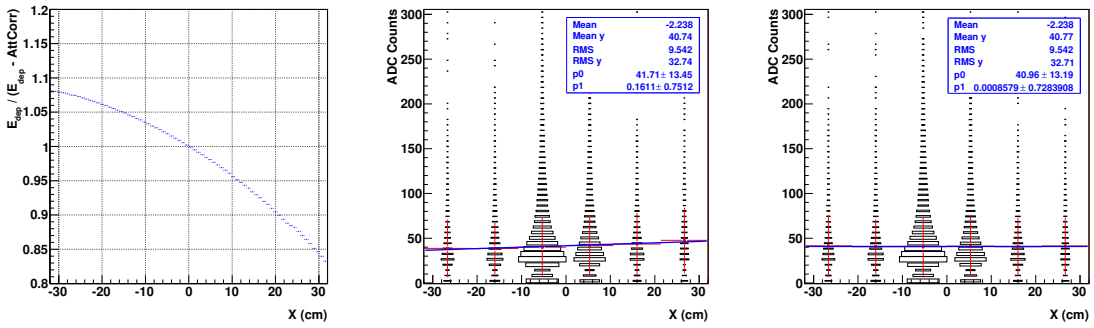

(a) (b) (c)

Figura 3.2: *Función de corrección de la atenuación aplicada en la reconstrucción (figura 3.2(a)). Cuentas ADC sin procesar ajustadas a una línea recta (figura 3.2(b)). Cuentas ADC corregidas (figura 3.2(c)) para un canal particular usando la media de la distribución.*

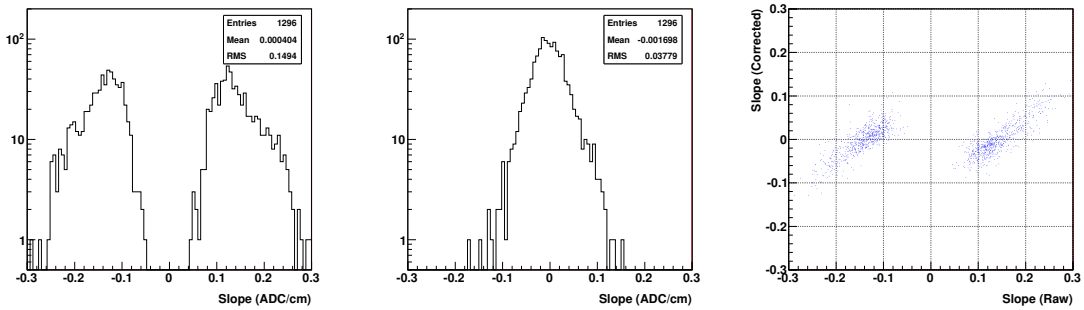

(a) (b) (c)

Figura 3.3: *Distribución de las pendientes que se obtienen a partir del ajuste de las cuentas ADC sin procesar (figura 3.3(a)) y a partir del ajuste de las cuentas ADC corregidas (figura 3.3(b)). Una distribución frente a otra (figura 3.3(c)), usando la media de la distribución.*

Las partículas de mínima ionización se utilizan para ecualizar los canales en alta ganancia. La distribución de la señal en cuentas ADC de todos los canales se ajusta a una función Landau, siendo el valor más probable (MPV) del ajuste la referencia utilizada en la ecualización de los canales. La distribución de los valores más probables de los 1296 canales tiene una media de 28 cuentas ADC y una anchura del 17 % (figura 3.4(a)), debido a la dispersión intrínsica en cada fotomultiplicador. Cada canal tiene su propio factor de calibración que convierte las cuentas ADC en energía depositada, los factores de calibración extraídos del software de reconstrucción tienen un valor medio de 0.48 MeV/ADC (figura 3.4(b)). Esto hace que cuando se ajusta a una Landau la distribución en energía de todos los canales, la distribución de los valores más probables tenga un valor medio de 13 MeV y una anchura de 3 % (figura 3.4(c)), lo que demuestra que la mayoría de los canales están bien ecualizados y tan sólo unos pocos (16 canales con MPV(canal) $> \langle MPV \rangle + 4\sigma$) precisarían de una recalibración. Por último, si los MPV[MeV] se dividen por los MPV[ADC] se obtienen unos factores de calibración en buen acuerdo con los de la reconstrucción (figura 3.4(b)).

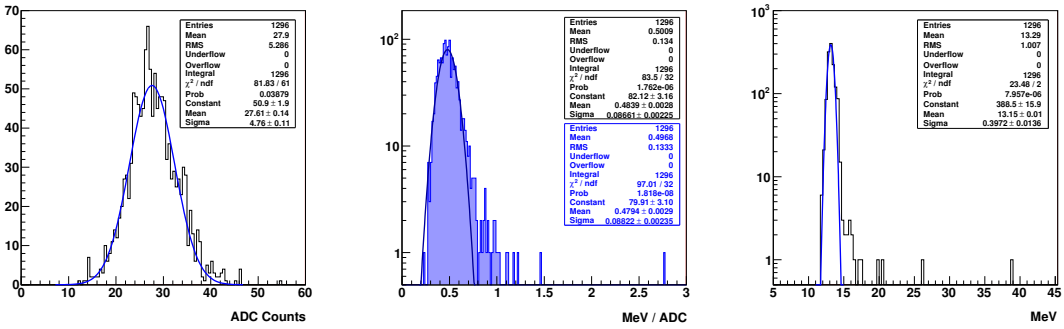

(a) (b) (c)

Figura 3.4: *Distribución de los valores más probables de todos los canales en cuentas ADC (figura 3.4(a)). Distribución de los factores de calibración que se obtienen a partir del análisis (figura 3.4(b)) con la caja de estadística en azul, mientras que la caja negra hace referencia a los factores de calibración del software de reconstrucción. Distribución de los valores más probables de todos los canales en MeV (figura 3.4(c)).*

3.1.1.b Calibración con cascadas electromagnéticas

La calibración absoluta que proporcionan las partículas de mínima ionización ecualiza los canales en alta ganancia. Cuando la señal en alta ganancia se satura, se utiliza la señal en baja ganancia, siendo el ratio entre ambas de aproximadamente 33.

La gran ventaja de las partículas de mínima ionización es que depositan la misma energía en todas las celdas y capas a los largo de su trayectoria. Sin embargo, esta energía difiere en tres órdenes de magnitud con la energía depositada por un electrón de 250 GeV en el eje de la cascada y en las capas centrales del calorímetro. Por lo tanto, se pueden utilizar cascadas electromagnéticas para realizar una calibración posterior. Para ello se debe tener en cuenta tanto el perfil transversal de la energía, que obliga a usar tan sólo la energía depositada por el eje de la cascada, como el perfil longitudinal de la energía, que obliga a ecualizar las diferentes capas de forma independiente. La calibración realizada con cascadas electromagnéticas consta de cuatro pasos, que son la revisión de la corrección por atenuación en las fibras, la ecualización

de las celdas, la implementación de la corrección por punto de impacto dentro de la celda y la revisión de la corrección por pérdidas traseras.

Selección de cascadas electromagnéticas El haz de electrones contiene una contaminación de piones, por lo que se necesita aplicar un conjunto de cortes para seleccionar la señal de electrones:

1. **Máximo de la cascada** (*ShowerMax*). El máximo del perfil longitudinal de la energía de una cascada electromagnética es proporcional al logaritmo natural de la energía de la cascada. El corte aplicado [3] en el máximo de la cascada tiene esta dependencia logarítmica con la energía reconstruída. Los resultados del corte para un haz de electrones de 250 GeV se puede ver en la figura 3.5(a).

2. **Pérdidas longitudinales** (*RearLeak*). La cascada puede no estar contenida completamente en el calorímetro, por lo que la energía faltante se debe estimar [67] para obtener la energía de la partícula incidente. El corte aplicado [4] en la fracción de energía faltante tiene una dependencia logarítmica con la energía reconstruída. Los resultados para electrones de 250 GeV se pueden ver en la figura 3.5(b).

3. **Energía por señal** (*Energy/Hit*). La equipartición de la energía de la cascada electromagnética entre el número de señales de la cascada tiene una dependencia lineal con la energía, incluso cuando las señales con decenas de MeV son excluídas. La exclusión de señales con energía inferior a 52 MeV significa un reducción del 50 % en la multiplicidad de señales pero solo un 1.5 % de reducción en la energía de la cascada. El corte aplicado [5] en la variable de energía por señal tiene una dependencia lineal con la energía reconstruída. Los resultados para electrones de 250 GeV se puede ver en la figura 3.5(c).

4. **Tamaño transversal de la cascada** (*Moliere*). Las variables de forma de la cascada relacionadas con el perfil transversal de la energía se utilizan para identificar las cascadas electromagnéticas, ya que por ejemplo, el 90 % de la energía de una cascada electromagnética se encuentra dentro de un cilindro alrededor del eje de la cascada de un radio de Moliere. El corte aplicado [6] en la energía contenida en un cilindro de 2 cm de radio alrededor del eje de la cascada no depende de la energía. Los resultados para electrones de 250 GeV se pueden ver en la figura 3.5(d).

5. **Acuerdo entre la energía y el momento** (*EPMatch*). Además del conjunto de corte electromagnéticos, *ShowerMax*, *RearLeak*, *Energy/Hit* and *Moliere*, la energía reconstruída por el calorímetro debe ser compatible con el momento reconstruído de la partícula medido por el detector de trazas. El corte aplicado [7] en el ratio $E/|P|$ es independiente de la energía. Los resultados para electrones de 250 GeV se pueden ver en la figura 3.5(e).

[3] $\log(E(\text{MeV})/a_0) - a_1 - a_2 \cdot E^{-a_3}(\text{GeV}) < \textit{ShowerMax} < \log(E(\text{MeV})/b_0) + b_1 + \exp(b_2 - b_3 \cdot E(\text{GeV}))$, donde los parámetros del corte han sido ajustados usando muestras Monte Carlo a los valores $a = \{a_0, a_1, a_2, a_3\} = \{7.803, 3.61, 2.55, 0.71\}$ y $b = \{b_0, b_1, b_2, b_3\} = \{32.66, 2.143, 1.727, 0.242\}$.

[4] $\textit{RearLeak} < a_0 + a_1 \cdot \log(E(\text{GeV}))$, donde el valor de los parámetros $a = \{0.1, 0.0195\}$ se han obtenido a partir de los datos de la prueba de haz.

[5] $\textit{Energy/Hit} > a_0 + a_1 \cdot E(\text{GeV})$, donde el valor de los parámetros $a = \{9.3147 \times 10^{-2}, 2.538 \times 10^{-3}\}$ se han obtenido a partir de los datos de la prueba de haz.

[6] $\text{Energy}_{\pm 2\,\text{cm}}/\text{TotalEnergy} > 0.955$, donde el valor del parámetro se ha obtenido a partir de los datos de la prueba de haz.

[7] $E/|P| > 0.8$, donde el valor del parámetro se ha obtenido a partir de la simulación MC.

Se considera señal a los sucesos dentro de un rango de energía, una vez substraído un fondo exponencial en esa región, y fondo a los sucesos fuera de ese rango. El conjunto de cortes tiene una eficiencia para la señal de 77 % y de 0.07 % para el fondo usando electrones de 250 GeV con incidencia normal (figura 3.5(f)).

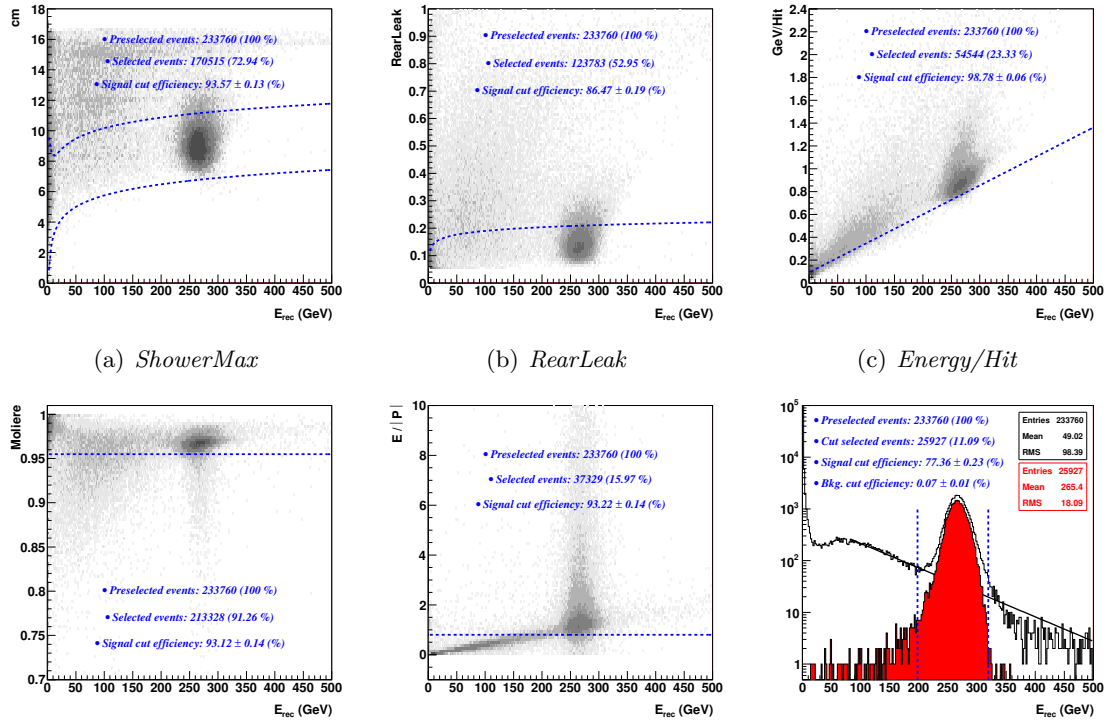

(a) *ShowerMax* (b) *RearLeak* (c) *Energy/Hit*

(d) *Moliere* (e) *EPMatch* (f)

Figura 3.5: *Dependencia de la variable de corte con la energía reconstruída, donde la línea azul de puntos representa el valor de corte (figuras 3.5(a), 3.5(b), 3.5(c), 3.5(d) y 3.5(e)). Distribución de la energía reconstruída de la muestra preseleccionada (negro) y de los sucesos después de la secuencia de cortes ShowerMax + RearLeak + Energy/Hit + Moliere + EPMatch, donde la línea azul de puntos define la señal (figura 3.5(f)).*

Corrección por atenuación Para comparar la energía depositada en una misma celda en diferentes longitudes de la fibra se han utilizado posiciones del haz que comparten una misma coordenada, ya sea en x o en y ($\{x_1 = x_2, y_1 = -y_2\}$ o $\{x_1 = -x_2, y_1 = y_2\}$). Las diferencias en energía en las celdas más alejadas al centro del calorímetro pueden alcanzar valores de hasta el 40 %, descendiendo hacia el centro del calorímetro (figura 3.6(a)). Por el contrario, la simulación MC no exhibe tal comportamiento (figura 3.6(b)).

Si la energía de la corrección por atenuación α se escribe como una fracción de la energía sin corrección por atenuación E^0

$$\alpha = \kappa \cdot E^0 \tag{3.1}$$

donde κ es una constante para una posición fija a lo largo de la fibra, la energía depositada en la misma celda en dos posiciones del haz opuestas debe ser igual

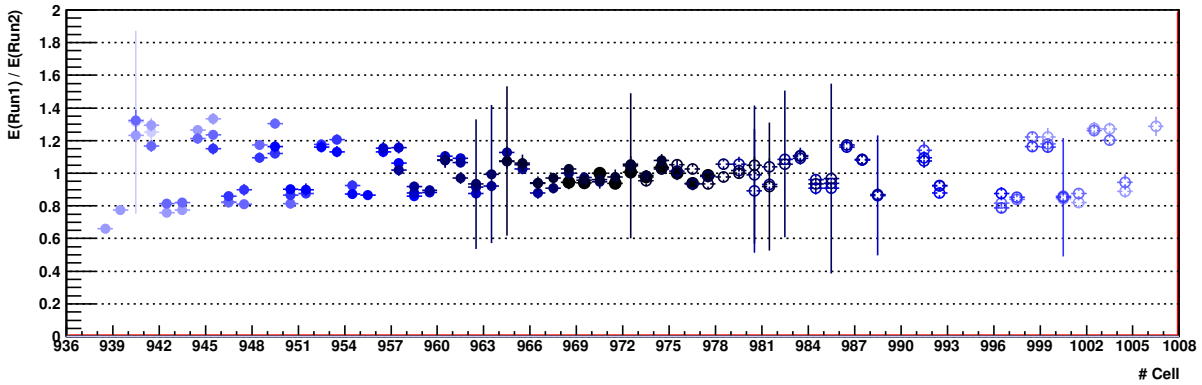

(a) Datos

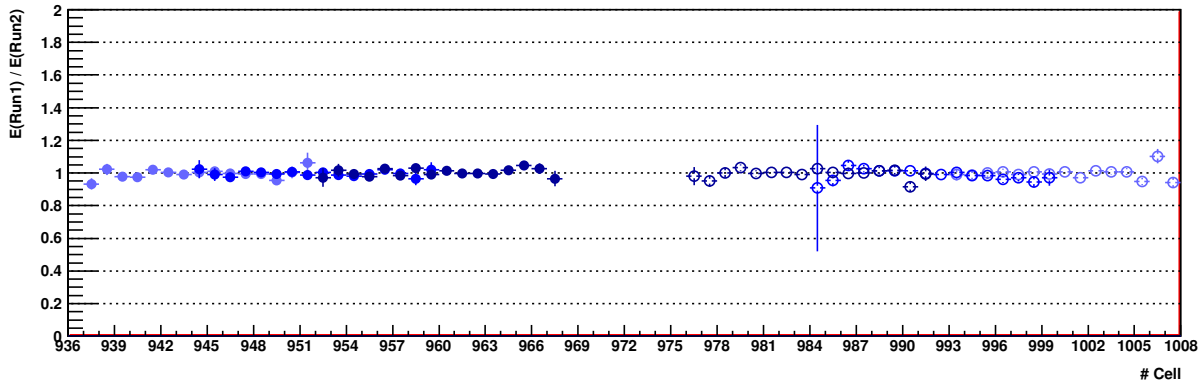

(b) MC

Figura 3.6: *Cociente de las energías depositadas en una misma celda para posiciones del haz opuestas, utilizando datos de la prueba de haz (figura. 3.6(a)) y simulación MC (figura 3.6(b)) para la capa 13.*

$$E_1^0 + f \cdot \alpha_1 = E_2^0 + f \cdot \alpha_2 \quad \Rightarrow \quad E_1^0(1 + \kappa_1 \cdot f) = E_2^0(1 + \kappa_2 \cdot f) \tag{3.2}$$

donde f es un factor de amplificación, y los subíndices $1, 2$ significan posición 1 y posición 2. Definiendo la variable δ como

$$\delta \equiv \frac{1 + \kappa_1 \cdot f}{1 + \kappa_2 \cdot f} = \frac{E_2^0}{E_1^0} \quad ; \quad \frac{\sigma(\delta)}{\delta} = \sqrt{\frac{\sigma^2(E_1^0)}{(E_1^0)^2} + \frac{\sigma^2(E_2^0)}{(E_2^0)^2}} \tag{3.3}$$

la amplificación f se puede escribir como

$$f = \frac{\delta - 1}{\kappa_1 - \delta \cdot \kappa_2} \quad ; \quad \frac{\sigma(f)}{f} = \sigma(\delta) \left[\frac{\kappa_1 - \kappa_2}{(\kappa_1 - \delta\kappa_2)(\delta - 1)} \right] \tag{3.4}$$

Las figuras 3.7(a) y 3.7(b) muestran el factor de amplificación de todas las capas para datos y MC respectivamente, lo que confirma la necesidad de una recorrección por atenuación usando un factor de amplificación para cada capa (figura 3.8). Además, de la figura 3.7(a) se deduce que existe un mismo comportamiento de las fibras al nivel de supercapa, que tiene su origen al pertenecer éstas a diferentes partidas de fabricación.

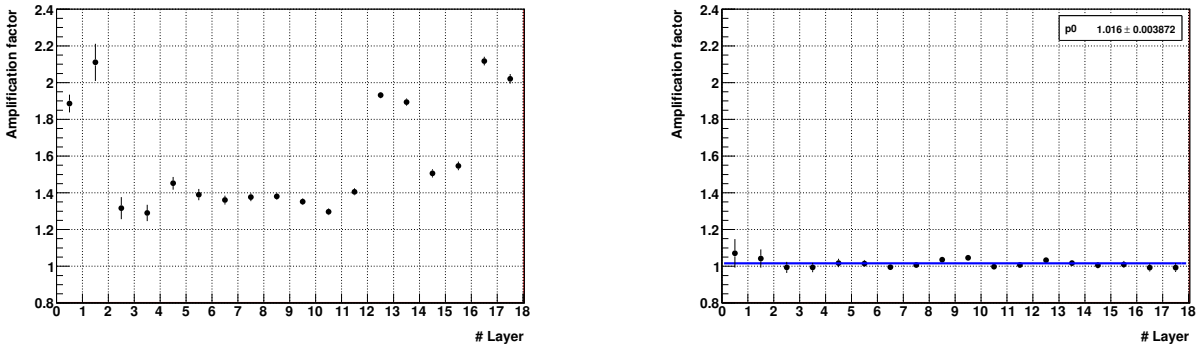

(a) Datos (b) MC

Figura 3.7: *Factores de amplificación para todas la capas, usando datos de la prueba de haz (figura 3.7(a)) y simulación MC (figura 3.7(b))*

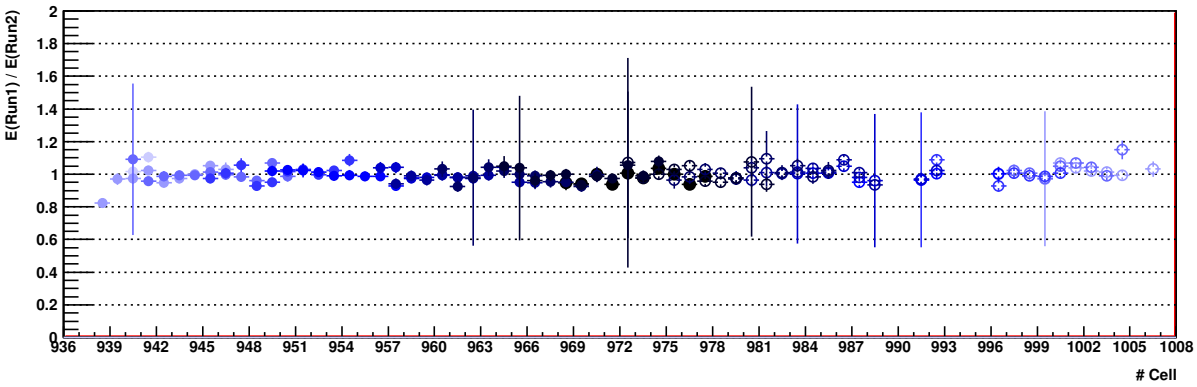

Figura 3.8: *Cociente de las energías depositadas en una misma celda para posiciones del haz opuestas, usando datos de la prueba de haz después de aplicar el factor de amplificación para la capa 13.*

Ecualización de las celdas Una vez la atenuación ha sido recorregida, cualquier posición del haz puede ser usada para ecualizar las celdas del calorímetro. Los valores de la energía depositada por el eje de la cascada en cada capa se pueden obtener utilizando diferentes muestras:

- Todas las celdas con la estadística acumulada por todas las posiciones del haz.
- Celdas en el centro del haz para posiciones individuales.
- Celdas a 2 cm a la derecha del centro del haz para posiciones individuales.
- Celdas a 2 cm a la izquierda del centro del haz para posiciones individuales.

Las figuras 3.9 y 3.10 muestran que la energía de las celdas en los datos de la prueba de haz necesitan una ecualización, mientras que la simulción MC está bien ecualizada. En todas las muestras utilizadas, la energía media de las celdas se ajusta a una línea recta una vez excluidas del ajuste las celdas que puedan introducir un sesgo.

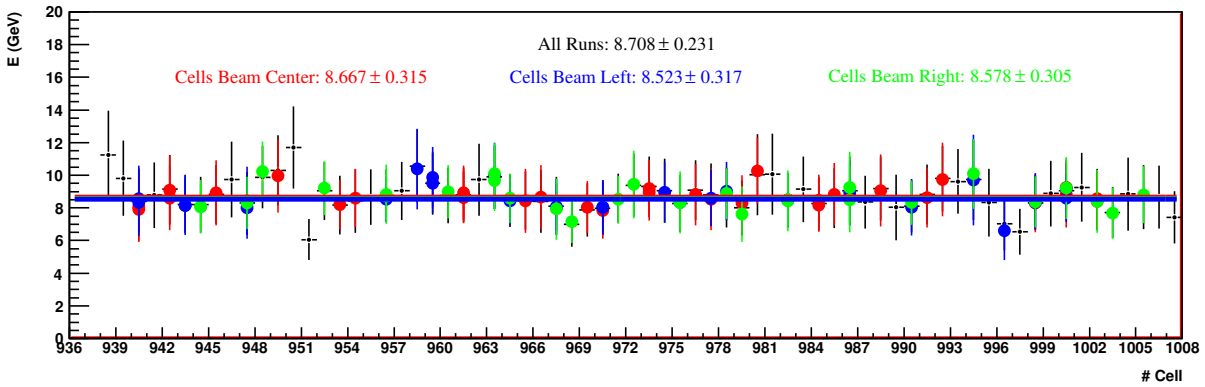

Figura 3.9: *Energía depositada por el eje de la cascada en las celdas de la capa 13, usando toda la estadística (negro), celdas en el centro del haz para posiciones individuales (rojo), celdas a 2 cm a la derecha del centro del haz (verda) y celdas a 2 cm a la izquierda del centro del haz (azul). Datos de la prueba de haz.*

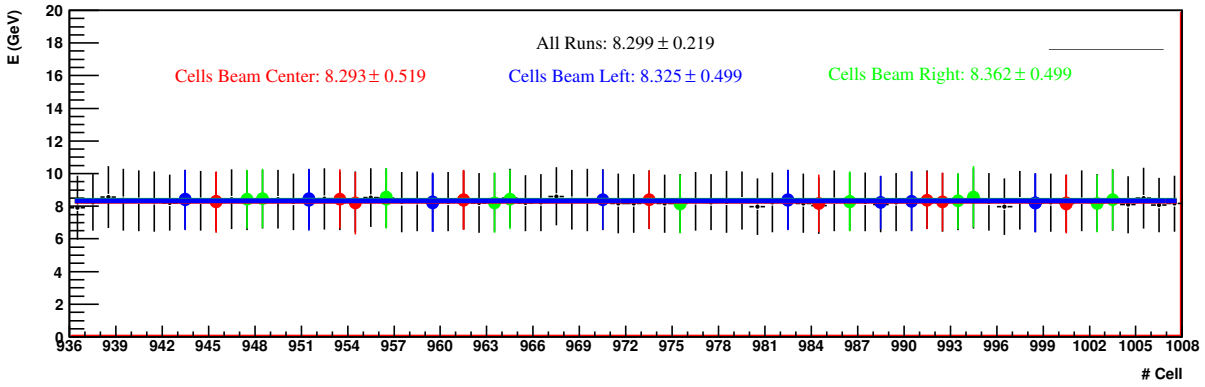

Figura 3.10: *Energía depositada por el eje de la cascada en las celdas de la capa 13, usando toda la estadística (negro), celdas en el centro del haz para posiciones individuales (rojo), celdas a 2 cm a la derecha del centro del haz (verda) y celdas a 2 cm a la izquierda del centro del haz (azul). Simulación MC.*

Los valores de la energía que se obtienen en cada capa se representan en la figura 3.11 para todas las muestras. Los resultados de las diferentes muestras son compatibles entre sí (figura 3.12(a)), por lo que los valores utilizados para ecualizar las celdas son las energías medias que se obtienen con toda la estadística.

Los factores de corrección (figura 3.12(b)) se calculan como el cociente entre la energía media de cada capa y la energía individual de cada celda (Factores de corrección $= E(Capa)/E(Celda)$).

Para comprobar que el método utilizado para ecualizar la energía de las celdas se puede aplicar a un caso más general de toma de datos, se han obtenido los factores de corrección para un haz de electrones de 250 GeV a 5°,10° y 15°, de tal forma que los valores respectivos que se obtienen, se mantienen estables dentro del 4 % (figura 3.13), lo que confirma que el método no se limita a sucesos con incidencia normal y asegura su uso hasta al menos los 10° sin apenas desviaciones en el valor medio (figura 3.13(d)).

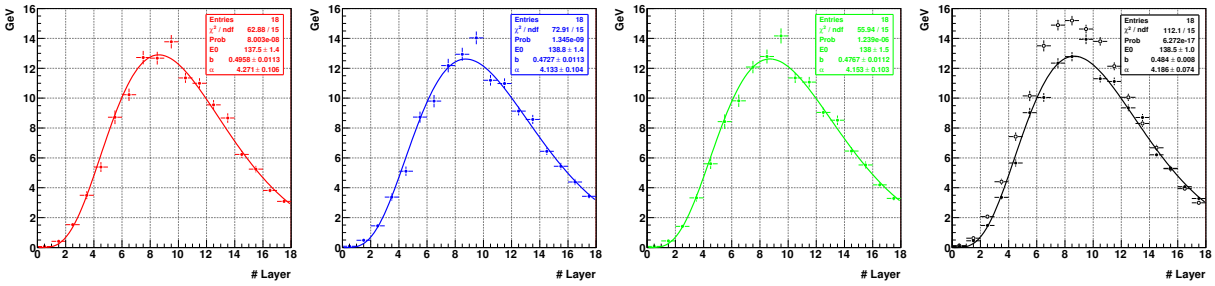

(a) Centro haz (b) Izquierda haz (c) Derecha haz (d) Todos sucesos

Figura 3.11: *Valores de energía de cada capa que se obtienen usando celdas en el centro del haz para posiciones individuales (figura 3.11(a)), celdas a 2 cm a la izquierda del centro del haz (figura 3.11(b)), celdas a 2 cm a la derecha del centro del haz (figura 3.11(c)) y toda la estadística (figura 3.11(d)), donde los puntos negros representan los datos de la prueba de haz y los puntos huecos simulación MC.*

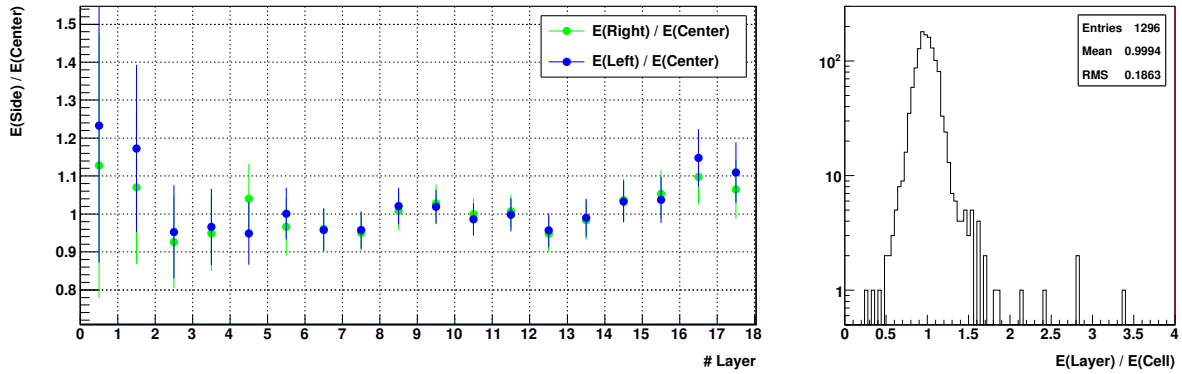

(a) (b)

Figura 3.12: *Comparación entre la energía de las celdas a la derecha y a la izquierda del centro del haz con las energías en el centro del haz (figura 3.12(a)). Distribución de los factores de corrección necesarios para ecualizar la energía en cada capa (figura 3.12(b)).*

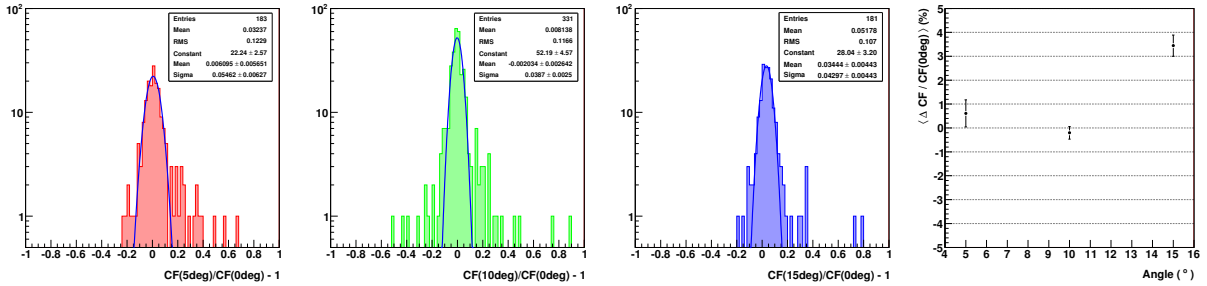

(a) (b) (c) (d)

Figura 3.13: *Comparación entre los factores de corrección se que obtienen a 0° con lo factores de corrección que se obtienen a 5° (figura 3.13(a)), 10° (figura 3.13(b)) y 15° (figura 3.13(c)).*

Corrección por punto de impacto La energía depositada es sensible al punto de impacto de la partícula dentro de la propia celda [59]. Esta dependencia en la energía se puede corregir usando el ratio S1/S3, donde S1 es la energía depositada en una celda que contiene el eje de la cascada y S3 es la energía en las celdas adyacentes más S1. Este ratio tiene una gran sensibilidad al punto de impacto y su comportamiento es el mismo para diferentes energías y ángulos (figura 3.14).

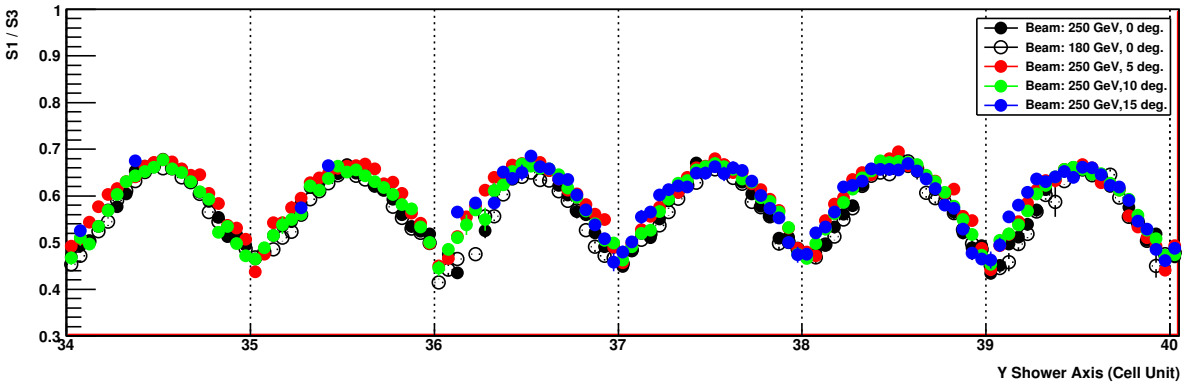

Figura 3.14: *Sensibilidad del ratio S1/S3 al punto de impacto en unidades de número de celda para diferentes energías y ángulos.*

El ratio S1/S3 se puede calcular para una vista en particular si S1 y S3 se calculan usando las capas en x e y. En la vista en x, S1/S3 tiene un valor medio de 0.68 (figura 3.15(a)), además de una dependencia con la energía (figura 3.15(b)), la cual se puede parametrizar con la función

$$p0 \cdot (\tanh(p1 \cdot x + p2) + p3) \tag{3.5}$$

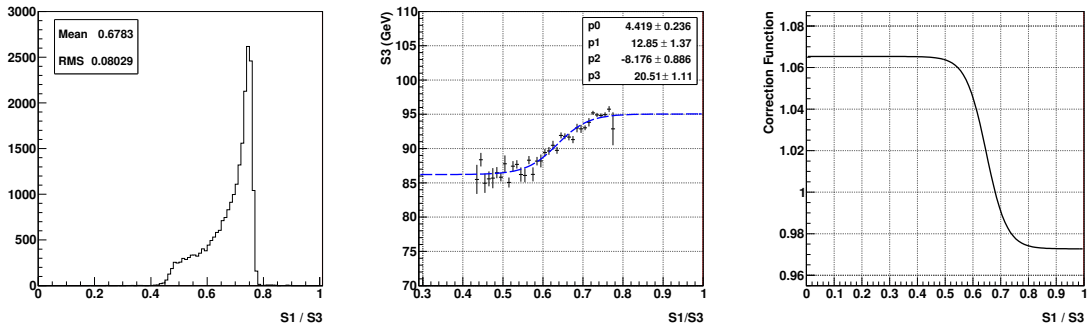

(a) (b) (c)

Figura 3.15: *Distribución de S1/S3 en la vista x (figura 3.15(a)). Dependencia de S1/S3 con la energía en la vista x (figura 3.15(b)). Función de corrección aplicada a los datos (figura 3.15(c)).*

donde $p0, \ldots, p3$ son parámetros a determinar. Los valores de $S1/S3 < 0.5$ y $S1/S3 > 0.8$ se corresponden con el mínimo y el máximo de la energía depositada respectivamente, con un diferencia de 20 GeV en electrones de 250 GeV entre la corrección mínima ($f(S1/S3) = f(0) = 1$) y la corrección máxima ($f(S1/S3) = f(1) = 1$). La función de corrección aplicada está definida

con la media de la distribución $S1/S3$ ($f(\langle S1/S3\rangle)$=1), ya que su valor es estable para al menos los electrones de 250 GeV y 180 GeV (Fig. 3.15(c)). Esta corrección se aplica a todas la capas, de tal forma que la energía de la cascada después de la corrección permanece estable con $S1/S3$ dentro del 1 % (figura 3.16).

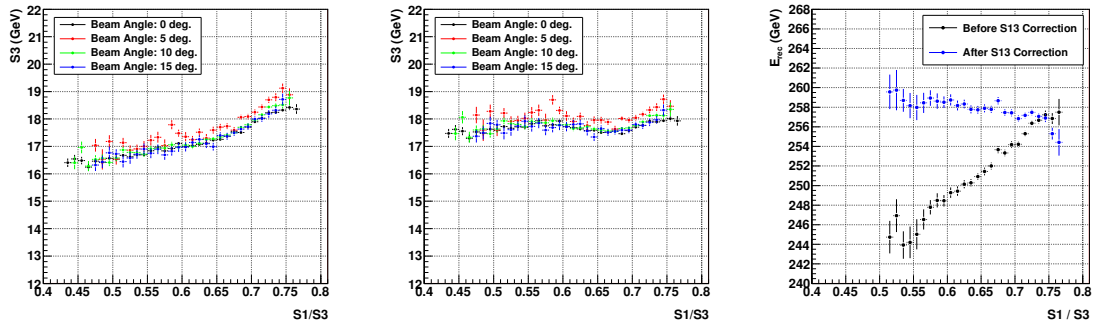

(a) Capa 11 antes de la corrección S1/S3

(b) capa 11 despúes de la corrección S1/S3

(c) Energía cascada

Figura 3.16: *Dependencia de S1/S3 con la energía antes (figura 3.16(a)) y después (figura 3.16(b)) de la corrección en la capa 11 para diferentes ángulos y energía del haz de 250 GeV. Dependencia de la energía reconstruída con $S1/S3$ antes y después de la corrección para una posición del haz con incidencia normal en el centro del calorímetro (figura 3.16(c)).*

Corrección por pérdidas traseras Las cascadas electromagnéticas no están contenidas en su totalidad en el calorímetro a las energías de la prueba de haz, por lo que se deben estimar las pérdidas de energía. La corrección por pérdidas traseras se basa en la dependencia lineal de la energía no vista con la fracción de energía depositada en la última capa [67, 68]

$$E - E_{dep} = \alpha \frac{E_{last}}{E_{dep}} \tag{3.6}$$

donde E es la energía de la partícula incidente, E_{dep} es la energía depositada en el calorímetro, E_{last} es la energía depositada en la última capa y α es una constante.

El valor medio de la energía depositada (sin pérdidas traseras) es de 225 GeV, mientras que la energía reconstruída (con pérdidas traseras) es 260 GeV, lo que significa un 86 % de energía depositada y un 14 % de pérdidas traseras en electrones de 250 GeV. Para comprobrar que la corrección está bien implementada, la energía depositada y la energía reconstruída se representan frente a la fracción de energía depositada en la última capa (figura 3.17(a) y 3.17(b)), la cual es del 4 % para electrones de 250 GeV (figura 3.17(c)). El conjunto de correcciones aplicadas a los datos resconstruídos: la recorrección de la atenuación, la ecualización de las celdas y la corrección por punto de impacto, no introduce ninguna dependencia en la energía reconstruída.

Otro método para estimar la energía faltante es utilizar el ajuste del perfil longitudinal de la energía. Los resultados para electrones de 250 GeV son 13.4 % de pérdidas traseras para un 3.9 % de energía depositada en la última capa. Por lo tanto, la corrección por pérdidas traseras se podría ajustar teniendo en cuenta el resultado del ajuste, ya que existe una dependencia lineal entre las pérdidas traseras y la energía depositada en la última capa (figura 3.17(c)).

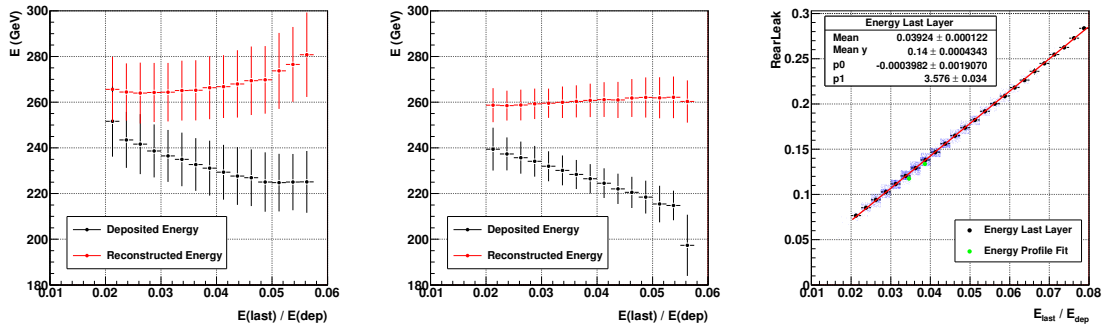

(a) Antes de correcciones (b) Después de correcciones (c)

Figura 3.17: *Dependencia de la energía depositada(sin pérdidas traseras, negro) y la energía reconstruída (con pérdidas traseras, rojo) con la fracción de la energía depositada en la última capa, antes de correcciones (figura 3.17(a)) y después de correcciones (atenuación, ecualización y punto de impacto, figura 3.17(b)). Dependiencia lineal de las pérdidas traseras con el energía depositada en la última capa, donde los puntos verdes pertenecen al ajuste del perfil longitudinal de la energía (figura 3.17(c)).*

3.1.2 Prestaciones del calorímetro electromagnético

La reconstrucción de las cascadas se realiza a partir de las celdas con señales por encima de un cierto umbral. La distribución de la ocupación de las celdas en número de señales de las figuras 3.18(a) y 3.18(b) muestra que el 100 % de las celdas estaban activas tanto en la prueba de haz de febrero como en la de agosto.

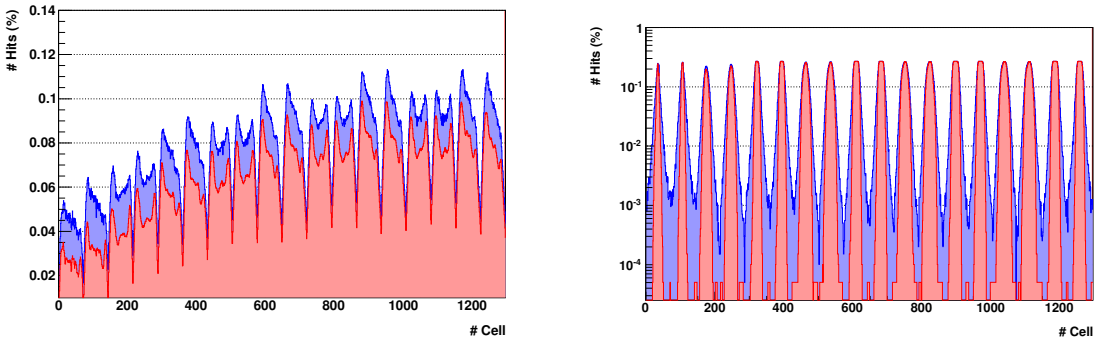

(a) (b)

Figura 3.18: *Distribución de la ocupación de las celdas en número de señales totales (azul) y usadas (rojo) para electrones de 250 GeV en la prueba de haz de febrero (figura 3.18(a)) y para electrones de 180 GeV en la prueba de haz de agosto (figura 3.18(b)). El número de celda va aumentando según se va pasando de la capa superior a la inferior.*

La fracción de señales usadas es de aproximadamente el 82 % es las últimas capas para electrones de 180 GeV, con un buen acuerdo entre datos (pruebas de haz de febrero y agosto) y simulación MC (figura 3.19(a)). Por otra parte, el número de señales totales y usadas por capa y suceso es prácticamente la misma en las pruebas de haz de febrero y agosto, pero la simulación

MC contiene unas 3 ó 4 señales menos por capa y suceso que los datos (figura 3.19(b)), lo cual es consecuencia de una menor multiplicidad en el número de señales por cluster (figura 3.19(c)).

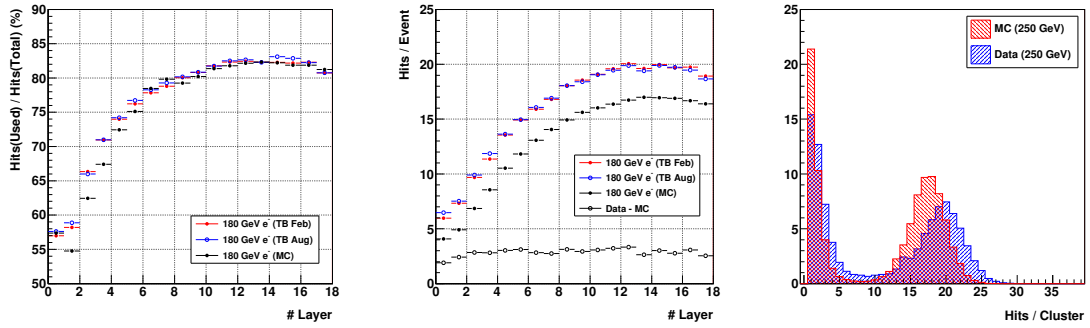

(a) (b) (c)

Figura 3.19: *Ratio de señales usadas y totales para cada capa con electrones de 180 GeV (figura 3.19(a)). Número de señales usadas por capa y suceso con electrones de 180 GeV (figura 3.19(b)) donde los puntos huecos muestran la diferencia en número de señales entre datos (febrero) y simulación MC. Distribución del número de señales por cluster (1D y usados) (figura 3.19(c)).*

3.1.2.a Resolución en energía

Si se reconstruye la energía a partir de las señales en cuentas ADC usando los factores de calibración que convierten las cuentas ADC en energía depositada (figura 3.4(b)), un ratio de alta a baja ganancia de 33.5 para todos los canales y teniendo en cuenta además el conjunto de correcciones presentadas en la calibración con cascadas electromagnéticas, es decir, los factores de amplificación de la corrección por atenuación (figura 3.7(a)), los factores de ecualización de la ganancia (figura 3.12(b)) y la corrección por punto de punto de impacto, la resolución en energía para electrones de 180 GeV en la prueba de haz de febrero es de $1.97 \pm 0.03\,\%$ (figura 3.20(a)), en buen acuerdo con la resolución en energía que se obtiene en la prueba de haz de agosto de $1.91 \pm 0.03\,\%$ (figura 3.20(b)).

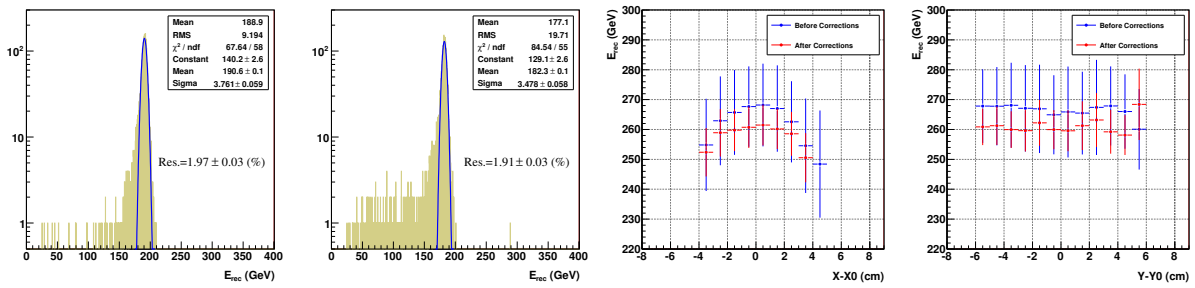

(a) Febrero (b) Agosto (c) x (d) y

Figura 3.20: *Distribución de la energía reconstruída para electrones de 180 GeV a 0° después de la calibración en la prueba de haz de febrero (figura 3.20(a)) y agosto (figura 3.20(b)). Perfil de energía del haz en la prueba de febrero para electrones de 250 GeV antes de la calibración (azul) y después de la calibración (rojo) para el eje x (figura 3.20(c)) e y (figura. 3.20(d)).*

No obstante, ambos resultados están por encima de la resolución en energía del 1.12 % que se obtiene para electrones de 180 GeV en la simulación MC, por lo que cabe preguntarse si se puede mejorar el resultado que se obtiene en datos a tenor de la estructura en el perfil del haz de energía que muestran las figuras 3.20(c) y 3.20(d), la cual permanece tras la calibración. Tomando tan sólo el centro del haz (± 1 cm), la resolución baja hasta 1.84 ± 0.03 % en febrero y a 1.63 ± 0.06 % en agosto.

3.1.2.b Separación electrón/protón

Uno de los propósitos del calorímetro es proporcionar una separación e/p para reducir el fondo de protones en los rayos cósmicos. Una vez ajustados los parámetros [8] del conjunto de cortes presentado en la sección anterior, es decir el conjunto de cortes electromagnéticos más el acuerdo entre la energía y el momento, a los datos calibrados, se obtiene una eficiencia del 0.067 % en protones de 400 GeV para una eficiencia del 75 % en electrones de 250 GeV.

Comparación con la simulación MC La comparación de los datos de la prueba de haz de febrero con la simulación Monte Carlo de la configuración con imán superconductor muestra diferencias en el perfil de energía longitudinal y en el número de señales por capa, lo que explica el desacuerdo que se observa en las cantidades electromagnéticas utilizadas para discriminar electrones de protones. Las diferencias en el perfil longitudinal de energía afectan al máximo de la cascada y a las pérdidas traseras. La discrepancia en el máximo de la cascada es compatible con un desarrollo más trempano de la cascada en el MC debido a una cantidad extra de material equivalente a 0.25 radiaciones de longitud. Este desplazamiento en el máximo de la cascada afecta a su vez a la estimación de las pérdidas traseras, ya que esta estimación depende de la energía depositada en la última capa. Si el perfil longitudinal de energía se utiliza para estimar las pérdidas traseras en lugar del método de la última capa, el porcentaje de pérdidas traseras se incrementa hasta el 13.3 % teniendo en cuenta las $0.25\,X_0$ extra, lo cual es un resultado más cercano al observado en datos. Por otra parte, las distribuciones de la equipartición de la energía (*Energy/Hit*) y de la energía contenida en un cilindro de 2 cm de radio alrededor del eje de la cascada (*Moliere*) presentan un acuerdo entre datos y MC cuando se impone un umbral en la energía de las señales ($E_{hit} > 39$ MeV), lo que supone un reducción del 45 % en el número de señales de la cascada pero tan sólo una reducción del 1 % en la energía de la cascada.

Una vez los parámetros de los cortes de selección se ajustan para acercar el valor de las eficiencias individuales de los cortes de la simulación MC a los datos, se obtiene una eficiencia total del 0.07 % en protones de 400 GeV para una eficiencia del 77 % en electrones de 250 GeV, valores muy próximos a los de la prueba de haz de febrero.

Comparación con la configuración de vuelo Teniendo en cuenta los cortes electromagnéticos presentados anteriormente (*ShowerMax*, *Rearleak*, *Energy/Hit* y *Moliere*), la eficiencia que se obtiene, normalizada a la preselección, para protones de 400 GeV en febrero (1.3 %) es similar a la que se obtiene en agosto (1.4 %) (figura 3.21) para una eficiencia en electrones de 180 GeV por encima del 80 %.

No obstante, la degradación en la resolución de momento debida al cambio del imán superconductor por el imán permanente afecta al corte del acuerdo entre la energía y el momento (*EPMatch*). Para una eficiencia prácticamente igual del 13 % para protones de 400 GeV cuando

[8] *ShowerMax*: $a = \{7.803, 3.61, 2.55, 0.71\}$, $b = \{32.66, 2.300, 1.727, 0.242\}$. *RearLeak*: $a = \{0.1, 0.0209\}$. *Energy/Hit*: $a = \{9.3147 \times 10^{-2}, 2.538 \times 10^{-3}\}$. *Moliere*: $\text{Energy}_{\pm 2\,\text{cm}}/\text{TotalEner} > 0.957$. *EPMatch*: $E/|P| > 0.9$

se usa como primer corte, la eficiencia en electrones de 180 GeV baja del 94 % en febrero al 84 % en agosto (figura 3.22). El resultado es que la eficiencia en protones difiere por una factor 3 entre ambas configuraciones, a la vez que la eficiencia en electrones se reduce al 65 % cuando el corte *EPMatch* se aplica con el conjunto de cortes electromagnéticos. La tabla 3.2 resume todas la eficiencias.

En lugar del uso de un conjunto de cortes electromagnéticos, existen métodos alternativos con los que se puede intentar maximizar la separación e/p del calorímetro, como es el análisis multivariante [69]. Usando datos reales de vuelo, existe una mejora de un factor 3 en la eficiencia para protones a 100 GV con una eficiencia del 90 % en electrones cuando el análisis multivariante se utiliza en lugar del conjunto de cortes electromagnéticos presentados en este análisis.

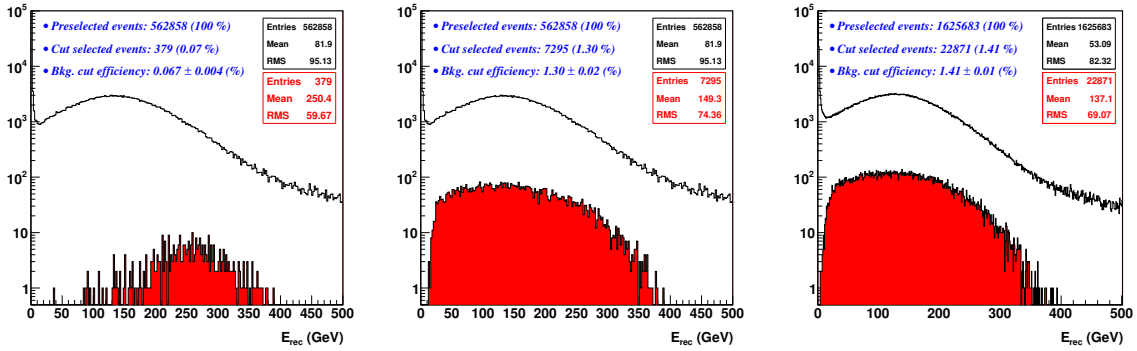

(a) Febrero (cortes e.m. + $E/|P|$) (b) Febrero (cortes e.m.) (c) Agosto (cortes e.m.)

Figura 3.21: *Distribución de la energía reconstruída de la muestra preseleccionada (negro) y de los sucesos después de los cortes electromagnéticos (rojo) para protones de 400 GeV de la prueba de haz de febrero (figuras 3.21(a) y 3.21(b)) y agosto (figura 3.21(c)).*

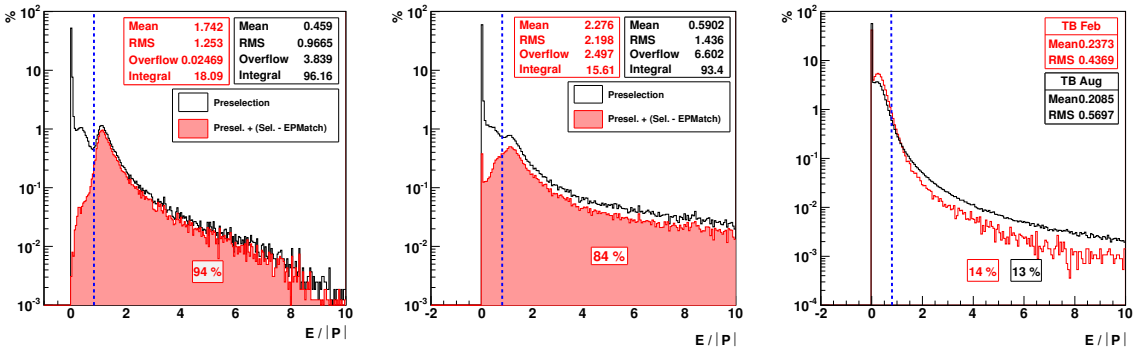

(a) 180 GeV e^- (Feb) (b) 180 GeV e^- (Ago) (c) 400 GeV p

Figura 3.22: *Distribución del cociente $E/|P|$ para electrones de 180 GeV en la prueba de haz de febrero (figura 3.22(a)), para electrones de 180 GeV electrons en la prueba de haz de agosto (figura 3.22(b)) y para protones de 400 GeV en la prueba de haz de febrero y agosto (figura 3.22(c)). La distribución en rojo contienen sucesos tras el conjunto de cortes electromagnéticos sin el acuerdo energía/momento y el número que aparece en cada figura representa la eficiencia del corte EPMatch como primer corte.*

TABLA 3.2: *Eficiencias de los cortes de selección de cascadas electromagnéticas para electrones y protones con errores binomiales. Los valores están normalizados a la muestra de sucesos preseleccionados.*

	180 GeV electrones		**400 GeV protones**	
Eff. (%)	cortes e.m.	cortes e.m. + *EPMatch*	cortes e.m.	cortes e.m. + *EPMatch*
Febrero	87.74 ± 0.08	85.50 ± 0.09	1.30 ± 0.02	0.067 ± 0.004
Agosto	80.01 ± 0.33	65.61 ± 0.34	1.41 ± 0.01	0.210 ± 0.004
MC	87.48 ± 0.20	85.85 ± 0.27	1.31 ± 0.02	0.071 ± 0.005

3.2 El detector de radiación de transición

El detector de radiación de transición proporciona una separación electrón/protón adicional a la del calorímetro para reducir el fondo de protones cósmicos. Los datos tomados durante la prueba de haz de febrero de 2010 se han utilizado para verificar la calibración del TRD así como para obtener las prestaciones del mismo en la separación e/p, comparando los resultados obtenidos con los datos de la prueba de haz de agosto y con la simulación MC del detector con la configuración de imán superconductor.

3.2.1 Verificación de la calibración del TRD

A partir de las señales detectadas en los tubos se reconstruye la traza dentro del TRD. Además, la cantidad de energía depositada en ellos proporciona la información necesaria para realizar la separación e/p. La distribución de la ocupación de los tubos en número de señales (figura 3.23) muestra que el 100 % de los 5248 tubos estaba activo durante la prueba de haz de febrero, mientras que la misma distribución para la prueba de haz de agosto (figura 3.24) muestra que 5247 tubos (99.98 %) estaban activos y tan sólo un tubo no tiene señales.

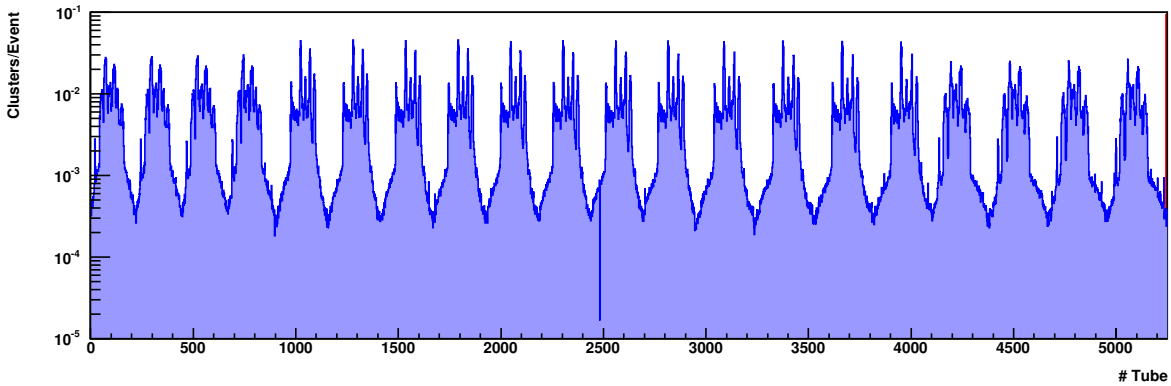

Figura 3.23: *Distribución de la ocupación de los tubos en número de señales totales por suceso para electrones de 250 GeV en la prueba de haz de febrero.*

La traza del TRD se reconstruye a partir de los grupos de señales que deja el paso de un partícula a lo largo de las 20 capas. La multiplicidad en número de grupos de señales usadas en las trazas del TRD, tanto para electrones de 180 GeV y 250 GeV como para protones de 400 GeV,

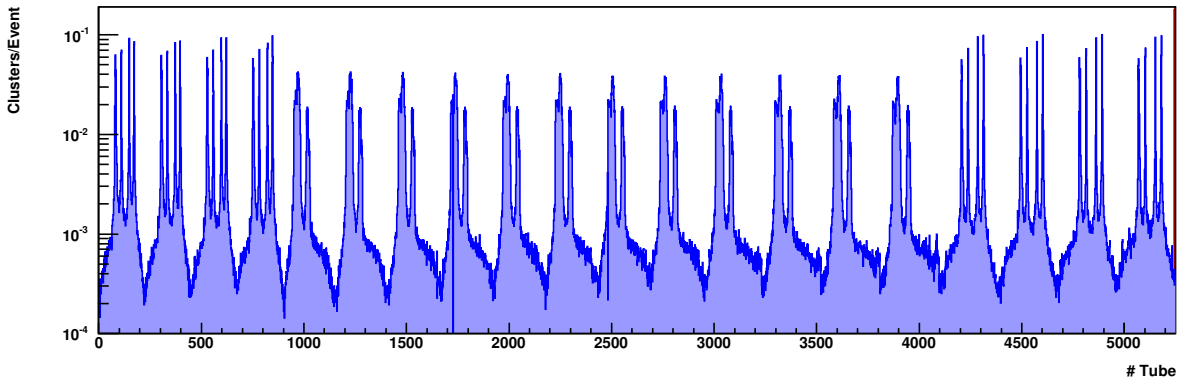

Figura 3.24: *Distribución de la ocupación de los tubos en número de señales totales por suceso para electrones de 180 GeV en la prueba de haz de agosto.*

es de aproximadamente 19 en la prueba de haz de febrero y en la de agosto, mientras que para la simulación MC la multiplicidad es algo más baja (figura 3.25(a)).

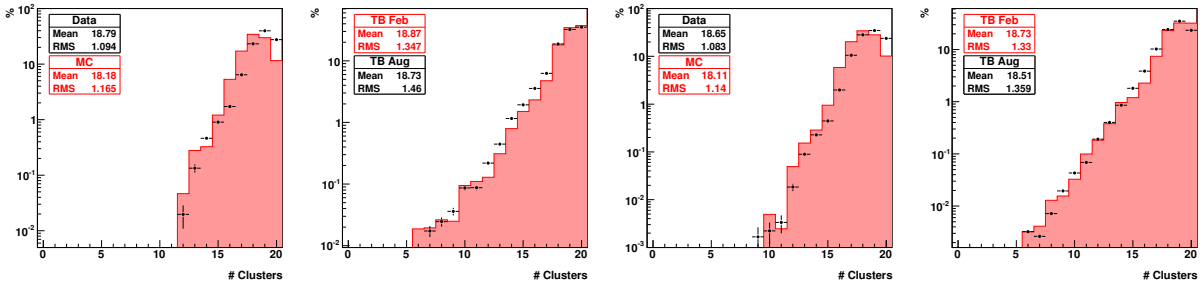

(a) 250 GeV e^- a 5° (b) 180 GeV e^- (c) 400 GeV p a 5° (d) 400 GeV p

Figura 3.25: *Distribución de la multiplicidad en número de grupos de señales usados en las trazas del TRD para electrones de 250 GeV a 5° (figura 3.25(a), febrero frente a MC), electrones de 180 GeV (figura 3.25(b), febrero frente a agosto), protones de 400 GeV a 5° (figura 3.25(c), febrero frente MC) y protones de 400 GeV (figura 3.25(d), febrero frente agosto).*

3.2.1.a Energía depositada en los tubos

La distribución de energía deposita en los tubos puede ser pura ionización o una suma de ionización y radiación de transición en el caso de que esta última se haya emitido y cuya cantidad se incrementa con el factor de Lorentz γ. La distribución de energía de la suma de todos los tubos para electrones de 180 GeV muestra un buen acuerdo entre la prueba de haz de febrero y agosto, ya que el cociente entre ambas permanece por debajo del 5 %. Sin embargo, en el caso de protones de 400 GeV el acuerdo empeora, con una diferencia en el cociente del 15 % a 15 keV debido a una menor cantidad de energía depositada en la muestra de agosto. Para la comparación con la simulación MC del detector con la configuración con el imán superconductor, la energía depositada en el MC se ajustó a los datos de la prueba de haz de febrero bajo el supuesto de la no existencia de correlaciones entre capas en la deposición de energía (figura 3.26).

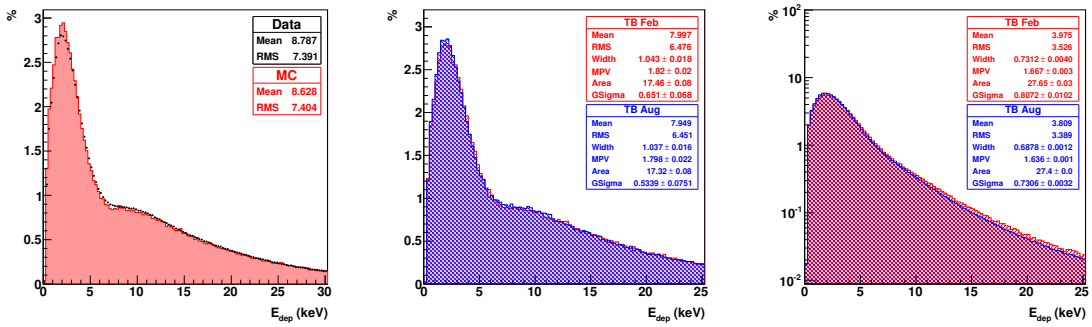

(a) 250 GeV e^- (b) 180 GeV e^- (c) 400 GeV e^-

Figura 3.26: *Espectro de la energía depositada en todos los tubos por electrones de 250 GeV (figura 3.26(a), la línea roja representa la simulación MC y los puntos negros la prueba de haz de febrero), electrones de 180 GeV (figura 3.26(b)), febrero (rojo) y agosto (azul)) y protones de 400 GeV (figura 3.26(c)), febrero (rojo) y agosto (azul)).*

Ionización El ajuste a una función Landau convolucionada con una Gausiana en el rango [0.5,6] keV de la distribución de energía, depositada proporcionada el valor más probable (MPV) de la distribución de ionización. Para electrones de 250 GeV los tubos individuales tienen un MPV medio de 1.8 keV (figura 3.27(a)). Usando electrones de 180 GeV para comparar las dos pruebas de haz, el MPV de ionización permanece estable dentro del 3 % en todas las capas alrededor de 1.8 keV (figura. 3.27(b)). Además, usando también la muestra de piones presente en el haz de electrones, así como los muones cósmicos tomados durante la prueba de haz de febrero, el MPV se puede representar frente al factor de Lorentz γ (figura 3.27(c))

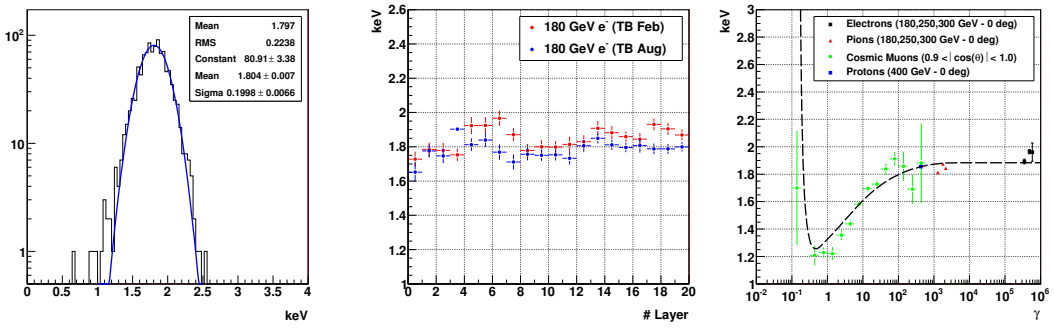

(a) 250 GeV e^- (b) 180 GeV e^- (c)

Figura 3.27: *Distribución de los valores más probables (MPV) de la distribución ionización para los 5248 tubos usando electrones de 250 GeV (figura 3.27(a)). MPV de la ionización para cada capa usando electrones de 180 GeV (figura 3.27(b), febrero (rojo) y agosto (azul)). Dependencia del MPV de ionización con el factor de Lorentz γ (figura 3.27(c)).*

Transición A partir de la simulación MC del detector con la configuración del imán superconductor, los protones de 400 GeV tienen una probabilidad de emisión de radiación de transición del 2 % usando protones de 32 GeV como patrón de ionización. Ante la ausencia de una muestra

mejor en la prueba de haz, la energía depositada en todos los tubos por protones de 400 GeV se ha usado como patrón de ionización. La distribución de la radiación de transición se puede obtener substrayendo la distribución de ionización a la energía depositada total en todos los tubos, una vez que la distribución de ionización se haya escalado de acuerdo con la dependencia del MPV con γ (figura 3.28(a)). El resultado que se obtiene en las pruebas de haz de febrero y agosto es muy parecido (figura 3.28(b)), con un MPV de 11 keV para electrones de 180 GeV.

Por otra parte, la probabilidad de emisión de la radiación de transición Prob(TR) se puede estimar a partir de la distribución de ionización, calculando primero la probabilidad de ionización

$$\text{Prob(IO)} = \frac{\int f_{ion}(E)\, dE}{\int f_{tot}(E)\, dE} \tag{3.7}$$

donde $f_{ion}(E)$ es la distribución de ionizacion y $f_{tot}(E)$ es la distribución de la energía total depositada, para luego poder calcular la probabilidad de emisión de la radiación de transición

$$\text{Prob(TR)} = 1 - \text{Prob(IO)} \tag{3.8}$$

con un valor del 42 % a γ altas (figura 3.28(c)).

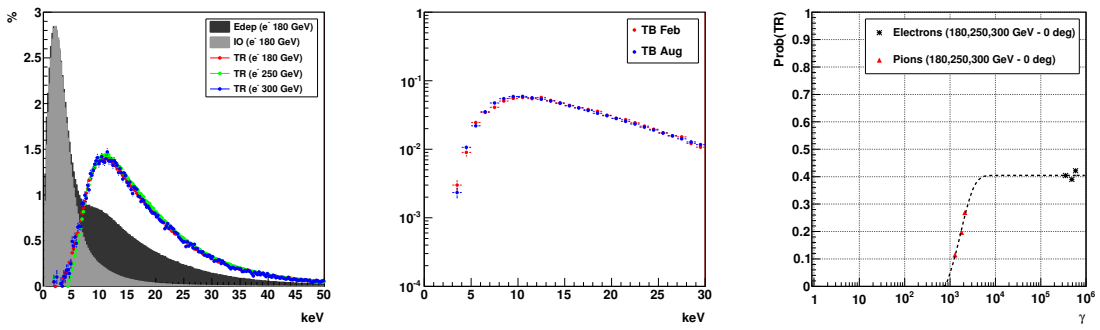

(a) (b) (c)

Figura 3.28: *Distribución de la energía total depositada en todos los tubos (gris oscuro), distribución de la ionización (gris) y distribuciones de la transición (puntos rojo, verde y azul) para electrones (figura 3.28(a)). Distribución de la radiación de transición para electrones de 180 GeV (figura 3.28(b)). Probabilidad de emisión de la radiación de transición representada en función del factor de Lorentz γ usando muestras de electrones y piones de la prueba de haz de febrero (figura 3.28(c)).*

3.2.2 Prestaciones del TRD

La separación e/p realizada por el TRD se basa en la dependencia de la energía depositada en los tubos con el factor de Lorentz γ. Se han utilizado los dos métodos más representativos para llevar a cabo esta separación [57]: el contaje de grupos de señales (*cluster counting*) y el método de verosimilitud (*likelihood*).

3.2.2.a Verosimilitud

El método de verosimilitud se basa en el test del ratio de verosimilitud, el cual se utiliza cuando existen sucesos que pueden ocurrir con dos distribuciones distintas y la hipótesis de

sucesos ocurriendo con una de ellas se debe descartar. El ratio de verosimilitud se puede definir como [57]

$$L = \frac{W_{tr}}{W_{tr} + W_{io}} \qquad ; \qquad W_{tr,io} = \sqrt[n]{\prod_{i=1}^{n} P^i_{tr,io}(E_i)} \tag{3.9}$$

donde n es el número de grupos de señales de cada suceso, $P^i_{tr,io}(E_i)$ es la probabilidad dada por las funciones de densidad de probabilidad ($p.d.f.$) para la ionización (io) y la transición (tr) (figuras 3.29(a) y 3.29(b)) y E_i es la energía de los grupos de señales. Para cada grupo de señales, $P^i_{tr,io}(E_i)$ toma el valor de la $p.d.f.$ correspondiente que tenga el valor más alto para la energía del grupo de señales. La distribución del logaritmo natural de L se usa para establecer la eficiencia del método introduciendo un valor umbral en la cantidad $-\log(L)$ (figura 3.29(c)). Las distribuciones del logaritmo natural de L para las muestras de electrones y protones de la prueba de haz de febrero, agosto y la simulación MC (figura 3.30) muestran un buen acuerdo. Integrando las distribuciones a lo largo del valor de $-\log(L)$ se determina la variación de la eficiencia con el valor umbral (figura 3.29(d)). El valor de la eficiencia para protones de 400 GeV es del 2 % para una eficiencia en electrones de aproximadamente el 90 % (tabla 3.3).

TABLA 3.3: *Eficiencia del método de verosimilitud con errores binomiales para un haz con un ángulo de incidencia de 5° para las muestras de la prueba de haz de febrero y agosto y la simulación MC.*

Partícula	**TB febrero (%)**	**TB agosto (%)**	**MC (%)**
180 GeV e^-	91.06 ± 0.13	89.89 ± 0.38	89.51 ± 0.41
400 GeV p	1.97 ± 0.03	1.95 ± 0.02	2.03 ± 0.04

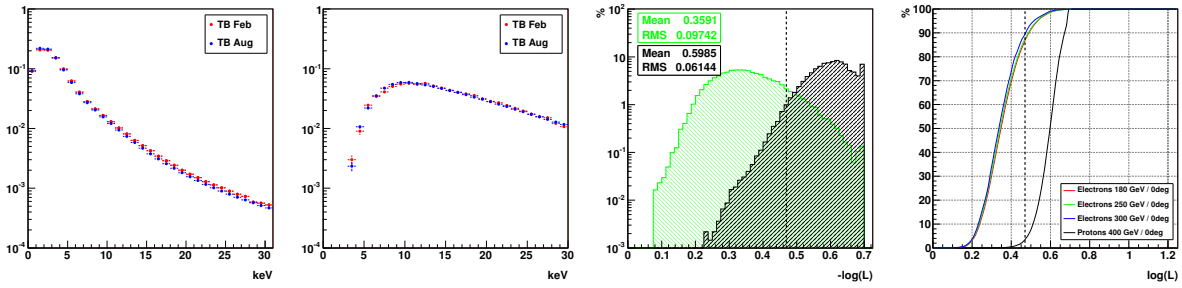

(a) Ionización (b) Transición (c) (d)

Figura 3.29: *Distribución de la función de densidad de probabilidad para la ionización (figura 3.29(a)) y para la transición (figura 3.29(b)). Distribuciones del logaritmo natural de L para electrones de 250 GeV (verde) y protones de 400 GeV (negro) a 0°, la línea vertical punteada representa el valor umbral para una eficiencia en los electrones del 90 % (figura 3.29(c)). Variación de la eficiencia del método de verosimilitud con el valor umbral para electrones y protones a 0°, la línea vertical punteada representa el valor umbral para una eficiencia en los electrones del 90 % (figura 3.29(d)).*

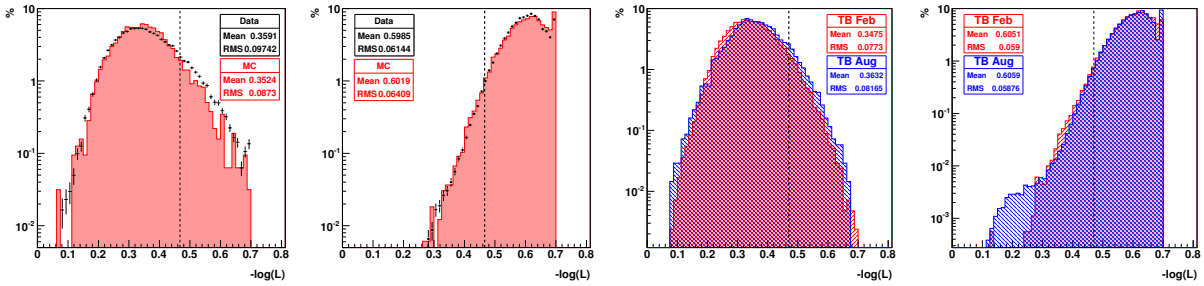

(a) 250 GeV e^- a 0° (b) 400 GeV p a 0° (c) 180 GeV e^- a 5° (d) 400 GeV p a 5°

Figura 3.30: *Distribución del logaritmo natural de L para electrones de 250 GeV a 0° (figura 3.30(a)), protones de 400 GeV a 0° (figura 3.30(b)), electrones de 180 GeV a 5° (figura 3.30(c)) y protones de 400 GeV a 5° (figura 3.30(d)).*

3.2.2.b Contaje de grupos de señales

El método del contaje de grupos de señales es un método directo, ya que un corte en el número de grupos de señales por suceso ($N_{cl} \geq 6$) con una energía por encima de un umbral ($E_{dep} > 6.5\,\text{keV}$), separa partículas con diferente factor de Lorentz γ. La eficiencia del método es del 8 % para protones de 400 GeV a 5° para una eficiencia del 98 % para electrones de 180 GeV a 5°, con un buen acuerdo entre datos y simulación MC para las distribuciones del número de grupos de señales con energía por encima de 6.5 keV (figuras 3.31(a) y 3.31(b)).

En lugar de utilizar un umbral de energía fijo, el método se puede modificar usando el número de grupos de señales identificados como de transición al aplicar el método de verosimilitud del apartado anterior (figuras 3.31(c) y 3.31(d)), ya que se basa en el valor de las $p.d.f.$ de ionización y transición a las energías de los grupos de señales. Un corte en el número de grupos de transición por suceso ($N_{cl} \geq 6$) da una eficiencia del 7 % para protones de 400 GeV a 5° para una eficiencia del 91 % para electrones de 180 GeV a 5° (tabla 3.4).

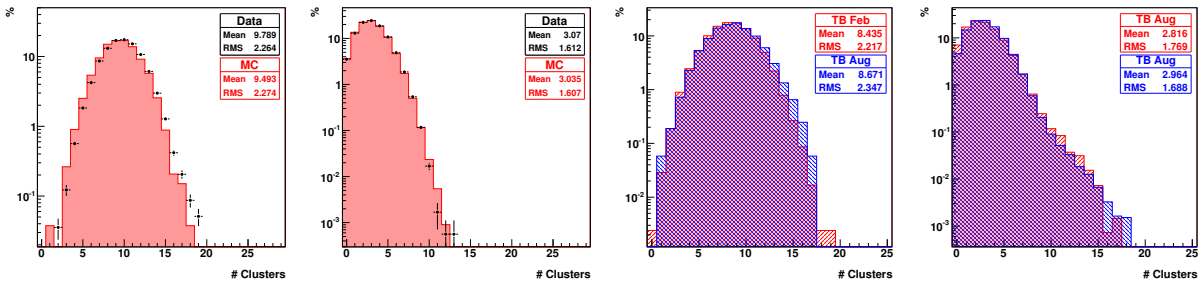

(a) 250 GeV e^- @ 5° (b) 400 GeV p @ 5° (c) 180 GeV e^- @ 5° (d) 400 GeV p @ 5°

Figura 3.31: *Distribución del número de grupos de señales con $E_{dep} > 6.5keV$ para electrones de 250 GeV a 5° (figura 3.31(a)) y protones de 400 GeV a 5° (figura 3.31(b)). Distribución del número de grupos de señales identificados como transición por suceso con el método de verosimilutud para electrones de 180 GeV a 5° (figura 3.31(c)) y protones de 400 GeV a 5° (figura 3.31(d)).*

TABLA 3.4: *Eficiencias del método del contaje de grupos de señales modificado, con errores binomiales y para un haz con un ángulo de incidencia de 5° para las muestras de la prueba de haz de febrero y agosto y la simulación MC.*

Partícula	**TB febrero**	**TB agosto**	**MC**
180 GeV e^-	91.10 ± 0.14	91.47 ± 0.34	88.70 ± 0.41
400 GeV p	7.12 ± 0.07	7.18 ± 0.03	6.97 ± 0.07

3.3 Prestaciones de AMS-02 en la separación electrón/protón

El factor de rechazo es el resulado de dividir la aceptancia de la señal (electrón) por la aceptancia del fondo (protón)

$$R(E) = \frac{A_{sig}(E)}{A_{bkg}(E)} \tag{3.10}$$

donde la aceptancia A se puede escribir como el producto de la aceptancia del *trigger*, la eficiencia del conjunto de cortes de preselección y la eficiencia del conjunto de cortes de selección de electrones

$$A = A_{trig} \cdot \epsilon_{pre} \cdot \epsilon_{sel} \tag{3.11}$$

Esta aceptancia debe ser corregida para protones, ya que la energía reconstruída por el calorímetro es inferior a la del proton incidente y además, la contribución del fondo a una energía E proviene de una región de espectro de protones cósmicos con menor flujo.

3.3.1 Eficiencia de los cortes de preselección

Para normalizar las muestras de los datos de la prueba de haz y de la simulación MC, se utilizan unos cortes de preselección que uniformizan los sucesos en base a multiplicidades de objetos reconstruídos. La figura 3.32 muestra el conjunto de cortes utilizado.

La eficiencia que se obtiene para protones de 400 GeV de la prueba de haz de febrero es del 34 %. mientras que para electrones de 180 GeV se obtiene una eficiencia del $\sim$ 42 %. La tabla 3.5 resume los valores para datos y simulación MC.

TABLA 3.5: *Eficiencia de los cortes de preselección con errores binomiales para datos de la prueba de haz de febrero y simulación MC.*

Partícula	**TB febrero (%)**	**MC (%)**
180 GeV e^-	42.33 ± 0.10	42.50 ± 0.25
400 GeV p	33.57 ± 0.04	38.68 ± 0.06

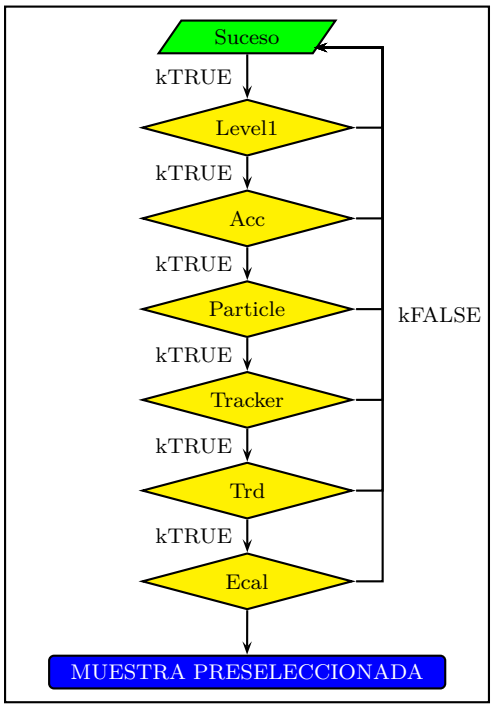

1. ***Level 1*:** Level1 trigger presente.
2. ***Acc*:** Número de anticontadores disparados ≤ 4.
3. ***Particle*:** 1 ó 2 partículas reconstruídas.
4. ***Tracker*:**
   (a) $0 <$ trazas reconstruídas ≤ 3.
   (b) Chi-cuadrado de la traza (`Chi2FastFit`) ≤ 35
5. ***Trd*:** 1 traza reconstruída.
6. ***Ecal*:**
   (a) 1 cascada reconstruída.
   (b) $|x(track)| < 32\,\text{cm}$ (traza partícula dentro ECAL).
   (c) $|y(track)| < 32\,\text{cm}$ (traza partícula dentro ECAL).
   (d) $|x(track) - x(ecal)| < 1\,\text{cm}$ (Acuerdo espacial traza/cascada)
   (e) $|y(track) - y(ecal)| < 1\,\text{cm}$(Acuerdo espacial traza/cascada)

Figura 3.32: *Conjunto de cortes de preselección utilizado en el análisis.*

3.3.2 Eficiencia del conjunto de cortes de selección ECAL+TRD

A lo largo del trabajo se ha demostrado que las prestaciones del ECAL y del TRD en la separación e/p no cambian a pesar de la última altualización del detector que supuso el cambio del imán superconductor por el imán permanente y el reajuste de los planos del detector de trazas. El conjunto de cortes electromagnéticos más el método de verosimilitud del TRD tiene una eficiencia para protones de 400 GeV del 0.03 %, con un buen acuerdo entre los datos de la prueba de haz de febrero y de agosto y de la simulación MC. Cuando se añade el acuerdo entre la energía y el momento, se llega a una eficiencia del 0.0018 % en protones de 400 GeV para una eficiencia del 77 % en electrones de 180 GeV (figura 3.33). No obstante, existe un factor 3 de

TABLA 3.6: *Eficiencia de los cortes electromagnéticos, de verosimilitud del TRD y del acuerdo energía/momento con errores binomiales para datos de las pruebas de haz de febrero y agosto y simulación MC.*

Partícula	**TB febrero (%)**	**TB agosto (%)**	**MC (%)**
	ECAL + TRD		
180 GeV e^-	79.80 ± 0.10	73.27 ± 0.30	83.16 ± 0.29
400 GeV p	0.033 ± 0.002	0.030 ± 0.003	0.033 ± 0.003
	ECAL + TRD + EPMatch		
180 GeV e^-	76.76 ± 0.10	51.63 ± 0.36	77.14 ± 0.32
400 GeV p	0.0018 ± 0.0006	0.0044 ± 0.0006	0.0020 ± 0.0008

de diferencia en la eficiencia para protones entre los datos de febrero y agosto debido a la degradación en el momento producida por el cambio de imán. Los datos se resumen en la tabla 3.6.

Como se ha comentado en el apartado 3.1.2.b, en lugar del uso de un conjunto de cortes electromagnéticos, existen métodos alternativos con los que se puede intentar maximizar la separación e/p del calorímetro, como es el análisis multivariante, con el que se está obtiendo una mejora de un factor 3 en la eficiencia para protones a 100 GV con una eficiencia del 90 % en electrones usando datos reales de vuelo.

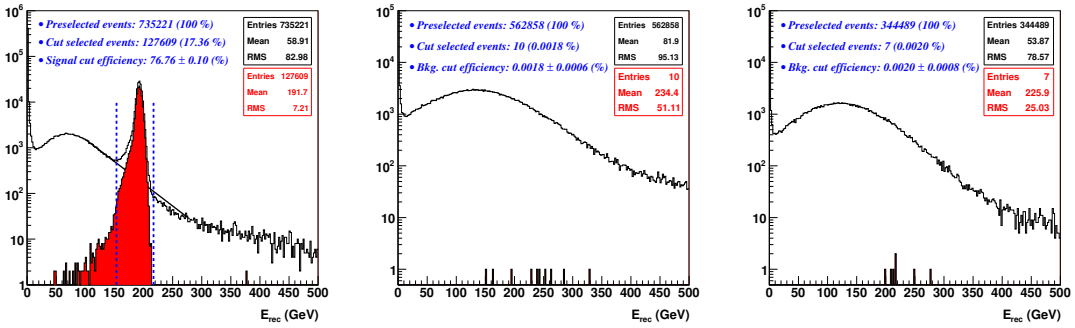

(a) TB feb 180 GeV e^- (b) TB feb 400 GeV p (c) MC 400 GeV p

Figura 3.33: *Distribución de la energía reconstruída por el calorímetro de la muestra preseleccionada (negro) y de los sucesos después de cortes (ECAL+TRD+EPMatch) (rojo) para electrones de 180 GeV de la prueba de haz de febrero (figura 3.33(a)), protones de 400 GeV de la prueba de haz de febrero (figura 3.33(b)) y protones de 400 GeV de la simulación MC (figura 3.33(c)). La línea negra representa el fondo exponencial que se substrae a la señal dentro del rango de energía delimitado por la dos líneas azules punteadas.*

4

Capacidades de AMS-02 para la medida de e^+

Los resultados que arrojan las dos pruebas de haz a las que se sometió AMS-02 en el año 2010, demuestran que las prestaciones del ECAL y del TRD en la separación e/p no se ven afectadas a pesar de los cambios introducidos en el detector. Sin embargo, los resultados de la supresión de protones en la prueba de haz están limitados a un punto de energía. Desde entonces, el software de AMS se ha actualizado para incorporar la calibración de los subdetectores a la reconstrucción y para tener una simulación Monte Carlo más realista. Esta versión actualizada se ha usado para simular protones y electrones con el fin de obtener el factor de rechazo a diferentes energías y determinar una cota superior de energía para la medida de positrones donde ésta no se vea comprometida por el fondo de protones.

4.1 Muestra de simulación Monte Carlo

El intervalo de energía de generación para protones y electrones se dividió en tres subintervalos: (0.5,10), (10,200) y (200,4000) GeV. Los sucesos en cada intervalo se generan de manera isotrópica siguiendo un espectro logarítmico en momento con una estadística total de 2.6×10^{10} sucesos en el caso de protones y de 3.9×10^8 sucesos en el caso de electrones (table 4.1).

Tabla 4.1: *Estadísta de la simualción MC de protones y electrones.*

Partícula	Intervalo energía (GeV)	Sucesos generados
Proton	0.5–10	1.95×10^{10}
	10–200	5.92×10^9
	200–4000	2.92×10^8
Electron	0.5–10	9.99×10^7
	10–200	9.59×10^7
	200–4000	1.97×10^8

4.2 Prestaciones de AMS-02 en la separación e/p

La actualización del detector, que consistió en el cambio del imán superconductor por el permanente además del reajuste de los planos del detector de trazas, no interfiere en las capacidades intrínsecas del ECAL y del TRD para suprimir el fondo de protones, ya que las prestaciones de ambos en la separación e/p no se ve afectada. Sin embargo, cuando se añade el acuerdo entre la energía y el momento, la eficiencia de AMS-02 para protones de 400 GeV difiere en un factor 3 entre ambas configuraciones debido a la degradación en la resolución en el momento. Para extender las prestaciones de AMS-02 en la separación e/p a otras energías, los cortes electromagnéticos se ajustaron de forma independiente para que existiera un acuerdo con los datos de la prueba de haz a 400 GeV, de tal forma que se llega a un acuerdo entre datos y MC cuando se aplican todos ellos de forma conjunta (figura 4.1).

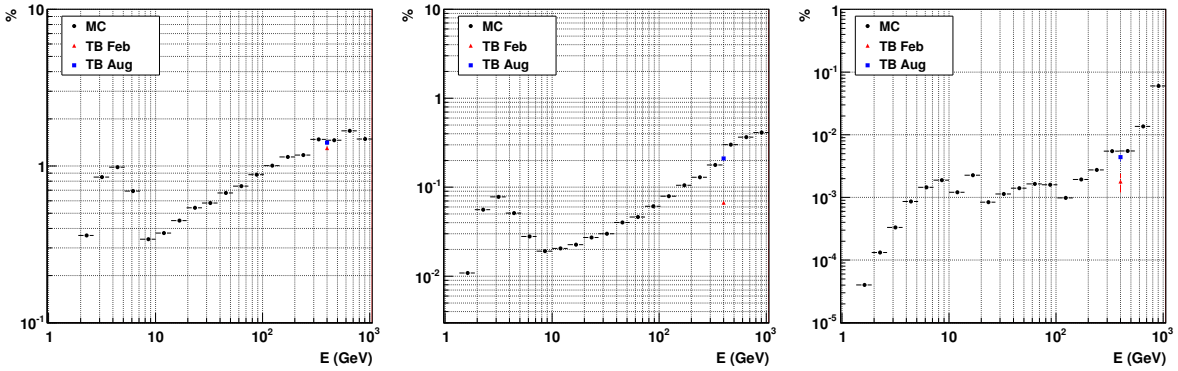

(a) *ECAL* (b) *ECAL + EPMatch* (c) *ECAL + EPMatch + TRD*

Figura 4.1: *Eficiencia de los cortes electromagnéticos del ECAL (figura 4.1(a)), más el acuerdo entre energía y momento (figura 4.1(b)) y más el método de verosimilitud del TRD (figura 4.1(c)) para protones, con la comparación con los resultados de las pruebas de haz a 400 GeV.*

4.2.1 Aceptancia de AMS-02

Para obtener la frecuencia de detección, es decir, el número de sucesos detectados por segundo, a partir de un flujo de partículas, se necesita una aceptancia en unidades de $m^2\,sr$, la cual se obtiene de la simulación MC al multiplicar la eficiencia de detección N_{cut}/N_{gen} por la aceptancia generada A_{gen}

$$A(E) = \frac{N_{cut}(E)}{N_{gen}(E)} \cdot A_{gen}(E) \tag{4.1}$$

donde N_{cut} es el número de sucesos que pasan los cortes a una cierta energía y N_{gen} es el número de sucesos generados a una cierta energía. La aceptancia generada es $A_{gen} = \pi L^2$, que resulta de generar partículas en la cara superior de un cubo que es concéntrico y coaxial a AMS-02. El lado del cubo tiene un valor de 3.9 m para que concuerde con el campo de visión de AMS-02 de 45° en la dirección cenital [65]. La figura 4.2 muestra la aceptancia para protones y electrones depués de los cortes de preselección y selección.

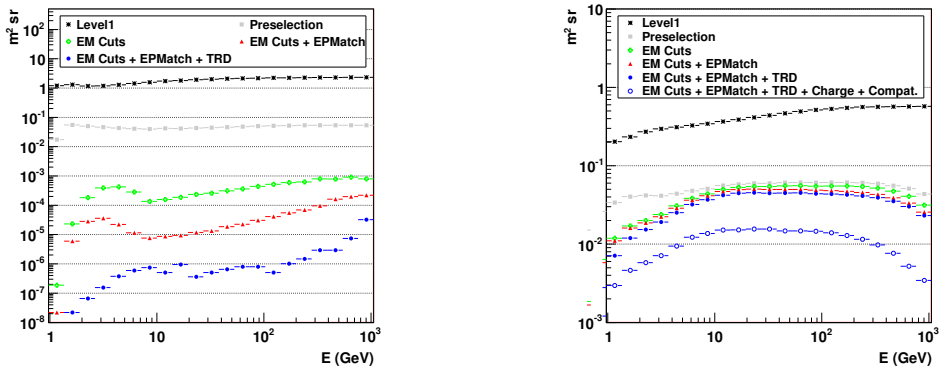

(a) protones (b) electrones

Figura 4.2: *Aceptancia para protones (figura 4.2(a)) y electrones (figura 4.2(b)) usando cortes electromagnéticos, acuerdo entre energía y momento y el método de verosimilitud del TRD, donde el corte Charge selecciona partículas reconstruídas con carga negativa y el corte Compat introduce una compatibilidad entre las rigidices reconstruídas con diferentes combinaciones de los planos del detector de trazas.*

4.2.2 Factor de rechazo a protones de AMS-02

El flujo de protones cósmicos es 10^3–10^5 veces mayor que el flujo de positrones (apartado 1.4, pág. 4), por lo que se necesita un factor de rechazo a protones de 10^4–10^6 , además de una medida precisa del signo de la carga para evitar confusiones con electrones. La frecuencia de detección de positrones $\dot{n}_{sig}$ a una cierta energía se calcula a partir de la ecuación

$$\dot{n}_{sig}(E) = A_{sig}(E) \cdot \phi_{sig}(E) \cdot \Delta E \tag{4.2}$$

donde A es la aceptancia en unidades de $\mathrm{m}^2\,\mathrm{sr}$ y ϕ es el flujo de partículas en unidades de $(\mathrm{m}^2\,\mathrm{sr}\,\mathrm{GeVs})^{-1}$. Para el caso del fondo de protones, la energía reconstruída por el calorímetro es inferior a la del proton incidente. Además, la contribución del fondo a una energía E proviene de una región de espectro de protones cósmicos con menor flujo. Por lo tanto, el número de sucesos de fondo por segundo se calcula con la ecuación

$$\dot{n}_{bkg} = \int_{E'} A_{bkg}(E') \cdot P_{bkg}\left(E' \to (E, E+\Delta E)\right) \cdot \phi_{bkg}(E')\, dE' \tag{4.3}$$

donde $P_{bkg}(E' \to (E, E+\Delta E))$ es la probabilidad de que un protón con energía E' sea reconstruído con una energía dentro del intervalo $(E, E+\Delta E)$. Además, si se introduce una aceptancia corregida $\tilde{A}_{bkg}$, la frecuencia de detección $\dot{n}_{bkg}$ se puede escribir también como

$$\dot{n}_{bkg}(E) = \tilde{A}_{bkg}(E) \cdot \phi_{bkg}(E) \cdot \Delta E \tag{4.4}$$

donde $\tilde{A}_{bkg}$ es

$$\tilde{A}_{bkg}(E) = \int_{E'} A_{bkg}(E') \cdot \frac{P_{bkg}\left(E' \to (E, E+\Delta E)\right)}{\Delta E} \cdot \frac{\phi_{bkg}(E')}{\phi_{bkg}(E)}\, dE' \tag{4.5}$$

Finalmente, el factor de rechazo se define como el cociente entre la aceptancia de la señal y la aceptancia del fondo

$$R(E) = \frac{A_{sig}(E)}{A_{bkg}(E)} \tag{4.6}$$

el cual, a partir de las ecuaciones (4.2) y (4.4) se puede reescribir utilizando la aceptancia corregida $\tilde{A}_{bkg}$

$$\tilde{R}(E) = \frac{A_{sig}(E)}{\tilde{A}_{bkg}(E)} = \left(\frac{\dot{n}_{sig}(E)}{\dot{n}_{bkg}(E)}\right) \cdot \left(\frac{\phi_{bkg}(E)}{\phi_{sig}(E)}\right) \tag{4.7}$$

Para estimar el número de positrones cósmicos medidos por AMS-02 y el consiguiente fondo de protones a partir de las ecuaciones 4.2 y 4.3, se ha utilizado un modelo de propagación [43, 46] para calcular el flujo de positrones y de protones en la órbita baja de la Tierra (figura 1.2(a), pág. 5). Se ha introducido una función de transferencia efectiva para tener en cuenta el umbral en la rigidez vertical (apartado 1.3.2.a) a la altitud de la órbita de la Estación Espacial Internacional. Esta función toma valores que van desde el 5 % a 1 GeV hasta el 100 % a 20 GeV y en adelante. Además, en el caso de protones se ha utilizado una matriz de migración para tener en cuenta el hecho de que el calorímetro reconstruye los protones con una energía inferior a la incidente. Esta matriz de migración, que representa el número de sucesos generados dentro de un grupo de intervalos de energía y el número de sucesos reconstruídos dentro de los mismos intervalos de energía, se normaliza para obtener la probabilidad de que un proton generado con energía E' se reconstruya con una energía dentro del intervalo $(E, E + \Delta E)$. Las probabilidades de todas las posibles energías reconstruídas para una cierta energía generada suman 1 (figura. 4.3).

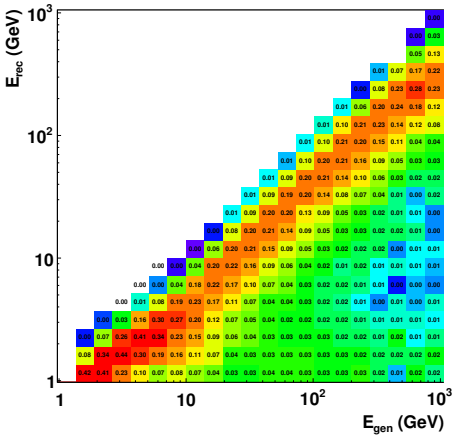

Figura 4.3: *Matriz de probabilidad para protones después de los cortes electromagnéticos.*

La figura 4.4 muestra el número de positrones [1] y de fondo protones que AMS-02 detectaría en 5 años usando la aceptancia después de cortes de selección ($ECAL + EPMatch + TRD$) obtenida en el apartado anterior. El fondo de protones representa una fracción de la señal por debajo del 10 % hasta los 400 GeV, con un factor de rechazo que está por encima de 10^5 hasta los 400 GeV cuando se requiere también una carga resconstruída positiva, además de una compatibilidad entre las rigideces reconstruídas con diferentes combinaciones de los planos del detector de trazas. En el caso de los electrones, el flujo es 4–200 veces mayor que el flujo de positrones, por lo que se necesita un factor de rechazo inferior al de los protones. La confusión de carga permanece por debajo del 0.1 % hasta los 400 GeV cuando se requiere una compatibilidad entre las rigideces reconstruídas con diferentes combinaciones de los planos del detector de trazas.

[1] No se ha introducido ninguna fuente primaria de positrones en el modelo de propagación.

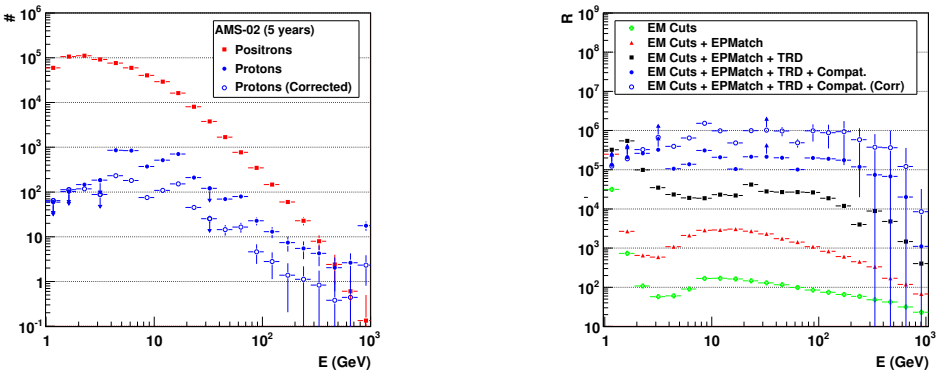

(a) (b)

Figura 4.4: *Estimación del número positrones y protones detectados por AMS-02 en 5 años (figura 4.4(a)), usando las aceptancias después de cortes de selección (ECAL+EPMatch+TRD) más el signo de la carga y la compatibilidad de rigideces, la matriz de migración para protones y un modelo de propagación que no incluye una fuente primaria de positrones. Factor de rechazo a protones (figura 4.4(b)).*

4.3 Estimación en la medida de la señal de positrones cósmicos con AMS-02

Los resultados de otros experimentos [30–33] indican que existe un exceso de positrones con respecto a los modelos de propagación estándar por encima de los 10 GeV (figura 1.1(a), pág.5). Este incremento implica la existencia de una fuente primaria de positrones no tenida en cuenta en los modelos de propagación y cuya naturaleza ha sido ampliamente discutida, con propuestas que van desde púlsares cercanos [34] hasta la aniquilación de materia oscura en el halo galáctico [35]. La fracción de positrones se define como

$$\frac{e^+}{e^+ + e^-} = \frac{N_{e^+}}{N_{e^+} + N_{e^-}} \tag{4.8}$$

donde $N_{e^+,-}$ es el número de electrones y positrones calculados a partir de la frecuencia de detección (ecuación 4.2) durante un período de tiempo. Tanto los electrones como los positrones comparten la misma aceptancia representada en la figura 4.2(b). Si no existiera contaminación, tanto en la medida de positrones como del espectro conjunto $(e^+ + e^-)$, la fracción de positrones resultante no presentaría ningún sesgo y reproduciría la predicción del modelo de propagación estándar [2] a todas las energías (figura 4.5(a)). Sin embargo, existe un fondo residual de protones B_p y de electrones B_{e-} en la medida de positrones y un fondo de protones en la medida del espectro conjunto. Por lo tanto, para reproducir la medida con la simulación MC, la fracción de positrones se puede reescribir como

$$\frac{e^+}{e^+ + e^-} = \frac{N_{e^+} + B_p + B_{e^-}}{N_{e^+} + N_{e^-} + B_p + B_{e^-} + B_{e^+}} \tag{4.9}$$

donde el fondo de protones B_p es el número de protones calculado en el apartado anterior después del conjunto de cortes $(ECAL + EPMatch + TRD)$ más el signo de la carga y la compatibilidad de rigideces.

[2] No se ha introducido ninguna fuente primaria de positrones en el modelo de propagación.

La fracción de positrones se mide hasta los 400 GeV con un fondo de protones lo suficientemente reducido y un fondo de electrones/positrones $B_{e^{-,+}}$, a causa de la confusión de carga, lo suficientemente bajo como para no sesgar la medida (Fig. 4.5). Además, cuando se introduce una fuente primaria de positrones [70] en el modelo de propagación que reproduce los resultados obtenidos por otros experimentos, el rango de energía se puede extender más allá de los 500 GeV (Fig. 4.6).

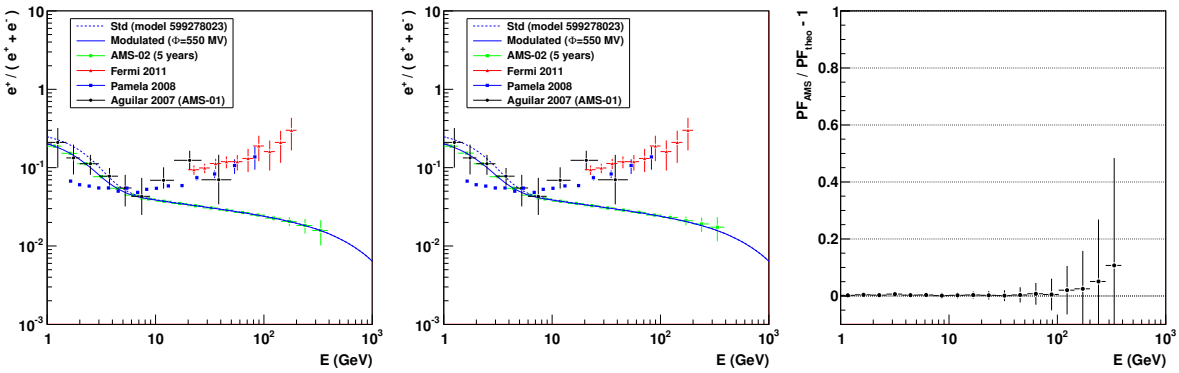

(a) (b) (c)

Figura 4.5: *Estimación de la fracción de positrones (puntos verdes) sin contaminación de protones (figura 4.5(a)) y teniendo en cuenta una contaminación de protones (figura 4.5(b)) en la medida de positrones. La línea azul representa el modelo estándar de propagación el cual no incluye una fuente primaria de positrones. Cociente entre la predicción teórica y la estimación de AMS-02 de las fracciones de positrones (figura 4.5(c)).*

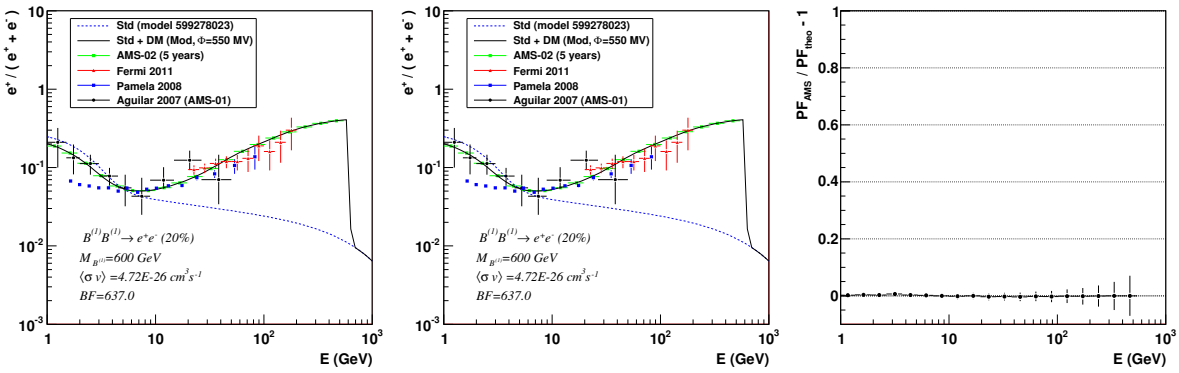

(a) (b) (c)

Figura 4.6: *Estimación de la fracción de positrones (puntos verdes) sin contaminación de protones (figura 4.6(a)) y teniendo en cuenta una contaminación de protones (figura 4.6(b)) en la medida de positrones. La línea azul representa el modelo estándar de propagación el cual no incluye una fuente primaria de positrones y la línea negra representa un modelo de propagación que incluye una fuente primaria de positrones [70] que reproduce los resultados obtenidos por otros experimentos. Cociente entre la predicción teórica y la estimación de AMS-02 de las fracciones de positrones (figura 4.6(c)).*

Conclusiones

Desde que AMS-02 se sometió a dos pruebas de haz en las instalaciones del CERN en el año 2010, el software de AMS se ha ido actualizando tanto para incorporar unos subdetectores calibrados a la reconstrucción como para tener una simulación Monte Carlo más realista. La mayor parte del trabajo presentado en este documento se remonta a la época de la primera prueba de haz y constituye la base de las consiguientes actualizaciones implementadas en el software relacionadas principalmente con el calorímetro.

Del abanico de estudios que ofrece AMS-02, el documento se centra en la medida de los positrones cósmicos, para lo cual introduce todo aquello que guarda relación con el tema a excepción del mecanismo físico que da cuenta del exceso de positrones observado por encima de los 10 GeV, ya que lo primero es evaluar la capacidad del detector para obtener una medida de la señal de positrones que no se vea comprometida por la contaminación del fondo de protones.

Una vez hecha la introducción teórica que motiva el estudio de la señal de positrones y explicar la física en la que se fundamenta el detector, se pasa al estudio de las prestaciones del calorímetro electromagnético y del detector de radiación de transición, dos subdetectores clave en la supresión del fondo de protones, usando para ello los datos de las pruebas de haz a las que se sometió el detector a energías fijas. Para obtener la prestaciones de ambos subdetectores en la separación e/p, se usó un conjunto de cortes electromagnéticos en el caso del calorímetro y un método de verosimilitud en el caso del detector de radiación de transición. Los resultados demuestran que la última actualización del detector no interfiere en sus prestaciones. Además, también se desarrolló un método de calibración para el calorímetro. Finalmente, se usó una simulación MC de la configuración de vuelo del detector, la cual se beneficia de las últimas actualizaciones del software, para ampliar los resultados de la supresión de protones a otras energías con el objetivo de determinar una cota superior de energía para la medida de positrones donde ésta no se vea comprometida por el fondo de protones. A continuación se relata de forma más pormenorizada todo aquello concerniente al calorímetro, al detector de radiación de transición y a la medida de positrones:

El calorímetro electromagnético Los datos de la prueba de haz tomados con la configuración del imán superconductor de AMS-02 se usaron para desarrollar un método de calibración del calorímetro. El motivo de usar estos datos en lugar de los de la prueba de haz con la configuración de vuelo se debe a que en la primera prueba de haz existían posiciones específicas del detector para el estudio del ECAL. Además del método de calibración, también se vió que las prestaciones del calorímetro en la separación e/p no se veían afectadas por esta última actualización del detector.

Calibración El método de calibración parte de una calibracíon absoluta ya existente que se obtuvo con partículas de mínima ioniación (MIP), para acabar con una calibración realizada con cascadas electromagnéticas. Para verificar la ecualización de los canales existente, se usó una muestra de partículas de mínima ionización para validar la corrección por atenuación y la señal en alta ganancia, ya que para ecualizar los canales se utiliza la respuesta de los fotomultiplicadores al paso de un MIP, la cual además debe ser corregida por la atenuación existente en la fibras.

Para validar la corrección por atenuación con partículas de mínima ionización, las cuentas ADC medidas en diferentes puntos a lo largo de las fibras ópticas, una vez corregidas y para cada canal, se ajustaron a una línea recta usando para ello la media de la distribución en cada punto. La distribución resultante de las pendientes del ajuste estaba centrada en 0 y con una anchura del 3.8 %, lo que confirma que los efectos de atenuación se contrarrestan apropiadamente. No obstante, como la distribución de las cuentas ADC presenta una incertidumbre inherente debido a la proximidad del máximo al umbral electrónico, se utilizó también la media truncada y el valor más probable del ajuste a una función Landau de la distribución obteniéndose resultados similares.

Para verificar la ecualización de los canales ya existente con partículas de mínima ionización, la distribución de cuentas ADC medida por cada canal se ajustó a una función Landau. La distribución de los valores más probables de todos los canales estaba centrada en 28 cuentas ADC con una anchura del 17 % a causa de una dispersión intrínsica de los fotomultiplicadores. No obstante, lo señal medida por los canales en cuentas ADC se convierte en una medida de las energía depositada a través de un factor de calibración. La distribución de los valores más probables de la deposición en energía de todos los canales estaba centrada en 13 MeV con una anchura del 3 %, lo que valida la calibración existente. La gran ventaja de usar MIP para calibrar es que la energía depositada es la misma en todas las celdas y capas a lo largo de la trayectoria de la partícula. Sin embargo, esta energía difiere por 3 órdenes de magnitud con la energía depositada por un electrón en el eje de la cascada y en las capas centrales del calorímetro a las energías de la prueba de haz. Por lo tanto, se utilizó una consiguiente calibración con cascadas electromagnéticas para ecualizar la energía depositada en las celdas, teniendo en cuenta que el perfil transversal de la energía hace que se utilice el eje de la cascada como patrón y que el perfil longitudinal obliga a hacer una ecualización capa a capa. Esta calibración consiste en una verificación de la atenuación, una ecualización de las celdas, la implimentación de la corrección por punto de impacto y la verificación de la corrección por pérdidas traseras:

1. Al utilizar cascadas electromagnéticas para verificar la corrección por atenuación, se vió que se necesitaba un factor de amplificación en cada capa para poder ecualizar la energía depositada en las celdas a lo largo de las fibras, ya que existían diferencias de hasta el 40 % en la energía depositada entre los extremos de una misma celda. Además, los valores de estos factores de amplificación reflejaban un mismo comportamiento de las fibras al nivel de supercapas debido a que pertenecían a diferentes partidas de fabricación.

2. Una vez la atenuación se corrigió, las celdas se ecualizaron al valor medio de la energía del eje de la cascada en cada capa. Los factores de corrección que se obtuvieron a diferentes ángulos hasta los 15° permanecen estables dentro del 4 %, lo que confirma que el método utilizado no se limita a sucesos con incidencia normal.

3. Aunque la deposición de energía se ecualizó a un mismo valor en cada capa, la energía depositada en cada celda tiene una dependencia con el punto de impacto de la partícula dentro de la celda, la cual se corrigió con el ratio S1/S3. Este ratio tiene una dependencia

con la energía que se parametrizó con una función de la tangente hiperbólica, donde el *plateau* a derecha e izquierda se corresponden con el máximo y el mínimo de la deposición de energía respectivamente. La función de corrección aplicada se definió con la media de la distribución $S1/S3$ ($f(\langle S1/S3\rangle)$=1), ya que su valor es estable al menos para las energías usadas en la prueba de haz. Una vez que la corrección se aplicó, la variación de la energía de la cascada con $S1/S3$ se redujo del 5 % al 1 %.

4. Las cascadas electromagnéticas no están contenidas completamente en el calorímetro a las energías usadas en la prueba de haz, por lo que se debe estimar esta pérdida de energía. La corrección por pérdidas traseras se basa en la dependencia lineal de la energía faltante con la fracción de energía depositada en la última capa. Otro método para estimar la energía faltante es a través del ajuste del perfil longitudinal de la energía, cuyos resultados son compatibles con los del método de la última capa (14 % de pérdidas traseras para electrones de 250 GeV).

Una vez calibrado, se consigue una resolución en energía por debajo del 2 % para electrones de 180 GeV en ambas configuraciones, la del imán superconductor y la de vuelo. Por otra parte, la comparación de los datos de la primera prueba de haz con el MC simulado de la configuración con imán supercoductor arrojó unas diferencias en el perfil longitudinal de la energía y en el número de señales por capa, lo que explica las discrepancias observadas en las cantidades electromagnéticas utilizadas para discriminar electrones de protones. La diferencia en el perfil de la energía afecta al máximo de la cascada y a las pérdidas traseras. La discrepancia en el máximo de la cascada es compatible con un desarrollo temprano de la cascada en el MC debido a una cantidad extra de material equivalente a 0.25 radiaciones de longitud. Este desplazamiento en el máximo de la cascada afecta también a la estimación de las pérdidas traseras, estando éstas infraestimadas. Por otra parte, la energía contenida en un cilindro de 2 cm de radio alrededor del eje de la cascada presenta un acuerdo sólo cuando se tiene en cuenta un umbral en la energía de la señal de 39 MeV, lo que supone una reducción del 45 % en el número de señales de la cascada pero tan sólo un 1 % en la energía de la cascada. No obstante, estas diferencias no tienen ningún impacto en la separación electrón/protón, aunque si se deben tener en cuenta para conseguir una simulación MC más realista.

Separación electrón/protón Uno de los propósitos del calorímetro es el de proporcionar una separación e/p para reducir el fondo de protones cósmicos. La selección de sucesos electromagnéticos se realizó con un conjunto de cortes basados en cantidades electromagnéticas que proporcionan una eficiencia cercana al 1.3 % para protones de 400 GeV con una eficiencia en electrones de 180 GeV por encima del 80 % en ambas configuraciones. Por lo tanto, la actualización del detector no afectó a las prestaciones intrínsecas del calorímetro. Si además se añade el acuerdo entre la energía y el momento reconstruído, se aumenta el rechazo a protones, reduciendo la eficiencia al 0.067 % para protones de 400 GeV. Sin embargo, debido a la degradación en el momento a causa del cambio de imán, la eficiencia para protones de 400 GeV difiere por un factor 3 entre ambas configuraciones al mismo tiempo que la eficiencia para electrones de 180 GeV se reduce al 65 % en la configuración de vuelo.

Actualmente se está trabajando en métodos alternativos que maximizen el rechazo a protones del calorímetro. Por ejemplo, el uso del análisis multivariante en lugar del conjunto de corte electromagnéticos representa una mejora de un factor 3 en la eficiencia en protones a 100 GV para una eficiencia del 90 % en electrones usando datos reales de vuelo.

El detector de radiación de transición Una vez validada la calibración existente en el TRD se obtuvieron las prestaciones del TRD en la separación e/p, con el resultado de que el cambio de imán junto con el reajuste de los planos del detector de trazas no afectó a la separación e/p del TRD.

Calibración La calibración existente se validó con la energía depositada en los tubos, ya que la cantidad de energía depositada en ellos proporciona la información necesaria para realizar la separación e/p. Por otra parte, la traza del TRD se reconstruye a partir de los grupos de señales que deja el paso de un partícula a lo largo de las 20 capas, siendo la multiplicidad del número de grupos de señales usadas, tanto para electrones como para protones, de aproximadamente 19 en ambas configuraciones, mientras que para la simulación MC la multiplicidad es algo más baja.

La distribución de la energía depositada en los tubos puede ser pura ionización o una suma de ionización y radiación de transición en el caso de que esta última se haya emitido y cuya cantidad se incrementa con el factor de Lorentz γ. La distribución de ionización se ajustó a una función Landau convolucionada con una Gausiana en el rango [0.5,6] keV. Los tubos individuales tienen un valor más probable medio de 1.8 keV para electrones de 250 GeV y el MPV que se obtiene para los tubos de cada capa se mantiene estable dentro del 3 % en ambas configuraciones, lo que valida la equalización en los tubos. Además, el MPV de la ionización tiene una dependencia con el factor de Lorentz γ según lo esperado por la ecuación de Bethe-Block. Por otra parte, la distribución de la transición se obtuvo al substraer el patrón de ionización a la energía total depositada, una vez escalada la distribución de ionización de acuerdo a la dependencia del MPV con γ. La distribución de transición resultante tiene un MPV de 11 keV en ambas configuraciones y la probabilidad de emisión es del 42 % a γ altas.

Separación electrón / protón El detector de radiación de transición proporciona una separación e/p adicional que contribuye a reducir el fondo de protones. Las prestaciones del TRD se obtuvieron utilizando dos métodos. Por un lado, el método del contaje de grupos de señales, el cual es un método directo ya que un corte en el número de grupos de señales por suceso con una energía por encima de un umbral separa partículas con diferentes factores Lorentz γ. Por otro lado, el método de verosimilitud, el cual necesita dos funciones de densidad de probabilidad para poder comprobar dos hipótesis, siendo el que mejor resultados ofrece. Se obtiene una eficiencia del 2 % en protones de 400 GeV en ambas configuraciones para una enficiencia del 90 % en electrones de 180 GeV.

Capacidades de AMS-02 para la medida de positrones cósmicos Para poder medir la señal de positrones sin que se vea sesgada por ninguna contaminación, se necesita una factor de rechazo a protones del orden de 10^4–10^6 además de una medida precisa del signo de la carga para evitar confusiones con electrones mal reconstruídos.

Los resultados obtenidos en la prueba de haz para la supresión de protones estan limitados a un punto de energía, por lo que se utilizó una versión actualizada del software para simular protones y electrones con el fin de obtener el factor de rechazo a diferentes energías y determinar una cota superior de energía para la medida de positrones donde ésta no se vea comprometida por el fondo de protones.

A lo largo del documento ha quedado demostrado que la actualización del detector no afectó a las capacidades intrínsecas del ECAL y del TRD para discriminar electrones de protones. Sin embargo, cuando se hace uso del acuerdo entre la energía y el momento, la eficiencia total de AMS-02 para protones de 400 GeV difiere por un factor 3 entre ambas configuraciones debido a

la degradación en la resolución en el momento. No obstante, se puede contrarrestar si se usan métodos alternativos que mejoren las prestaciones del ECAL en la separación e/p en lugar de utilizar cortes en cantidades electromagnéticas.

El factor de rechazo para protones que se obtiene usando los cortes electromagnéticos en el ECAL, el método de verosimilitud en el TRD y el acuerdo entre la energía y el momento, es superior a 10^5 hasta los 400 GeV cuando se hace uso también del signo de la carga y de la compatibilidad entre las rigideces reconstruídas con diferentes combinaciones de los planos del detector de trazas, lo que representa un fondo residual de protones por debajo del 10 % hasta los 400 GeV. En el caso de los electrones, la confusión de carga se mantiene por debajo del 0.1 % hasta los 400 GeV cuando se impone una compatibilidad entre las rigideces reconstruídas con diferentes combinaciones de los planos del detector de trazas. Con este nivel de contaminación en la medida de positrones, la fracción de positrones se mide hasta los 400 GeV con un fondo de protones lo suficientemente reducido y un fondo de electrones, a causa de la confusión de carga, lo suficientemente bajo como para no sesgar la medida. Además, cuando se introduce una fuente primaria de positrones en el modelo de propagación que reproduce los resultados obtenidos por otros experimentos, el rango de energía se puede extender más allá de los 500 GeV.

Bibliografía

[1] Schlickeiser, R.: *Cosmic Ray Astrophysics.* Springer, 2002. Second Corrected Printing 2003.

[2] Dorman, L. I., D. Venkatesan, and L. I. Dorman: *Solar Cosmic Rays.* Space Science Reviews, 64:183–+, January 1993.

[3] McDonald, F. B., B. J. Teegarden, J. H. Trainor, and W. R. Webber: *The Anomalous Abundance of Cosmic-Ray Nitrogen and Oxygen Nuclei at Low Energies.* The Astrophysical Journal, 187:L105–L108, February 1974.

[4] Cummings, A. C. and E. C. Stone: *Elemental Composition of the Anomalous Cosmic-Ray component.* In *Proceedings of the 20th International Cosmic Ray Conference Moscow*, volume 3, pages 413–+, 1987.

[5] Fisk, L. A., B. Kozlovsky, and R. Ramaty: *An Interpretation of the Observed Oxygen and Nitrogen Enhancements in Low-Energy Cosmic Rays.* The Astrophysical Journal, 190:L35–L37, May 1974.

[6] Pesses, M. E., D. Eichler, and J. R. Jokipii: *Cosmic Ray Drift, Shock Wave Acceleration, and the Anomalous Component of Cosmic Rays.* Astrophysical Journal Letters, 246:L85–L88, June 1981.

[7] Uchiyama, Y., F. A. Aharonian, T. Tanaka, T. Takahashi, and Y. Maeda: *Extremely Fast Acceleration of Cosmic Rays in a Supernova Remnant.* Nature, 449:576–578, October 2007.

[8] Cronin, J. W.: *Cosmic Rays: the Most Energetic Particles in the Universe.* Reviews of Modern Physics Supplement, 71:165–+, March 1999.

[9] Grupen, Claus: *Astroparticle Physics.* Springer, 2005.

[10] Abbasi, R. U. and et al.: *First Observation of the Greisen-Zatsepin-Kuzmin Suppression.* Physical Review Letters, 100(10):101101–+, March 2008.

[11] The Pierre AUGER Collaboration, J. Abraham, and et al.: *Correlation of the Highest-Energy Cosmic Rays with the Positions of Nearby Active Galactic Nuclei.* Astroparticle Physics, 29:188–204, April 2008.

[12] Sokolsky, P. and G. B. Thomson: *Highest Energy Cosmic-Rays and Results from the HiRes Experiment.* Journal of Physics G Nuclear Physics, 34:401–+, November 2007.

[13] Berezinsky, V.: *Ultra High Energy Cosmic Ray Protons: Signatures and Observations.* Nuclear Physics B Proceedings Supplements, 188:227–232, March 2009.

[14] Egorova, V. P. and et al.: *The Spectrum Features of UHECRs below and Surrounding GZK.* Nuclear Physics B Proceedings Supplements, 136:3–11, November 2004.

[15] Shinozaki, K. and M. Teshima: *Agasa results.* Nuclear Physics B Proceedings Supplements, 136:18–27, November 2004.

[16] Roulet, E.: *Latest Results from the Pierre Auger Observatory.* ArXiv e-prints, January 2011.

[17] Farrar, G. R. and A. Gruzinov: *Giant AGN Flares and Cosmic Ray Bursts.* The Astrophysical Journal, 693:329–332, March 2009.

[18] Perkins, Donald: *Particle Astrophysics.* Oxford University Press, 2003.

[19] Smart, D. F. and M. A. Shea: *A review of Geomagnetic Cutoff Rigidities for Earth-Orbiting Spacecraft.* Advances in Space Research, 36:2012–2020, 2005.

[20] Korte, M. and et al.: *New geomagnetic field observations in the south atlantic anomaly region.* Annals of Geophysics, 52(1), 2010.

[21] Fürst, F. and et al.: *Temporal Variations of Strength and Location of the South Atlantic Anomaly as Measured by RXTE.* Earth and Planetary Science Letters, 281:125–133, May 2009.

[22] Parker, E. N.: *The Passage of Energetic Charged Particles Through Interplanetary Space.* Planetary and Space Science, 13:9–+, January 1965.

[23] Potgieter, M. S.: *The Modulation of Galactic Cosmic Rays in the Heliosphere: Theory and Models.* Space Science Reviews, 83:147–158, January 1998.

[24] Gleeson, L. J. and W. I. Axford: *Solar Modulation of Galactic Cosmic Rays.* The Astrophysical Journal, 154:1011–1026, December 1968.

[25] Maestro, P.: *Indirect Search for Dark Matter by Measurements of the Cosmic Ray Positron Spectrum with the AMS-02 Experiment.* PhD thesis, Università degli studi di Siena, September 2003.

[26] Garcia-Munoz, M., P. Meyer, K. R. Pyle, J. A. Simpson, and P. Evenson: *The Dependence of Solar Modulation on the Sign of the Cosmic Ray Particle Charge.* Journal of Geophysical Research, 91:2858–2866, March 1986.

[27] Clem, J. M., D. P. Clements, J. Esposito, P. Evenson, D. Huber, J. L'Heureux, P. Meyer, and C. Constantin: *Solar Modulation of Cosmic Electrons.* The Astrophysical Journal, 464:507–+, June 1996.

[28] Golden, R. L. and et al.: *A Measurement of the Absolute Flux of Cosmic-Ray Electrons.* The Astrophysical Journal, 287:622–632, December 1984.

[29] Golden, R. L. and et al.: *Measurement of the Positron to Electron Ratio in Cosmic Rays above 5 GeV.* The Astrophysical Journal Letters, 457:L103+, February 1996.

[30] Adriani, O. and et al.: *An Anomalous Positron Abundance in Cosmic rays with Energies 1.5-100 GeV*. Nature, 458:607–609, April 2009.

[31] Ackermann, M. and et al.: *Measurement of Separate Cosmic-Ray Electron and Positron Spectra with the Fermi Large Area Telescope*. ArXiv e-prints, September 2011.

[32] Beatty, J. J. and et al.: *New Measurement of the Cosmic-Ray Positron Fraction from 5 to 15 GeV*. Physical Review Letters, 93(24):241102–+, December 2004.

[33] Aguilar, M. and et al.: *Cosmic-Ray Positron Fraction Measurement from 1 to 30 GeV with AMS-01*. Physics Letters B, 646:145–154, March 2007.

[34] Hooper, D., P. Blasi, and P. Dario Serpico: *Pulsars as the sources of High Energy Cosmic Ray Positrons*. Journal of Cosmology and Astroparticle Physics, 1:25–+, January 2009.

[35] Cholis, I., L. Goodenough, D. Hooper, M. Simet, and N. Weiner: *High energy positrons from annihilating dark matter*. Physical Review D, 80(12):123511–+, December 2009.

[36] Chang, J. and et al.: *An Excess of Cosmic Ray Electrons at Energies of 300-800 GeV*. Nature, 456:362–365, November 2008.

[37] Yoshida, K. and et al.: *Cosmic-Ray Electron Spectrum Above 100 GeV from PPB-BETS Experiment in Antarctica*. Advances in Space Research, 42:1670–1675, November 2008.

[38] Ackermann, M. and et al.: *Fermi LAT Observations of Cosmic-Ray Electrons from 7 GeV to 1 TeV*. Physical Review D, 82(9):092004–+, November 2010.

[39] Adriani, O. and et al.: *Cosmic-Ray Electron Flux Measured by the PAMELA Experiment between 1 and 625 GeV*. Physical Review Letters, 106(20):201101–+, May 2011.

[40] Barwick, S. W. and et al.: *Measurements of the Cosmic-Ray Positron Fraction from 1 to 50 GeV*. The Astrophysical Journal Letters, 482:L191+, June 1997.

[41] Boezio, M. and et al.: *The Cosmic-Ray Electron and Positron Spectra Measured at 1 AU during Solar Minimum Activity*. The Astrophysical Journal, 532:653–669, March 2000.

[42] `http://galprop.stanford.edu`.

[43] Moskalenko, I. V. and A. W. Strong: *Production and Propagation of Cosmic-Ray Positrons and Electrons*. The Astrophysical Journal, 493:694–+, January 1998.

[44] Barwick, S. W. et al.: *The Energy Spectra and Relative Abundances of Electrons and Positrons in the Galactic Cosmic Radiation*. The Astrophysical Journal, 498:779–+, May 1998.

[45] Sanuki, T. and et al.: *Precise Measurement of Cosmic-Ray Proton and Helium Spectra with the BESS Spectrometer*. The Astrophysical Journal, 545:1135–1142, December 2000.

[46] Strong, A. W., I. V. Moskalenko, and V. S. Ptuskin: *Cosmic-Ray Propagation and Interactions in the Galaxy*. Annual Review of Nuclear and Particle Science, 57:285–327, November 2007.

[47] Ahlen, S. and et al.: *An Antimatter Spectrometer in Space*. Nuclear Instruments and Methods in Physics Research A, 350:351–367, October 1994.

[48] Blau, B., S. M. Harrison, H. Hofer, S. R. Milward, J. S. H. Ross, S. C. C. Ting, J. Ulbricht, and G. Viertel: *The Superconducting Magnet of AMS-02.* Nuclear Physics B Proceedings Supplements, 113:125–132, 2002.

[49] Battiston, R.: *The Anti Matter Spectrometer (AMS-02):. a Particle Physics Detector in Space.* In C. Leroy, P.-G. Rancoita, M. Barone, A. Gaddi, L. Price, & R. Ruchti (editor): *Astroparticle, Particle and Space Physics, Detectors and Medical Physics Applications*, pages 741–750, April 2010.

[50] Hauler, F. and et al.: *The AMS-02 TRD for the International Space Station.* IEEE Transactions on Nuclear Science, 51:1365–1372, August 2004.

[51] Doetinchem, P. V. and et al.: *Performance of the AMS-02 Transition Radiation Detector.* Nuclear Instruments and Methods in Physics Research A, 558:526–535, March 2006.

[52] Bindi, V. and et al.: *The Scintillator Detector for the Fast Trigger and Time-of-Flight (TOF) Measurement of the Space Experiment AMS-02.* Nuclear Instruments and Methods in Physics Research A, 623:968–981, November 2010.

[53] Zuccon, P. and the AMS Tracker collaboration: *The AMS Silicon Tracker: Construction and Performance.* Nuclear Instruments and Methods in Physics Research A, 596:74–78, October 2008.

[54] Alcaraz, J. and et al.: *The Alpha Magnetic Spectrometer Silicon Tracker: Performance Results with Protons and Helium Nuclei.* Nuclear Instruments and Methods in Physics Research A, 593:376–398, August 2008.

[55] Alpat, B. and et al.: *Charge Determination of Nuclei with the AMS-02 Silicon Tracker.* Nuclear Instruments and Methods in Physics Research A, 540:121–130, March 2005.

[56] Alpat, B. and et al.: *The Internal Alignment and Position Resolution of the AMS-02 Silicon Tracker Determined with Cosmic-Ray Muons.* Nuclear Instruments and Methods in Physics Research A, 613:207–217, February 2010.

[57] von Doetinchem, P., W. Karpinski, T. Kirn, K. Lübelsmeyer, S. Schael, and M. Wlochal: *The AMS-02 Anticoincidence Counter.* Nuclear Physics B Proceedings Supplements, 197:15–18, December 2009.

[58] Pereira, R.: *The AMS-02 RICH Detector: Performance During Ground-Based Data Taking at CERN.* Nuclear Instruments and Methods in Physics Research A, 639(1):37–41, May 2011. Proceedings of the Seventh International Workshop on Ring Imaging Cherenkov Detectors.

[59] Goy, C. and the AMS calorimeter group: *The AMS-02 3D-imaging calorimeter: A tool for cosmic rays in space.* Journal of Physics Conference Series, 160(1):012041–+, April 2009.

[60] Falco, S. D.: *Results of 2007 Test Beam of AMS-02 Electromagnetic Calorimeter.* Advances in Space Research, 45:112–122, January 2010.

[61] Kounine, A.: *Status of the AMS Experiment.* ArXiv e-prints, September 2010.

[62] K., Lübelsmeyer and et al.: *Upgrade of the Alpha Magnetic Spectrometer (AMS-02) for Long Term Operation on the International Space Station (ISS).* Nuclear Instruments and Methods in Physics Research Section A: Accelerators, Spectrometers, Detectors and Associated Equipment, 654(1):639–648, 2011.

[63] `http://geant4.cern.ch`.

[64] `http://root.cern.ch`.

[65] Caraffini, D.: *Anti-proton Flux Detection and Indirect Search for Dark Matter with the AMS-02 Experiment.* PhD thesis, Università degli studi di Perugia, 2004.

[66] `http://ams.cern.ch/AMS/Analysis/hpl3itp1/root02_v5/html/index.html`.

[67] Falchini, E.: *AMS-02 Dark Matter Search Inspecting Cosmic Ray Positron Spectrum.* AMS Note, December 2004.

[68] Goy, C. and S. Rosier: *The AMS Calorimeter Performance Studies with the 2007 Test Beam Data.* AMS Note, July 2008.

[69] Fiasson, A.: *e/p Rejection Study with the ECAL Esing Multivariate Approach on Test Beam Data.* AMS Note, January 2011.

[70] Hooper, D. and S. Profumo: *Dark matter and collider phenomenology of universal extra dimensions.* Physics Reports, 453:29–115, December 2007.